Ab initio lattice dynamics of complex structures

Computational design of novel materials for hydrogen storage

Voss, Johannes

Publication date:
2008

Document Version
Early version, also known as pre-print

Ab initio lattice dynamics of complex structures

Computational design of novel materials for hydrogen storage

Johannes Voss

Ph.D. Thesis
October 2008

Center for Atomic-scale Materials Design
Department of Physics
Technical University of Denmark
DK-2800 Kongens Lyngby

and

Materials Research Division
Risø National Laboratory for Sustainable Energy
Technical University of Denmark
DK-4000 Roskilde

Contents

Preface

This thesis is submitted in candidacy for the Ph.D. degree from the Technical University of Denmark (DTU). The work has been carried out over the last three years in the Materials Research Division, Risø National Laboratory for Sustainable Energy, DTU (Risø DTU) and at the Center for Atomic-scale Materials Physics (CAMP)/the Center for Atomic-scale Materials Design (CAMD), Department of Physics, DTU. Supervision at CAMP/CAMD, Department of Physics, DTU was provided by Professor Jens K. Nørskov. Dr. Tejs Vegge was the supervisor in the Materials Research Division, Risø DTU. Financial support was provided by the NABIIT program funded by the Danish Research Councils for Strategic Research.

I would like to thank my supervisors for offering their expertise and guidance and for their dedication to this project. My office-mate Qing Shi is thanked for his contribution of experimental data and their laborious evaluation and for having introduced me to the culinary delights of Chinese cuisine. Jens S. Hummelshøj is thanked for his collaboration on the crystal structure search, contributing his expertise in coordination analysis and structural visualization. I thank PD Dr. Zbigniew Łodziana for collaboration and fruitful discussion on the topic of structural instabilities. Thanks for proofreading of the Danish abstract go to Nicolai C. Bork. I furthermore thank my former and present colleagues Dr. Anders Andreasen, Dr. Didier Blanchard, Dr. Pavel Fursikov, Dr. Liga Grinberga, Hjalte S. Jacobsen, Jan Kehres, Assoc. Prof. Kim Lefmann, Dr. Allan S. Pedersen, and Dr. Adem Tekin for inspiring discussions.

My warmest thanks to my family, Margret, Gerhard, Nilde, Giuseppe, and especially to Annamaria and Erika, for their love and support.

Kongens Lyngby, October 2008

Johannes Voss

Abstract

In this thesis, density functional theory is applied in a study of thermodynamic properties of so-called complex metal hydrides, which are promising materials for hydrogen storage applications.

Since the unit cells of these crystals can be relatively large with many symmetrically inequivalent atomic coordinates, we have developed a new numerical optimization scheme, which allows for a fast convergence of the coordinate relaxation.

Moreover, a method for the efficient calculation of phonon frequencies has been developed, which is based on a combination of density functional theory calculations and the electrostatics of effective point charge systems. The method is $O(N)$ times faster than conventional approaches employing a calculation of the full Hessian matrix (N: number of atoms per unit cell) and is thus suitable for the assessment of thermodynamic stabilities based on the vibrational entropies of large systems in particular.

A more detailed analysis of the phonon spectrum has been performed for the compound $Mg(BH_4)_2$, where several crystal symmetries have been proposed theoretically and experimentally. By means of an analysis of the instabilities of these structures, a new, stable phase has been determined.

Aiming at finding scaling relationships between alloy stabilities and computationally inexpensive properties, the stabilities of cation-alloyed metal aluminum hexahydrides have been studied. The analysis shows that charge density symmetries are correlated to the stability. In addition, the vibrational entropies of these systems have been estimated in a maximally localized Wannier function basis without calculating charge density perturbations.

In a combined experimental and computational approach, the kinetic properties of hydrogen diffusion processes in sodium aluminum hydride have been studied, showing that the mobility of hydrogen is limited by high energetic barriers in the intermediate decomposition product Na_3AlH_6 in particular, and that the effect of titanium as a dopant on the dynamics is negligible.

The presented methods and studies demonstrate possibilities for a design of new materials for hydrogen storage applications based on qualitative screening and the precise analysis of known structures.

Resumé

I denne afhandling bliver tæthedsfunktionalteori anvendt i en række studier af termodynamiske egenskaber af såkaldte komplekse metalhydrider, som er potentielle materialer til brintlagring.

Fordi enhedscellerne af disse krystaller kan være store med mange symmetrisk uafhængige koordinater, er en ny numerisk strukturoptimeringsmetode blevet udviklet. Denne algoritme sikrer en hurtig konvergens af relaksationen af atomernes koordinater.

Derudover er en hurtig algoritme til beregningen af fonon frekvenser blevet udviklet, baseret på en kombination af tæthedsfunktionalteori og en model Hamilton operator konstrueret fra effektive elektrostatiske systemer. Metoden er $O(N)$ gange hurtigere end konventionelle algoritme (N: antal af atomer i enhedscellen) og er derfor velegnet til berigningen af termodynamisk stabilitet af komplekse systemer baseret på vibrationernes bidrag til entropien.

En mere præcis beregning af fononspektret er blevet udført for systemet $Mg(BH_4)_2$, hvor mange forskellige krystalsymmetrier er blevet foreslået teoretisk og eksperimentelt. Ved hjælp af en analyse af ustabilitet af disse strukturer er en ny stabil fase blevet fundet.

Fordi legeringer kan vise gunstige termodynamiske egenskaber, er stabiliteten af legerede metal aluminum hexahydrider blevet beregnet. Analysen viser, at symmetrier i ladningstæthed er korrelerede med stabiliteten. Baseret på en transformation til maksimalt lokaliserede Wannier funktioner, er vibrationsentropier blevet vurderet uden beregning af perturbationer.

For systemet $NaAlH_4$, er kinetiske egenskaber af brintdiffusionsprocesser blevet beregnet og derudover undersøgt eksperimentelt. Dette kombinerede studie viser, at bevægelighed af brint er indskrænket af høje energetiske barrierer samt at dotering med titanium har kun en begrænset effekt på denne dynamik.

De præsenterede metoder og studier antyder mulighederne for udvikling af nye materialer til brintlagring baseret på kvalitativ screening og præcise

analyser af kendte strukturer.

Included publications

[P1] J. Voss and T. Vegge, *Symmetry enhanced convergence of crystal structure optimization.* Submitted to J. Comp. Phys.

[P2] J. Voss and T. Vegge, *Γ-point lattice free energy estimates from O(1) force calculations.* J. Chem. Phys. **128**, 184708 (2008).

[P3] J. Voss, J. S. Hummelshøj, Z. Łodziana, and T. Vegge, *Structural stability and decomposition of $Mg(BH_4)_2$ isomorphs — an ab initio free energy study.* Accepted for publication in J. Phys.: Condens. Matter.

[P4] J. Voss and T. Vegge, *Understanding the thermodynamic stabilities of cation-alloyed complex metal hydrides from ground state properties of model structures.* Submitted to Model. Simul. Mater. Sci. Eng.

[P5] J. Voss, Q. Shi, H. S. Jacobsen, M. Zamponi, K. Lefmann, and T. Vegge, *Hydrogen dynamics in Na_3AlH_6: A combined density functional theory and quasielastic neutron scattering study.* J. Phys. Chem. B **111**, 3886 (2007).

[P6] Q. Shi, J. Voss, H. S. Jacobsen, K. Lefmann, M. Zamponi, and T. Vegge, *Point defect dynamics in sodium aluminum hydrides — A combined quasielastic neutron scattering and density functional theory study.* J. Alloys Compd. **446**, 469 (2007).

1

Introduction

Computational materials design

The prediction of materials properties and their optimization with respect to the composition before synthesis in experiments is a key problem in computational materials science. Two major challenges for the design of new materials based on simulations at the atomic scale are the prediction of crystal structures [1] and the assessment of properties at larger scales than the length and time scales accessible to atomistic modeling approaches [2]. Recent advances in the field of crystal structure prediction are the metadynamics technique [3], including order parameters as dynamic variables in addition to the atomic coordinates for a simulation of phase transitions, and evolutionary algorithms [4]. Multiscale approaches [5] bridge the gaps from atomistic up to mesoscopic and macroscopic scales, where transition state theory [6–8], *e.g.*, allows for an estimate of the rates of rarely occurring processes.

For the calculation of properties at the atomic scale, so-called *ab initio* or first-principles approaches, which are based on a quantum mechanical description of the interactions between electrons and atomic nuclei with the atomic numbers and masses as only input, have the advantage of a wider range of applicability with respect to *e.g.* different chemical environments of the atomic nuclei compared to empirical methods at the price of higher computational complexity [9]. The *ab initio* calculation of the electronic ground state structure within density functional theory [10] in the Kohn-Sham scheme [11] has become a standard approach to study bulk crystal structures, surfaces, and molecules (in particular for systems containing $\gg$10 electrons, where an accurate treatment using wave-function-based methods usually is computationally

unfeasible) [12].

In order to predict the phase stabilities of crystal structures, the dominant entropic contributions to the free energy can be obtained from the numerically calculated phonon density of states for solid phases with negligible disorder [13–16] or *e.g.* within the cluster expansion approach for crystalline alloys with occupational disorder [17, 18]. The computational studies presented in this thesis focus on the former type of systems, *i.e.* ideal crystal structures, where an analysis of the phonon dispersion can identify thermodynamic instabilities and phase transition paths to lower energetic structures.

The calculations and developed methods presented here aim at demonstrating ways to a design of novel solid state hydrogen storage materials, based on an understanding of known structures and correspondingly derived strategies for qualitative screening studies of new materials.

Hydrogen as an energy carrier

Hydrogen as a synthetic fuel — if produced by the splitting of water using renewable, carbon-neutral energy resources — could become a solution to the global problems of climate change due to CO_2 emissions [19, 20] and increasing demand for fossile fuels, especially in the transportation sector, confronted with limited resources [21]. Burning of hydrogen with oxygen yields water as only exhaust product. Hydrogen is furthermore the ideal fuel for fuel cells, where the achievable efficiency of energy conversion is not subject to the thermodynamic constraints of Carnot processes, which require a cyclic dissipation of entropy.

Besides a sustainable and efficient production of hydrogen, ideally based *e.g.* on photovoltaic cells and electrolysis of water or direct splitting in photochemical cells [22–25], an approach to store hydrogen with sufficient capacity at safe pressures needs to be developed for mobile applications in particular [26]. Hydrogen can be stored reversibly *e.g.* as a pressurized gas, a liquid, by physisorption on surfaces, or by chemisorption in solid matrices.

Hydrogen storage

Conventional high-pressure tanks consisting of steel are used to store hydrogen gas at pressures up to 20 MPa. Since the wall thickness has to be increased with the pressure, thus limiting the gravimetric storage capacity, light weight composite cylinders are developed that withstand pressures up to 80 MPa, approaching capacities of $\gtrsim$10 mass-% hydrogen [27]. The maximally achievable volumetric capacity, however, is only $\lesssim$40 kg H_2/m^3 [27], and there are safety concerns related to the storage at these high pressures [26, 27].

A higher volumetric capacity of ∼70 kg H_2/m^3 is achieved by storing liquid hydrogen in cryogenic tanks [27]. For a liquefaction by isenthalpic Joule-Thomson expansion, hydrogen is pre-cooled with liquefied nitrogen, since the inversion temperature of hydrogen (∼200 K) lies below room temperature. The total process requires a third of the energy content of the stored hydrogen [28]. A further disadvantage is a permanent boil-off of hydrogen.

In physisorption-based storage approaches, the adsorption of molecular hydrogen onto surfaces is mediated by van der Waals interactions. Due to this weak type of interaction, storage by physisorption requires low temperatures. Maximally achievable gravimetric hydrogen storage capacities using carbon nanotubes and other carbon nanostructures are *e.g.* only of the order of 1 mass-% at room temperature and high pressures, and only a few percent higher at liquid nitrogen temperature (77 K) [29, 30]. In order to reduce the limitations given by the weak van der Waals forces, hydrogen molecules can be trapped in micro-porous materials [31]. The proposed storage of hydrogen in zeolites [32] has the disadvantage of a high mass density of the aluminosilicate framework [33]. Due to their low densities, metal-organic frameworks could be candidates for on-board hydrogen storage applications [34–36]. While reversible hydrogen uptake of up to 7.5 mass-% at 77 K has been reported, at room temperature the storage of only $\lesssim$1.5 mass-% hydrogen has been achieved [37]. Moreover, encapsulation of hydrogen molecules in clathrates [38] has been proposed as an approach to hydrogen storage [39]. High pressures of over 200 MPa required for a formation of the clathrate hydride can be reduced by the addition of *e.g.* tetrahydrofuran for stabilization [40], reducing the storage capacity, however, to only ∼1 mass-% for pressures <60 MPa [41, 42].

In chemisorption-based approaches, molecular hydrogen is dissociated before integration in a metal lattice or formation of a chemical compound and recombined upon release. For the storage in form of metal hydrides, hydrogen atoms occupy interstitial sites in the metal lattice. Charging can be performed by absorption of hydrogen dissociated at the surface or of hydrogen atoms from an electrolyte. During a first order phase transition between an initial solid solution of hydrogen and a sub-lattice of hydrogen, the sorption of hydrogen takes place at constant pressure. For host alloys of lanthanides and *e.g.* Ni, Al, Mn, or Co (on the basis of the prototype structure $LaNi_5$), which are used as anodes for nickel metal hydride batteries, this allows for desorption of the stored hydrogen at pressures of the order of 0.1 MPa at room temperature [43]. Due to the large masses of the metal atoms, gravimetric densities are typically limited to 1–2 mass-% depending on the alloy. The binary hydride MgH_2 has a storage capacity of 7.6 mass-%, but exhibits a desorption temperature of ∼570 K and slow sorption kinetics, which can be improved upon by ball milling of magnesium with *e.g.* vanadium [44]. Alloying with *e.g.* nickel [45] has the

disadvantage of a reduced gravimetric storage capacity.

The so-called complex metal hydrides formed by alkali or earth-alkali metals and $(AlH_{n\in\{4,6\}})^{(n-3)-}$, $(NH_2)^-$, or $(BH_4)^-$ groups (despite the compounds corresponding to the former two groups not containing ionic metal complexes) are considered as potential hydrogen storage materials for on-board applications due to their both good volumetric and gravimetric capacities [46, 47]. However, the storage of hydrogen by the formation of chemical compounds, where the decomposition often proceeds in several steps with significant structural changes, can lead to a desorption at impractically high temperatures and to slow sorption kinetics requiring high pressures for hydrogenation. Complex hydrides have thus only attracted interested as storage materials, since Bogdanović and Schwickardi [48] have shown in 1997 that doping of $NaAlH_4$ with titanium lowers the desorption temperature and allows for cyclic re-hydrogenation at pressures around 6–15 MPa. As titanium also improves the sorption properties of other complex hydrides [49, 50], understanding the role of the titanium dopant can be of importance for the design of catalysts. Experiments indicate a dispersion of titanium atoms into aluminum particles [51], where density functional theory calculations show that titanium could catalyze H–H bond breaking [52, 53]. Furthermore, volatile Al_nH_{3n} species are observed, which could improve the mass transport between the decomposition products Al and NaH [54].

Lithium amide, $LiNH_2$, mixed with lithium hydride has been proposed as a hydrogen storage material with a capacity of ∼10 mass-% H_2 [55]. The high desorption temperature of ∼700 K can be reduced to about 370 K by replacing a third of the lithium by magnesium atoms [56], only reducing the theoretical gravimetric storage capacity to about 7 mass-%.

Excluding the hydrogen content in lithium hydride, which decomposes at too high temperatures for practical applications, lithium borohydride, $LiBH_4$, has a high storage capacity of about 14 mass-%, where the decomposition temperature of ∼570 K can be lowered by about 100 K by a mixture with SiO_2 powder [57]. A further borohydride of interest for hydrogen storage applications is $Mg(BH_4)_2$. The phases involved in the decomposition process, which is not fully understood yet, depend on the experimental conditions [58–61]. Powder diffraction patterns reveal large unit cells for a low- and an idealized high-temperature phase of $Mg(BH_4)_2$, containing 330 (see Fig. 1.1) and 176 atoms per asymmetric unit, respectively [62, 63]. The high-temperature phase is furthermore proposed to consist of a disordered arrangement of layers of ∼20 Å thickness. This list of proposed solid state hydrogen storage materials is not comprehensive; other approaches are *e.g.* based on a mixture of borohydrides and amides [64].

Besides the generally difficult task of structural prediction, the challenges for

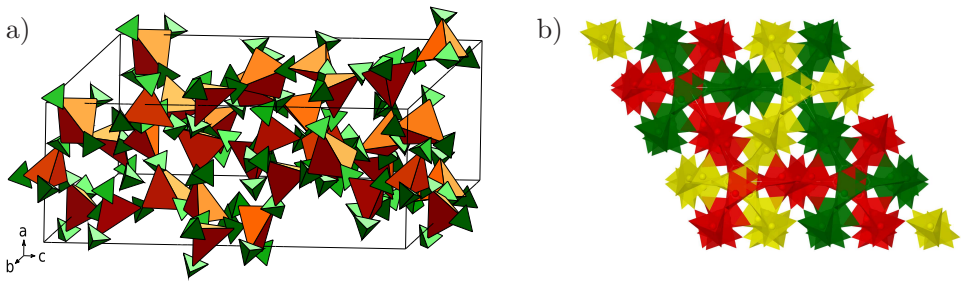

Figure 1.1: Depiction of computationally relaxed unit cells and atomic coordinates of a hexagonal low-temperature phase of $Mg(BH_4)_2$ containing 30 formula units per primitive cell. The coordination of magnesium with boron atoms is represented by orange tetrahedra (a) and by different colors indicating rings of coordination polyhedra (b; from [P3]; figure created by Jens S. Hummelshøj), respectively. The coordination of boron with hydrogen atoms is depicted as green tetrahedra (omitted for simplicity in the figure to the right).

the computational design of novel complex hydrides for hydrogen storage applications in particular are *i.a.* related to the complexity of the crystal structures, requiring a large computational effort for the determination of the equilibrium coordinates within density functional theory. Since furthermore the coordinates of several structures have to be optimized for a search for stable phases, an optimization scheme minimizing the number of the computationally expensive electronic structure calculations is of particular importance. Similarly, the calculation of lattice free energies for a comparison of phase stabilities and estimates of decomposition temperatures is computationally expensive for large structures with many symmetrically inequivalent sites.

Outline

Followed by a description of new approaches to these computational problems, the theoretical background for the calculations is summarized. In Ch. 2, the theory for the calculation of the electronic structure is described. Ch. 3 deals with the dynamics of the degrees of freedom of the atomic nuclei, explaining the calculation of the phonon dispersion and of the rates of dynamic events in solids, *e.g.* diffusive hydrogen jumps.

In Ch. 4, a structure optimization procedure is presented, which takes advantage of crystal symmetries, leading to an improved convergence for systems with many atoms per unit cell in particular, which allows for an efficient determination of the equilibrium coordinates of *e.g.* the experimentally proposed phases of $Mg(BH_4)_2$. Furthermore, a new approach to the calculation of ap-

proximate lattice free energies is presented, which has the same computational complexity as a ground state calculation, irrespective of the number of symmetrically inequivalent atomic displacements, and is therefore suitable for screening studies of *e.g.* alloy stabilities.

In Ch. 5, results for stabilities of complex metal hydrides and point defect dynamics in sodium aluminum hydride are presented. An analysis of phase stabilities and transitions for magnesium borohydride is followed by a numerical charge density analysis of model structures for cation-alloyed metal aluminum hexahydrides, showing a correlation between symmetries and alloy stabilities. Finally, the results of a combined experimental and computational study of the influence of the titanium dopant on bulk diffusion of hydrogen in sodium aluminum hydride are summarized, demonstrating the advantages of this approach for the analysis of dopants for complex hydrides.

2

Electronic structure

The quantum mechanical problem of interacting electrons and atomic nuclei is of fundamental importance to the fields of condensed matter physics, chemistry, and materials science. A system of electrons and atomic nuclei is described by the many-particle Hamiltonian

$$\begin{aligned}\hat{\mathcal{H}} &= \sum_i \frac{\hat{p}_i^2}{2m} + \sum_I \frac{\hat{P}_I^2}{2M_I} - e^2 \sum_{i,I} \frac{Z_I}{\left|\hat{\boldsymbol{r}}_i - \hat{\boldsymbol{R}}_I\right|} \\ &+ \frac{e^2}{2} \sum_{i,j\neq i} \frac{1}{|\hat{\boldsymbol{r}}_i - \hat{\boldsymbol{r}}_j|} + \frac{e^2}{2} \sum_{I,J\neq I} \frac{Z_I Z_J}{\left|\hat{\boldsymbol{R}}_i - \hat{\boldsymbol{R}}_j\right|},\end{aligned} \tag{2.1}$$

where M_I and Z_I are the nuclear masses and proton numbers, respectively. $\hat{\boldsymbol{P}}_I$ and $\hat{\boldsymbol{R}}_I$ are the nuclear and $\hat{\boldsymbol{p}}_i$ and $\hat{\boldsymbol{R}}_i$ the electronic momentum and position operators, respectively (in real space coordinates, $\hat{\boldsymbol{p}} \rightarrow -i\hbar\boldsymbol{\nabla}$). $h = 2\pi\hbar$ is Planck's constant, e is the elementary charge, and m is the electron mass. The first two terms in Eq. (2.1) are the kinetic energy operators for the electronic and nuclear subsystems, respectively. The following term accounts for the Coulomb attraction between electrons and nuclei. The remaining sums accounting for Coulomb repulsion are divided by two, because all particle pairs enter the sums twice. In the following, we use atomic units by defining $e = m = \hbar = 1$; lengths are given in units of the Bohr radius $a_0 \approx 0.529$ Å and energies in Hartree H ≈ 27.211 eV.

The eigenenergies $\mathcal{E}$ of the system are given by the time-independent Schrödinger equation [65]

$$\hat{\mathcal{H}}|\mathcal{E}\rangle = \mathcal{E}|\mathcal{E}\rangle. \tag{2.2}$$

A first approximation to this complex problem is the Born-Oppenheimer approximation [66], which is a separation of nuclear and electronic timescales, as the nuclear masses are at least three orders of magnitude larger than the electron mass. The electronic system is assumed to adiabatically follow changes in the nuclear coordinates $\boldsymbol{R}_I$, *i.e.* nuclear motion does not cause excitations in the electronic system. The wave functions $|\mathcal{E}\rangle$ separate into products of electronic and nuclear wave functions, and the electronic Schrödinger equation can be solved separately for a fixed nuclear coordinate configuration. The corresponding electronic Hamiltonian is given in real space coordinates as

$$H = -\frac{1}{2}\sum_i \nabla_i^2 + \frac{1}{2}\sum_{i,j\neq i}\frac{1}{|\boldsymbol{r}_i - \boldsymbol{r}_j|} - \sum_{i,I}\frac{Z_I}{|\boldsymbol{r}_i - \boldsymbol{R}_I|}. \tag{2.3}$$

This Hamiltonian and the corresponding electronic eigenenergies and eigenvectors only depend parametrically on the nuclear coordinates R_I. For the calculation of the total energy, the electrostatic energy of the nuclei, assumed as point charges, is added to the energy of the electronic system.

In order to calculate the adiabatic forces acting on the nuclear point charges, *i.e.* the gradient of the total energy in the space of the nuclear coordinates, one considers the derivative of the total energy with respect to a variable, the electronic Hamiltonian depends parametrically on. The contribution of the ion-ion interaction is simply given by the classical Coulomb forces in a system of point charges. The derivative of the electronic energy E with respect to a parameter λ, *e.g.* a nuclear coordinate, is (using that the norm of the electronic ground state $|\Psi\rangle$ does not depend on λ)

$$\begin{aligned}\frac{\partial E}{\partial \lambda} &= \left\langle \Psi \middle| \frac{\partial \hat{H}}{\partial \lambda} \middle| \Psi \right\rangle + \left\langle \frac{\partial \Psi}{\partial \lambda} \middle| \hat{H} \middle| \Psi \right\rangle + \left\langle \Psi \middle| \hat{H} \middle| \frac{\partial \Psi}{\partial \lambda} \right\rangle \\ &= \left\langle \Psi \middle| \frac{\partial \hat{H}}{\partial \lambda} \middle| \Psi \right\rangle + E \underbrace{\frac{\partial}{\partial \lambda} \langle \Psi | \Psi \rangle}_{=0}.\end{aligned} \tag{2.4}$$

As the kinetic energy operator of the electrons does not depend on the nuclear coordinates, the electronic contribution to the adiabatic forces is only due to the (negative of the) expectation value of the potential energy gradient. Since the corresponding terms in (2.3) depending on the nuclear coordinates are sums of single electron operators, the integral over the electronic degrees of freedom reduces to a three-dimensional integral of the potential gradient times the probability density to find an electron (not depending on an electronic index, as electrons are indistinguishable particles; this will be discussed in more detail in Sec. 2.1). The gradient can thus be calculated from the classical electrostatic interaction of the nuclear point charges with the electronic ground state

charge density. Eq. (2.4) is known as the Hellmann-Feynman theorem [67, 68]. This theorem reflects the fact that first order variations in the eigenvectors change the corresponding eigenvalues only to second order — the eigenstates $|\Psi\rangle$ are stationary points of the energy functional $E[|\Psi\rangle]$. Once the electronic ground state is calculated, the gradient at the Born-Oppenheimer surface can be obtained efficiently from the unperturbed ground state density, which is of importance for optimization of the nuclear coordinates and molecular dynamics simulations.

The electronic Schrödinger equation

$$\hat{H}|\Psi\rangle = E|\Psi\rangle \tag{2.5}$$

allows for numerical solution only for systems containing a very small number of electrons due to the Coulomb interaction between the electrons. Further approximations are necessary to handle larger systems. In the following, two standard approaches are summarized, which map the many-particle problem onto effective single-particle problems. Essential for these approximations is the Rayleigh-Ritz variational principle [69, 70] for the ground state energy E_0:

$$\forall\,|\Phi\rangle \;\mid\; \langle\Phi|\Phi\rangle < \infty : \quad E[|\Phi\rangle] = \frac{\left\langle \Phi \left| \hat{H} \right| \Phi \right\rangle}{\langle\Phi|\Phi\rangle} \geq E_0. \tag{2.6}$$

The functional (2.6) is minimal if, and only if $|\Phi\rangle$ is a ground state wave function.

Before starting to discuss the density functional theory approach which was used for the calculations presented in this thesis, we begin with an outline of the Hartree-Fock approach, to show the differences between considering the electronic ground state energy as functionals of the density and the many-electron wave function, respectively, and the implications for approximating correlations.

2.1 Hartree-Fock theory

In the Hartree approximation [71], the many-electron ground state is assumed to separate into a product of single-electron wave functions. In a mean field approach, the Coulomb interaction of a single electron with the remaining $N-1$ electrons with wave functions $\langle r|j\rangle$ is approximated by the interaction with the electrostatic potential generated by the sum of the charge densities of the remaining electrons (V_{ext} is the external potential given by *e.g.* a fixed config-

uration of atomic nuclei):

$$V_{\text{eff}}^{(i)} = V_{\text{ext}} + \int \mathrm{d}^3 r' \frac{\sum_{j \neq i} |\langle \boldsymbol{r}' | j \rangle|^2}{|\boldsymbol{r} - \boldsymbol{r}'|}, \tag{2.7}$$

resulting in a set of N coupled single-electron Schrödinger equations with effective potentials $V_{\text{eff}}^{(i)}$:

$$\left[-\frac{\nabla^2}{2} + V_{\text{eff}}^{(i)} \right] \langle \boldsymbol{r} | i \rangle = \varepsilon_i \langle \boldsymbol{r} | i \rangle. \tag{2.8}$$

In order to calculate the many-electron ground state energy E, the Coulomb repulsion energy has to be subtracted from the sum of the effective single-electron energies:

$$E = \sum_i \varepsilon_i - \frac{1}{2} \sum_{j \neq k} \int \mathrm{d}^3 r \int \mathrm{d}^3 r' \frac{|\langle \boldsymbol{r} | j \rangle \ \langle \boldsymbol{r}' | k \rangle|^2}{|\boldsymbol{r} - \boldsymbol{r}'|}, \tag{2.9}$$

because the effective potentials $V_{\text{eff}}^{(i)}$ cause the electron-electron interaction to be counted twice.

Since electrons are indistinguishable fermions, electronic wave functions must be antisymmetric with respect to the exchange of two electrons, which implies a vanishing wave function for two electrons in the same single-electron state (Pauli exclusion principle [72]). This is taken into account by the Hartree-Fock approximation [73], which antisymmetrizes the Hartree ansatz by assuming that the electronic ground state $\langle x_1, ..., x_N | \Psi \rangle$ can be expressed as a single Slater determinant [74]:

$$\langle x_1, ..., x_N | \Psi \rangle = \frac{1}{\sqrt{N!}} \begin{vmatrix} \langle x_1 | \psi_1 \rangle & \cdots & \langle x_1 | \psi_N \rangle \\ \vdots & \ddots & \vdots \\ \langle x_N | \psi_1 \rangle & \cdots & \langle x_N | \psi_N \rangle \end{vmatrix}, \tag{2.10}$$

where $x_i = (\boldsymbol{r}_i, \sigma \in \{\uparrow, \downarrow\})$ is a combined orbital and spin coordinate, and $|\psi_j\rangle$ is a spin-orbital occupied by one electron. The resulting set of equations can be transformed into the eigenvalue problem [75]

$$\hat{\mathcal{F}} |\psi_k\rangle = f_k |\psi_k\rangle, \tag{2.11}$$

with the Fock operator $\hat{\mathcal{F}}$ defined as

$$\begin{aligned} \left\langle x \left| \hat{\mathcal{F}} \right| \psi_k \right\rangle &= \left[-\frac{\nabla^2}{2} + V_{\text{ext}} + \sum_{i,\sigma'} \int \mathrm{d}^3 r' |\langle x' | \psi_i \rangle|^2 \frac{1}{|\boldsymbol{r} - \boldsymbol{r}'|} \right] \langle x | \psi_k \rangle \\ &- \sum_{j,\sigma'} \int \mathrm{d}^3 r' \ \langle \psi_j | x' \rangle \frac{1}{|\boldsymbol{r} - \boldsymbol{r}'|} \langle x' | \psi_k \rangle \ \langle x | \psi_j \rangle . \end{aligned} \tag{2.12}$$

The effective electrostatic potential or Hartree potential in (2.12) includes the contributions from all electrons, but the self-interaction for $i = k$ is canceled exactly by the last term, a sum over the exchange integrals, for $j = k$. The many-electron ground state energy E is given as

$$E = \frac{1}{2}\sum_{k=1}^{N}\left(f_k + \left\langle \psi_k \left| -\frac{\nabla^2}{2} + V_{\text{ext}} \right| \psi_k \right\rangle\right). \tag{2.13}$$

Both the Hartree and Hartree-Fock partial differential equations (Eqs. (2.8) and (2.11), respectively) contain potentials, which depend on the solution of the partial differential equations. Solutions minimizing the many-electron ground state energy according to Eq. (2.6) can be obtained by variation of the parameters of trial wave functions or by optimizing the expansion coefficients in a suitable, finite basis set. Most commonly, however, the solutions are obtained iteratively by starting with a construction of the potentials from a guess for the wave functions and updating the potentials according to the resulting wave functions, until self-consistency is reached.

2.1.1 Density matrices

In the Hartree ansatz, the probability of finding electrons is given by a product of the corresponding single-electron densities; the electrons are uncorrelated. To study systems of indistinguishable particles, it is convenient to introduce single- and two-particle density matrices, as all operators in the Hamiltonian (2.3) act on single electrons or pairs of electrons, respectively. Since the particles are indistinguishable, tracing out all electronic degrees of freedom except for the ones of one or two electrons, respectively, discards the information of the many-particle wave function that is redundant for the calculation of the energy. The diagonal $n(x)$ of the single-particle density matrix $\rho(x; x')$

$$n(x) = \rho(x; x) \tag{2.14}$$

$$\begin{aligned}\rho(x; x') &= N \sum_{\sigma_2 \cdots \sigma_N} \int \mathrm{d}^3 r_2 \cdots \mathrm{d}^3 r_N \Psi(x, x_2, ..., x_N) \\ &\times \Psi^*(x', x_2, ..., x_N)\end{aligned} \tag{2.15}$$

yields the particle density at coordinate x. For a single Slater determinant, the particle density simply is the sum of the spin-orbital densities. The trace over the spin degree of freedom yields

$$n(\boldsymbol{r}) = \sum_{\sigma} n(x) \tag{2.16}$$

$$\rho(\boldsymbol{r};\boldsymbol{r}') = \sum_{\sigma,\sigma'} \delta_{\sigma,\sigma'} \rho(x;x'). \tag{2.17}$$

The two-particle density matrix $\rho_2(x_1,x_2;x_1',x_2')$ can be expressed as [76]

$$\begin{aligned}\rho_2(x_1,x_2;x_1',x_2') &= \frac{N(N-1)}{2} \sum_{\sigma_3\cdots\sigma_N} \int \mathrm{d}^3 r_3 \cdots \mathrm{d}^3 r_N \Psi(x_1,x_2,x_3,...,x_N) \\ &\times \Psi^*(x_1',x_2',x_3,...,x_N).\end{aligned} \tag{2.18}$$

The pair density

$$n_2(x_1;x_2) = 2\rho_2(x_1,x_2;x_1,x_2) \tag{2.19}$$

is the probability density to find one particle at x_1 and another at x_2. Tracing out the spin degrees of freedom yields the spin-independent pair density

$$n_2(\boldsymbol{r}_1;\boldsymbol{r}_2) = \sum_{\sigma,\sigma'} n_2(x_1;x_2). \tag{2.20}$$

The pair density of a single Slater determinant is

$$\begin{aligned}n_2^{\mathrm{HF}}(x_1;x_2) &= \sum_{i,j} \left[\psi_i(x_1)\psi_j(x_2)\psi_i^*(x_1')\psi_j^*(x_2')\right. \\ &- \left.\psi_i(x_1)\psi_j(x_2)\psi_j^*(x_1')\psi_i^*(x_2')\right].\end{aligned} \tag{2.21}$$

The particles are correlated due to the antisymmetry of the many-particle wave function. In many-particle physics, this phenomenon is called 'exchange', while the term 'correlation' is restricted to the additional correlations in interacting systems, where the ground state generally is a linear combination of Slater determinants. This correlation is neglected in the Hartree-Fock approach.

The effect of exchange and correlation on the energy can be seen by expressing the Coulomb interaction in terms of density matrices (single-electron contributions are not affected by exchange and correlation) [76]:

$$E_{\mathrm{Coulomb}} = \frac{1}{2}\int \mathrm{d}^3 r \mathrm{d}^3 r' |\boldsymbol{r}-\boldsymbol{r}'|^{-1} n_2(\boldsymbol{r};\boldsymbol{r}') \tag{2.22}$$

$$=: \frac{1}{2}\int \mathrm{d}^3 r \mathrm{d}^3 r' |\boldsymbol{r}-\boldsymbol{r}'|^{-1} n(\boldsymbol{r}) n(\boldsymbol{r}') + \frac{1}{2}\int \mathrm{d}^3 r \mathrm{d}^3 r' |\boldsymbol{r}-\boldsymbol{r}'|^{-1} n(\boldsymbol{r}) h_{\mathrm{xc}}(\boldsymbol{r},\boldsymbol{r}'). \tag{2.23}$$

The first term in Eq. (2.23) is the Hartree energy, *i.e.* the electrostatic interaction of the charge density $n(\boldsymbol{r})$ with itself; the second term is the exchange-correlation energy, which can be interpreted as the interaction of the charge

density with an exchange-correlation hole

$$h_{\mathrm{xc}}(\boldsymbol{r},\boldsymbol{r}') = h(\boldsymbol{r},\boldsymbol{r}')/n(\boldsymbol{r}), \tag{2.24}$$

with the pair correlation function

$$h(\boldsymbol{r},\boldsymbol{r}') = n_2(\boldsymbol{r};\boldsymbol{r}') - n(\boldsymbol{r})n(\boldsymbol{r}'). \tag{2.25}$$

In the Hartree-Fock approximation, *i.e.* for a single Slater determinant, the hole is only due to exchange; the interaction with this positively charged hole cancels the self-interaction in the Hartree energy. Considering a system with $N/2$ orbitals $|\varphi_i\rangle$ occupied by two electrons each, we can write the pair density (2.21) as (taking into account the antisymmetry of the spin wave functions for tracing out the spin degrees of freedom)

$$n_2(\boldsymbol{r};\boldsymbol{r}') = n(\boldsymbol{r})n(\boldsymbol{r}') - \frac{1}{2}|\rho(\boldsymbol{r};\boldsymbol{r}')|^2, \tag{2.26}$$

with

$$n(\boldsymbol{r}) = 2\sum_{i=1}^{N/2} \varphi_i^*(\boldsymbol{r})\varphi_i(\boldsymbol{r}) \tag{2.27}$$

$$\rho(\boldsymbol{r};\boldsymbol{r}') = 2\sum_{i=1}^{N/2} \varphi_i^*(\boldsymbol{r}')\varphi_i(\boldsymbol{r}). \tag{2.28}$$

Using Eq. (2.26) the exchange hole can be expressed as

$$h_{\mathrm{x}}(\boldsymbol{r},\boldsymbol{r}') = -\frac{\left|\sum_{i=1}^{N/2} \varphi_i^*(\boldsymbol{r}')\varphi_i(\boldsymbol{r})\right|^2}{\sum_{j=1}^{N/2} \varphi_j^*(\boldsymbol{r})\varphi_j(\boldsymbol{r})}. \tag{2.29}$$

The limit $\lim_{\boldsymbol{r}\to\boldsymbol{r}'} h_{\mathrm{x}}(\boldsymbol{r},\boldsymbol{r}') = -n(\boldsymbol{r})/2$ reflects that for a single Slater determinant, the origin of the hole is only exchange, not affecting electrons with different spin. An expansion of the many-electron wave function in Slater determinants, *i.e.* the inclusion of correlation, lowers the magnitude of this limit due to Coulomb repulsion.

A way to introduce correlation into the Hartree-Fock scheme is the configuration interaction approach, approximating the ground state wave function by a linear combination of Slater determinants. These Slater determinants are obtained from Hartree-Fock spin orbitals by also occupying excited single-particle states. The many-particle Hamiltonian is diagonalized in a basis of these Slater determinants. Due to the computational expense for the corresponding matrix

elements, the number of particles or the number of Slater determinants that can be taken into account is limited.

A simplification of the Hartree-Fock method is the Hartree-Fock-Slater approach [77], where the computationally expensive exchange integrals are replaced by a local density approximation. The exchange energy is approximated as a spatial integral over an energy density that is approximated at each coordinate $\boldsymbol{r}$ by the exchange energy density of a free electron gas of constant density $n_{\text{const}} = n(\boldsymbol{r})$.

2.2 Density functional theory

All single- and two-particle contributions to the many-particle Hamiltonian (2.3) can be expressed in terms of the single-particle density matrix and the pair density, since the corresponding integrals over the electronic degrees of freedom reduce to integrals over the degrees of freedom of one and two electrons, respectively, the remaining degrees of freedom being traced out. The knowledge of these two matrices would thus suffice to calculate the ground state energy. Hohenberg and Kohn [10] have shown, however, that all ground state properties are uniquely determined by the particle density, which means a reduction of degrees of freedom to a minimum of the problem to be solved.

The first Hohenberg-Kohn theorem [10] states that no two external potentials not only differing by a constant

$$V_{\text{ext}}^{(1)}(\boldsymbol{r}) - V_{\text{ext}}^{(2)}(\boldsymbol{r}) \neq \text{const}, \tag{2.30}$$

with ($\hat{T}$ and $\hat{U}$ are the kinetic energy and particle-particle interaction operators, respectively)

$$\hat{H}^{(1,2)} = \hat{T} + \hat{U} + \hat{V}_{\text{ext}}^{(1,2)}, \tag{2.31}$$

can lead to the same ground state charge density $n(\boldsymbol{r})$. If the corresponding many-particle Hamiltonians (2.31), differing only in their external potentials $V_{\text{ext}}^{(1)}$ and $V_{\text{ext}}^{(2)}$, with ground states $|\Psi^{(1)}\rangle$ and $|\Psi^{(2)}\rangle$ had the same charge density $n(\boldsymbol{r})$, the following inequality would hold for non-degenerate ground states due to the variational principle (2.6):

$$\begin{aligned} E^{(1)} &= \left\langle \Psi^{(1)} \middle| \hat{H}^{(1)} \middle| \Psi^{(1)} \right\rangle \\ &< \left\langle \Psi^{(2)} \middle| \hat{H}^{(1)} \middle| \Psi^{(2)} \right\rangle = \left\langle \Psi^{(2)} \middle| \hat{H}^{(2)} + \hat{V}_{\text{ext}}^{(1)} - \hat{V}_{\text{ext}}^{(2)} \middle| \Psi^{(2)} \right\rangle, \end{aligned} \tag{2.32}$$

and hence

$$E^{(1)} < E^{(2)} + \int \mathrm{d}^3 r \left(V_{\text{ext}}^{(1)}(\boldsymbol{r}) - V_{\text{ext}}^{(2)}(\boldsymbol{r}) \right) n(\boldsymbol{r}). \tag{2.33}$$

Exchanging the superscripts (1) and (2), an inequality for $E^{(2)}$ is obtained that is a contradiction to (2.33), and therefore, $V_{\text{ext}}^{(1)}$ and $V_{\text{ext}}^{(2)}$ cannot lead to the same ground state charge density. For a given number of particles and their interaction, the density uniquely determines the external potential, which in turn determines the Hamiltonian and therefore all observables.

The second Hohenberg-Kohn theorem [10] states that the energy as a functional of the density is minimal for the ground state charge density under the constraint that the density integrates to the number of particles. Using that the wave function $|\Psi\rangle$ is a functional of the density n for non-degenerate ground states,[1] we can express the Rayleigh-Ritz variational principle as

$$\begin{aligned} E_0 &= \min_{|\Psi[n]\rangle} \left\langle \Psi[n] \,\middle|\, \hat{H} \,\middle|\, \Psi[n] \right\rangle \\ &= \min_{|\Psi[n]\rangle} \left\langle \Psi[n] \,\middle|\, \hat{T} + \hat{U} + \hat{V}_{\text{ext}} \,\middle|\, \Psi[n] \right\rangle \\ &= \min_{n} \left\langle \Psi[n] \,\middle|\, F[n] + \int \mathrm{d}^3 r v(\boldsymbol{r}) n(\boldsymbol{r}) \,\middle|\, \Psi[n] \right\rangle, \end{aligned} \tag{2.34}$$

with $v(\boldsymbol{r}) = V_{\text{ext}}(\boldsymbol{r})$ and the functional $F[n]$, which is universal since it does not depend on the external potential. A first order variation of the ground state density leaves the energy unchanged:

$$\frac{\delta}{\delta n} \left(F[n] + \int \mathrm{d}^3 r v(\boldsymbol{r}) n(\boldsymbol{r}) - \mu \left[\int \mathrm{d}^3 r n(\boldsymbol{r}) - N \right] \right) = 0, \tag{2.35}$$

where the chemical potential μ has been introduced as a Lagrangian multiplier for the integral constraint of the number of particles N:

$$\mu = \frac{\delta F[n]}{\delta n} + v(\boldsymbol{r}). \tag{2.36}$$

With the knowledge of $F[n]$ the ground state density could be calculated using Eq. (2.35). The Hohenberg-Kohn theorems, however, provide no concept for constructing the universal potential.

The Hohenberg-Kohn theorems assume a spin-independent external potential $v(\boldsymbol{r})$. For spin-dependent external potentials $v = v^{\uparrow} + v^{\downarrow}$, *e.g.* a Zeeman coupling of the electron spins to an external magnetic field,[2] the energetic contributions are $\int \mathrm{d}^3 r v^{\uparrow}(\boldsymbol{r}) n^{\uparrow}(\boldsymbol{r})$ and $\int \mathrm{d}^3 r v^{\downarrow}(\boldsymbol{r}) n^{\downarrow}(\boldsymbol{r})$, with the spin up and down

[1] For degenerate ground states, there exists no unique functional $|\Psi[n]\rangle$. A further subtlety is that not all charge densities are v-representable, *i.e.* these densities do not correspond to the ground state given by any external potential [78]. These problems are solved within the constrained search formulation, where all antisymmetric N-particle wave functions are considered that correspond to a fixed trial density [79–81].

[2] In the presence of a vector potential $\boldsymbol{A}$, the canonical electronic momentum becomes

densities $n^{\uparrow}(\boldsymbol{r})$ and $n^{\downarrow}(\boldsymbol{r})$, respectively. The Hohenberg-Kohn formalism can be extended to energetic functionals $\mathrm{E}[n^{\uparrow},n^{\downarrow}]$, or equivalently, to energetic functionals of the density $n = n^{\uparrow} + n^{\downarrow}$ and the spin polarization $\xi = (n^{\uparrow} - n^{\downarrow})/n$. Spin density functional theory is furthermore applied to magnetic solids and atoms and molecules with unpaired spins [83, 84].

First attempts to solve the electronic structure problem in terms of the density predate the Hohenberg-Kohn theorems: Thomas [85] and Fermi [86] have independently considered a density functional, where the kinetic energy is approximated by that of a homogeneous non-interacting electron gas:

$$\begin{aligned} E_{\mathrm{TF}} &= \frac{3}{10}(3\pi^2)^{2/3}\int \mathrm{d}^3 r n^{5/3}(\boldsymbol{r}) \\ &+ \int \mathrm{d}^3 r v(\boldsymbol{r}) n(\boldsymbol{r}) + \frac{1}{2}\int \mathrm{d}^3 r \int \mathrm{d}^3 r' \frac{n(\boldsymbol{r})n(\boldsymbol{r}')}{|\boldsymbol{r}-\boldsymbol{r}'|}. \end{aligned} \tag{2.37}$$

Apart from single atoms with large atomic numbers, this approximation to the kinetic energy generally turns out to be too inaccurate: the Thomas-Fermi approach *e.g.* does not predict stable molecules [87]. This no-binding theorem persists [87] when extending Eq. (2.37) by Dirac's exchange term [88] for the homogeneous interacting electron gas:

$$E_{\mathrm{x}} = -\frac{3}{4}\left(\frac{3}{\pi}\right)^{1/3}\int \mathrm{d}^3 r n^{4/3}(\boldsymbol{r}). \tag{2.38}$$

With a density gradient correction to the kinetic energy functional due to von Weizsäcker [89], molecules may be formed. Unfortunately, the gradient expansion of the kinetic energy functional diverges at sixth order, and the construction of kinetic energy functionals is difficult [90]. The introduction of an auxiliary system of non-interacting electrons in an effective potential, the so-called Kohn-Sham system [11], allows for a generally more accurate calculation of the kinetic energy, accounting for the neglected kinetic correlations in the non-interacting auxiliary system by a density functional.

2.2.1 The Kohn-Sham system and the local density approximation

Kohn and Sham [11] have proposed to express the functional $E[n]$ as a sum of the kinetic energy $T_0[n]$ of the ground state of a non-interacting system of same

$\boldsymbol{p} = \boldsymbol{v} - \alpha\boldsymbol{A}$ ($\alpha \approx 1/137$ is the fine structure constant and $\boldsymbol{v}$ the electronic velocity). Therefore, expectation values of the kinetic energy operator depend on the external potential $\boldsymbol{A}$, and the charge density based Hohenberg-Kohn formalism breaks down. In order to treat the effect of an external magnetic field $\boldsymbol{B} = \boldsymbol{\nabla} \times \boldsymbol{A}$ on the orbitals as well, an extension to current density functional theory has been developed [82].

density as the interacting system, the electrostatic energy of the charge density interacting classically with itself — the Hartree energy, and the exchange-correlation energy E_{xc}, containing all remaining energetic contributions and corrections due to many-body terms:

$$E_{\mathrm{KS}}[n] = T_0[n] + \frac{1}{2}\int \mathrm{d}^3r \int \mathrm{d}^3r' \frac{n(\boldsymbol{r})n(\boldsymbol{r}')}{|\boldsymbol{r}-\boldsymbol{r}'|} + E_{\mathrm{xc}}[n]. \tag{2.39}$$

According to the first Hohenberg-Kohn theorem, the ground state density uniquely determines the external potential v_{eff} for the auxiliary non-interacting system. For non-interacting fermions, the ground state is a single Slater determinant, and the many-particle problem reduces to the calculation of single-particle spin-orbitals, which are singly occupied up to the Kohn-Sham Fermi energy.[3]

For closed-shell systems systems with zero spin-polarization, *i.e.* $n^{\uparrow} = n^{\downarrow}$, $N/2$ Kohn-Sham orbitals $|\varphi_i\rangle$ with lowest eigenlevels are doubly occupied, resulting in the density

$$n(\boldsymbol{r}) = 2\sum_{i=1}^{N/2} |\varphi_i(\boldsymbol{r})|^2. \tag{2.40}$$

The kinetic energy of the non-interacting system is given as

$$T_0 = -\sum_{i=1}^{N/2} \int \mathrm{d}^3r \varphi_i^*(\boldsymbol{r})\boldsymbol{\nabla}^2\varphi_i(\boldsymbol{r}) = \sum_{i=1}^{N/2} \int \mathrm{d}^3r |\boldsymbol{\nabla}\varphi_i(\boldsymbol{r})|^2. \tag{2.41}$$

First order variations of the Kohn-Sham wave functions leave E_{KS} unchanged:

[3] To avoid algorithmic instabilities due to the changing occupation of states crossing the Fermi surface during the minimization of Eq. (2.39) (problematic in particular for metallic systems), the restriction of integer occupation numbers is lifted near the Fermi surface. Occupying the Kohn-Sham eigenstates according to the Fermi-Dirac distribution

$$f_{\mathrm{FD}}(\varepsilon_i) = \frac{1}{\exp[(\varepsilon_i - \mu)/\tau] + 1}$$

for a fictitious electronic temperature τ (usually an order of magnitude higher than the room temperature value of $\sim$25 meV), the Helmholtz free energy $F_{\mathrm{KS}} = E_{\mathrm{KS}} - \tau S/k_{\mathrm{B}}$ is minimized [91] (S is the electronic entropy and k_{B} is Boltzmann's constant). Since F_{KS} and E_{KS} depend to lowest order quadratically on τ with opposite signs [92], E_{KS} can be extrapolated to zero temperature as [93]

$$E_{\mathrm{KS}}^0 = \frac{1}{2}\left(E_{\mathrm{KS}} + F_{\mathrm{KS}}\right) + O(\tau^3).$$

As a further advantage, the smoother occupation near the Fermi surface allows for a coarser Brillouin zone sampling (see Sec. 2.3).

$$\frac{\delta E_{\rm KS}}{\delta\varphi_i^*(\boldsymbol{r})} = \frac{\delta T_0}{\delta\varphi_i^*(\boldsymbol{r})} + \int \mathrm{d}^3r' \Bigg[V_{\rm ext}(\boldsymbol{r}') + \int \mathrm{d}^3r'' \frac{n(\boldsymbol{r}'')}{|\boldsymbol{r}' - \boldsymbol{r}''|} + v_{\rm xc}(\boldsymbol{r}') \Bigg] \frac{\delta n(\boldsymbol{r}')}{\delta\varphi_i^*(\boldsymbol{r})} = 0, \tag{2.42}$$

with the exchange-correlation potential

$$v_{\rm xc}(\boldsymbol{r}) = \frac{\delta E_{\rm xc}}{\delta n(\boldsymbol{r})}. \tag{2.43}$$

From Eqs. (2.40) and (2.41) follows

$$\frac{\delta n(\boldsymbol{r}')}{\delta\varphi_i^*(\boldsymbol{r})} = 2\varphi_i(\boldsymbol{r})\delta(\boldsymbol{r} - \boldsymbol{r}'), \tag{2.44}$$

and

$$\frac{\delta T_0}{\delta\varphi_i^*(\boldsymbol{r})} = -\boldsymbol{\nabla}^2\varphi_i(\boldsymbol{r}), \tag{2.45}$$

respectively. The constraint of orthonormal Kohn-Sham orbitals leads to the single-particle Schrödinger-like equation

$$\left(-\frac{1}{2}\boldsymbol{\nabla}^2 + v_{\rm eff}(\boldsymbol{r}) \right) \varphi_i(\boldsymbol{r}) = \varepsilon_i\varphi_i(\boldsymbol{r}), \tag{2.46}$$

with the effective potential

$$v_{\rm eff}(\boldsymbol{r}) = V_{\rm ext}(\boldsymbol{r}) + \int \mathrm{d}^3r' \frac{n(\boldsymbol{r}')}{|\boldsymbol{r} - \boldsymbol{r}'|} + v_{\rm xc}(\boldsymbol{r}). \tag{2.47}$$

Since the effective potential depends on the density and hence on the Kohn-Sham wave functions through the Hartree and exchange-correlation potentials, Eq. (2.46) is solved self-consistently by iteratively diagonalizing Eq. (2.46) and updating $v_{\rm eff}$, to calculate the ground state charge density $n(\boldsymbol{r})$ of the interacting system.[4] Correcting for double-counting terms due to the effective potential, the electronic energy reads

$$E_{\rm KS}[n] = 2\sum_i \varepsilon_i - \frac{1}{2}\int \mathrm{d}^3r \int \mathrm{d}^3r' \frac{n(\boldsymbol{r})n(\boldsymbol{r}')}{|\boldsymbol{r} - \boldsymbol{r}'|} + E_{\rm xc}[n] - \int \mathrm{d}^3r v_{\rm xc}[n](\boldsymbol{r})n(\boldsymbol{r}). \tag{2.48}$$

[4] An alternative to this self-consistent field approach is the direct minimization of Eq. (2.39) with respect to the expansion coefficients of the Kohn-Sham eigenfunctions in a given basis set [94, 95].

For spin-polarized systems, Kohn-Sham systems are constructed for each spin direction $\sigma \in \{\uparrow, \downarrow\}$ with spin-dependent effective potentials

$$v_{\text{eff}}^{\sigma}(\boldsymbol{r}) = V_{\text{ext}}^{(\sigma)}(\boldsymbol{r}) + \int \mathrm{d}^3 r' \frac{n(\boldsymbol{r}')}{|\boldsymbol{r} - \boldsymbol{r}'|} + v_{\text{xc}}^{\sigma}(\boldsymbol{r}), \tag{2.49}$$

with

$$v_{\text{xc}}^{\sigma} = \frac{\delta E_{\text{xc}}[n^{\uparrow}, n^{\downarrow}]}{\delta n^{\sigma}(\boldsymbol{r})}. \tag{2.50}$$

The spin up and down densities are constructed from $N^{\uparrow}$ and $N^{\downarrow}$ singly occupied Kohn-Sham states of the corresponding auxiliary systems, respectively.

Provided that the ground state density of the interacting system can be constructed from the density of a single Slater determinant, the Kohn-Sham ansatz so far is an exact approach to the electronic structure problem. Approximations have to be made to the universal (*i.e.* independent of V_{ext}) exchange-correlation functional $E_{\text{xc}}[n]$.

In order to represent $E_{\text{xc}}[n]$ by the interaction with an exchange-correlation hole (cf. Eq. (2.23)), the hole has to be adjusted to take the kinetic correlations into account, being neglected by $T_0[n]$. This can be achieved by integrating over the strength of the electronic Coulomb interaction, which is turned on adiabatically, under the constraint that the ground state density remains unchanged [96, 97]. Using the Hellmann-Feynman theorem (2.4), the change in energy from zero ($\lambda = 0$) to full ($\lambda = 1$; the interaction is scaled linearly with λ) Coulomb interaction $\hat{V}_{ee}$ is

$$\Delta E = \int_0^1 \mathrm{d}\lambda \left\langle \Psi(\lambda) \left| \frac{\partial \hat{H}}{\partial \lambda} \right| \Psi(\lambda) \right\rangle = \int_0^1 \mathrm{d}\lambda \left\langle \Psi(\lambda) \left| \hat{V}_{ee} \right| \Psi(\lambda) \right\rangle. \tag{2.51}$$

Since the density is fixed, the Hartree potential is not affected; the exchange-correlation hole (2.24), however, is averaged over the coupling parameter λ:

$$\bar{h}_{\text{xc}}(\boldsymbol{r}, \boldsymbol{r}') = \int_0^1 \mathrm{d}\lambda h_{\text{xc}}(\lambda; \boldsymbol{r}, \boldsymbol{r}'), \tag{2.52}$$

and the exchange-correlation functional in the Kohn-Sham approach correspondingly reads

$$E_{\text{xc}}[n] = \frac{1}{2} \int \mathrm{d}^3 r n(\boldsymbol{r}) \int \mathrm{d}^3 r' \frac{\bar{h}_{\text{xc}}(\boldsymbol{r}, \boldsymbol{r}')}{|\boldsymbol{r} - \boldsymbol{r}'|}. \tag{2.53}$$

From Eqs. (2.14)–(2.19) follows for the density n and the pair density n_2

$$n(\boldsymbol{r}) = \frac{1}{N-1} \int \mathrm{d}^3 r' n_2(\boldsymbol{r}; \boldsymbol{r}'). \tag{2.54}$$

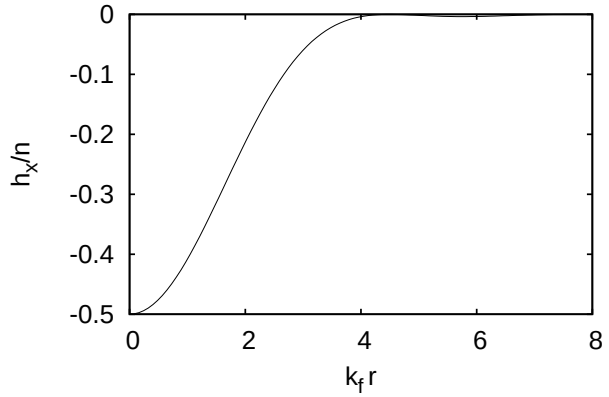

Figure 2.1: Exchange hole of the unpolarized, homogeneous, non-interacting electron gas, given by $h_{\mathrm{x}}(u/k_{\mathrm{F}}) = -9n/2 \cdot [(\sin u - u\cos u)/u^3]^2$, with $u = k_{\mathrm{F}}|\boldsymbol{r} - \boldsymbol{r}'|$ and the Fermi wave vector $k_{\mathrm{F}} = (3\pi^2 n)^{1/3}$. At the center, the hole has the value $-n/2$, since electrons with opposite spin are not affected by exchange. Properties of the determinantal ground state are obtained from the single-particle density matrix, which is diagonal in momentum space and at zero temperature simply given by $\langle \boldsymbol{k}\,|\rho|\,\boldsymbol{k}'\rangle = \delta_{\boldsymbol{k}\boldsymbol{k}'} 2\Theta(k_F - k)$, corresponding to an occupation of the momentum eigenstates with spin up and down up to k_{F}. Fourier transformation to the real space representation yields the two-particle density matrix via Eq. (2.26) (see *e.g.* [76] or [99]).

This leads to a sum rule for the exchange-correlation hole (cf. Eqs. (2.24) and (2.25)):

$$\int \mathrm{d}^3 r' h_{\mathrm{xc}}(\boldsymbol{r}, \boldsymbol{r}') = \int \mathrm{d}^3 r' \left(\frac{n_2(\boldsymbol{r}, \boldsymbol{r}')}{n(\boldsymbol{r})} - n(\boldsymbol{r}') \right) = -1, \tag{2.55}$$

which holds independently of the system and type of interaction, and hence also for the interaction-strength-averaged $\bar{h}_{\mathrm{xc}}(\boldsymbol{r}, \boldsymbol{r}')$. The charge depletion in the exchange-correlation hole corresponds to exactly one electron. Eq. (2.55) applies also to the exchange-only holes (2.29) of single Slater determinants. Therefore, the remaining correlation part of an exchange-correlation hole corresponds to a neutral charge distribution [98].

In developing approximations to $\bar{h}_{\mathrm{xc}}(\boldsymbol{r}, \boldsymbol{r}')$, the fulfillment of the sum rule (2.55) has proven to be crucial [100]. Since the kinetic energy apart from correlation and the long range Hartree terms are accounted for in the Kohn-Sham equations (2.46) and (2.47), Kohn and Sham [11] have proposed a local density approximation (LDA) to the remaining energetic contribution $E_{\mathrm{xc}}[n]$, in analogy to the approach to exchange in the Hartree-Fock-Slater method

[77] mentioned above. In this approach, the exchange correlation density is approximated locally by the energy density corresponding to the interaction of a homogeneous electron gas with its exchange-correlation hole, and hence the sum rule is obeyed. For the homogeneous electron gas, $\bar{h}_{\mathrm{xc}}(\boldsymbol{r}, \boldsymbol{r}')$ is a function of the distance $|\boldsymbol{r}-\boldsymbol{r}'|$. Also the pair density n_2, *i.e.* the probability to find one electron at $\boldsymbol{r}$ and another at $\boldsymbol{r}'$, only depends on this difference. From Eqs. (2.26) and (2.28) follows that the homogeneous Hartree-Fock ground state therefore is formed from plane wave single-particle states. Hence, the ground state wave functions of the non-interacting and interacting homogeneous electron gases are equal in the Hartree-Hock approximation (while only for the latter exchange causes a change in energy), and the exchange hole is the same for both systems (see Fig. 2.1); the interaction strength average only affects the correlation hole.

The exchange-correlation energy is expressed in the form

$$E_{\mathrm{xc}}^{\mathrm{LDA}}[n] = \int \mathrm{d}^3 r n(\boldsymbol{r}) \varepsilon_{\mathrm{xc}}^{\mathrm{hom}}(n(\boldsymbol{r})), \tag{2.56}$$

where $\varepsilon_{\mathrm{xc}}^{\mathrm{hom}}(n(\boldsymbol{r}))$ is the exchange-correlation energy per electron of the homogeneous electron gas of constant density equal to the value of the generally inhomogeneous density n at coordinate $\boldsymbol{r}$. The corresponding exchange-correlation potential is given as

$$v_{\mathrm{xc}}^{\mathrm{LDA}}(\boldsymbol{r}) = \varepsilon_{\mathrm{xc}}^{\mathrm{hom}}(n(\boldsymbol{r})) + n(\boldsymbol{r}) \left.\frac{\partial \varepsilon_{\mathrm{xc}}^{\mathrm{hom}}}{\partial n}\right|_{n=n(\boldsymbol{r})}. \tag{2.57}$$

For the homogeneous Hartree-Fock ground state, an analytical expression for $\varepsilon_{\mathrm{x}}^{\mathrm{hom}}(n(\boldsymbol{r}))$ is known (cf. Eq. (2.38)) [88]:

$$\varepsilon_{\mathrm{x}}^{\mathrm{hom}}(n(\boldsymbol{r})) = -\frac{3}{4\pi}[3\pi^2 n(\boldsymbol{r})]^{1/3}. \tag{2.58}$$

The correlation energy per electron in the homogeneous electron gas, $\varepsilon_{\mathrm{c}}^{\mathrm{hom}}(n(\boldsymbol{r})) = \varepsilon_{\mathrm{xc}}^{\mathrm{hom}}(n(\boldsymbol{r})) - \varepsilon_{\mathrm{x}}^{\mathrm{hom}}(n(\boldsymbol{r}))$, has been parametrized by fitting [101, 102] to random-phase approximations [103] and in principal exact numerical quantum Monte Carlo calculations [104]. For spin-polarized systems, the local spin density approximation is used [83].

In contrast to Hartree-Fock theory, where the self-interaction in the Hartree-term is canceled by exchange, the self-interaction is canceled in the LDA completely only in the limit of a homogeneous density. The success of the LDA can be attributed to its representation of the exchange-correlation hole with the correct sum rule (2.55). For an inhomogeneous system the exchange-correlation energy per electron in terms of the exchange-correlation $\bar{h}_{\mathrm{xc}}(\boldsymbol{r}, \boldsymbol{r}')$ hole reads

$$\varepsilon_{\mathrm{xc}}[n](\boldsymbol{r}) = \frac{1}{2} \int \mathrm{d}^3 r' \frac{\bar{h}_{\mathrm{xc}}(\boldsymbol{r}, \boldsymbol{r}')}{|\boldsymbol{r} - \boldsymbol{r}'|}. \tag{2.59}$$

Hence, the spherical average of the hole enters the exchange-correlation energy due to the isotropy of the Coulomb interaction. This average is represented relatively well by the spherically symmetric exchange-correlation hole in the LDA, which indicates another advantage of this approximation [84].

In the case of large charge density variations, the local density approximation becomes insufficient, a problem in particular for finite and semi-finite systems. In order to improve upon the LDA in terms of the density gradient $\boldsymbol{\nabla} n(\boldsymbol{r})$, gradient corrections have to be generalized from an expansion of E_{xc} to effectively account for re-summation to infinite order [90] and to maintain correct properties of the LDA, *e.g.* the sum rule (2.55) [100]. Compared to results obtained within the LDA only, generalized gradient approximations (GGA) improve upon binding and atomic energies; furthermore, structure relaxations based on the GGA yield improved bond lengths and angles [98]. For the calculation of the electronic structure of solids, the generalized gradient approximations according to Perdew and Wang [105, 106] or Perdew, Burke, and Ernzerhof [107] are commonly used.[5] Further approximations include *e.g.* the so-called Meta-GGA, which also depends on the Laplacian of the charge density or the kinetic energy density of the occupied Kohn-Sham orbitals [109–111].

With the local approximation to exchange in the Hartree-Fock-Slater approach, the computational complexity is basically equal to that of the Kohn-Sham approach. The difference lies in the fact, that in the Hartree-Fock-Slater method, the optimal determinantal (*i.e.* neglecting correlations due to the Coulomb interaction) ground state is obtained, while in the Kohn-Sham approach to density functional theory the ground state density is calculated taking correlations approximately into account. The Slater determinant of the auxiliary Kohn-Sham wave functions is not an approximation to the ground state wave function. Hence, with the calculation of the ground state density, generally corresponding to a non-determinantal ground state wave function of interacting electrons, correlations due to the Coulomb interaction are accounted for, and the electronic ground state energy is generally approximated better than in the Hartree-Fock-Slater method. With the knowledge of an approximation to the ground state wave function in the latter approach, however, the energy for removal of an electron under the assumption that the remaining single-particle states keep unchanged is given by the Fock-operator eigenvalue of the emptied state [112]. In the Kohn-Sham scheme only the highest occupied Kohn-Sham eigenlevel can be identified with the negative of the ionization energy for finite systems [113].

[5] A revised form of the GGA due to Perdew, Burke, and Ernzerhof improves upon adsorption energetics [108].

2.3 Periodic systems

In crystalline solids, the nuclear equilibrium positions are ordered periodically in space. With the resulting periodic external potential $v(\boldsymbol{r})$ for an infinite crystal, the ground state charge density $n(\boldsymbol{r})$ and all other local physical properties have the same periodicity as the nuclear coordinate configuration. The corresponding Hamiltonian is invariant with respect to translation by a lattice vector $\boldsymbol{T}$, which can be expressed as a sum of integer multiples of the basis vectors $\boldsymbol{a}_1$, $\boldsymbol{a}_2$, and $\boldsymbol{a}_3$ spanning a unit cell of the system:

$$\boldsymbol{T} = \sum_{i=1}^{3} n_i \boldsymbol{a}_i, \qquad n_i \in \mathbb{Z}. \tag{2.60}$$

The atomic positions that are repeated with the unit cell form the atomic basis. Unit cells with minimal volume $\Omega^{\mathrm{P}} = \det(\boldsymbol{a}_1^{\mathrm{P}}, \boldsymbol{a}_2^{\mathrm{P}}, \boldsymbol{a}_3^{\mathrm{P}})$ are called primitive cells. The vectors $\boldsymbol{a}_i^{\mathrm{P}}$ are the corresponding primitive basis vectors. Primitive cells contain a minimal atomic basis. The primitive cell comprising all points that are closer to its center than to the periodic images of the center is called Wigner-Seitz cell.

A periodic function, *e.g.* the charge density $n(\boldsymbol{r})$, can be expanded into a Fourier series:

$$n(\boldsymbol{r}) = \sum_{\boldsymbol{G}} n_{\boldsymbol{G}} \exp(i\boldsymbol{G}\boldsymbol{r}), \tag{2.61}$$

with

$$n_{\boldsymbol{G}} = \frac{1}{\Omega} \int_{\Omega} \mathrm{d}^3 r \, n(\boldsymbol{r}) \exp(-i\boldsymbol{G}\boldsymbol{r}), \tag{2.62}$$

where Ω is the unit cell volume. The reciprocal lattice vectors $\boldsymbol{G}$ are characterized by

$$\exp(i\boldsymbol{G}\boldsymbol{T}) = 1, \tag{2.63}$$

and can be expressed as sums of integer multiples of the reciprocal basis vectors

$$\boldsymbol{b}_i = 2\pi \frac{\boldsymbol{a}_j \times \boldsymbol{a}_k}{\Omega}, \qquad \boldsymbol{b}_i \cdot \boldsymbol{a}_\ell = 2\pi\delta_{i\ell}, \tag{2.64}$$

where (i, j, k) is a cyclic permutation of $(1, 2, 3)$. The Wigner-Seitz cell in reciprocal space is called first Brillouin zone.

The operator $\hat{\boldsymbol{\mathcal{T}}}_{\boldsymbol{\varepsilon}}$ translating a single-particle state $|\varphi\rangle$ in an effective potential, *e.g.* a Kohn-Sham wave function, by a vector of infinitesimal length can be derived by a Taylor expansion of the wave function:

$$\left\langle \boldsymbol{r} \left| \hat{\boldsymbol{\mathcal{T}}}_{\boldsymbol{\varepsilon}} \right| \varphi \right\rangle \;:=\; \langle \boldsymbol{r} + \boldsymbol{\varepsilon} | \varphi \rangle$$

$$\begin{aligned} &= \varphi(\boldsymbol{r}) + i\boldsymbol{\varepsilon}\boldsymbol{\nabla}\varphi|_{\boldsymbol{r}} \\ &= \left\langle \boldsymbol{r} \left| 1 + i\boldsymbol{\varepsilon}\hat{\boldsymbol{k}} \right| \varphi \right\rangle + O(\varepsilon^2). \end{aligned} \tag{2.65}$$

Decomposing a finite translation into a product of infinitesimal translations, we obtain for the operator $\hat{\boldsymbol{\mathcal{T}}}$ for translation by a lattice vector:

$$\begin{aligned} \left\langle \boldsymbol{r} \left| \hat{\boldsymbol{\mathcal{T}}} \right| \varphi \right\rangle &= \langle \boldsymbol{r} + \boldsymbol{T} | \varphi \rangle \\ &= \lim_{\ell \to \infty} \left(1 + i\hat{\boldsymbol{k}} \frac{\boldsymbol{T}}{\ell} \right)^{\ell} \\ &= \left\langle \boldsymbol{r} \left| \exp(i\hat{\boldsymbol{k}}\boldsymbol{T}) \right| \varphi \right\rangle . \end{aligned} \tag{2.66}$$

Since the Hamiltonian $\hat{H}$ is invariant with respect to translation by a lattice vector $\boldsymbol{T}$, the operators $\hat{H}$ and $\hat{\boldsymbol{\mathcal{T}}}$ commute

$$[\hat{\boldsymbol{\mathcal{T}}}, \hat{H}] = 0. \tag{2.67}$$

Therefore $\hat{\boldsymbol{\mathcal{T}}}$ and $\hat{H}$ have a common eigenbasis (in the case of degenerate subspaces, a set of vectors spanning these subspaces can be chosen to be eigenvectors of both $\hat{\boldsymbol{\mathcal{T}}}$ and $\hat{H}$). Hence, the so-called crystal momentum $\boldsymbol{k}$ (the generator of the translation) is conserved modulo the addition of a reciprocal lattice vector, leaving the eigenvalue $\exp(i\boldsymbol{k}\boldsymbol{T})$ of the translation operator $\hat{\boldsymbol{\mathcal{T}}}$ unchanged. Translation by a lattice vector only changes the phase of the single-particle wave functions.

Labeling the eigenstates of the Hamiltonian $\hat{H}$ with the quantum number $\boldsymbol{k}$ and an orbital quantum number n, the wave functions can be written as a lattice-periodic function $\langle \boldsymbol{r} | u_{n,\boldsymbol{k}} \rangle$ modulated by a plane wave with wave vector $\boldsymbol{k}$ (which is an eigenfunction of $\hat{\boldsymbol{k}}$ and therefore also of $\hat{\boldsymbol{\mathcal{T}}}$):

$$\langle \boldsymbol{r} | \varphi_{n,\boldsymbol{k}} \rangle = \exp(i\boldsymbol{k}\boldsymbol{r}) \langle \boldsymbol{r} | u_{n,\boldsymbol{k}} \rangle. \tag{2.68}$$

Eq. (2.68) and the equation

$$\hat{\boldsymbol{\mathcal{T}}} | \varphi_{n,\boldsymbol{k}} \rangle = \exp(i\boldsymbol{k}\boldsymbol{T}) | \varphi_{n,\boldsymbol{k}} \rangle \tag{2.69}$$

are known as Bloch's theorem [114]. The eigenenergies $\varepsilon_{n,\boldsymbol{k}}$ corresponding to the Bloch functions (2.68) depend on the crystal momentum $\boldsymbol{k}$. Using the commutator $[\hat{\boldsymbol{p}}, \exp(i\boldsymbol{k}\hat{\boldsymbol{r}})] = \boldsymbol{k} \exp(i\boldsymbol{k}\hat{\boldsymbol{r}})$, an eigenvalue problem of a $\boldsymbol{k}$-dependent Hamiltonian with the lattice-periodic $\langle \boldsymbol{r} | u_{n,\boldsymbol{k}} \rangle$ as eigenfunctions can be formulated:

$$\left[-\frac{1}{2} (\boldsymbol{\nabla} + i\boldsymbol{k})^2 + v(\boldsymbol{r}) \right] \langle \boldsymbol{r} | u_{n,\boldsymbol{k}} \rangle = \varepsilon_{n,\boldsymbol{k}} \langle \boldsymbol{r} | u_{n,\boldsymbol{k}} \rangle. \tag{2.70}$$

The allowed values for the wave vectors are obtained by imposing Born-von Kármán boundary conditions [115] on electronic excitations, *i.e.* assuming that excitations are periodic on a lattice with basis vectors $N_j \boldsymbol{a}_j, j \in \{1,2,3\}$, where the N_j are large integers such that the errors introduced by this approximation are small. Translation by these basis vectors maps the system onto itself. The corresponding phase factors thus equal one

$$\exp(iN_j \boldsymbol{k} \boldsymbol{a}_j) = 1. \tag{2.71}$$

Decomposing this translation into N_j steps, the wave vectors allowed by the cyclic boundary conditions are given as sums of integer multiples of $\boldsymbol{b}_j/N_j$. In the limit $N_j \to \infty$, this set of allowed wave vectors becomes continuous.

By subtraction of a reciprocal lattice vector $\boldsymbol{G}$, each wave vector $\boldsymbol{k}'$ can be reduced to a vector

$$\boldsymbol{k} = \boldsymbol{k}' - \boldsymbol{G} \tag{2.72}$$

in the first Brillouin zone with

$$\exp(i\boldsymbol{k}'\boldsymbol{r})\langle \boldsymbol{r}|u_{n,\boldsymbol{k}'}\rangle = \exp[i(\boldsymbol{k}+\boldsymbol{G})\boldsymbol{r}]\langle \boldsymbol{r}|u_{n,\boldsymbol{k}'}\rangle = \exp(i\boldsymbol{k}\boldsymbol{r})\langle \boldsymbol{r}|u_{n,\boldsymbol{k}}\rangle, \tag{2.73}$$

where, in analogy to Eq. (2.70), the transformation $\exp(-i\boldsymbol{G}\boldsymbol{r})\hat{H}\exp(i\boldsymbol{G}\boldsymbol{r})$ yields[6]

$$\langle \boldsymbol{r}|u_{n,\boldsymbol{k}}\rangle = \exp(i\boldsymbol{G}\boldsymbol{r})\langle \boldsymbol{r}|u_{n,\boldsymbol{k}+\boldsymbol{G}}\rangle. \tag{2.74}$$

Reducing the dispersion of a free electron, $\varepsilon(\boldsymbol{k}) = \boldsymbol{k}^2/2$, to a reciprocal cell, degeneracies with respect to the quantum number $\boldsymbol{k}$ at the Brillouin zone boundaries appear, where the dispersion corresponding to plane wave eigenstates with opposite phases is reduced to the same $\boldsymbol{k}$-points. These degeneracies are lifted by a periodic, non-constant potential, leading to energy gaps between continuous electronic bands for infinite systems.

The electronic ground state energy and other properties of an infinite periodic system per unit cell can be obtained by solving (2.70) with periodic boundary conditions for the finite number of electrons contained in the unit cell, integrating the dispersion with respect to the continuous set of wave vectors $\boldsymbol{k}$ over the volume of the first Brillouin zone (in numerical calculations this integral is usually approximated by a sum over a finite set of points).

2.3.1 Plane wave basis sets

In the limit of a constant potential, the eigenfunctions $|u_{n,\boldsymbol{k}}\rangle$ are plane waves $|\boldsymbol{G}\rangle$ with reciprocal lattice vectors (including zero) as wave vectors. In a pe-

[6] The multiplication of the eigenfunction $\langle \boldsymbol{r}|u_{n,\boldsymbol{k}+\boldsymbol{G}}\rangle$ by the phase factor $\exp(i\boldsymbol{G}\boldsymbol{r})$ means a similarity transformation $(\hat{\boldsymbol{p}}, \hat{\boldsymbol{r}}) \to (\hat{\boldsymbol{p}} - \boldsymbol{G}, \hat{\boldsymbol{r}})$ [116]. The kinetic energy operator in (2.70) becomes $-(\boldsymbol{\nabla} + i\boldsymbol{k})^2/2 \to -(\boldsymbol{\nabla} + i\{\boldsymbol{k}+\boldsymbol{G}\})^2/2$.

riodic, non-constant potential the plane wave states are mixed, and the eigenfunctions can be expanded in the basis of plane waves:

$$\langle \boldsymbol{r}|u_{n,\boldsymbol{k}}\rangle = \sum_{\boldsymbol{G}} c_{n,\boldsymbol{k}}^{(\boldsymbol{G})} \langle \boldsymbol{r}|\boldsymbol{G}\rangle, \tag{2.75}$$

with

$$c_{n,\boldsymbol{k}}^{(\boldsymbol{G})} = \langle \boldsymbol{G}|u_{n,\boldsymbol{k}}\rangle. \tag{2.76}$$

Using Eqs. (2.70) and (2.75), the Kohn-Sham differential equations (2.46) can be converted into a set of linear equations (with non-linear dependence of the effective potential on the solution) [99]:

$$\sum_{\boldsymbol{G}'} \left[\frac{1}{2}|\boldsymbol{k}+\boldsymbol{G}|^2 \delta_{\boldsymbol{G}\boldsymbol{G}'} + V_{\boldsymbol{G}-\boldsymbol{G}'}\right] c_{n,\boldsymbol{k}}^{(\boldsymbol{G}')} = \varepsilon_{n,\boldsymbol{k}} c_{n,\boldsymbol{k}}^{(\boldsymbol{G})}. \tag{2.77}$$

$V_{\boldsymbol{G}}$ is a Fourier expansion coefficient of the effective potential (2.47):

$$V_{\boldsymbol{G}} = \frac{1}{\Omega}\int_{\Omega} \mathrm{d}^3 r\, v_{\mathrm{eff}}(\boldsymbol{r}) \exp(-i\boldsymbol{G}\boldsymbol{r}). \tag{2.78}$$

The Fourier coefficients of the Hartree potential can be obtained by Fourier transformation of the Poisson equation $\boldsymbol{\nabla}^2 V^{\mathrm{H}}(\boldsymbol{r}) = -4\pi n(\boldsymbol{r})$:

$$V_{\boldsymbol{G}}^{\mathrm{H}} = \frac{4\pi n_{\boldsymbol{G}}}{\boldsymbol{G}^2}. \tag{2.79}$$

The divergence of $V_{\boldsymbol{G}=0}^{\mathrm{H}}$, which is due to the contribution from the average electronic charge density, is canceled by corresponding terms for the electronic interaction with the nuclei and interactions between the nuclei for electrically neutral systems.

The kinetic energy operator is diagonal in the plane wave basis and the corresponding matrix elements are therefore calculated efficiently in momentum space. The calculation of terms which contain powers of the wave functions in real space, *e.g.* the charge density, are calculated more efficiently in real space, since these multiplications correspond to convolutions in Fourier space. The charge density and wave functions are transformed efficiently between real and momentum space using discrete fast Fourier transforms, in order to allow for a calculation of all terms in diagonal form.

The size of the plane wave basis is limited by a cutoff for the kinetic energy:

$$\frac{1}{2}|\boldsymbol{k}+\boldsymbol{G}|^2 \leq E_{\mathrm{cut}}. \tag{2.80}$$

For a given effective potential, Eq. (2.77) is solved separately in this finite basis for a set $\mathcal{K}$ of $\boldsymbol{k}$-points sampling the Brillouin zone. The resulting charge density

is a sum of the densities of the eigenfunctions over $\boldsymbol{k} \in \mathcal{K}$. Hence, the effective potential to be updated iteratively depends on the solutions of (2.77) for all $\boldsymbol{k} \in \mathcal{K}$.[7]

2.3.2 Pseudopotentials

Strongly bound core states require large kinetic energy cutoffs to be expanded to sufficient accuracy in the plane wave basis. The nodal structure of valence electron wave functions in the core regions, owing to their orthogonality to the core states, also corresponds to high energetic Fourier components. The size of the plane wave basis can be reduced significantly by the introduction of pseudopotentials [118], which are constructed to yield nodeless valence pseudo-wave functions within the core regions surrounding the nuclei; the core states are assumed to be frozen in their atomic configurations. This leads to a further reduction of the size of the electronic structure problem by less effective single-particle states entering the Kohn-Sham equations.

Since the angular momentum ℓ is conserved for spherically symmetric systems, the radial part of the wave function of an isolated atom has only to be orthogonal to the radial parts of states with same quantum number ℓ. Hence, the most general form of an atomic pseudopotential is

$$\hat{V}^{\mathrm{PS}} = \sum_{\ell} \sum_{m=-\ell}^{\ell} V_{\ell}^{\mathrm{PS}}(\hat{r}) \cdot |\ell m\rangle\langle \ell m|. \tag{2.81}$$

Instead of projecting onto the spherical harmonics $|\ell m\rangle$, it is advantageous in terms of computational effort, to introduce projectors with angular and radial dependence, that are constructed such that the integration due to the radial dependence of the $V_{\ell}^{\mathrm{PS}}(r)$ is taken into account by the projection operations, leading to a separable form of the pseudopotential [119]:

$$\hat{V}^{\mathrm{PS}} = V_{\mathrm{loc}}^{\mathrm{PS}}(\hat{r}) + \sum_{\ell} \sum_{m=-\ell}^{\ell} \frac{|\psi_{\ell m}^{\mathrm{PS}} \delta V_{\ell}^{\mathrm{PS}}\rangle\langle \delta V_{\ell}^{\mathrm{PS}} \psi_{\ell m}^{\mathrm{PS}}|}{\langle \psi_{\ell m}^{\mathrm{PS}} | \delta V_{\ell}^{\mathrm{PS}} | \psi_{\ell m}^{\mathrm{PS}}\rangle}, \tag{2.82}$$

with the reference pseudo-wave functions $\psi_{\ell m}^{\mathrm{PS}}$ of the isolated atom, the local potential $V_{\mathrm{loc}}^{\mathrm{PS}}(r)$ that equals $V(r)$ outside the core sphere, and the potentials $\delta V_{\ell}^{\mathrm{PS}}(r)$ that are the differences of $V_{\ell}^{\mathrm{PS}}(r)$ to the local potential and hence are zero outside the sphere.

[7] The number of $\boldsymbol{k}$-points can be reduced due to symmetries in the crystal in addition to the periodicity, *e.g.* with respect to inversion, rotation, or reflection (cf. Sec. 4.1). Equivalent $\boldsymbol{k}$-points are represented by a single $\boldsymbol{k}$-point with an accordingly increased weight for sums over $\boldsymbol{k}$.

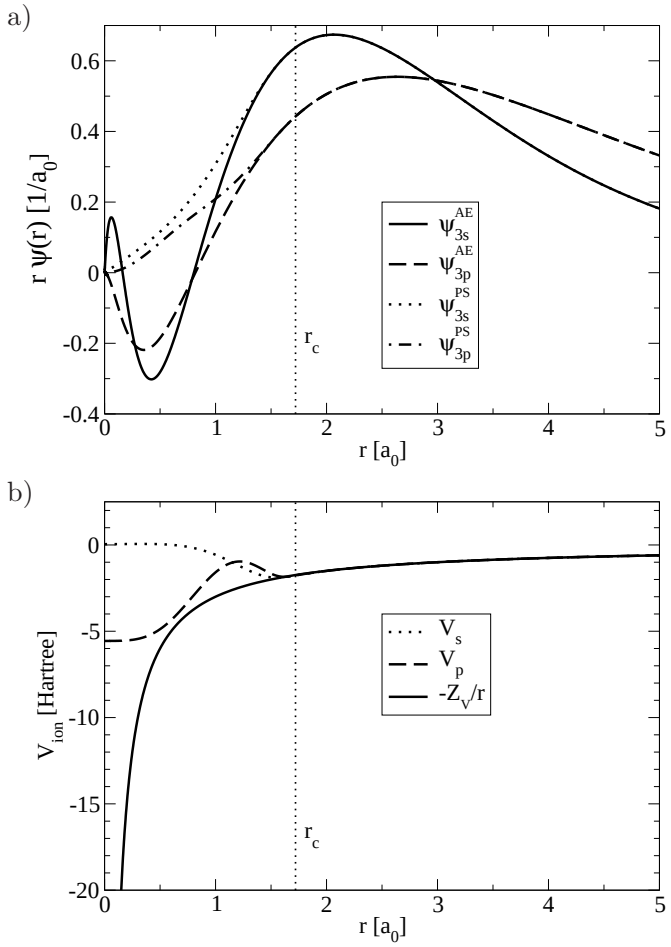

Figure 2.2: All-electron (AE) and pseudo- (PS) wave functions (a) and pseudopotentials (b) for the $3s$ and $3p$ valence states of an isolated aluminum atom (calculated with the pseudopotential generator code OPIUM [117]). $-Z_{\mathrm{V}}/r$ is the asymptotic behavior of the Coulomb potential seen by the valence states at large distances from the ionic core ($Z_{\mathrm{V}} = 3$).

Ab initio pseudopotentials are constructed from Kohn-Sham calculations for single atoms including all core and valence electrons. The lowest energetic valence state of a given angular momentum (higher energetic states with same angular momentum are excited states of the corresponding pseudo-Hamiltonian) is replaced by a nodeless pseudo-wave function, matching the original wave functions outside a sphere of radius r_c. The corresponding pseudopotential can be calculated by inverting the radial Schrödinger equation for the pseudo-wave function and a given reference energy (often the Kohn-Sham eigenvalue obtained from the all-electron calculation). The resulting potential is then to be unscreened by subtracting the contributions from the pseudo-valence density, which is straightforward for the Hartree potential being linear in the density. The non-linear dependence of the exchange-correlation potential can be taken into account by non-linear core corrections [120].

For norm-conserving pseudopotentials, the norm of the pseudo-wave functions is constrained to be equal inside the core sphere to the norm of the corresponding all-electron wave functions. Apart from leading to the same electrostatic potential outside the sphere, this ensures that first order deviations from the free-atom eigenvalues only change the logarithmic derivatives of the pseudo-wave functions outside the sphere to second order [121]. This means a good transferability of the pseudopotential to chemical environments which do not alter the characteristics of the atomic spectra significantly. Fig. 2.2 shows an example of norm-conserving pseudopotentials for the valence states of aluminum and the corresponding pseudo-wave functions generated in the Troullier-Martins scheme [122].

In the ultrasoft pseudopotential formalism [123], the norm-conservation constraint inside the core sphere is lifted, allowing for pseudo-wave functions without high Fourier components even if the radial all-electron wave function for $r > 0$ already is nodeless (*i.e.* for $\ell = n-1$; n: principal quantum number) and strongly localized. The separable representation (2.82) is extended to more than one reference energy for each angular momentum and the corresponding projectors, to re-introduce transferability of the ultrasoft pseudopotential despite the lack of norm conservation. The pseudo-valence charge density is corrected by an augmentation charge, which is calculated by tracing out all reference state ($|s_{\ell m}\rangle$, $|s'_{\ell m}\rangle$) degrees of freedom of auxiliary functions $\Delta Q_{s,s'}(r)$ (subscripts ℓm dropped for simplicity) over the space spanned by the occupied pseudo-valence states. These auxiliary functions are non-zero only inside the core region:

$$\Delta Q_{s,s'} = \langle \psi_s^{\mathrm{AE}} | r \rangle \langle r | \psi_{s'}^{\mathrm{AE}} \rangle - \langle \psi_s^{\mathrm{PS}} | r \rangle \langle r | \psi_{s'}^{\mathrm{PS}} \rangle, \tag{2.83}$$

with the all-electron and pseudo-wave functions $|\psi_s^{\mathrm{AE}}\rangle$ and $|\psi_s^{\mathrm{PS}}\rangle$ of the isolated atom, respectively. The resulting Kohn-Sham eigenstates overlap in the core regions, leading to a generalized eigenvalue problem. Although the introduction

of several reference state projectors per angular momentum in the ultrasoft pseudopotential approach means additional complexity for the total energy calculation, the reduction of the size of the plane wave basis generally still lowers the overall computational effort significantly.

An alternative approach to introduce pseudized wave functions is the projector-augmented wave method [124], where a linear transformation $\hat{\mathfrak{T}}$ mediates between the states $|\psi^{\mathrm{PS}}\rangle$, pseudized in the so-called augmentation sphere around the atom with radius r_{c}, and the all-electron states $|\psi^{\mathrm{AE}}\rangle$:

$$|\psi^{\mathrm{AE}}\rangle = \hat{\mathfrak{T}}|\psi^{\mathrm{PS}}\rangle. \tag{2.84}$$

The Schrödinger equation for the pseudo-wave functions reads:

$$\hat{\mathfrak{T}}^{+}\hat{H}\hat{\mathfrak{T}}|\psi_i^{\mathrm{PS}}\rangle = \varepsilon_i\hat{\mathfrak{T}}^{+}\hat{\mathfrak{T}}|\psi_i^{\mathrm{PS}}\rangle, \tag{2.85}$$

with the eigenvalue ε_i corresponding to the eigenstate $|\psi_i^{\mathrm{PS}}\rangle$. Similar to the case of ultrasoft pseudopotentials, the pseudized wave functions overlap inside the augmentation sphere. Outside the sphere, the operator $\hat{\mathfrak{T}}$ is identity:

$$\hat{\mathfrak{T}} = 1 + \sum_i \left(|\psi_i^{\mathrm{AE}}\rangle - |\psi_i^{\mathrm{PS}}\rangle\right)\langle\alpha_i|, \tag{2.86}$$

where $|\alpha_i\rangle$ is a projector function with $\sum_i |\psi_i^{\mathrm{PS}}\rangle\langle\alpha_i| = 1$ for $r \leq r_{\mathrm{c}}$ and $\langle\alpha_i|\psi_j^{\mathrm{PS}}\rangle = \delta_{ij}$. By adding $0 = \hat{\Lambda} - \sum_{ij}|\alpha_i\rangle\langle\psi_i^{\mathrm{PS}}|\hat{\Lambda}|\psi_j^{\mathrm{PS}}\rangle\langle\alpha_j|$ to Eq. (2.85) for an operator $\hat{\Lambda}$ vanishing outside the sphere, terms that require high plane wave cutoffs can be canceled in the plane wave expansion, being accounted for by a radial integration over the augmentation sphere instead.

An advantage of the projector-augmented wave method is that the transformation (2.84) allows for a calculation of the all-electron wave functions (a similar transformation can be applied in the ultrasoft pseudopotential formalism to reconstruct the all-electron wave functions [125]).

Implementations of the density functional formalism used in this work

For the calculation of the electronic structures and total energies of complex metal hydrides, which are presented in Chs. 4 and 5, we have relied on established implementations of the density functional theory formalism, namely, the pseudopotential plane wave codes DACAPO by Hammer, Hansen, Nørskov, *et al.* [108] and PWSCF by Baroni, de Gironcoli, Dal Corso, Giannozzi, *et al.* [126] and the projector-augmented wave implementation in the VASP code by Kresse

and Furthmüller [127]. The usage of different codes has allowed for a verification of the general applicability of the implementation of the methods presented in Ch. 4. Furthermore, the different features of the implementations have been used, *e.g.*, for a calculation of core electron charge densities in the projector-augmented wave formalism or for a Kohn-Sham orbital analysis taking advantage of the possibility to use different types of pseudopotentials.

3

Born-Oppenheimer dynamics

3.1 Lattice dynamics

So far, we have considered a fixed configuration of nuclear coordinates. As mentioned above, we can assume a parametrical dependence of the electronic Hamiltonian on the nuclear coordinates in the Born-Oppenheimer approximation [66]. We will first consider a finite system containing N atoms (periodic systems will be considered in Sec. 3.1.1). With the nuclear coordinates $\boldsymbol{R} \in \mathbb{R}^{3N}$, the Hamiltonian $\hat{H}_\mathrm{n}$ for the ionic degrees of freedom reads

$$\hat{H}_\mathrm{n} = -\boldsymbol{\mathcal{M}}^{-1} \frac{\boldsymbol{\nabla}_{\boldsymbol{R}}^2}{2} + V(\boldsymbol{R}), \tag{3.1}$$

where, due to the separation of nuclear and electronic timescales, the potential $V(\boldsymbol{R})$ is given by the sum of the electronic ground state energy for the parameters $\boldsymbol{R}$ and the electrostatic energy of the nuclear point charge system. $\mathcal{M}_{ij} = \delta_{ij} M_{\lfloor i/3 \rfloor}$ is the mass matrix, where $M_{\lfloor i/3 \rfloor}$ is the mass of the nucleus corresponding to the coordinate R_i.

In the harmonic approximation, the potential is expanded to second order in the nuclear coordinates around a configuration $\boldsymbol{R}_0$ the potential energy is minimal for, and hence the gradient vanishes:

$$V(\boldsymbol{R} - \boldsymbol{R}_0) \approx V_0 + \frac{1}{2} \sum_{ij=1}^{3N} \mathcal{H}_{ij} \left(R_i - R_{0,i}\right) \left(R_j - R_{0,j}\right), \tag{3.2}$$

where

$$\mathcal{H}_{ij} = \left.\frac{\partial^2 V}{\partial R_i \partial R_j}\right|_{\boldsymbol{R}_0} \tag{3.3}$$

is the Hessian matrix of the potential energy. The potential (3.2) results in a Schrödinger equation for $3N$ coupled one-dimensional harmonic oscillators.

The eigenstates of the Hamiltonian of a single one-dimensional harmonic oscillator (ω is the classical eigenfrequency, m is the particle mass in units of the electron mass (atomic units), and $\hat{x}$ and $\hat{p}$ are the position and momentum operators, respectively)

$$\hat{H}_{\mathrm{osc}} = \frac{\hat{p}^2}{2m} + \frac{1}{2} m\omega^2 \hat{x}^2 \tag{3.4}$$

can be obtained from an ansatz for the wave functions as products of polynomials and Gaussians [128] or by algebraically transforming the Schrödinger equation [129]. In the latter approach, the position and momentum operators are replaced by the operators

$$\hat{b} = \frac{1}{\sqrt{2}} \left(\sqrt{m\omega}\hat{x} + \frac{i}{\sqrt{m\omega}}\hat{p} \right) \tag{3.5}$$

$$\hat{b}^+ = \frac{1}{\sqrt{2}} \left(\sqrt{m\omega}\hat{x} - \frac{i}{\sqrt{m\omega}}\hat{p} \right), \tag{3.6}$$

yielding

$$\hat{H}_{\mathrm{osc}} = \omega \left(\hat{b}^+ \hat{b} + \frac{1}{2} \right). \tag{3.7}$$

From the commutator $[\hat{x}, \hat{p}] = i$ follows $[\hat{b}, \hat{b}^+] = 1$. From this relation follows for the operators $\hat{b}$ and $\hat{b}^+$ acting on an eigenstate $|n\rangle$, that also $\hat{b}|n\rangle$ and $\hat{b}^+|n\rangle$ are eigenstates, with an eigenlevel lowered or raised by the energy ω, respectively. $\hat{b}$ is the annihilation and $\hat{b}^+$ the creation operator for a bosonic quasi particle of energy ω. The uncertainty principle ensures that the eigenenergies of bound states cannot be lower than the potential energy minimum. Thus the annihilation operator acting on the ground state yields zero. From the corresponding differential equation follows that the ground state energy is $\omega/2$. The eigenenergies of the harmonic oscillator are

$$\varepsilon_n = \omega \left(n + \frac{1}{2} \right), \tag{3.8}$$

with the number of vibrational quanta $n \in \{0, 1, 2, ...\}$.

The classical equations of motion for a system of the $3N$ coupled one-dimensional harmonic oscillators with the potential energy (3.2) and kinetic energies $M_{\lfloor j/3 \rfloor}\dot{x}_j^2/2$ are

$$M_{\lfloor j/3 \rfloor}\ddot{x}_j = -\sum_k \mathcal{H}_{jk}x_k, \tag{3.9}$$

with the coordinates $x_j = R_j - R_{0,j}$. With the ansatz $x_j = u_j \exp(i\omega t)$ a generalized eigenvalue problem in the space of the displacement amplitudes u_j can be obtained:

$$\boldsymbol{\mathcal{H}u} = \omega^2 \boldsymbol{\mathcal{M}u}. \tag{3.10}$$

The transformation $\tilde{\boldsymbol{\mathcal{H}}} = \boldsymbol{\mathcal{L}}^{-1}\boldsymbol{\mathcal{H}}\boldsymbol{\mathcal{L}}^{-1}$ with $\boldsymbol{\mathcal{L}}_{ij} = M_{\lfloor i/3 \rfloor}^{1/2}\delta_{ij}$, results in the equivalent eigenvalue problem

$$\tilde{\boldsymbol{\mathcal{H}}}\tilde{\boldsymbol{u}} = \omega^2 \tilde{\boldsymbol{u}}, \tag{3.11}$$

with the polarization vectors $\tilde{\boldsymbol{u}} = \boldsymbol{\mathcal{L}u}$. Bosonic annihilation and creation operators for a mode with frequency ω_μ are constructed in analogy to Eqs. (3.5) and (3.6) by projection of the $3N$ dimensional position and momentum operators onto the polarization vector $\tilde{\boldsymbol{u}}_\mu$ [130]. The commutators for the resulting operators are

$$\begin{aligned} [\hat{b}_\mu, \hat{b}_\nu] &= [\hat{b}_\mu^+, \hat{b}_\nu^+] = 0 \\ [\hat{b}_\mu, \hat{b}_\nu^+] &= \delta_{\mu\nu}, \end{aligned} \tag{3.12}$$

i.e. vibrational quanta in different modes $\mu \neq \nu$ are annihilated and created independently. The corresponding Hamiltonian therefore becomes a sum of the Hamiltonians of one-dimensional harmonic oscillators (defining $V_0 := 0$):

$$\hat{H}_{3N-\mathrm{osc}} = \sum_\mu \omega_\mu \left(\hat{b}_\mu^+ \hat{b}_\mu + \frac{1}{2} \right), \tag{3.13}$$

with the eigenvalues

$$E(n_1, ..., n_{3N-6}) = \sum_\mu \omega_\mu \left(n_\mu + \frac{1}{2} \right), \tag{3.14}$$

where $n_\mu \in \{0, 1, 2, ...\}$ is the number of vibrational quanta in mode μ (six degrees of freedom do not correspond to vibrational normal modes but to invariance of the energy with respect to translation and rotation of the system).[1]

[1] If the configuration $\boldsymbol{R}_0$ with vanishing total energy gradient refers to a saddle point on the potential energy surface, negative Hessian eigenvalues appear, corresponding to imaginary frequencies, *i.e.* non-oscillatory motion. The system is unstable with respect to displacements in the corresponding directions (cf. Sec. 5.1).

3.1.1 Energetic dispersion in periodic systems

For a periodic system, the corresponding Hamiltonian $\hat{H}$ of coupled harmonic oscillators is invariant with respect to a translation by a lattice vector. Therefore, in analogy to Bloch's theorem (2.69), an eigenstate translated by a lattice vector $\boldsymbol{T}$ also is an eigenstate of the Hamiltonian, differing only by a phase factor $\exp(i\boldsymbol{q}\boldsymbol{T})$. In analogy to electronic excitations discussed in Sec. 2.3, the allowed wave vectors form a continuous set. Wave vectors $\boldsymbol{q}$ outside the first Brillouin zone correspond to waves with oscillations between atomic positions, and hence describe the same elastic waves of atomic displacements as wave vectors $\boldsymbol{q}' = \boldsymbol{q} - \boldsymbol{G}$ in the first Brillouin zone. In contrast to the reduction of the dispersion of the electronic eigenenergies, the wave vectors $\boldsymbol{q}$ can thus be restricted to the first Brillouin zone. In order to take advantage of this restriction, we look for a representation of the Hamiltonian in terms of integrals over the first Brillouin zone. The operators for the nuclear coordinates $\boldsymbol{x}_{\boldsymbol{T}} \in \mathbb{R}^{3s}$ in a primitive cell (containing s atoms) translated from a chosen origin by a lattice vector $\boldsymbol{T}$ are correspondingly replaced by the integral

$$\hat{\boldsymbol{x}}_{\boldsymbol{T}} = \sqrt{\frac{\Omega}{(2\pi)^3}} \int_{\mathrm{BZ}} \mathrm{d}^3 q \exp(-i\boldsymbol{q}\boldsymbol{T}) \hat{\boldsymbol{X}}_{\boldsymbol{q}}, \tag{3.15}$$

where Ω is the unit cell volume. Multiplication of Eq. (3.15) by $[\Omega/(2\pi)^3]^{1/2} \times \exp(i\boldsymbol{q}'\boldsymbol{T})$ and summation over the lattice vectors $\boldsymbol{T}$ yields a Fourier series for the operator $\hat{\boldsymbol{X}}_{\boldsymbol{q}}$:

$$\hat{\boldsymbol{X}}_{\boldsymbol{q}} = \sqrt{\frac{\Omega}{(2\pi)^3}} \sum_{\boldsymbol{T}} \exp(i\boldsymbol{q}\boldsymbol{T}) \hat{\boldsymbol{x}}_{\boldsymbol{T}}, \tag{3.16}$$

where we have used that

$$\sum_{\boldsymbol{T}} \exp(i\boldsymbol{q}\boldsymbol{T}) = \frac{(2\pi)^3}{\Omega} \sum_{\boldsymbol{G}} \delta(\boldsymbol{q} + \boldsymbol{G}), \tag{3.17}$$

which follows from a Fourier expansion of the right-hand side of Eq. (3.17). A corresponding expansion in the momentum operators $\hat{\boldsymbol{p}}_{\boldsymbol{T}}$ can be used to construct operators $\hat{\boldsymbol{P}}_{\boldsymbol{q}}$, that are conjugate to the operators (3.16) [131]:

$$\hat{\boldsymbol{P}}_{\boldsymbol{q}} = \sqrt{\frac{\Omega}{(2\pi)^3}} \sum_{\boldsymbol{T}} \exp(-i\boldsymbol{q}\boldsymbol{T}) \hat{\boldsymbol{p}}_{\boldsymbol{T}}, \tag{3.18}$$

with the commutator

$$[\hat{\boldsymbol{X}}_{\boldsymbol{q}}, \hat{\boldsymbol{P}}_{\boldsymbol{q}'}] = i\delta_{\boldsymbol{q}\boldsymbol{q}'}. \tag{3.19}$$

Inversion of (3.18) yields

$$\hat{\boldsymbol{p}}_{\boldsymbol{T}} = \sqrt{\frac{\Omega}{(2\pi)^3}} \int\limits_{\mathrm{BZ}} \mathrm{d}^3 q \exp(i\boldsymbol{q}\boldsymbol{T}) \hat{\boldsymbol{P}}_{\boldsymbol{q}}. \tag{3.20}$$

Using Eqs. (3.15) and (3.20), the Hamiltonian for the nuclear degrees of freedom can be written in the harmonic approximation as

$$\begin{aligned} \hat{H} &= \frac{\Omega}{2(2\pi)^3} \int\limits_{\mathrm{BZ}} \mathrm{d}^3 q \int\limits_{\mathrm{BZ}} \mathrm{d}^3 q' \left(\sum_{\boldsymbol{T}} \hat{\boldsymbol{P}}_{\boldsymbol{q}} \boldsymbol{\mathcal{M}}^{-1} \hat{\boldsymbol{P}}_{\boldsymbol{q}'} \exp[i(\boldsymbol{q}+\boldsymbol{q}')\boldsymbol{T}] \right. \\ &+ \left. \sum_{\boldsymbol{T},\boldsymbol{T}'} \hat{\boldsymbol{X}}_{\boldsymbol{q}} \boldsymbol{\mathcal{H}}_{\boldsymbol{T}-\boldsymbol{T}'} \hat{\boldsymbol{X}}_{\boldsymbol{q}'} \exp[-i\boldsymbol{q}\boldsymbol{T} - i\boldsymbol{q}'\boldsymbol{T}'] \right), \end{aligned} \tag{3.21}$$

with the mass matrix $\boldsymbol{\mathcal{M}}$ of the atoms in the unit cell and the Hessian

$$\mathcal{H}_{\boldsymbol{T}-\boldsymbol{T}',i,j} = \partial^2 V / \partial x_{\boldsymbol{T},i} \partial x_{\boldsymbol{T}',j}. \tag{3.22}$$

Since $\boldsymbol{q}$ is restricted to the first Brillouin zone, it follows from Eq. (3.17) that lattice sums over phase factors of the form $\exp[i(\boldsymbol{q}+\boldsymbol{q}')\boldsymbol{T}]$ imply $\boldsymbol{q} = -\boldsymbol{q}'$. The Hessian matrix elements do not depend on the absolute positions of the corresponding unit cells in the lattice, but on the difference vector of their origins (denoted by the subscript $\boldsymbol{T}-\boldsymbol{T}'$). We correspondingly replace the summation over $\boldsymbol{T}'$ by a summation over $\boldsymbol{T}'' = \boldsymbol{T} - \boldsymbol{T}'$ and introduce the Fourier transform $\boldsymbol{\mathcal{D}}(\boldsymbol{q}) \in \mathbb{C}^{3s} \times \mathbb{C}^{3s}$ of the Hessian matrix:

$$\boldsymbol{\mathcal{D}}(\boldsymbol{q}) = \sum_{\boldsymbol{T}''} \exp(-i\boldsymbol{q}\boldsymbol{T}'') \boldsymbol{\mathcal{H}}_{\boldsymbol{T}''}. \tag{3.23}$$

Using that $\hat{\boldsymbol{X}}_{-\boldsymbol{q}} = \hat{\boldsymbol{X}}_{\boldsymbol{q}}^{+}$ and $\hat{\boldsymbol{P}}_{-\boldsymbol{q}} = \hat{\boldsymbol{P}}_{\boldsymbol{q}}^{+}$, the Hamiltonian (3.21) can be rewritten as

$$\hat{H} = \frac{1}{2} \int\limits_{\mathrm{BZ}} \mathrm{d}^3 q \left(\hat{\boldsymbol{P}}_{\boldsymbol{q}} \boldsymbol{\mathcal{M}}^{-1} \hat{\boldsymbol{P}}_{\boldsymbol{q}}^{+} + \hat{\boldsymbol{X}}_{\boldsymbol{q}} \boldsymbol{\mathcal{D}}(\boldsymbol{q}) \hat{\boldsymbol{X}}_{\boldsymbol{q}}^{+} \right). \tag{3.24}$$

Using the commutator (3.19), the corresponding eigenvalues can be obtained for a given wave vector by algebraical transformation of the integrand of (3.24), introducing annihilation and creation operators for a phonon with wave vector $\boldsymbol{q}$ and energy $\omega_{\boldsymbol{q},\alpha}$, yielding a phonon dispersion with 3 acoustic and $3s-3$ optical branches labeled by the mode index α [131]. The acoustic modes have zero energy for $\boldsymbol{q} = 0$, due to the translational invariance of the atomic basis in the unit cell, and show a linear dispersion in the limit of long wavelengths compared to the lattice constants, in analogy to acoustic waves in a continuous

medium. The energies of optical phonons are nonzero for $\boldsymbol{q} = 0$, corresponding to oscillations in the atomic basis with opposite phases, which in the case of different atomic species can be excited by electromagnetic radiation with typical frequencies of the order of 10 THz (infrared).

In the harmonic approximation, phonons with different wave vectors or energies are created and annihilated independently. In the presence of anharmonic terms in the potential energy the modes are coupled, corresponding to interactions between the phonons, dominating *e.g.* the thermal conductivity of insulators. Further examples of materials properties that are due to anharmonic potentials include the effect of thermal expansion of solids and the temperature dependence of elastic coefficients [132].

3.1.2 Thermodynamics of the phonon gas

We assume that small thermal displacements of the nuclei from their equilibrium positions can be approximated sufficiently well by harmonic potentials. Thus the energetic spectrum is described by Eq. (3.14) (with $N \to \infty$ for an infinite crystal; expressions in terms of the phonon dispersion will be discussed later). Thermodynamic properties of the phonon gas can be derived from the corresponding partition function of independent, distinguishable harmonic oscillators

$$\begin{aligned} Z &= \prod_{\mu} \sum_{n_\mu=0}^{\infty} \exp\left[-\beta\omega_\mu \left(n_\mu + \frac{1}{2}\right)\right] \\ &= \prod_{\mu} \exp\left(-\frac{\beta\omega_\mu}{2}\right) \sum_{n_\mu=0}^{\infty} \left[\exp(-\beta\omega_\mu)\right]^{n_\mu} \\ &= \prod_{\mu} \frac{1}{2\sinh\left(\frac{\beta\omega_\mu}{2}\right)}, \end{aligned} \tag{3.25}$$

with $\beta = (k_\mathrm{B}T)^{-1}$ ($k_\mathrm{B} \approx 3.17 \cdot 10^{-6}$ Hartree/K is Boltzmann's constant) and μ enumerating all modes in the crystal. The free energy of the phonon gas is

$$F = -\frac{1}{\beta} \ln Z = \frac{1}{\beta} \sum_{\mu} \ln\left[2\sinh\left(\frac{\beta\omega_\mu}{2}\right)\right]. \tag{3.26}$$

A uniform rescaling of the nuclear coordinates corresponds to a multiplication of (3.9) by a constant factor, not affecting the classical eigenfrequencies, which determine the quantum mechanical energetic spectrum. Therefore, the free

energy does not depend on the volume in the harmonic approximation.[2] The pressure $p = (\partial F/\partial V)_{T=\text{const}}$ is zero, and hence the Gibbs free energy $G = E - TS + pV = F + pV$ equals the free energy F in the harmonic approximation.

The entropy of the phonon gas is[3]

$$\begin{aligned} S &= -\frac{\partial F}{\partial T} \\ &= k_\mathrm{B} \sum_\mu \left[\frac{\beta\omega_\mu}{2} \coth\left(\frac{\beta\omega_\mu}{2}\right) - \ln\left(2\sinh\left\{\frac{\beta\omega_\mu}{2}\right\}\right)\right], \end{aligned} \tag{3.27}$$

vanishing at zero temperature. With the equality of the thermodynamical potentials F and G, the heat capacities at constant volume and constant pressure are equal:

$$\begin{aligned} C_V &= C_p = T\frac{\partial S}{\partial T} \\ &= \sum_\mu \frac{k_\mathrm{B}\beta^2\omega_\mu^2}{4\left[\cosh^2\left(\frac{\beta\omega_\mu}{2}\right) - 1\right]}. \end{aligned} \tag{3.28}$$

In the limit of large temperatures $\beta^{-1} \gg \omega_{\max}/2$ and a large number of atoms, the heat capacity per atom approaches the value $3k_\mathrm{B}$, which is the Dulong-Petit law, corresponding to a classical equipartition of the thermal energy; the classical mean value in thermal equilibrium of both potential and kinetic energy, being equal on average for a harmonic oscillator, is $\beta^{-1}/2$ for each mode.

The sums over modes in Eqs. (3.26)–(3.28) can alternatively be expressed as integrals over the phonon density of states. In terms of a normalized phonon density of states $g(\omega)$ with

$$\int_0^\infty \mathrm{d}\omega g(\omega) = 1, \tag{3.29}$$

the free energy per primitive unit cell (containing s atoms) reads

$$F = \frac{3s}{\beta} \int_0^\infty \mathrm{d}\omega g(\omega) \ln\left[2\sinh\left(\frac{\beta\omega}{2}\right)\right]. \tag{3.30}$$

[2] In the so-called quasi-harmonic approximation, anharmonicities are taken into account to the extent that the force constants, *i.e.* the matrix elements of the Hessian are calculated for different unit cell volumes.

[3] Non-phononic contributions to the entropy in solids can be due to molecular rotations or due to structural disorder. Disorder is negligible in (most of) the solids we will consider. Rotations of *e.g.* complex ions require relatively high energies of the order of 1 eV in most of the systems studied here, such that these degrees of freedom can be assumed to be frozen out at near ambient temperatures and below.

The contribution of each branch $\alpha \in 3s$ can be calculated as an integral over the density in $\boldsymbol{q}$-space over the volume $V_{\omega+\mathrm{d}\omega}$, for which the dispersion of the branch lies in the interval $[\omega, \omega + \mathrm{d}\omega]$:

$$g_\alpha(\omega)\mathrm{d}\omega = \frac{\Omega}{3s(2\pi)^3} \int\limits_{V_{\omega+\mathrm{d}\omega}} \mathrm{d}^3 q. \tag{3.31}$$

With $\mathrm{d}\omega = \mathrm{d}\boldsymbol{q} \cdot (\boldsymbol{\nabla}_{\boldsymbol{q}}\omega)$, the density of states due to branch α is given as an integral over the surface of constant energy ω in $\boldsymbol{q}$-space:

$$g_\alpha(\omega) = \frac{\Omega}{3s(2\pi)^3} \int\limits_{\omega=\mathrm{const}} \frac{\mathrm{d}\sigma}{v_{\boldsymbol{q}}^{(\alpha)}}, \tag{3.32}$$

with the group velocity $\boldsymbol{v}_{\boldsymbol{q}}^{(\alpha)} = \boldsymbol{\nabla}_{\boldsymbol{q}}\omega$ of branch α.

3.1.3 Calculation of the phonon dispersion

While the total energy gradient with respect to the nuclear coordinates is due to the electrostatics of the nuclear point charge system and the unperturbed charge density of the electronic system (Hellmann-Feynman theorem, cf. Eq. (2.4)), the calculation of the Hessian involves first order perturbations of the electronic charge density. There are three categories of computational approaches to *ab initio* lattice dynamics: approximation of the Hessian by finite force differences obtained from total energy calculations for displaced configurations [13, 14, 133–136], spectral analysis of the velocity autocorrelation from molecular dynamics simulations [16], and calculation of the linear response of the charge density within density functional perturbation theory [15, 137–139]. The latter approach has the advantage that responses to perturbations of different wave vectors are decoupled [15], while the former two methods require supercells such that Hessian matrix elements between periodic images can be neglected. Due to large atomic mass differences in the compounds considered here, consisting of metal and hydrogen atoms, a large number of discrete time steps would be required to resolve the oscillations of the larger atoms using molecular dynamics simulations, the lighter elements requiring short time steps. We have used atomic-displacement-based approaches for the calculation of vibrational spectra, with the advantage that the computational solution to the electronic structure problem only needs to provide total energy gradients, *i.e.* unperturbed ground state properties of displaced configurations. The linear response method has been considered to benchmark the computational complexity of a new approach to estimate phonon frequencies [P2] presented in Sec. 4.2.

3.1.3.1 Finite force differences approach

In the displacement-based methods, Hessian-vector products are approximated by finite force differences:

$$\boldsymbol{\mathcal{H}}\boldsymbol{d} \approx \varepsilon^{-1} \left[\boldsymbol{\nabla} E(\boldsymbol{R}_0 + \varepsilon \boldsymbol{d}) - \boldsymbol{\nabla} E(\boldsymbol{R}_0)\right], \tag{3.33}$$

where ε is used to scale the displacement $\boldsymbol{d}$ (the leading error of Eq. (3.33) can be reduced from $O(\varepsilon)$ to $O(\varepsilon^2)$ by considering symmetric force differences for $\boldsymbol{R}_0 \pm \varepsilon \boldsymbol{d}$). The total energy gradient $\boldsymbol{\nabla} E(\boldsymbol{R}_0)$ vanishes if $\boldsymbol{R}_0$ represents a configuration extremizing the total energy. Projecting Eq. (3.33) for a given displacement $\boldsymbol{d}$ of the u atoms in the supercell onto a displacement $\boldsymbol{d}'$ yields a matrix element of the Hessian $\boldsymbol{\mathcal{H}}^{\text{super}} \in \mathbb{R}^{3u} \times \mathbb{R}^{3u}$. By considering symmetries in the super cell, the number of $3u$ *ab initio* force calculations to construct $\boldsymbol{\mathcal{H}}^{\text{super}}$ can be reduced to the number of displacements that are not mapped by point group symmetry operations $\boldsymbol{\mathcal{S}}$ onto each other. The forces due to symmetrically equivalent displacements are related by the corresponding transformations $\boldsymbol{\mathcal{S}}$.

With the displacement of an atom in the supercell all periodic images of this atom are displaced as well. The calculated Hessian $\boldsymbol{\mathcal{H}}^{\text{super}}$ therefore is a linear combination of Hessian matrices $\boldsymbol{\mathcal{H}}^{\text{super}}_{\tilde{\boldsymbol{T}}}$ of the form of Eq. (3.22) [13]:

$$\boldsymbol{\mathcal{H}}^{\text{super}} = \sum_{\tilde{\boldsymbol{T}}} \boldsymbol{\mathcal{H}}^{\text{super}}_{\tilde{\boldsymbol{T}}}, \tag{3.34}$$

where $\tilde{\boldsymbol{T}}$ is a vector of the supercell lattice. In order to calculate the Fourier transform of the Hessian of the extended system according to Eq. (3.23), Eq. (3.34) generally has to be decoupled into the contributions from supercell Hessian matrices with different distances between the periodic images. An exception is the Fourier transform for wave vectors that are vectors $\tilde{\boldsymbol{G}}$ of the supercell reciprocal lattice. If the supercell is *e.g.* formed by repeating an orthorhombic primitive cell once in x-direction, the $\boldsymbol{X}$-point ($\boldsymbol{q} = (1/2, 0, 0)$ in units of the reciprocal lattice corresponding to the primitive cell) becomes the reciprocal lattice vector $\tilde{\boldsymbol{G}} = (1, 0, 0)$. For a supercell consisting of n primitive cells, $\boldsymbol{\mathcal{H}}^{\text{super}}$ can be split into n^2 blocks $\mathcal{H}^{\text{prim.}}_{\boldsymbol{U};t,t'}$, where t and t' label the atomic coordinates in primitive cells with origins separated by a vector $\boldsymbol{U}$ inside the supercell, respectively. The matrices $\boldsymbol{\mathcal{H}}^{\text{prim.}}_{\boldsymbol{U}}$ are supercell lattice sums over the blocks $\boldsymbol{\mathcal{H}}^{\text{prim.}}_{\boldsymbol{U};\tilde{\boldsymbol{T}}}$ of $\boldsymbol{\mathcal{H}}^{\text{super}}_{\tilde{\boldsymbol{T}}}$ in analogy to Eq. (3.34). If $\boldsymbol{q}$ is a reciprocal lattice vector $\tilde{\boldsymbol{G}}$, all terms in the Hessian Fourier transform (3.23) which correspond to a lattice vector $\boldsymbol{U} + \tilde{\boldsymbol{T}}$ are added with the same phases $\exp[-i\tilde{\boldsymbol{G}}(\boldsymbol{U} + \tilde{\boldsymbol{T}})] = \exp(-i\tilde{\boldsymbol{G}}\boldsymbol{U})$. Hence, Eq. (3.23) becomes

$$\boldsymbol{\mathcal{D}}(\tilde{\boldsymbol{G}}) = \sum_{\boldsymbol{U}} \exp(-i\tilde{\boldsymbol{G}}\boldsymbol{U}) \boldsymbol{\mathcal{H}}^{\text{prim.}}_{\boldsymbol{U}}. \tag{3.35}$$

For $\boldsymbol{q} \notin \{\tilde{\boldsymbol{G}}\}$, the calculated linear combinations of Hessian matrices have to be decoupled into the matrices $\boldsymbol{\mathcal{H}}^{\text{prim.}}_{\boldsymbol{U};\tilde{\boldsymbol{T}}}$, which are then added with phase factors $\exp[-i\boldsymbol{q}(\boldsymbol{U}+\tilde{\boldsymbol{T}})] \neq \exp(-i\boldsymbol{q}\boldsymbol{U})$. If the supercell is chosen sufficiently large, such that interatomic force constants for atoms separated by a supercell basis or longer vector can be neglected, the remaining Hessian matrix elements $\mathcal{H}^{\text{prim.}}_{\boldsymbol{U};\tilde{\boldsymbol{T}};t,t'}$ can be obtained by considering coordination shells of equivalent atoms surrounding the atom corresponding to the degree of freedom t. The Hessian matrix elements can then be approximated as [136]

$$\mathcal{H}^{\text{prim.}}_{\boldsymbol{U};\tilde{\boldsymbol{T}};t,t'} = w_{t,t'}\mathcal{H}^{\text{prim.}}_{\boldsymbol{U}}, \tag{3.36}$$

where $w_{t,t'}$ is a weight equal for all contributions from the same coordination shell. The weights are given by the constraint that the Fourier transform (3.23) calculated from the matrices (3.36) coincides with Eq. (3.35) for reciprocal lattice vectors $\tilde{\boldsymbol{G}}$ [136].

Since the second order energy derivatives for the Hessian $\boldsymbol{\mathcal{H}}^{\text{super}}$ are approximated by finite differences in numerically calculated first order derivatives, the results for the $\boldsymbol{\mathcal{H}}^{\text{super}}$ can deviate (generally slightly) from the symmetry $\mathcal{H}^{\text{super}}_{s,s'} = \mathcal{H}^{\text{super}}_{s',s}$, which can be corrected for by forming the average of $\boldsymbol{\mathcal{H}}^{\text{super}}$ with its transpose. Another general property of the Hessian follows from the translational invariance with respect to a rigid translation of the crystal, *e.g.* along one of the cartesian axes. The sum of the Hessian matrix elements over the u corresponding coordinate indices v_α ($\alpha \in \{x,y,z\}$) vanishes, since the forces exerted on the nuclei remain unchanged for a rigid translation:

$$\sum_{v_\alpha} \frac{\partial^2 E}{\partial r_{v_\alpha} \partial r_{v'_\alpha}} = -\sum_{v_\alpha} \frac{\partial F_{v'_\alpha}}{\partial r_{v_\alpha}} = 0 \quad \forall\, v'_\alpha. \tag{3.37}$$

Due to the usage of finite basis sets, *e.g.* grids in numerical approaches to the electronic structure problem, the translational invariance is not (fully) resolved, and hence Eq. (3.37) is not fulfilled. The translational invariance reflected in Eq. (3.37) is important for the behavior of acoustic modes for small wave vectors, and can be corrected for by replacing the diagonal elements of the Hessian with the negative of the sums of the corresponding off-diagonal elements [134], or by imposing Eq. (3.37) as a constraint with a certain weight for the fitting of harmonic force fields to *ab initio* force constants [136, 140].

Free energies can be calculated by approximating a Brillouin zone integral over the contributions to the free energy by a sum over a finite set of $\boldsymbol{q}$-points, or as an integral over the phonon density of states obtained from a Monte Carlo sampling of the dispersion [136, 140].

3.1.3.2 Linear response

Within density functional perturbation theory, the Hessian of the total energy is calculated according to

$$\begin{aligned}\frac{\partial^2 E}{\partial R_i \partial R_j} &= -\frac{\partial F_j}{\partial R_i} \\ &= \frac{\partial}{\partial R_i}\left(\frac{\partial E_{\mathrm{N}}}{\partial R_j} + \int \mathrm{d}^3 r n(\boldsymbol{r}) \frac{\partial V(\boldsymbol{r})}{\partial R_j}\right) \\ &= \frac{\partial^2 E_{\mathrm{N}}}{\partial R_i \partial R_j} + \int \mathrm{d}^3 r \left(\frac{\partial n(\boldsymbol{r})}{\partial R_i}\frac{\partial V(\boldsymbol{r})}{\partial R_j} \right. \\ &\quad \left. + n(\boldsymbol{r})\frac{\partial^2 V(\boldsymbol{r})}{\partial R_i \partial R_j}\right), \end{aligned} \tag{3.38}$$

where we have used that the electronic contribution to the adiabatic forces F_j is given by electrostatic interaction of the nuclear point charges with the ground state charge density $n(\boldsymbol{r})$. The contribution of the derivatives of the energy E_{N} of the nuclear point charge system is calculated using Ewald summation (see App. A). In addition to these electrostatic contributions, the calculation of the Hessian involves the linear response $\partial n(\boldsymbol{r})/\partial R_i$.

With the finite difference operator (ΔR_i is the displacement of a nuclear coordinate)

$$\Delta_i f := \frac{\partial f}{\partial R_i}\Delta R_i, \tag{3.39}$$

a linearized finite difference response of the charge density in the Kohn-Sham scheme can be formulated [15]:

$$\Delta_i n(\boldsymbol{r}) = 4 \sum_{\ell=1}^{N_{\mathrm{occ}}/2} \psi_\ell^*(\boldsymbol{r}) \Delta_i \psi_\ell(\boldsymbol{r}), \tag{3.40}$$

where the sum runs over the doubly occupied Kohn-Sham orbitals $|\psi_\ell\rangle$.[4] First order perturbation theory yields for the variation $|\Delta_i \psi_\ell\rangle$ (see *e.g.* [141]):

$$(\hat{H} - \varepsilon_\ell)|\Delta_i \psi_\ell\rangle = -(\Delta_i \hat{V} - \Delta_i \varepsilon_\ell)|\psi_\ell\rangle, \tag{3.41}$$

[4]Since we consider systems with time-reversal symmetry (external magnetic fields, *e.g.*, are not considered), non-degenerate eigenstates are real (or have a constant complex phase that can be chosen unity) and degenerate eigenstates are either real or appear as complex conjugate pairs. Therefore, the right-hand side of Eq. (3.40) is real (if a complex-valued state is occupied, so is also its degenerate complex conjugate). Without time-reversal symmetry, the real part of the right-hand side would have to be taken.

where $\hat{H}$ is the unperturbed Kohn-Sham Hamiltonian with eigenvalues ε_n (the first order variation of the eigenvalues is $\Delta_i\varepsilon_\ell = \langle\psi_\ell|\Delta_i\hat{V}|\psi_\ell\rangle$). The perturbing self-consistent potential $\Delta_i\hat{V}$ is given as

$$\Delta_i V(\boldsymbol{r}) = \Delta_i V_{\text{ext}}(\boldsymbol{r}) + \int \mathrm{d}^3 r \frac{\Delta_i n(\boldsymbol{r}')}{|\boldsymbol{r}-\boldsymbol{r}'|} + \left.\frac{\partial v_{\text{xc}}}{\partial n}\right|_{n=n(\boldsymbol{r})} \Delta_i n(\boldsymbol{r}). \tag{3.42}$$

Due to the dependence of (3.40) on the variations of all occupied Kohn-Sham orbitals, Eq. (3.41) is solved self-consistently for each $|\Delta_i\psi_\ell\rangle$ (alternatively, the equations can be converted to a system of coupled linear equations, since (3.42) is a linear functional of the charge density variation, which depends linearly on the variations of the Kohn-Sham orbitals).

Expanding the first order corrections to the Kohn-Sham orbitals in the basis of the unperturbed orbitals, the variation of the charge density reads

$$\Delta_i n(\boldsymbol{r}) = 4 \sum_{\ell=1}^{N_{\text{occ}}/2} \sum_{m\neq\ell} \psi_\ell^*(\boldsymbol{r}) \frac{\left\langle \psi_m \left| \Delta_i\hat{V} \right| \psi_\ell \right\rangle}{\varepsilon_\ell - \varepsilon_m} \psi_m(\boldsymbol{r}), \tag{3.43}$$

where the sum over m includes all unoccupied and occupied orbitals apart from $|\psi_\ell\rangle$. The coupling of occupied states does not contribute to the charge density variation, because the corresponding terms cancel with opposite signs of the denominator in (3.43).[5] A calculation of the charge density variation according to (3.43) would require the calculation of all Kohn-Sham orbitals with a computational effort of $O(N_{\text{b}}^3)$, where N_{b} is the number of basis functions. N_{b} is generally much larger than the number of electron N_{e} (especially for general bases such as plane waves), such that an iterative diagonalization (based on Hamiltonian-vector products without explicit construction of the Hamiltonian) yielding only the occupied orbitals and scaling as $O(N_{\text{e}}^2 N_{\text{b}})$ [99] is preferable. However, the fact that the charge density response only depends on the coupling of the unoccupied to the occupied orbitals can be used to remove the singularity of $\hat{H}-\varepsilon_\ell$ in Eq. (3.41) [15]:

$$(\hat{H} + \alpha\hat{P}_{\text{o}} - \varepsilon_\ell)|\Delta_i\psi_\ell\rangle = -\hat{P}_{\text{e}}\Delta_i\hat{V}|\psi_\ell\rangle, \tag{3.44}$$

where α is a real scalar, and $\hat{P}_{\text{o}}$ and $\hat{P}_{\text{e}} = 1-\hat{P}_{\text{o}}$ are projectors for the occupied and empty subspaces, respectively. The additional term on the left-hand side removes the singularity due to the zero eigenvalue $\langle\psi_\ell|\hat{H}-\varepsilon_\ell|\psi_\ell\rangle$. The projector

[5] For the case of degeneracies in the occupied orbital manifold, linear combinations of the degenerate orbitals are formed, such that the expansion of the states in powers of the perturbation is continuous for zero coupling strength. Replacing degenerate sets of orbitals by these linear combinations, the contributions of couplings in the occupied manifold to the charge density variation cancel as well.

$\hat{P}_\mathrm{e}$ on the right-hand side ensures that this modification does not affect the components of the wave function variations contributing to the charge density variation, which are orthogonal to the occupied orbitals. This allows for an iterative solution of Eq. (3.44) requiring only the knowledge of the occupied part of the unperturbed spectrum, which scales per perturbation as the self-consistent calculation of the ground state charge density [15].[6]

From an expansion of the perturbing potential in a Fourier series follows that perturbations of different wavelengths decouple [15]. This is an advantage of the density functional perturbation theory approach over the force-based methods, since the linear response calculations can therefore be performed for the primitive unit cell. This advantage becomes less important for larger systems, where all significant interatomic force constants are resolved within the primitive unit cell, and therefore supercell calculations are unnecessary for force-based methods as well.

3.2 Solid state rate processes

If the motion of the nuclei can be described by classical mechanics, the calculation of the corresponding dynamics is substantially simplified compared to a quantum mechanical treatment. From the time-dependent Schrödinger equation

$$\frac{\mathrm{d}}{\mathrm{d}t}|\Psi\rangle = -i\hat{H}|\Psi\rangle \tag{3.45}$$

follows Ehrenfest's theorem [143] about the temporal evolution of expectation values

$$\frac{\mathrm{d}}{\mathrm{d}t}\left\langle\hat{\Lambda}\right\rangle = -i\left\langle\left[\hat{\Lambda},\hat{H}\right]\right\rangle + \left\langle\frac{\mathrm{d}\hat{\Lambda}}{\mathrm{d}t}\right\rangle, \tag{3.46}$$

representing the correspondence between the equation of motion of a classical variable and a quantum mechanical expectation value. With the commutators

$$\begin{aligned}\left[\hat{\boldsymbol{P}}, f\left(\hat{\boldsymbol{R}}\right)\right] &= -i\boldsymbol{\nabla}_{\hat{\boldsymbol{R}}} f\left(\hat{\boldsymbol{R}}\right)\\ \left[\hat{\boldsymbol{R}}, g\left(\hat{\boldsymbol{P}}\right)\right] &= i\boldsymbol{\nabla}_{\hat{\boldsymbol{P}}} g\left(\hat{\boldsymbol{P}}\right)\end{aligned} \tag{3.47}$$

for the position and momentum operators $\hat{\boldsymbol{R}}$ and $\hat{\boldsymbol{P}}$ (which are not explicitly time-dependent), equations of motion resembling Hamilton's equations of

[6] Modifications to allow for a smearing of the electronic occupation near the Fermi surface to reduce the number of sampling $\boldsymbol{q}$-points have been introduced by de Gironcoli [142].

motion for classical mechanics can be derived:

$$\begin{aligned} \frac{\mathrm{d}}{\mathrm{d}t}\left\langle \hat{\boldsymbol{R}} \right\rangle &= \left\langle \boldsymbol{\nabla}_{\hat{\boldsymbol{P}}} \hat{H} \right\rangle \\ \frac{\mathrm{d}}{\mathrm{d}t}\left\langle \hat{\boldsymbol{P}} \right\rangle &= -\left\langle \boldsymbol{\nabla}_{\hat{\boldsymbol{R}}} \hat{H} \right\rangle . \end{aligned} \tag{3.48}$$

For a potential of the form $\hat{V} = \hat{V}(\hat{\boldsymbol{R}})$, one obtains an equation of motion similar to Newton's second law ($\boldsymbol{\mathcal{M}}$ is the diagonal mass matrix):

$$\boldsymbol{\mathcal{M}} \frac{\mathrm{d}^2}{\mathrm{d}t^2}\left\langle \hat{\boldsymbol{R}} \right\rangle = -\left\langle \boldsymbol{\nabla}_{\hat{\boldsymbol{R}}} \hat{V} \right\rangle . \tag{3.49}$$

Quantum mechanical expectation values evolve like classical variables, if the operators for gradient and average on the right-hand sides of Eqs. (3.48) and (3.49) can be exchanged, respectively, which is approximately the case, if the wave functions are sufficiently localized in time and space with respect to typical length scales given by the potential.

The thermal wavelength $\lambda = [2\pi/(Mk_{\mathrm{B}}T)]^{1/2}$ of a ^{4}He nucleus or a nucleus with larger mass M is less than 1 Å at the boiling temperature of nitrogen ($k_{\mathrm{B}}T \approx 7$ meV) and only half in length at room temperature, such that quantum mechanical coherence at larger distances can be neglected for nuclei with sufficiently large masses at sufficiently high temperatures. For hydrogen atoms, however, the thermal wavelength is 1 Å at room temperature, *i.e.* a classical description of the corresponding degrees of freedom can already become insufficient for near ambient temperatures.

Assuming a potential energy barrier of parabolic shape separating the initial and final configurations of nuclear coordinates of a dynamical process, a simple expression can be obtained for the so-called cross-over temperature T_{c} below which tunneling dominates over classical dynamics [144–146]: for tunneling to be dominant, the ratio of thermal wavelength to typical classical length scale must be larger than the ratio of thermal energy $k_{\mathrm{B}}T$ to energy barrier. In the simple case of a parabolic barrier, the classical length scale is given by the radius of curvature, *i.e.* the inverse curvature. With these assumptions, the cross-over temperature reads [146]

$$T_{\mathrm{c}} = \frac{\omega_{\mathrm{b}}}{2\pi k_{\mathrm{B}}}, \tag{3.50}$$

where ω_{b} is the magnitude of the imaginary frequency corresponding to the instability at the barrier top.

For all diffusion processes involving hydrogen atoms considered here, we have numerically obtained (as described in the following) values for the crossing temperature below 200 K, such that tunneling of nuclei can be neglected at

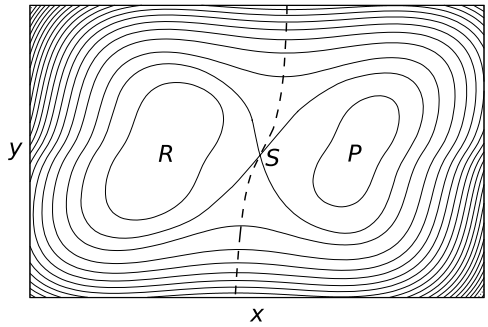

Figure 3.1: Schematic contour plot of a two-dimensional potential energy surface. The dashed line represents the one-dimensional surface dividing the regions R and P. S denotes a saddle point on the dividing surface (which is the only saddle point for this simple example).

near ambient temperatures. For the investigation of jump processes, we will therefore assume the nuclear coordinates to obey classical equations of motion, where the forces are due to the electrostatics of the nuclear point charge system and the charge density of the electronic system, adiabatically following the changes in the nuclear coordinates.

3.2.1 Transition state theory

Within transition state theory [6–8], the configuration space of a system with $3N$ degrees of freedom obeying classical mechanics is divided by a $(3N-1)$-dimensional surface into two regions attributed to the reactants R and the products P of a reaction $R \rightarrow P$, respectively (see Fig. 3.1). R and P could *e.g.* represent adjacent vacant sites. The calculation of an estimate for the corresponding rate constant by means of a simulation of the nuclear dynamics with finite time steps is infeasible,[7] since transitions from R to P usually are so-called rare events occurring typically several orders of magnitude less frequently than vibrations around an energetic minimum configuration in either R or P. This separation of timescales, however, allows for a calculation of the rate constant from equilibrium properties, if the separation is large enough such that the system can establish a Boltzmann equilibrium in R, and if the transition is slow enough such that a corresponding equilibrium is formed at each point of the trajectory in R.

[7] An approach to extend the timescales that are accessible to molecular dynamics simulations is the so-called hyperdynamics method [147], in which bias potentials are added in the simulations to raise the energy basin corresponding to R.

A dividing surface is placed between the energy basins corresponding to R and P so that all classical trajectories between R and P pass the surface. Only those trajectories contribute to the rate, that lead from R to P with the system remaining in P for a long time compared to vibrational timescales. Defining the rate as the unidirectional flux from R to P through the dividing surface (without subtracting the flux from P to R), trajectories which cross the surface more than once cause the transition rate to always be overestimated within transition state theory, since trajectories passing the surface several times, before the systems remains in either P or R (so-called dynamical recrossing), are counted as several reactions instead of one or zero reactions, respectively. Hence, a variational principle with respect to the placement of the dividing surface can be established [148–150], corresponding to a maximization of the free energy of the surface [151–153].[8] The dividing surface hence becomes a bottleneck for the transition, both in terms of potential energy and entropy barriers.

With the assumption, that the system is in Boltzmann equilibrium for all points of the trajectory in R, and that, once the dividing surface as a bottleneck is reached, the system will be led into P without recrossing the surface, an estimate for the rate can be obtained from the average velocity for passing through the surface and from the probability of finding the system close to the dividing surface. This probability is calculated as an integral over the configuration space volume TS of the so-called transition state, which has an infinitesimal width σ perpendicular to the dividing surface.

For dynamic events in crystal structures, it is usually sufficient (for moderate temperatures below the melting point) to expand the potential energy to second order in the coordinates with respect to the points in R and TS the system is most probable to be found at, respectively, neglecting the insufficient description by these expansions of the potential energy in regions of configuration space with low probabilities [155, 156]. For R, the point with highest probability is an energetic minimum and for TS, generally a saddle point. Introducing mass-scaled normal coordinates $\boldsymbol{u}_\mathrm{I}, \boldsymbol{u}_\mathrm{S} \in \mathbb{R}^{3N}$ (which are given as eigenvectors of mass-scaled Hessian matrices — cf. Eq. (3.11)) for the expansions around the minimum in R with potential energy V_I and the saddle point in TS with potential energy V_S, respectively, the probability P_{TS} of finding the system in TS reads

$$P_{TS} = \frac{[\det(\boldsymbol{\mathcal{L}})]^{-1}\,\tilde{\sigma}\int \mathrm{d}^{3N-1}u_\mathrm{S}\exp\left[-\frac{1}{k_\mathrm{B}T}\left(V_\mathrm{S}+\frac{1}{2}\sum_{i=1}^{3N-1}\omega_{\mathrm{S},i}^2 u_{\mathrm{S},i}^2\right)\right]}{[\det(\boldsymbol{\mathcal{L}})]^{-1}\int \mathrm{d}^{3N}u_\mathrm{I}\exp\left[-\frac{1}{k_\mathrm{B}T}\left(V_\mathrm{I}+\frac{1}{2}\sum_{j=1}^{3N}\omega_{\mathrm{I},j}^2 u_{\mathrm{I},j}^2\right)\right]}$$

[8] The free energy of the surface can *e.g.* be calculated as the reversible work for moving the surface from the energy basin minimum in R along the path of minimum energy towards the considered surface [154].

$$= \frac{\tilde{\sigma}}{\sqrt{2\pi k_\mathrm{B}T}} \frac{\prod_{j=1}^{3N} \omega_{\mathrm{I},j}}{\prod_{i=1}^{3N-1} \omega_{\mathrm{S},i}} \exp\left(-\frac{V_\mathrm{S} - V_\mathrm{I}}{k_\mathrm{B}T}\right), \tag{3.51}$$

where we have assumed the potential energy in TS to be constant in the direction of the infinitesimal mass-scaled width $\tilde{\sigma}$ (scaled with the corresponding unstable mode), omitting this degree of freedom from the expansion. The normalizing integral corresponding to the probability to initially find the system in R has been extended to all of configuration space, assuming errors from a non-vanishing probability in P due to finite values of the expansion of the potential to be negligible. $\omega_{\mathrm{I},i}$ and $\omega_{\mathrm{S},i}$ are the eigenfrequencies of the system for the minimum and saddle point configurations, respectively. The crystal is assumed to be macroscopically constrained, such that there are no zero frequencies owing to invariances with respect to rigid translations or rotations [155]. The factors $[\det(\boldsymbol{\mathcal{L}})]^{-1} = \prod_{i=1}^{N} M_i^{-3/2}$ (M_i are the masses of the nuclei) are due to the mass scaling of the coordinates in the integrals over the Boltzmann factors.

The average rate of crossing through TS — once the system has reached TS — is obtained from the Maxwell-Boltzmann distribution:

$$\frac{\tilde{v}_\mathrm{ave}}{\tilde{\sigma}} = \frac{\int_0^\infty \mathrm{d}\tilde{v}\tilde{v} \exp\left(-\frac{\tilde{v}^2}{2k_\mathrm{B}T}\right)}{\tilde{\sigma}\int_{-\infty}^\infty \mathrm{d}\tilde{v}' \exp\left(-\frac{\tilde{v}'^2}{2k_\mathrm{B}T}\right)} = \frac{\sqrt{k_\mathrm{B}T}}{\sqrt{2\pi}\tilde{\sigma}}, \tag{3.52}$$

where $\tilde{v}_\mathrm{ave}$ is the average unidirectional velocity through TS mass-scaled in the same proportion as the unstable mode at the saddle point perpendicular to the dividing surface. Multiplication of Eqs. (3.51) and (3.52) yields the estimate of the transition rate:

$$k_{R\to P} = \frac{1}{2\pi} \frac{\prod_{j=1}^{3N} \omega_{\mathrm{I},j}}{\prod_{i=1}^{3N-1} \omega_{\mathrm{S},i}} \exp\left(-\frac{V_\mathrm{S} - V_\mathrm{I}}{k_\mathrm{B}T}\right), \tag{3.53}$$

which has the form of Arrhenius' equation for thermally activated processes [157].

The Boltzmann factor in Eq. (3.53) corresponds to a potential energy barrier, while the frequency ratios represent an entropy barrier. If the frequencies ω_I are low, corresponding to a weak confinement in R, and the frequencies ω_S are high, corresponding to a strong confinement in TS, the rate is low compared to the opposite case of confinement strengths in R and TS, respectively.

3.2.2 Numerical saddle point determination

The calculation of the transition rate according to Eq. (3.53) only requires the knowledge of the potential energies and eigenfrequencies of the system for the

initial minimum and saddle point configurations, respectively. Within eigenmode following approaches [158–161], the sign of the projection of the potential energy gradient on the lowest eigenmode is inverted, following this modified gradient to a saddle point on the potential energy surface. We will use a different approach to obtain saddle points which only requires first-order energetic derivatives and generally is thus computationally more efficient. This method furthermore requires the knowledge of P and the minimum configuration of the corresponding energy basin. The minimum energy path connecting the minimum configurations of the initial and final states is sampled by a finite number of configurations, called images. This path is the trajectory with largest statistical weight; a variation of the path perpendicular to the trajectory always leads to an increased energy at the corresponding points. Only the tangential component of the potential energy gradient along the path is nonzero. Local maxima of the minimum energy path are saddle points on the potential energy surface, of which the highest maximum generally characterizes the overall rate, if the process is slow enough to allow for the formation of Boltzmann equilibria in the intermediate, metastable configurations [162].

3.2.2.1 The nudged elastic band approach

In the so-called nudged elastic band method [163], the images of an initial guess for the minimum energy path are moved in configuration space according to a gradient given by the projections of the potential gradient perpendicular to the path, and parallel projections of spring forces between adjacent images, maintaining an even sampling of the path. The tangential projection of the true potential gradient is not considered, because it would lead the intermediate images to the initial and final configurations, respectively. Perpendicular projections of the spring forces are generally not considered,[9] as this would cause a deviation of the optimized path from a minimum energy path.

Extensions to the nudged elastic band method allow for an improved saddle point localization. In the climbing image approach [162], the image with highest energy of a path pre-optimized using the regular nudged elastic band method is moved according to the potential energy gradient including the tangential projection with inverted sign. The other images are moved according to true perpendicular and parallel spring forces, allowing the path to adjust as the highest energy image approaches the saddle point.

[9] If the parallel spring force becomes large compared to the perpendicular forces, the optimization of the corresponding images can lead to kinks in the path, preventing convergence to the minimum energy path. In these cases, also the perpendicular projections of the spring forces are considered, with increasing weight for adjacent pairs of path elements approaching perpendicularity [163]. Alternatively, the tangent of the discretized path is calculated from asymmetric finite differences around each image, which are weighted according to potential energy differences [164].

In the adaptive nudged elastic band method [165], consecutive regular nudged elastic band calculations with relatively few images are performed. For a converged path, a new nudged elastic band is constructed between the two images adjacent to the image with maximal energy. This is repeated until a sufficient resolution near the saddle point is obtained.

We have used the nudged elastic band implementation in the CAMPOS project [166] for the calculation of jump paths of point defects in complex hydrides (see Sec. 5.3). Due to the computational efficiency of the adaptive nudged elastic band method given by the small number of simultaneously optimized images, we have used this approach for the localization of saddle points.

4

New methods

4.1 Crystal structure optimization with symmetry-enhanced convergence

4.1.1 Introduction

The calculation of the phonon dispersion or of transition rates described in the previous chapter depends on the determination of a configuration of nuclear coordinates minimizing the total energy. In order to find such a configuration, the total energy gradient for a starting guess of coordinates is calculated from the electrostatics of the nuclear point charges (see App. A) and the interaction with the corresponding electronic ground state density using the Hellmann-Feynman theorem (2.4). The negative of the gradient, *i.e.* the forces are followed to a new set of coordinates, for which again the electronic charge density and the total energy gradient are calculated. This procedure is repeated until sufficient convergence in total energy and forces is reached. Similarly, the lattice constants are optimized according to the stress tensor of the unit cell [167] (generally involving consecutive coordinate and unit cell relaxations).

In addition to the translational symmetry of the lattice, crystals can display further symmetries *e.g.* with respect to rotations, inversions, or reflections. Since consecutive symmetry operations form a new symmetry operation, the translations and possible other operations form a group, the so-called space group.

There are seven crystal systems, which are categorized with respect to three, two, or no equal lattice constants and with respect to equal or unequal angles

of $\pi/2$, $2\pi/3$, or arbitrary values between the basis vectors. Triclinic systems have the lowest symmetry with all lattice constants being different, and all angles being different and unequal to $\pi/2$ and $2\pi/3$. Cubic systems have the highest symmetry. The seven crystal systems can be further divided into 14 Bravais lattices with respect to up to four possible centerings of the atomic basis: primitive, base-centered, body-centered, and face-centered. In the former three cases, the conventional unit cell can be divided into primitive cells. In combination with 32 point group and compound symmetry operations, there are 230 space groups [168].

Since the electronic ground state charge density has the same symmetry as the nuclear coordinates, the forces exerted on nuclei with coordinates coinciding with symmetry elements such as mirror planes, rotation axes, or inversion centers have one or more force components that vanish independently of the (symmetric) configuration of the other nuclei, depending on the type and number of symmetry elements the position coincides with. The corresponding coordinates are thus fixed by symmetry. For coordinates that do not coincide with symmetry elements, the forces generally only vanish if the total energy is extremal for the given configuration. For these general sites there are n symmetrically equivalent sites, where n is the number of point group and compound symmetry operations of the space group.

For complex structures, there generally are many coordinates that are not fixed by symmetry and that are hence to be relaxed. Starting guesses for the coordinates of light elements based on X-ray diffraction patterns often require a significant amount of optimization steps until the equilibrium configuration is found. We have therefore implemented a coordinate relaxation scheme which takes advantage of the crystal symmetries leading to an enhanced convergence [P1].

4.1.2 Method

A set of symmetrically equivalent coordinates is generated from a reference coordinate by application of the symmetry operations. Using the so-called Wyckoff coordinates [169], the set of equivalent sites is given as linear equations in the coordinates scaled with the basis vectors. The reflection of a reference coordinate (x, y, z) with respect to the plane $y = 1/2$ *e.g.* is given as $(x, -y, z)$ (taking into account the y and $y + 1$ represent symmetrically equivalent coordinates; a reflection at $y = 1/2$ is thus equivalent to a reflection at $y = 0$).

We consider the reference coordinates $w_{j,\alpha}$ ($\alpha \in \{1, 2, 3\}$) as only degrees of freedom for the coordinate relaxation by mapping the total energy gradient

$\boldsymbol{\nabla} E$ on the corresponding coordinate subsystem:

$$\frac{\partial E}{\partial w_{j,\alpha}} := \frac{1}{\varepsilon}\Big[\Big(\boldsymbol{W}(w_{1,1},...,w_{j,\alpha}+\varepsilon,...,w_{n,3}) - \boldsymbol{W}(w_{1,1},...,w_{j,\alpha},...,w_{n,3})\Big)\cdot\boldsymbol{\nabla} E\left[\boldsymbol{W}(w_{i,\alpha})\right]\Big], \tag{4.1}$$

where $\boldsymbol{W}(w_{1,1},...,w_{n,3})$ are the cartesian coordinates of the atomic basis generated from the reference coordinates (implemented here using the Wyckoff coordinates of the given space group). Note that Eq. (4.1) does not depend on the magnitude of the displacement ε. The gradient components corresponding to fixed coordinates are set to zero, such that deviations from the symmetry due to numerical inaccuracies or symmetry breaking algorithms for the electronic structure calculation do not cause a drift of these coordinates. Due to the perfect symmetrization of the forces in Eq. (4.1), general coordinates are not affected by these numerical problems either. Symmetries cannot be broken because only the reference coordinates are changed directly, while the symmetrically equivalent coordinates are regenerated at each optimization step.

4.1.3 Computational details

We have used the gradient projection scheme in combination with a quasi-Newton optimization algorithm [170], where, in contrast to a standard Newton optimization, the iterative relaxation of the coordinates $\boldsymbol{R}_k$ according to $\boldsymbol{R}_{k+1} = \boldsymbol{R}_k - [\boldsymbol{\mathcal{H}}(\boldsymbol{R}_k)]^{-1}\cdot\boldsymbol{\nabla} E(\boldsymbol{R}_k)$ is only based on an approximate (inverse) Hessian, avoiding the computationally expensive calculation of second order derivatives of the total energy. With an initial guess for the Hessian, *e.g.* a scalar matrix, curvature information is approximated progressively from the calculated gradients $\boldsymbol{\nabla} E(\boldsymbol{R}_k)$.

For the examples in the following, total energies and gradients were calculated using the plane wave density functional theory codes DACAPO [108] (used for the Na_3AlH_6 example) and VASP [127, 171] (used for the remaining examples) to test the implementation of the gradient projection scheme. For DACAPO, ultrasoft pseudopotentials [123] were used, while the VASP calculations were performed in the projector-augmented wave [124] scheme. The Perdew-Wang-91 exchange-correlation functional [105, 106] was used for all calculations. A kinetic energy cutoff of 350 eV was used for the plane wave basis sets. The electronic Brillouin zones were sampled on Monkhorst-Pack grids [172] with mesh spacings of less than 0.05 Å^{-1}. The optimization processes were controlled within the CAMPOS Atomic Simulation Environment [166] using a symmetry conserving [173] quasi-Newton implementation.

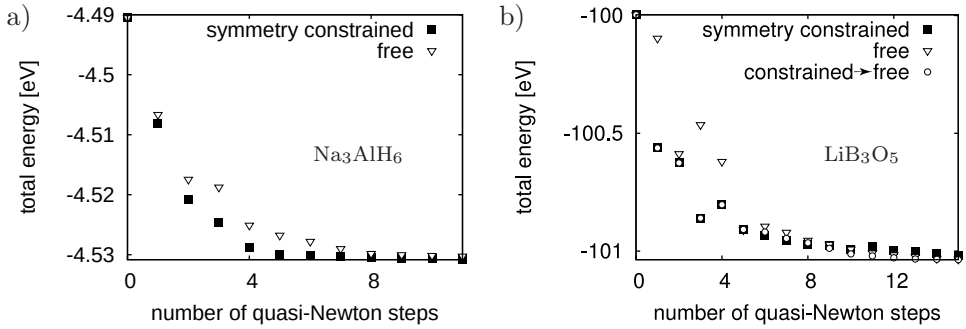

Figure 4.1: Relaxation of internal coordinates for Na_3AlH_6 (a) and LiB_3O_5 (b), using free and symmetry-constrained quasi-Newton optimization schemes, respectively. Total energies are specified per unit cell with respect to the cohesive energies of the constituting elements. (From [P1], submitted to the Journal of Computational Physics; `http://www.elsevier.com/locate/jcp`.)

4.1.4 Examples

In the following, the analysis of structure relaxations presented in Ref. [P1] is summarized. As a first simple example, the internal coordinates of the monoclinic crystal Na_3AlH_6 are optimized, an intermediate product in the decomposition process of $NaAlH_4$, which is a candidate material for reversible hydrogen storage in complex metal hydrides [48]. The energetic convergence with respect to the optimization steps starting with coordinates obtained from powder diffraction data for $P2_1/n$-Na_3AlH_6 [174] are shown in Fig. 4.1a. The optimization of the reference coordinates is faster and more monotonous than the direct optimization of all coordinates. The symmetry-constrained relaxation is *e.g.* within a 3‰ window of the converged energy after four steps, while the free relaxation requires 7 steps to reach this level of convergence.

The relaxation of the internal coordinates of LiB_3O_5 (space group $Pna2_1$ [175]), which is a nonlinear optical crystal [176], is shown in Fig. 4.1b. While the symmetry-constrained relaxation is faster for the first four steps, the free optimization converges better close to the energetic minimum. It is thus advantageous to perform a relaxation of the reference coordinates until the average residual forces have reached a given value (here: 0.1 eV/Å). The curvature information gathered so far by the quasi-Newton algorithm is used to construct a diagonal starting guess for an unconstrained relaxation by dividing the obtained diagonal Hessian matrix elements by the number of equivalent sites. This combined relaxation shows a good overall convergence (see Fig. 4.1b).

An optimal structure relaxation procedure is essential for the coordinate op-

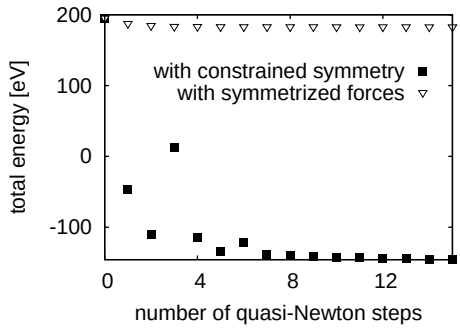

Figure 4.2: Free and symmetry-constrained internal coordinate optimization of the conventional unit cell of $Mg(BH_4)_2$ in space group *Fddd*. Total energies are specified per conventional unit cell with respect to the cohesive energies of the constituting elements. (From [P1], submitted to the Journal of Computational Physics; `http://www.elsevier.com/locate/jcp`.)

timization of large, complex structures with many symmetrically inequivalent degrees of freedom and a large computational effort for the calculation of the electronic structure. A proposed, idealized phase of $Mg(BH_4)_2$ (a material of possible interest for hydrogen storage applications) in space group *Fddd* [63] contains 176 atoms per primitive unit cell (704 atoms per conventional unit cell). The optimization of the reference coordinates only involves 62 degrees of freedom. Since the gradient obeys the crystal symmetries (neglecting the numerical problems mentioned above), the number of degrees of freedom is effectively reduced to the same extent for the direct optimization of all coordinates. Although the total energy gradient has been symmetrized by calculating the average forces with respect to the point group symmetry operations as implemented in VASP (Ref. [127]), a small drift in the coordinates in the free relaxation due to numerical inaccuracies leads this large system out of symmetry and prevents convergence (see Fig. 4.2).[1] The symmetry-constrained relaxation, on the other hand, converges well in about ten steps.

The *Fddd* phase is proposed to show structural disorder with half unit cells shifted with respect to each other [63] (see Fig. 4.3). The gradient projection technique allows for the inclusion of symmetry breaking parameters, *e.g.* shifts for the considered system, into the relaxation scheme. The total energy gradient is correspondingly mapped onto a difference vector due to a small change in the shift in analogy to Eq. (4.1). Starting from arbitrary shifts and relaxing

[1] Due to the high uncertainty in hydrogen coordinates obtained from powder diffraction patterns, one could relax these positions first keeping the other coordinates fixed, in order to prevent the loss of symmetry.

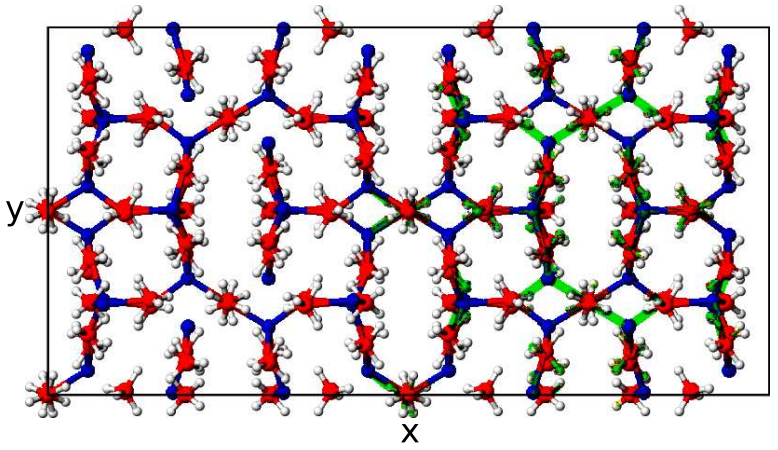

Figure 4.3: Conventional unit cell of *Fddd*-$Mg(BH_4)_2$. Magnesium is represented by blue, boron by red, and hydrogen by white spheres. Changes in the configuration due to a shift of the unit cell half with $x > 1/2$ by $y = 1/2$ are shown in green. (From [P1], submitted to the Journal of Computational Physics; `http://www.elsevier.com/locate/jcp`.)

both shifts and internal coordinates, we find shifts for $x > 1/2$ in both y- and z-direction by 0, $\pm 1/4$, and $1/2$ to correspond to local energetic minima, with the displacements by $\pm 1/4$ resulting in an increase in total energy of 0.1 eV per formula unit compared to displacements by 0 and $1/2$.

4.1.5 Conclusion

The presented gradient projection approach for a relaxation of the reference coordinates, from which symmetrically equivalent sites are regenerated at each optimization step, generally shows a faster convergence than a direct optimization of all coordinates. Close to convergence, lifting the symmetry constraints can accelerate the relaxation, where approximations to the Hessian diagonal elements obtained within the preceding symmetry-constrained optimization can be reused. For large systems, the gradient projection technique has the advantage that crystal symmetries are maintained irrespective of numerical deviations from the symmetries in the total energy gradient. For further implementations based on the symmetry-regeneration scheme see Ref. [P1].

4.2 Γ-point lattice free energies from $O(1)$ force calculations

4.2.1 Introduction

Once configurations corresponding to energetic minima are found, thermodynamic stabilities can be compared by calculating the free energies of the crystal structures. In the case of negligible structural disorder, phononic contributions to the entropy are generally dominant.

As described in Sec. 3.1.3, the determination of the Hessian matrix of the energy involves the calculation of the charge densities for $O(N)$ displaced configurations or of the charge density responses to $O(N)$ perturbations. With a ground state charge density calculation scaling with the cube of the system size (based on *e.g.* density functional theory calculations using a plane wave basis set), the total effort for the calculation of the Hessian is thus $O(N^4)$.[2] If a few or only one eigenmode has to be calculated, *e.g.* for an eigenmode following scheme to find saddle points on the potential energy surface, iterative diagonalization algorithms can be employed that only require products of the Hessian matrix and vectors. In this way a construction of the full Hessian matrix is avoided, reducing the overall computational effort [158–161, 177].

We have proposed a method for estimates of lattice free energies [P2], which is also based on approximate Hessian-vector products, however, only requiring $O(1)$ charge density calculations to roughly approximate the full frequency spectrum.

4.2.2 Method

The approach is based on the idea that only one force calculation (in addition to the structure optimization) would be required to calculate the eigenfrequencies of a system, if the Hessian eigenvectors were known. The product of the Hessian $\boldsymbol{\mathcal{H}}$ and the sum of eigenvectors $\boldsymbol{w} := \sum_i \boldsymbol{u}_i$ is approximated as

$$\boldsymbol{\mathcal{H}}\boldsymbol{w} \approx \frac{1}{\varepsilon}\big[\boldsymbol{\nabla} E(\boldsymbol{R}_0 + \varepsilon \boldsymbol{w}) - \boldsymbol{\nabla} E(\boldsymbol{R}_0)\big], \tag{4.2}$$

[2] The structure optimization also requires several charge density calculations. Due to weak interatomic couplings at long distances, the optimization of large structures can require significantly less steps than the number of degrees of freedom (cf. the symmetry-constrained relaxation shown in Fig. 4.2). However, only in a certain vicinity of the minimum the potential energy is approximately harmonic and thus the minimization problem quadratic in the coordinates. With starting guesses at further distance from the minimum, the relaxation of the coordinates using quasi-Newton or conjugate gradient algorithms can require more than $O(N)$ steps.

where ε is used to scale the displacement and the term $\boldsymbol{\nabla} E(\boldsymbol{R}_0)$ accounts for possible residual forces of the optimized structure. Approximations to the Hessian eigenvalues h_i are obtained by projection of the finite force difference (4.2) onto the Hessian eigenvectors $\boldsymbol{u}_i$:

$$h_i = \boldsymbol{u}_i^T \boldsymbol{\mathcal{H}} \boldsymbol{w}. \tag{4.3}$$

We calculate rough estimates to the vibrational eigenvectors using a model Hamiltonian, the construction and evaluation of which is negligible compared to a ground state calculation within density functional theory. Besides the low computational cost for the calculation of the Hessian matrix, the model Hamiltonian must allow for an inexpensive adjustment to yield an energetic minimum for the equilibrium coordinates of the Hamiltonian that is used to calculate the finite force difference (4.2). Here, we use a simple effective point charge model to calculate the eigenvectors, which is described in Sec. 4.2.2.1.

The calculation of the eigenfrequencies corresponds to the diagonalization of a mass-scaled Hessian (cf. Eq. (3.11)). The mass scaling can either be performed for the Hessian constructed from the above described eigenpairs as

$$\tilde{\mathcal{H}}_{ij} = \frac{\mathcal{H}_{ij}}{\sqrt{M_{\lfloor i/3 \rfloor} M_{\lfloor j/3 \rfloor}}} \tag{4.4}$$

or by mass scaling both the displacement and the resulting forces according to

$$w_i' = \frac{w_i}{\sqrt{M_{\lfloor i/3 \rfloor}}}, \tag{4.5}$$

where $M_{\lfloor i/3 \rfloor}$ are the nuclear masses. Note that Eq. (4.5) does not correspond to the sum of polarization vectors.

4.2.2.1 Construction of the model Hamiltonian

As a starting point for the construction of the point charge model system, we perform a Bader analysis [178] of the electronic ground state density, where the charge density is divided into regions in real space which are separated by surfaces defined by a vanishing normal component of the charge density gradient. We have used the Bader analysis code by Henkelman *et al.* [179, 180], which employs an algorithm marking steepest ascent paths on a charge density grid until maxima are found. Paths that cross already visited grid points will follow the corresponding path to a maximum and therefore receive the same marking as this path, hereby being attributed to the same Bader region. Charge density maxima which coincide with nuclear coordinates and maxima with closest distance to a certain nucleus are attributed with the surrounding Bader regions to the corresponding atoms.

The integrated charge density in the Bader regions is added to the corresponding nuclear charges to form an effective point charge system. The electrostatic energy of this system and energetic derivatives with respect to the nuclear coordinates are evaluated using Ewald lattice sums (see App. A). We optimize the magnitudes of the charges using a nonlinear least squares algorithm [181] to yield an energetic minimum for the equilibrium coordinates given by the more accurate Hamiltonian. The sums of positive and negative point charges are each constrained to be constant to avoid the trivial solution of zero charges.

4.2.3 Computational details

Ground state charge densities were calculated using the plane wave density functional theory code DACAPO [108], describing the ionic cores by ultrasoft pseudopotentials [123], and the projector-augmented wave [124] code VASP [127, 171] for the K_2NaAlH_6 and $MgZn_2$ structures, respectively. The Perdew-Wang-91 approximation [105, 106] to the exchange-correlation functional was used, and the size of the plane wave basis sets was limited by a cutoff of 350 eV. Electronic Brillouin sampling was performed on a Monkhorst-Pack grid [172] with a spacing of $\sim$0.1 Å^{-1}.

4.2.4 Examples

The compound K_2NaAlH_6 is a cation-alloyed complex metal hydride. Crystal symmetry and decomposition temperature are known from experiments [182, 183]. This system is hence interesting for testing whether *ab initio* lattice free energies can be used to estimate decomposition temperatures of alloyed complex metal hydrides with the potential of predicting new stable alloys.

Within the presented approach, the structural relaxation is followed by a Bader analysis of the electronic ground state charge density (see Fig. 4.4a). The sum of approximate mass-scaled eigenvectors calculated from the optimized point charge model is compared to the corresponding sum obtained from $O(N)$ force calculations within density functional theory for displaced configurations in Fig. 4.4b. The polarization vector sums are similar with an average error in the cartesian components of the approximate eigenvectors of $\sim$30%, allowing for rough estimates of the eigenvalues which are only affected to second order by these errors. Off-diagonal elements of the Hessian matrix in the canonical coordinate basis constructed from these eigenpairs, however, correspondingly have too large errors to allow for *e.g.* a decoupling of the calculated Hessian into contributions of interatomic coupling between different supercells to calculate the phonon dispersion. The method presented here is thus restricted to the cal-

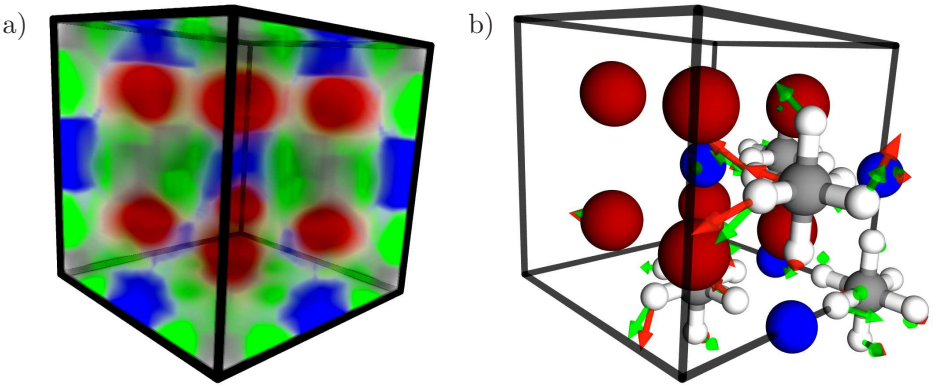

Figure 4.4: Bader charges (a) and comparison of polarization vector sums (b) for the conventional unit cell of the alloy K_2NaAlH_6 in space group $Fm\bar{3}m$. The representing spheres of the nuclei and attributed Bader charges are shown in red for potassium, blue for sodium, and gray for aluminum. White spheres represent hydrogen; the corresponding Bader volumes are shown in green. The green and red arrows represent the sum of polarization vectors based on the model Hamiltonian and $O(N)$ charge density calculations, respectively. In order to show the similarities in the modes, the eigenvectors obtained in the different approaches are added with aligned phases, by adding two such eigenvectors with maximum overlap to the corresponding sums with the same phase $\varphi \in \{\pm 1\}$.

culation of phonon frequencies at the Γ-point, providing a good approximation to the lattice free energy for sufficiently large unit cells.

A comparison of the Γ-point frequencies for the conventional unit cell of K_2NaAlH_6 calculated from the single displacement method and from $O(N)$ displacements, respectively, is shown in Fig. 4.5. The overall frequency range is covered by the rough Γ-point frequency estimates, interpolating the more accurately calculated spectrum.

The phonon dispersion of K_2NaAlH_6 (Fig. 4.6) consists of four separate bands. The lowest band with phonon energies up to ∼30 meV corresponds to acoustic modes and to optical modes in the metal atom framework. The band within the energetic range of ∼40–60 meV is due to libration modes. The band in the range ∼90–120 meV is dominated by Al–H bond bending vibrations, and the bands in the range ∼140–180 meV and at about 190 meV are due to antisymmetric and symmetric bond stretching vibrations, respectively. The Γ-point frequencies obtained from one displacement do not resolve the corresponding gaps in the spectrum (Fig. 4.5). Due to the rough approximation to the polarization vectors, the correct eigenfrequencies are mixed, which leads

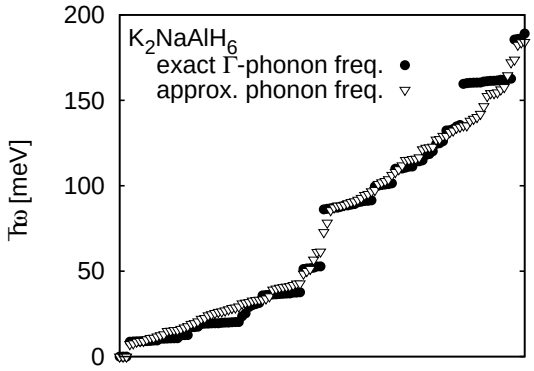

Figure 4.5: Phonon energies at the Γ-point of the conventional unit cell of K_2NaAlH_6 calculated from 1 and $O(N)$ displacements, respectively. (From [P2], Copyright 2008 American Institute of Physics; `http://link.aip.org/link/?JCP/128/184708`.)

to a smearing of the spectrum such that gaps and degeneracies are generally not resolved.

A large fraction of the phonon energies of crystals with high energetic bond bending and stretching modes, however, is large compared to k_BT at near ambient temperatures. In the limit $T \to 0$, the lattice free energy (3.26) is given by (half) the arithmetic mean of the phonon energies. For temperatures low compared to the high phonon energies, a mixing of these frequencies does thus not cause large errors in the lattice free energy.

The lattice free energies of K_2NaAlH_6 and the decomposition products KH and NaH in the reaction

$$K_2NaAlH_6 \to 2KH + NaH + Al + \frac{3}{2}H_2 \tag{4.6}$$

have been obtained from phonon dispersion calculations, the corresponding Γ-point frequencies of the conventional unit cells, and the approximations to these frequencies obtained within the approach presented here, respectively. The Gibbs free energy for Al has been generated from data in Ref. [184], and data for H_2 have been taken from Ref. [185]. For K_2NaAlH_6 and the metal hydride phases, pV terms have been neglected. The difference in the decomposition temperatures obtained from the Γ-point contributions to the lattice free energies obtained from 1 and $O(N)$ displacements is relatively small (see Fig. 4.7). The approximate and accurate Γ-point free energies of 450 K and 470 K are fortuitously closer to the experimentally observed decomposition

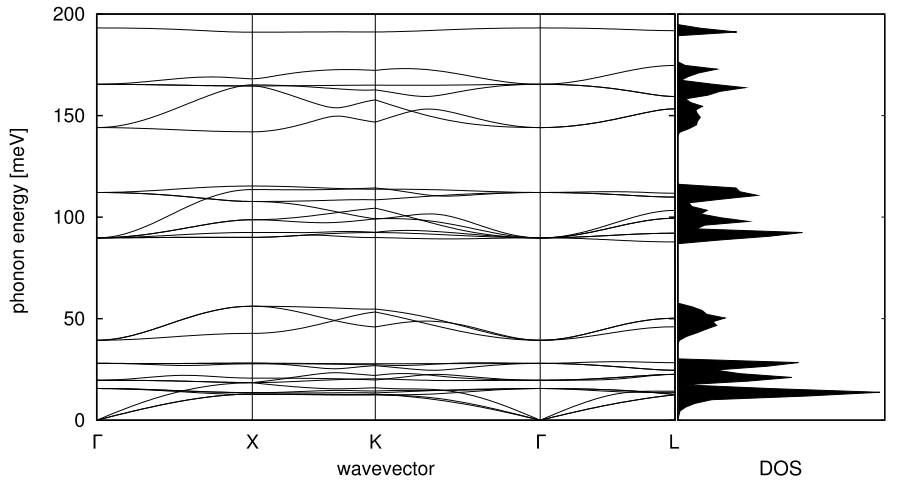

Figure 4.6: Phonon dispersion and density of states (DOS) of K_2NaAlH_6 calculated using finite force differences as implemented in Ref. [140] along the directions $\Gamma = (0,0,0) \rightarrow X = (1/2,1/2,0) \rightarrow K = (3/4,3/8,3/8) \rightarrow \Gamma \rightarrow L = (1/2,1/2,1/2)$ (phonon wave vectors specified in units of the reciprocal lattice basis vectors).

temperature of 530 K [182] than the value of 430 K obtained from the full phonon dispersion. Considering that the energies for these elevated temperatures have been obtained within a harmonic approximation, *e.g.* neglecting the volume dependence of the force constants, the decomposition temperature estimates are relatively good.

Decomposition temperatures of complex crystals with high phonon frequencies due to bond bending and stretching modes can be roughly estimated using the single displacement method (cf. also Fig. 2 in Ref. [P2]). For systems without high frequency modes, a different approach to the lattice free energy estimate is necessary. The maximum phonon energies of *e.g.* the metallic, standard Laves phase structure $MgZn_2$ (space group $P6_3/mmc$ [186]) are about 30 meV (see Fig. 4.8a) due to the absence of "molecular-like" modes. Therefore, the errors in the approximate frequencies cause a significant deviation from the lattice free energies calculated using $O(N)$ displacements already for near ambient temperatures, and the approximation to the free energy based on a single displacement generally is inadequate (Fig. 4.8b).

In analogy to the Einstein model for solids [187], which is a reasonable approximation for high temperatures, we neglect interatomic couplings, *i.e.* the nuclei are assumed to oscillate independently (in contrast to the Einstein model,

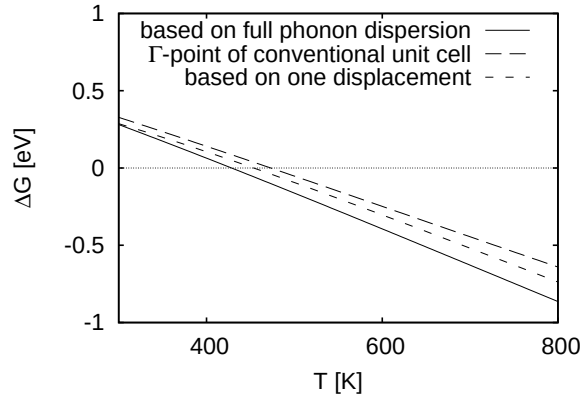

Figure 4.7: Gibbs free energy difference between the decomposition products and the reactant K_2NaAlH_6 in reaction (4.6) calculated from the full phonon dispersion and the Γ-point frequencies of the conventional unit cells of K_2NaAlH_6 and the metal hydride phases obtained from 1 and $O(N)$ displacements, respectively.

we will not restrict the phonon spectrum to a single frequency). With this assumption, the product of Hessian eigenvalues can be approximated as

$$\prod_i h_i \approx \prod_j \left(\boldsymbol{x}_j^T \boldsymbol{\mathcal{H}} \boldsymbol{w} \right) \Big/ \left(\sum_k \boldsymbol{x}_j^T \boldsymbol{u}_k \right), \tag{4.7}$$

where $\boldsymbol{x}_j$ are the canonical basis vectors of the atomic coordinate system and the product $\boldsymbol{\mathcal{H}}\boldsymbol{w}$ is approximated using a single displacement according to Eq. (4.2). With the high-temperature limit of Eq. (3.26) approaching the logarithm of the product of the phonon frequencies (the prime denotes that zero frequencies due to translational invariance are left out):

$$F_{\mathrm{vib}}(k_{\mathrm{B}}T \gg \omega_{\max}) \to k_{\mathrm{B}}T \ln \left(\frac{\prod'_\mu \omega_\mu}{(k_{\mathrm{B}}T)^{3N-3}} \right), \tag{4.8}$$

the lattice free energies at high temperatures can be estimated using Eq. (4.7) without extraction of the phonon frequencies. This approximation yields good results for the free energy for temperatures large compared to relatively low maximum phonon energies in the absence of bond stretching and bending modes (Fig. 4.8b; see also Fig. 4b in Ref. [P2]).

Further examples for the application of the single-displacement approach can be found in Ref. [P2].

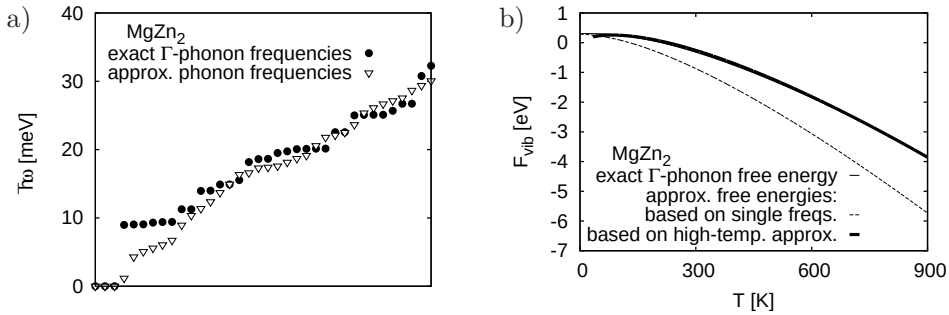

Figure 4.8: Γ-point phonon energies (a) and lattice free energies (b) for the hexagonal $P6_3/mmc$ phase of $MgZn_2$ calculated from 1 and $O(N)$ displacements, respectively. (Adapted from [P2], Copyright 2008 American Institute of Physics; `http://link.aip.org/link/?JCP/128/184708`.)

4.2.5 Conclusion

The presented approach to the approximation of the Γ-point phonon frequencies is based on a model Hamiltonian for the calculation of rough estimates to the eigenmodes and on $O(1)$ charge density calculations for the approximation of the eigenspectrum. Degeneracies and gaps in the phonon spectrum are usually not resolved, but lattice free energy estimates for temperatures low compared to the energies of the dominant part of the phonon spectrum are approximately given by the average phonon frequency and are hence affected only little by the interpolating behavior of the estimated spectrum. For temperatures high compared to the maximum phonon energies, a reasonable approximation of the lattice free energy based on a single displacement is possible using a direct approximation of the product of frequencies.

As only the Γ-point frequencies can be obtained with this method, the unit cell (or supercell used for the calculation) of the crystal must be sufficiently large to yield reasonable results for the lattice free energy. Since for large systems no supercells are required to resolve all relevant force constants, both force-based and linear response methods (see Sec. 3.1.3.2) have a computational effort of $O(N)$ charge density calculations for the same system size. The fast single displacement scheme is thus preferable for large, complex systems, if only rough estimates to the lattice free energy are required, *e.g.* for screening studies of alloy stabilities.

5

Dynamics and stabilities of complex metal hydrides

5.1 Lattice dynamics and phase stabilities of $Mg(BH_4)_2$

5.1.1 Introduction

Complex metal hydrides exhibit both a good volumetric and gravimetric capacity to store hydrogen, and are therefore regarded as promising materials for on-board applications [46]. The considered systems include aluminum hydrides [48], amides [55], and borohydrides [57]. Besides high storage capacities, the material should release hydrogen (and preferably also allow for recharging) at controlled, near ambient conditions.

Magnesium borohydride, $Mg(BH_4)_2$, has a relatively high capacity of 14.9 mass-% hydrogen and releases a large fraction of its hydrogen content in the temperature range of 300–400°C [58]. The decomposition involves several steps which depend on the experimental conditions and are not fully understood yet [58–61]. Doping with $TiCl_3$ is reported to reduce the initial dehydriding temperature by ∼170 K, where the effect of the dopant is suggested be due to the formation of a new phase [49]. A detailed analysis of the phases involved in the decomposition is thus necessary to understand the limitations (or the potential) of $Mg(BH_4)_2$ or similar systems as solid state hydrogen storage materials.

Černý *et al.* [62] and Her *et al.* [63] have independently determined the crystal structure of a low-temperature phase of $Mg(BH_4)_2$ by powder diffrac-

tion. The structure belongs to space group $P6_1$ and contains 330 atoms, *i.e.* 30 formula units per unit cell. Her *et al.* [63] have furthermore proposed a high-temperature phase with idealized $Fddd$ symmetry, containing 176 atoms per primitive and 704 atoms per conventional unit cell. A disorder parameter had to be introduced to fit the diffraction pattern to this space group, indicating that half unit cells are shifted with respect to each other in *b*- or *c*-direction [63] (cf. Fig. 4.3).

Prior to the experimental characterization of the large structures, simpler structures had been proposed on the basis of density functional theory calculations with $P\bar{3}m_1$ [188] and $Pmc2_1$ [189] symmetry, respectively. A numerical optimization of the experimentally proposed $P6_1$ and $Fddd$ phases was performed by Ozoliņš *et al.* [190] and Dai *et al.* [191]. Moreover, Ozoliņš *et al.* [190] have obtained a low-density phase (space group $I\bar{4}m2$) with a lower energy than all other previously proposed phases using a screening procedure based on rigid-ion electrostatics [192]. Van Setten *et al.* [193] have estimated lattice free energies from the Γ-point phonon frequencies of the proposed $P6_1$ and $Pmc2_1$ phases, not resolving instabilities (corresponding to negative Hessian eigenvalues) at larger wave vectors.

We have calculated the phonon dispersion of all proposed phases of $Mg(BH_4)_2$. The structure with $I\bar{4}m2$ symmetry is found to have instabilities in the acoustic modes at the Brillouin zone boundary. Following the corresponding displacements, we have obtained a new phase with $F222$ symmetry [P3], which is free unstable modes and has a lower free energy than all previously proposed structures.

5.1.2 Computational details

Total energies and gradients were calculated with the projector-augmented wave [124] code VASP [127, 171], using the Perdew-Wang-91 exchange-correlation functional [105, 106]. The Kohn-Sham wave functions were expanded in plane wave basis sets with cutoffs of up to 500 eV, and the electronic Brillouin zones were samples with mesh spacings of less than 0.06 $Å^{-1}$ for the large $P6_1$ and $Fddd$ structures and less than 0.03 $Å^{-1}$ for the theoretically proposed structures.

For the latter phases, the phonon dispersion was calculated based on finite force differences using the program PHONON [140]. Due to limitations of this code, the larger, experimentally proposed $P6_1$ and $Fddd$ structures were treated separately, considering the Γ-point frequencies for cells containing 30 and 64 formula units $Mg(BH_4)_2$, respectively. To estimate the phonon density of states

	ρ [g/cm^3]	ΔE_{gs} [eV]
$F222$	0.54	-0.10
$I\bar{4}m2$	0.56	-0.09
$P6_1$	0.82	0.00
$Pmc2_1$	0.88	0.14
$Fddd$	0.90	0.10
Pm	0.91	0.23
$I4_1/amd$	1.01	0.14
$P\bar{3}m1$	1.04	0.35

Table 5.1: Comparison of densities and ground state energies ΔE_{gs} (relative to the ground state energy of the $P6_1$ phase) per formula unit of the considered $Mg(BH_4)_2$ phases. (Adapted from [P3], accepted for publication in J. Phys.: Condens. Matter; `http://www.iop.org/EJ/journal/JPhysCM`.)

for comparison to the theoretically proposed phases, the integrated density

$$G(\omega) = \sum_{i=1}^{3N} \Theta(\omega - \omega_i) \tag{5.1}$$

($\Theta(\omega)$ is the Heaviside function and ω_i are the eigenfrequencies) was interpolated and differentiated.

5.1.3 Results

In the following the results presented in Ref. [P3] are summarized. All previously proposed phases have been optimized to obtain the corresponding ground state energies (see Tab. 5.1). The low-density $I\bar{4}m2$ phase has the lowest ground state energy of all previously proposed phases, and the $P6_1$ structure has a lower ground state energy than the idealized $Fddd$ high-temperature phase. The relative phase stabilities are determined by the free energy. Neglecting the structural disorder proposed for the $Fddd$ phase, we calculate the phononic contributions to the entropy to estimate the structural stabilities.

A calculation of the phonon density of states (Fig. 5.1) shows that all considered structures which exhibit a tetrahedral coordination of magnesium with boron atoms have a similar phonon spectrum. The low-frequency band in the range 0–20 THz is due to acoustic modes and optical modes in the magnesium-boron framework, the band in the range 30–40 THz is due to librational modes, and the narrow high-frequency band at 70 THz is due to B–H bond stretching vibrations. The only phase not showing a tetrahedral coordination of Mg with

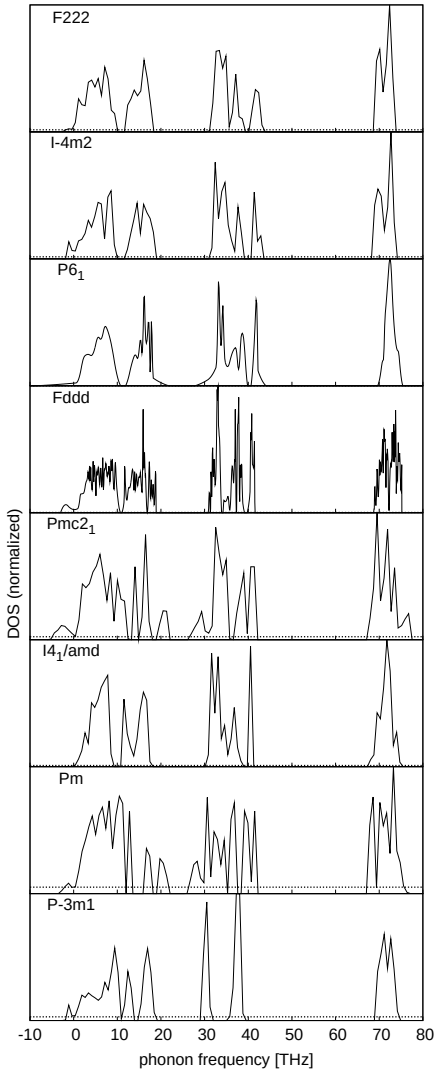

Figure 5.1: Calculated phonon densities of states of the proposed phases of $Mg(BH_4)_2$. Imaginary frequencies corresponding to unstable modes are represented by negative real values. The dashed lines indicate an error of 0.1/THz in the density of states associated to the modes due to the numerically unresolved invariance with respect to rigid translations. (From [P3], accepted for publication in J. Phys.: Condens. Matter; `http://www.iop.org/EJ/journal/JPhysCM`.)

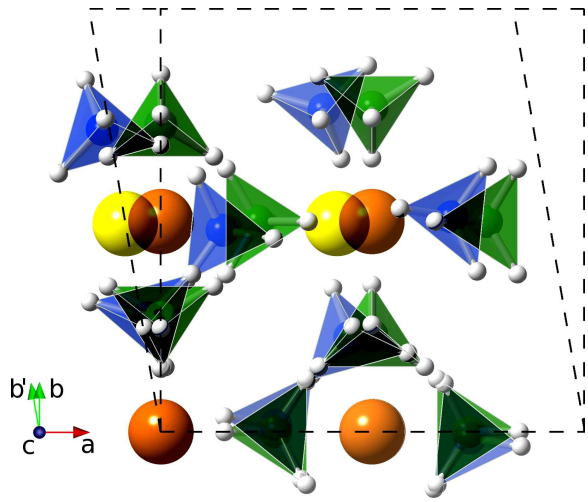

Figure 5.2: Shear transformation of the conventional unit cell of $Mg(BH_4)_2$ in space group $I\bar{4}m2$ and the resulting optimized atomic displacements (based on a VESTA [194] rendition). Magnesium is represented by orange and yellow spheres and the coordination of boron with hydrogen by green and blue tetrahedra for the undisplaced and displaced configurations, respectively.

B atoms is the hexagonal $P\bar{3}m1$ structure, which exhibits a sixfold coordination instead, resulting in a slightly different phonon density of states with a split librational band.

In addition to the previously proposed structures and the new $F222$ phase, which is described below, we have constructed a high-density phase in $I4_1/amd$ symmetry that is free of imaginary modes (see Fig. 5.1), *i.e.* sufficiently small displacements from the equilibrium coordinates always mean an increase in energy, supporting meta stability of this structure. We have furthermore considered a structure with Pm symmetry, which is the simplest structure (one formula unit per unit cell) obeying the tetrahedral coordination of Mg with B atoms.

Since the $I\bar{4}m2$ phase has the lowest ground state energy of the previously proposed structures, we have analyzed the phonon dispersion of this structure in detail. At the Γ-point all phonon frequencies are real within the numerical accuracy of the results. At the N-point (the facet center of the Brillouin zone boundary), however, two acoustic modes become unstable. Following the atomic displacements corresponding to these modes, the total energy of the system is lowered. Simultaneously relaxing the cell parameters, we find a $\varepsilon_{x,y}$ shear deformation (*i.e.* $\alpha = \beta = 90°$, $\gamma \neq 90°$; see Fig. 5.2) of the conventional

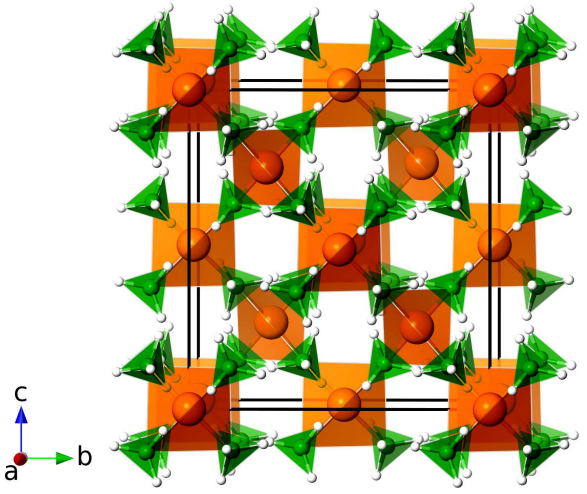

Figure 5.3: Conventional unit cell of $Mg(BH_4)_2$ in space group $F222$ (based on a VESTA [194] rendition). The coordination of magnesium with boron is represented by orange tetrahedra, the coordination of boron with hydrogen by green tetrahedra.

unit cell of the tetragonal $I\bar{4}m2$ structure. The resulting cell is the primitive cell of a phase with $C222_1$ symmetry. Further relaxation leads to a $F222$ structure (containing two formula units per primitive cell), which has a 10 meV lower total energy per formula unit than the $I\bar{4}m2$ phase and is free of instabilities (*i.e.* there are no imaginary phonon frequencies; see Fig. 5.1). This face-centered system shows a tetrahedral coordination of Mg with B atoms (see Fig. 5.3) and has thus a phonon density of states of similar shape compared to the other phases with same coordination.

Conversely, we have shear transformed the conventional unit cell of the $I\bar{4}m2$ phase (corresponding to a change of the angle γ of 2°) without imposing atomic displacements. Relaxing the internal coordinates and the unit cell volume, the energy of the system is lowered by 6 meV per formula unit compared to the undistorted $I\bar{4}m2$ structure, indicating negative elastic constants and thus structural instability. Macroscopic deformations can thus be used as an alternative to the calculation of the phonon dispersion for an investigation of corresponding instabilities due to acoustic modes.

In order to be able to estimate the stability of $Mg(BH_4)_2$ even if the symmetry of stable phases were not known, we have estimated lattice free energies for all phases by excluding imaginary frequencies (corresponding to 1% of the integrated phonon density of states of the unstable phases) from the integration

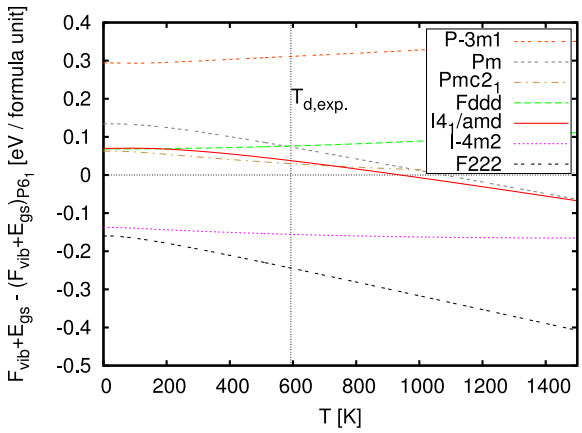

Figure 5.4: Comparison of free energies with respect to the proposed low-temperature $P6_1$ phase. $T_{\mathrm{d,exp.}} = 320°\mathrm{C}$ is the experimentally determined temperature for the first decomposition step of $Mg(BH_4)_2$ [58]. (From [P3], accepted for publication in J. Phys.: Condens. Matter; `http://www.iop.org/EJ/journal/JPhysCM`.)

in Eq. (3.30). The calculated free energies only differ significantly for phases with considerable density differences and for the $P\bar{3}m1$ phase with different coordination of the Mg atoms (Fig. 5.4). None of the calculated free energies (including the free energy of the proposed high-temperature $Fddd$ phase) intersects with the free energy of the low-temperature $P6_1$ structure below the experimentally determined temperature of 320°C for the first decomposition step of $Mg(BH_4)_2$. Since the $Fddd$ structure, however, is only proposed to be an idealized symmetry of a structure with disorder, other entropic terms should dominate the free energy, which have not been considered here.

For an estimate of the desorption temperature of $Mg(BH_4)_2$, we have assumed an idealized decomposition step, not considering further suggested decomposition products and steps [58, 60]:

$$\mathrm{Mg(BH_4)_2} \rightarrow \mathrm{MgH_2} + 2\mathrm{B} + 3\mathrm{H_2}. \tag{5.2}$$

The Gibbs free energy of H_2 has been interpolated from data in Ref. [185]. For solid phases, pV terms have been neglected. The lattice free energies of MgH_2 and B have been calculated for phases with $P4_2/mnm$ and $R\bar{3}m$ symmetry, respectively. Excluding the $P\bar{3}m1$ phase with energetically unfavorable coordination of Mg, the calculated initial decomposition temperatures lie in the range $T = 400$–500 K. Estimating the decomposition temperature based on lattice free energies of $Mg(BH_4)_2$ phases with similar densities, very simple

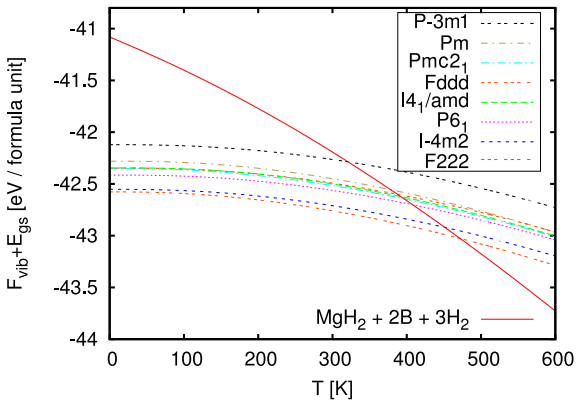

Figure 5.5: Calculated lattice free energies of the proposed phases of $Mg(BH_4)_2$ and Gibbs free energies of the decomposition products MgH_2 + 2B + $3H_2$. (From [P3], accepted for publication in J. Phys.: Condens. Matter; `http://www.iop.org/EJ/journal/JPhysCM`.)

structures, *e.g.* the Pm phase, yield similar results compared to the large $P6_1$ and $Fddd$ structures. Simple model structures can thus be used to estimate desorption temperatures of $Mg(BH_4)_2$ and possibly similar compounds, if the energetically favored tetrahedral coordination of Mg with B atoms is obeyed. The experimentally observed high temperature for the first decomposition step (for which (5.2) is only an assumption) of about 600 K is proposed to be due to kinetic limitations [58], which could explain the lower calculated estimate for the desorption temperature of 400 K for the high-density structures based on thermodynamic equilibrium conditions.

5.1.4 Conclusion

We have presented a comprehensive lattice free energy study of all proposed phases of $Mg(BH_4)_2$. Based on an analysis of the instabilities of the previously proposed low energetic $I\bar{4}m2$ phase, we have obtained a new structure with $F222$ symmetry which has a lower free energy than all previously proposed phases and is free of instabilities.

We have shown that a macroscopic deformation of the unit cell can be used to detect elastic instabilities due to imaginary frequencies in the acoustic spectrum, constituting a complementary approach to the calculation of the phonon dispersion for investigation of corresponding structural stabilities.

The lattice free energies and corresponding approximated desorption tem-

peratures are found to differ only little compared to the accuracy of the estimates for systems of similar density and coordination. Model structures with small unit cells could thus be used to approximate desorption temperatures, which allows for an estimate of the stability even if the symmetry of the system is not known *a priori*. Since the small structures yield similar decomposition temperatures compared to the large, complex phases, a computationally expensive calculation of the lattice free energy of the latter structures can be avoided, if only rough free energy estimates are required, *e.g.* for screening studies of alloy stabilities.

5.2 Thermodynamic stability of metal aluminum hexahydrides

5.2.1 Introduction

For a systematic design of new hydrogen storage materials, a way of predicting the structural properties of interest needs to be found. Besides good storage capacities, an optimal material should both be sufficiently stable at ambient conditions, to ensure safety, and release hydrogen at moderate temperatures. Alloying of structures, *e.g.*, with too high and too low decomposition temperatures, respectively, could lead to materials with desirable, intermediate thermodynamic properties.

Nakamori *et al.* [188] have found a linear correlation between the heat of formation and the cation electronegativity of metal borohydrides. Similar relations have also been established for metal aluminum hydrides [195]. Nickels *et al.* [196] have observed an intermediate decomposition temperature for the alloy $KLi(BH_4)_2$ compared to the constituents KBH_4 and $LiBH_4$, which suggests that the average cation electronegativity could be used as an indicator for the thermodynamic properties of the corresponding alloys.

Alkali metal aluminum hexahydrides of the stocheometry $M_2M'AlH_6$ have been studied experimentally [182] and numerically [197] for the cation species $M, M' \in \{\mathrm{Li}, \mathrm{Na}, \mathrm{K}\}$, observing that stable alloys (*i.e.* $M \neq M'$) only exist if M has a larger ionic radius than M'. Graetz *et al.* have reported intermediate decomposition temperatures for the alloys compared to the phases with $M = M'$ with the exception of Na_2LiAlH_6, which has a higher decomposition temperature than the constituting phases Na_3AlH_6 and Li_3AlH_6. Since the above mentioned alloy instabilities and the unexpectedly increased stability of Na_2LiAlH_6 cannot be predicted by means of an average cation electronegativity, we have analyzed the electronic ground state charge densities of these structures, in order to find computationally inexpensive properties which are

correlated to the alloy stabilities [P4].

As demonstrated in Sec. 5.1, the search for the symmetry of the ground state structure can be very complex and computationally expensive. We have noticed, however, that simple model structures with the energetically favored coordination of the cations can be used to estimate structural stabilities. Van Setten *et al.* [198] have shown that ground state energies of complex metal hydrides can be approximated by rigid-ion electrostatics neglecting the details of the crystal structure. For a first estimate of the ground state energy, the knowledge of the crystal symmetry is not necessary, as long as the energetically preferred local coordination is obeyed. Although the crystal symmetries of the stable cation-alloyed metal aluminum hexahydrides are known from experiments [182], we use the face-centered cubic structure of K_2NaAlH_6 (Fig. 5.6) as a model for all considered structures, in order to test whether this simplification allows for reasonable stability estimates. Due to the high symmetry of this phase, only one independent coordinate and the lattice constant have to be optimized, reducing the computational effort for a screening study to a minimum.

5.2.2 Computational methods

The electronic ground state charge densities were calculated with the projector-augmented wave [124] code VASP [127, 171], using the Perdew-Wang-91 exchange-correlation functional [105, 106]. The size of the plane wave basis sets were limited by cutoff energies of 350 eV. Electronic Brillouin zone sampling was performed with k-point grid spacings of $\sim$0.03 Å^{-1}. A Bader charge density analysis was performed as implemented in Refs. [179, 180] including gradient information from the core states in the projector-augmented wave scheme.

For an analysis of the Kohn-Sham Hamiltonians, we have furthermore calculated maximally localized Wannier function basis sets [199] using the WANNIER90 code [200]. Wannier functions [201] are Fourier transforms of the Bloch functions (2.68). In a generalized definition, Wannier functions are Fourier transforms of crystal momentum-dependent unitary transformations of the Bloch functions, allowing for a construction of localized real space basis sets that can *e.g.* be used to interpret chemical bonding in terms of molecular orbitals. Since the Bloch functions are unique except for a crystal momentum-dependent phase factor (corresponding to the arbitrary constant overall phase of an electronic eigenstate), the Wannier functions $|w\rangle$ can differ significantly in shape for different phase factors, and only the sum of Wannier function centers $\sum_w \langle w|\hat{\boldsymbol{r}}|w\rangle$ is invariant with respect to the corresponding gauge transformations [202]. Maximally localized Wannier functions are obtained by minimiza-

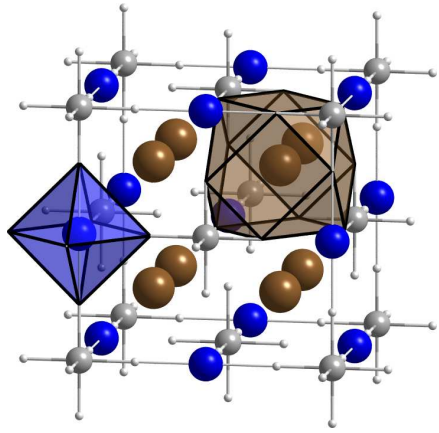

Figure 5.6: Conventional unit cell of $Fm\bar{3}m$-K_2NaAlH_6. Potassium, sodium, aluminum, and hydrogen are depicted as brown, blue, gray, and white spheres, respectively. The brown and blue polyhedra indicate the 12-fold and octahedral coordination of a potassium and a sodium cation, respectively. (From [P4], submitted to Modelling and Simulation in Materials Science and Engineering; `http://www.iop.org/EJ/journal/MSMSE`.)

tion of the mean square spread [199]

$$\Omega = \sum_{w} \left[\langle w | \hat{\boldsymbol{r}}^2 | w \rangle - \left(\langle w | \hat{\boldsymbol{r}} | w \rangle \right)^2 \right] . \tag{5.3}$$

The Bloch functions used for the transformation to the maximally localized Wannier functions were calculated with the plane wave density functional theory code PWSCF [126], using norm-conserving pseudopotentials [203] generated for the local density approximation to the exchange-correlation functional [101]. In order to obtain maximally localized Wannier function basis sets of minimal dimension for a simple analysis, only occupied bands and the Γ-point contribution to the electronic dispersion were considered, and single-valence electron pseudopotentials were used for all alkali metals.

Due to the different approximations and parameters, the structures were optimized independently for the calculations using the VASP and PWSCF codes, respectively.

5.2.3 Results

A Bader analysis of the charge densities of the model structures shows that the alloys Na_2LiAlH_6, K_2LiAlH_6, and K_2NaAlH_6 have lower integrated Bader

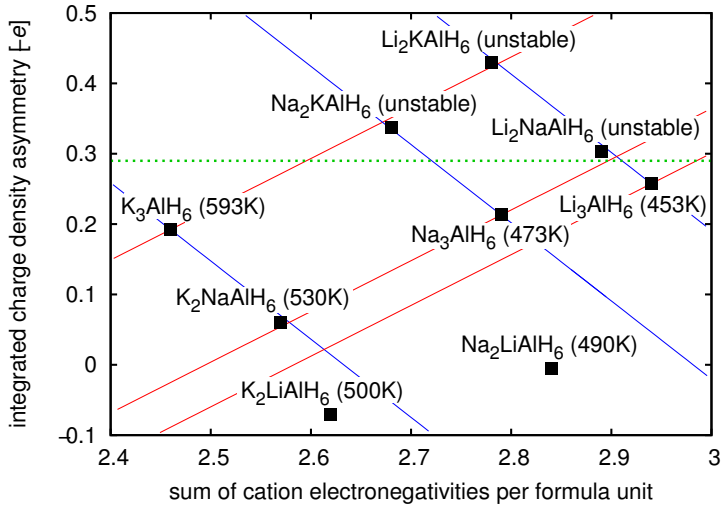

Figure 5.7: Bader charge differences between the cation sites with 12-fold and octahedral coordination of cubic metal aluminum hexahydride model phases in dependence of the sum of cation electronegativities per formula unit (decomposition temperatures of the experimentally observed phases from Ref. [182]). The green dotted line indicates an approximate asymmetry threshold above which no stable alloys exist. Apart from the alloys with lithium occupying the octahedral sites, the Bader charge differences show a linear correlation with respect to the sum of cation electronegativities for phases with the same cation species occupying the octahedral or 12-fold coordinated sites, indicated by red and blue lines, respectively. The slopes of the parallel lines have been fitted with respect to the phases where all cation sites are occupied by the same species. (From [P4], submitted to Modelling and Simulation in Materials Science and Engineering; `http://www.iop.org/EJ/journal/MSMSE`.)

valence charge density differences between the cation sites with octahedral (M') and 12-fold coordination (M; cf. Fig. 5.6) than the phases with $M = M'$ (see Fig. 5.7). The phases with increased Bader charge symmetry are just the stable alloys, for which species with larger ionic radii occupy the sites with 12-fold coordination compared to the octahedrally coordinated sites. Particularly symmetric are the Bader charges around the cation sites for the alloy Na_2LiAlH_6, where the corresponding charge difference of magnitude $5.8 \cdot 10^{-3}\, e$ in principle is zero in terms of the accuracy of the calculations. This symmetry might be an indicator for the higher decomposition temperature for the case $(M, M') = (\mathrm{Na}, \mathrm{Li})$ compared to the cases $M = M' = \mathrm{Li}$ and $M = M' = \mathrm{Na}$,

respectively.

For the unstable structures, where the species M have smaller ionic radii than M', the Bader charge differences are larger compared to the constituting phases. There is an asymmetry threshold of about $0.3\,e$, above which no stable phases exist. Although the calculation of the charge differences is based on cubic model structures for all phases, the estimated Bader charge asymmetries can be used to identify the stable and unstable structures.

The integrated charge density asymmetries for systems with equal M or M', respectively, show a linear relationship with respect to the sum of Pauling cation electronegativities per formula unit (Fig. 5.7), except for the alloys K_2LiAlH_6 and Na_2LiAlH_6 in particular, which will be treated separately in a vibrational free energy analysis in order to explain the increased stability. The linear correlations exhibit the same slopes for phases which are related by a substitution for either M or M', respectively. The slopes of the corresponding fits in Fig. 5.7 are (in atomic units) -1.11 ± 0.03 and 0.72 ± 0.02 for structures with the same species occupying the cation sites with 12-fold and octahedral coordination, respectively. With the knowledge of a few asymmetries to estimate the slopes, the asymmetries for the remaining phases could be approximated from the linear relationships. Although the linearly extrapolated asymmetry estimates for the K_2LiAlH_6 and Na_2LiAlH_6 structures would deviate by $\sim$0.1–$0.2\,e$ from the values based on the charge density analysis, the phases would still be identified as being stable due to low asymmetries.

In addition to the ground state properties, entropic terms have to be considered in order to assess the thermodynamic stabilities of the structures. We will estimate the vibrational zero point energies from the ground state Kohn-Sham orbitals without calculating charge density changes due to coordinate displacements. As we have noticed in Sec. 4.2, the lattice free energies of complex metal hydrides are dominated by high frequency librational and bond bending and stretching modes. This allows for a rough estimate to the zero point energy from the average frequencies of the hydrogen atom subsystem, neglecting the low frequency part of the phonon dispersion, which can exhibit imaginary frequencies for the compounds with a ground state symmetry different from that of the $Fm\bar{3}m$ model structure, corresponding to a rearrangement of the metal atom framework.

A transformation of the Bloch function eigenbasis to a maximally localized Wannier function basis yields six orbitals per primitive unit cell (Fig. 5.8), centered close to the hydrogen coordinates for all considered phases. We approximate the effect of the displacement of a hydrogen atom as a rigid translation of the nearby centered Wannier orbital. The corresponding transformation is

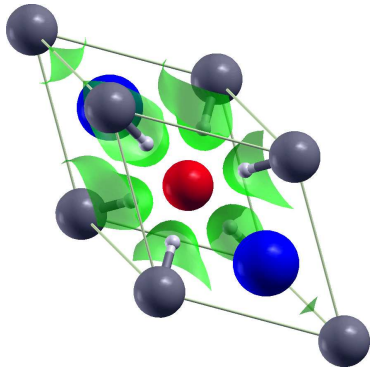

Figure 5.8: XCrySDen [204] rendition of maximally localized Wannier functions for the primitive unit cell of Na_2LiAlH_6. Sodium, lithium, aluminum, and hydrogen are depicted as blue, red, gray, and white spheres, respectively. (From [P4], submitted to Modelling and Simulation in Materials Science and Engineering; `http://www.iop.org/EJ/journal/MSMSE`.)

given as

$$\hat{\mathcal{T}} = 1 + \Big(|\tilde{w}\rangle - |w\rangle\Big)\langle w|, \tag{5.4}$$

where $|\tilde{w}\rangle$ denotes the Wannier orbital displaced from its center. For a simplification of the calculations, we define the electronic ground state energies of the unperturbed structures to be zero. This corresponds to vanishing Kohn-Sham Hamiltonian diagonal elements $\langle w|\hat{H}|w\rangle$ in the maximally localized Wannier function basis, being all equal due to the crystal symmetries. The energetic change due to the transformation (5.4) is given by the trace over the transformed Hamiltonian:

$$\mathrm{Tr}(\hat{\mathcal{T}}^{+}\hat{H}\hat{\mathcal{T}}) = \langle w|\hat{H}|\tilde{w}\rangle + \mathrm{h.c.}, \tag{5.5}$$

where we have used that the energy of the unperturbed system vanishes per definition. We estimate the electronic contribution to the diagonal elements of the Hessian of the hydrogen subsystem using finite displacements of the Wannier centers. The remaining contributions to the Hessian are approximated by Ewald sums (see App. A) over ionic core charges equaling the negative of the corresponding valence charges.

In Tab. 5.2, the estimated librational and bond stretching and bending contributions to the zero point energies are compared to more accurate results obtained from density functional theory calculations for displaced configurations. The approximated energies are found to be within 20% of the computationally

	$\tilde{F}$ [eV]	F [eV]
stable phases		
Li_3AlH_6	1.26	1.54
Na_2LiAlH_6	1.23	1.42
Na_3AlH_6	1.34	1.44
K_2LiAlH_6	1.24	1.27
K_2NaAlH_6	1.31	1.32
K_3AlH_6	1.39	1.33
unstable phases		
Li_2NaAlH_6	1.33	1.52
Li_2KAlH_6	1.40	1.46
Na_2KAlH_6	1.39	1.43

Table 5.2: Librational and bond stretching and bending contributions to the free energy at $T = 0$. The energies $\tilde{F}$ have been obtained from electrostatic contributions from the ionic cores and perturbations of the Wannier centers, while the energies F have been calculated within density functional theory using finite displacements. (From [P4], submitted to Modelling and Simulation in Materials Science and Engineering; `http://www.iop.org/EJ/journal/MSMSE`.)

more expensive results based on several charge density calculations. Both approaches yield the lowest vibrational free energy for the Na_2LiAlH_6 phase in the sector of stable alloys with $M, M' \in \{\mathrm{Li}, \mathrm{Na}\}$, which is an additional indication for the increased stability of Na_2LiAlH_6 besides the symmetric distribution of Bader charges.[1]

5.2.4 Conclusion

We have analyzed the stabilities of cation-alloyed metal aluminum hexahydrides based only on density functional theory calculations for unperturbed configurations of cubic model structures. The difference in Bader charge attributed to the cation sites is found to be correlated to the stability of the corresponding alloys, where high asymmetries indicate unstable phases. The charge differences show a linear relationship with respect to the sum of cation electronegativities per formula unit except for K_2LiAlH_6 and especially Na_2LiAlH_6, which could be an indication for the increased decomposition temperature of the latter alloy compared to the constituents. This is furthermore supported by the vibrational

[1] X-ray powder diffraction patterns of Na_2LiAlH_6 show no deviation from the stocheometry M=Na and M'=Li [205], and configurational contributions to the entropy can therefore be neglected.

zero point energies obtained from a distortion analysis of maximally localized Wannier function basis sets.

5.3 Point defect dynamics in $NaAlH_4$ and Na_3AlH_6

5.3.1 Introduction

Metal aluminum hydrides have attracted interest as hydrogen storage materials, since Bogdanović and Schwickardi [48] have shown that titanium-doped sodium aluminum tetrahydride can reversibly desorb and re-absorb hydrogen at near ambient conditions. $NaAlH_4$ decomposes in several steps:

$$\begin{aligned} NaAlH_4 &\leftrightarrow \frac{1}{3}Na_3AlH_6 + \frac{2}{3}Al + H_2 \\ &\leftrightarrow NaH + Al + \frac{3}{2}H_2. \end{aligned} \tag{5.6}$$

The decomposition temperature of NaH is too high (∼700 K) [185] for hydrogen storage applications. Although the reversible hydrogen storage capacity is only up to about 4 mass-% [48], understanding the effect of the titanium dopant can be important for the design of catalysts for other complex metal hydrides, as doping with titanium also improves the sorption kinetics of *e.g.* $Mg(AlH_4)_2$ and $Ca(AlH_4)_2$ [50].

A proposed model for the role of titanium is the formation of alloys with aluminum [206], supported by X-ray absorption fine structure measurements [51] showing that for the most part, titanium is atomically dispersed in the aluminum phase. Density functional theory calculations by Chaudhuri *et al.* [52, 53] indicate a catalyzation of H–H bond breaking on titanium-containing aluminum surfaces. Furthermore, volatile Al_nH_{3n} species experimentally observed during reforming of catalyst-doped $NaAlH_4$ [54] are suggested to mediate improved mass transport of Al to NaH.

Another model suggests that bulk-substituted titanium [207] improves bulk diffusion of hydrogen. Palumbo *et al.* [208] have observed fast point defect dynamics with a relatively low activation barrier of 0.126 eV using an anelastic spectroscopy technique with a larger fraction of mobile species for titanium-doped samples, proposing that this enhancement corresponds to improved bulk diffusion of hydrogen in the intermediate decomposition product Na_3AlH_6 [209].

In a combined computational and experimental approach, we have studied hydrogen dynamics in Ti-doped and undoped $NaAlH_4$ and Na_3AlH_6 [P5,P6]. We find hydrogen diffusion in Na_3AlH_6 to require significant activation and

enhanced hydrogen diffusion in both Ti-doped $NaAlH_4$ and Na_3AlH_6 to be unlikely. We propose that the dynamic process observed by Palumbo *et al.* [208] could be related to the diffusion of other point defects, *e.g.* Na vacancies.

5.3.2 Computational details

Total energies and gradients were calculated with the plane wave density functional theory code DACAPO [108], describing the ionic cores by ultrasoft pseudopotentials [123]. The Perdew-Wang-91 [105, 106] approximation to the exchange-correlation functional was used. The size of the plane wave basis sets was limited by a kinetic energy cutoff of 340 eV. Jump diffusion paths were calculated using $2 \times 2 \times 1$ supercells (corresponding to supercell volumes of $2 \cdot 4.99 \times 2 \cdot 4.99 \times 1 \cdot 11.12$ Å^3 and $2 \cdot 5.27 \times 2 \cdot 5.46 \times 1 \cdot 7.60$ Å^3 for $I4_1/a$-$NaAlH_4$ [210] and $P2_1/n$-Na_3AlH_6 [174], respectively). The electronic Brillouin zones were sampled on $2 \times 2 \times 2$ Monkhorst-Pack grids [172].

The nuclear coordinates of initial guesses for H vacancy or interstitial configurations were relaxed to obtain the corresponding formation energies. Two such configurations were considered as initial and final configurations of minimum energy jump paths. Initial guesses for the paths based on a linear interpolation of the initial and final coordinates were optimized within the nudged elastic band approach [163] using a finite number of images; for the determination of the saddle point on the potential energy surface characterizing the transition state the adaptive nudge elastic band method [165] was used (cf. Sec. 3.2.2). The vibrational frequencies corresponding to the initial state and saddle point configurations for a calculation of the jump rate using Eq. (3.53) were obtained from finite displacements, where the degrees of freedom of all nuclei inside a radius of ∼4 Å around the diffusing species at the initial or saddle point position were considered, assuming differences in the remaining frequencies between the initial and saddle point configurations to be negligible.

5.3.3 Incoherent quasielastic neutron scattering

In addition to the *ab initio* modeling of jump processes, we have performed incoherent quasielastic neutron scattering experiments. This technique provides information about jump geometries and rates, allowing for a direct comparison to the results obtained within transition state theory.

Quasielastic neutron scattering is sensitive to the motion of hydrogen in particular, owing to a stochastic distribution of scattering lengths of different magnitude and sign. In the limit of long neutron wavelengths compared to the range of interaction and the neutron radius ($\sim 10^{-4}$ Å), an elastic scattering process with an incoming plane wave $\exp(ikx)$ representing a neutron scattered

isotropically at the nucleus can be expressed in terms of incident and outgoing waves as (the nucleus is positioned at the origin)

$$\Psi(\boldsymbol{r}) = \exp(ikx) + \frac{-a}{r}\exp(ikr), \tag{5.7}$$

where a is the scattering length [211]. For the case of hydrogen, the spins of proton and scattered neutron couple to a singlet ($S^2 = 0$, $S_z = 0$) or to a triplet ($S^2 = 1$, $S_z \in \{\pm 1, 0\}$). For the singlet, the scattering length is negative corresponding to an unbound state, while for the triplets, the scattering length is positive indicating the existence of a bound state [211]. This leads to a large incoherent neutron scattering cross-section given by the variance of the scattering length [212].[2] In the case of inelastic scattering, the double differential incoherent scattering cross-section reads [213]

$$\begin{aligned}\frac{\mathrm{d}^2\sigma_\mathrm{i}}{\mathrm{d}\Omega\mathrm{d}\omega} &= \frac{1}{2\pi}\left(\left\langle a^2\right\rangle_S - \left\langle a\right\rangle_S^2\right)\frac{k_\mathrm{out}}{k_\mathrm{in}} \\ &\times \int_{-\infty}^{\infty}\mathrm{d}t\exp(i\omega t)\sum_j\left\langle\exp[-i\boldsymbol{q}\boldsymbol{R}_j(0)]\exp[i\boldsymbol{q}\boldsymbol{R}_j(t)]\right\rangle_T,\end{aligned} \tag{5.8}$$

where $\omega = (2m_\mathrm{n})^{-1}(\boldsymbol{k}_\mathrm{in}^2 - \boldsymbol{k}_\mathrm{out}^2)$ is the energy transferred to the sample (using atomic units; $m_\mathrm{n} \approx 1839$ is the neutron mass in units of the electron mass), and $\boldsymbol{q} = \boldsymbol{k}_\mathrm{in} - \boldsymbol{k}_\mathrm{out}$ is the momentum transfer. $\langle ...\rangle_S$ denotes here[3] the statistical average over singlet and triplet coupling. $\langle ...\rangle_T$ denotes the ensemble average over the trajectories $\boldsymbol{R}_j(t)$ of the jth nucleus in thermal equilibrium (*i.e.* there are no chemical potential gradients.). Ω is the solid angle in $\boldsymbol{q}$-space (we have performed the experiments on powder samples; the angular dependence is thus not resolved, and a powder average is obtained instead, depending on ω and the length of $\boldsymbol{q}$ only). The integral over time and the sum over nuclei correspond to Fourier transforms of the self-correlation function yielding the probability for a nucleus with position $\boldsymbol{R}_j(0)$ at time $t = 0$ to be found at position $\boldsymbol{R}_j(t')$ at time $t = t'$.

While only the coherent scattering cross-section resolves interference between neutrons scattered at different nuclei, Eq. (5.8) is characterized by single-particle dynamics. The transfer of the energy ω between neutron and sample results in a so-called quasielastic broadening of the scattered neutron intensity versus energy transfer with respect to the elastic scattering peak at $\omega = 0$ with finite width given by the instrumental resolution.

[2]Due to the dominance of incoherent over coherent neutron scattering in the case of hydrogen, the corresponding crystal structures generally are derived from the interference patterns of deuterated samples.

[3]Incoherent scattering can also be due to isotope disorder.

In the experiments presented here, the instrumental resolution was obtained for each sample from the scattering intensity at $T = 30$ K, assuming the probability for jump processes to be negligible at this temperature. Jump lengths and rates were obtained by fitting the quasielastic broadening to models for diffusive processes [214, 215], which will be discussed later.

5.3.4 Results

5.3.4.1 Density functional theory calculations

The calculated formation energies for hydrogen interstitials based on a relaxation of the internal coordinates corresponding to the point defect configurations are very high in both $NaAlH_4$ and Na_3AlH_6: 2.40 eV and 2.42 eV, respectively. The formation energies for hydrogen vacancies are 1.61 eV and 1.54 eV for $NaAlH_4$ and Na_3AlH_6, respectively. We therefore assume hydrogen diffusion to be vacancy mediated in these systems.

There are two types of hydrogen vacancy jumps in the considered systems: diffusional jumps between vacant sites bound to different aluminum atoms and localized jumps, where the vacancy remains bound to the same aluminum atom. While only the former promote macroscopic hydrogen diffusion, the latter could be of importance as connections between diffusional jumps. Both types of jumps contribute to the quasielastic broadening and must hence be considered for a jump geometry analysis based on the incoherent scattering cross-section.

For $NaAlH_4$, the calculated activation energies for diffusional jumps are $E_a \geq 0.31$ eV depending on the vacant sites, while the barrier for a localized jump is $E_a = 0.44$ eV (see Fig. 5.9). For Na_3AlH_6, however, the activation energies of diffusional jumps (Fig. 5.10a) are high with values of $E_a \geq 0.75$ eV, and the barrier for localized jumps (Fig. 5.10b) is lower with a value of $E_a = 0.41$ eV.

In order to study the influence of bulk-substituted titanium on the barriers for hydrogen vacancy jumps, we have compared the energies required for Ti@Al and Ti@Na substitutions. The calculated energy for a substitution at an aluminum site in $NaAlH_4$ is 0.86 eV. The corresponding energy for a Ti@Na substitution is 2.63 eV. For Na_3AlH_6, the energies for substitution at aluminum sites and at sodium sites with eightfold and octahedral coordination are 0.95 eV, 2.00 eV, and 2.44 eV, respectively. In the case that titanium does bulk substitute, substitution for aluminum is thus energetically preferred for both $NaAlH_4$ and Na_3AlH_6 in agreement with previous calculations also considering the cohesive energies of the metals as references [216, 217].

Based on the calculations using $2 \times 2 \times 1$ supercells, hydrogen is trapped by titanium in $Na_{16}(Ti@Al)Al_{15}H_{63}$, corresponding to Ti–H distances up to at

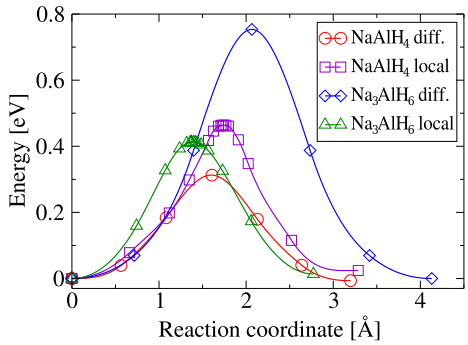

Figure 5.9: Total energy versus reaction coordinate for the calculated minimum energy paths in $Na_{16}Al_{16}H_{63}$ and $Na_{24}Al_8H_{47}$ for diffusional and localized hydrogen vacancy jumps. The reaction coordinate corresponds to the coordinate difference vector between adjacent images. (Adapted from [P6], Copyright 2007 Elsevier B. V.; `http://dx.doi.org/10.1016/j.jallcom.2007.04.041`.)

least ∼7 Å. For $Na_{24}(Ti@Al)Al_7H_{47}$, the activation energy of only two diffusional jumps per supercell is reduced to 0.36 eV. All localized hydrogen motion is trapped by titanium for the considered supercell dimensions. The trapping of hydrogen could lead to a formation of local hydrogen vacancies, *i.e.* without removing hydrogen from the system. For Na_3AlH_6, *e.g.*, the total cost, including the energy for the substitution of titanium, for a distant hydrogen atom transferred close to titanium is 1.21 eV, *i.e.* 0.33 eV cheaper than a vacancy formation in undoped Na_3AlH_6.

5.3.4.2 Experiment

Since the presented calculations of jump paths are not exhaustive with respect to larger supercell sizes for titanium doped systems in particular, a comparison to the results from incoherent neutron scattering can be used to examine whether *e.g.* the restriction of the maximal distance between hydrogen vacancy and titanium due to the supercell dimensions precludes the prediction of the observed vacancy dynamics in doped systems. Due to restrictions of the temperature ranges at the neutron scattering facility (Jülich), a calculation of activation energies from jump rates measured at different temperatures was not possible. Activation energies have been obtained from rates measured at a single temperature and the ratio of partition functions in Eq. (3.53) based on vibrational frequencies calculated using density functional theory for the initial and saddle point configurations of diffusional and localized jumps, respectively.

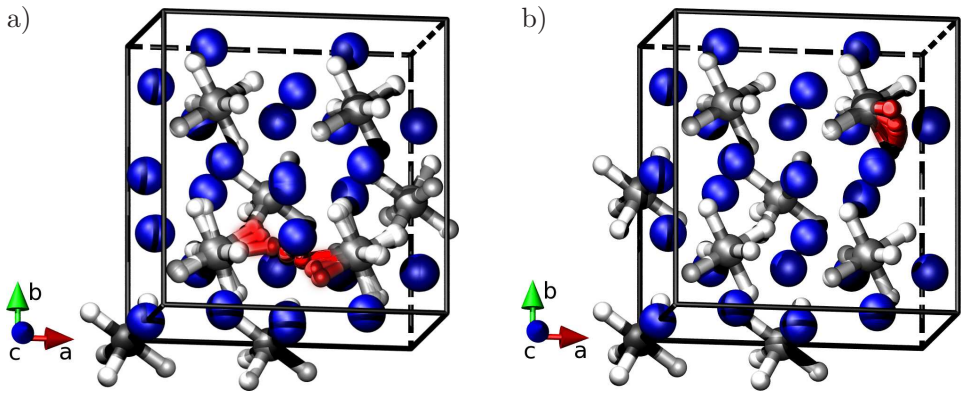

Figure 5.10: Minimum energy jump paths in $Na_{24}Al_8H_{47}$ between vacant hydrogen sites bound to different aluminum atoms (a) and the same aluminum atom (b), respectively. Sodium is represented by blue, aluminum by gray, and hydrogen by white spheres. The red spheres indicate the motion of hydrogen involved in the vacancy jumps.

As hydrogen diffusion is vacancy mediated in the considered systems, it has to be taken into account that the quasielastic broadening is due to the involved motion of hydrogen atoms. While hydrogen vacancy jumps contributing to macroscopic diffusion can be considered to constitute a random walk, the corresponding atomic jumps are correlated. In a zero-order approximation with one atomic jump per vacancy jump, the only effect is a rescaling of the jump rate, which is inversely proportional to the width of the broadening, while the shape of the broadening with respect to q is not affected [218]. Using the numerically obtained ratios of partition functions, an error of *e.g.* 50% in the estimated rate would only lead to an error of $k_BT/2$ in the calculated activation energy.

In order to identify hydrogen (vacancy) dynamics that are constricted to a certain volume, the ratio of elastically scattered neutron intensity to total intensity can be considered, which depends on the momentum transfer in the case of spatially restricted motion [215]. For $NaAlH_4$, this ratio is found to be independent of q (within the given experimental resolution), and a fit of the momentum transfer dependence of the quasielastic broadening measured at 390 K to a jump diffusion model corresponding to spatially unrestricted random walks [214] yields a jump rate of $k \approx 4 \times 10^8$ s^{-1} and a jump length of about 2.6 Å [P6], which is only a rough estimate, because the model assumes an isotropic jump geometry (the predicted jump lengths are 2.55 Å and 2.78 Å for localized and diffusional jumps, respectively). Using the ratio of partition

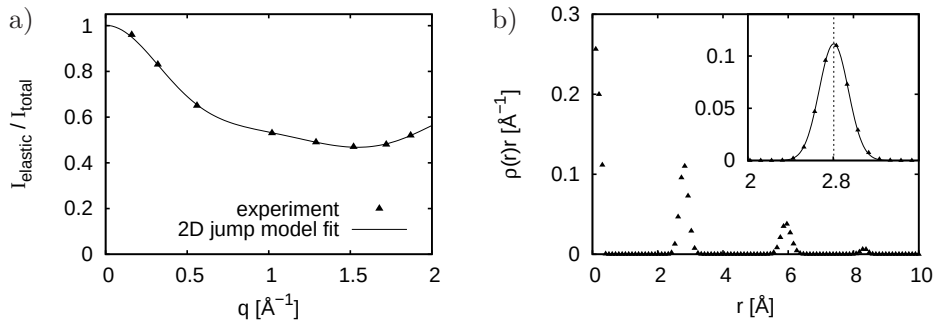

Figure 5.11: Ratio of elastic to total scattering intensity with respect to momentum transfer measured at 390 K (a) and radial probability density for finding a jumping species in two perpendicular planes (b) for undoped Na_3AlH_6. The inset shows a Gaussian fit to the peak at $r = (2.81 \pm 0.14)$ Å. (Adapted from [P6], Copyright 2007 Elsevier B. V.; `http://dx.doi.org/10.1016/j.jallcom.2007.04.041`.)

functions calculated for a diffusional vacancy jump in $Na_{16}Al_{16}H_{63}$, we obtain an activation energy of 0.39 eV from the experimentally observed rate, which could be due to an effective average of localized and diffusional jump rates [219].

For Na_3AlH_6, however, the predicted barrier for diffusional jumps is almost twice as high as the barrier for localized jumps, and the ratio of elastic to total scattering intensity measured at 390 K shows a clear q-dependence (Fig. 5.11a). To model the restricted motion of a vacancy in an $(AlH_5)^{2-}$ group, we consider two perpendicular planes which the jumping species are assumed to be constricted to. The ratio of elastic to total scattering intensity can be calculated as the absolute square of the Fourier transform of the accessible volume to $\boldsymbol{q}$-space [215]. Assuming circularly symmetric probability densities to find the diffusing species in the planes, the powder average is given as an integration over the polar angle θ in $\boldsymbol{q}$-space, aligning the q_z-axis with one of the plane normals. Approximating this integral by a three-point quadrature ($\theta \in \{0, \pi/2, \pi\}$), the ratio of elastic to total scattering intensity reads

$$\frac{I_{\text{elastic}}}{I_{\text{total}}} = \frac{1}{4}\left|\int_0^\infty \mathrm{d}r\rho(r)r\left[\mathrm{j}_0(qr)+1\right]\right|^2, \tag{5.9}$$

where $\rho(r)$ is the radial probability density in the planes and $\mathrm{j}_0(x) = \sin(x)/x$ is the spherical Bessel function of the first kind and order zero. From the measured ratio (5.9), we have obtained the radial probability density by a least

squares fit [181] to a spline interpolation of the ratio (see Fig. 5.11b). The large peak at $r = 0$ is due to immobile hydrogen. The peak at $r \approx 2.8$ Å corresponds to jumps between adjacent vacant sites in an $(AlH_5)^{2-}$ anion. This is only a rough estimate to the jump length due to the assumed circular symmetry in the planes (the predicted jump lengths for localized and diffusional jumps in $Na_{24}Al_8H_{47}$ are 2.50 Å and 3.08 Å, respectively). Based on the measured quasielastic broadening and the ratio of partition functions calculated from vibrational frequencies for the initial and saddle point configurations of the predicted localized hydrogen vacancy jump path, we obtain an activation energy of $E_a = 0.37$ eV, in agreement with the numerically predicted value of 0.41 eV for localized jumps.

The intensity ratio (5.9) for titanium doped Na_3AlH_6 also exhibits a clear q-dependence [P6], showing that bulk hydrogen vacancy diffusion is limited in space. The barriers for these localized events are lowered to 0.31 eV. Macroscopic bulk diffusion of hydrogen therefore is limited also for titanium doped Na_3AlH_6 in agreement with the numerically predicted activation energies.

5.3.4.3 Other point defect dynamics

Since the quasielastic broadening, which is dominated by incoherent scattering at jumping hydrogen atoms, revealed no dynamics with barriers below ∼0.3 eV, we have considered other point defect dynamics which could be related to the barrier of 0.126 eV observed by Palumbo *et al.* [208]. These dynamics are expected to occur in the intermediate product Na_3AlH_6 [209]. We have calculated an activation energy of $E_a = 0.12$ eV for sodium vacancy jumps in $Na_{23}Al_8H_{48}$ from sites with eightfold to sites with octahedral coordination (Fig. 5.12).

Palumbo *et al.* [208] have studied defect dynamics in sodium aluminum hydride by macroscopic oscillatory deformation with two different frequencies. The rate is tuned with the temperature, and at resonance, the jumping species follow the externally applied oscillations, observed as a loss of elastic energy. For an external frequency of ∼5 kHz, the resonance temperature was found to be about 70 K. From the shift in resonance temperature for a different frequency, the activation energy was determined.

From a vibrational analysis for the initial and saddle point configurations of the sodium vacancy diffusion path and the calculated barrier of 0.12 eV, we obtain a jump rate of 4.3×10^3 s^{-1} for $T = 70$ K, a further indication, that the observed point defect dynamics could be due to sodium vacancy jumps. For deuterated samples, a shift of the resonance temperature to 77 K for the external frequency of ∼5 kHz was observed [209]. The ratio of partition functions for the numerically obtained sodium vacancy jump rate is dominated by the vibrational frequencies of the diffusing sodium atom. The lower frequen-

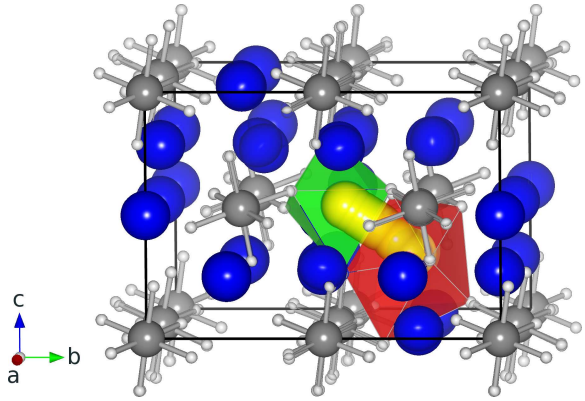

Figure 5.12: Minimum energy sodium vacancy jump path in $Na_{23}Al_8H_{48}$ (based on a VESTA [194] rendition). Sodium is represented by blue, aluminum by gray, and hydrogen by white spheres. The path of the sodium ion diffusing between the vacant sites is shown in yellow. The octahedral and eightfold coordination at the corresponding sites is depicted as green and red polyhedra, respectively.

cies of deuterium due to its larger mass compared to hydrogen can thus not explain a resonance shift of 7 K for the considered sodium vacancy dynamics. As *e.g.* the lattice constants of hydrides and deuterides can differ [220, 221], we have re-optimized the initial and final configurations and the minimum energy path, keeping the Al–D bond lengths fixed at the values obtained from powder diffraction patterns of Na_3AlD_6 [174]. Due to non-negligible residual forces exerted on the corresponding degrees of freedom, we approximate the change in the ratio of partition functions for the deuterated system by considering the changes in the frequencies of the diffusing sodium atom only. The correspondingly estimated resonance temperature for deuterated systems at a frequency of 5 kHz is $T = 76$ K, supporting that the observed dynamics might be due to sodium vacancy jumps.

5.3.5 Conclusion

In a combined computational and experimental approach, we have identified the dynamic processes related to bulk diffusion of hydrogen in sodium aluminum hydride. While macroscopic hydrogen diffusion has been observed in $NaAlH_4$ at near ambient temperatures, hydrogen jumps in Na_3AlH_6 have been found to be restricted in space with high activation energies $\gtrsim 0.8$ eV for diffusional vacancy jumps between $(AlH_5)^{2-}$ and $(AlH_6)^{3-}$ groups. The effect of the titanium dopant on bulk diffusion of hydrogen is found to be negligible.

Since the incoherent scattering shows no activation energies below ∼0.3 eV, we suggest that the point defect dynamics with a barrier of 0.126 eV observed using anelastic spectroscopy [208] are not related to hydrogen jumps but could *e.g.* be due to sodium vacancy dynamics in Na_3AlH_6.

An advantage of the combined approach is in general, that the numerically predicted activation energies can be used to examine whether a q-independence of the elastic to total intensity ratio is due to spatially unrestricted dynamics or due to insufficient experimental resolution. On the other hand, the experimentally observed jump lengths and rates can be used to examine whether larger supercell sizes allowing for more configurations of titanium dopant sites and hydrogen vacancy jump paths are needed to reproduce the observed rates and jump geometries.

6

Summary and outlook

The work presented in this thesis focuses on the thermodynamics of complex metal hydrides, which comprise several compounds with promising properties for hydrogen storage applications. On the basis of density functional theory, lattice free energies of these crystal structures have been calculated in order to compare phase stabilities and to estimate decomposition temperatures. Analyzing instabilities given by non-vibrational modes present in all previously proposed structures of magnesium borohydride, stable phases of this compound have been derived. Neglecting imaginary frequencies in the phonon dispersion of unstable phases exhibiting the energetically preferred local coordination, the correspondingly calculated free energies would allow for a rough decomposition temperature estimate, even if the crystal symmetries of the stable structures were not known.

In order to be able to efficiently optimize the atomic coordinates of crystal structures with many degrees of freedom per asymmetric unit, we have developed a coordinate relaxation scheme which preserves crystal symmetries in the presence of numerical inaccuracies in the total energy gradient and furthermore leads to an improved convergence with respect to the number of electronic structure calculations required to determine the equilibrium configuration.

Moreover, an optimally scaling approach to assess lattice free energies has been developed, which is based on a computationally inexpensive calculation of polarization vectors for an auxiliary effective point charge system, combined with a single total energy gradient calculation within density functional theory. Taking advantage of the asymptotic behavior of lattice free energies at low and high temperatures, reasonable estimates to the lattice free energy can be

obtained from roughly approximated phonon frequencies. This allows for an efficient assessment of *e.g.* alloy stabilities of insulators with high frequency bond stretching and bending modes, such as complex metal hydrides, and also of metals and semiconductors.

A combined experimental and computational analysis of hydrogen vacancy jump processes in sodium aluminum hydride has shown that bulk diffusion of hydrogen is limited especially in the intermediate decomposition product Na_3AlH_6, and the effect of titanium as a dopant on the diffusional dynamics has been found to be negligible. The integration of the incoherent quasielastic neutron scattering technique, which is sensitive to single-particle dynamics of hydrogen in particular, and the *ab initio* prediction of jump geometries and rates is a promising approach to the understanding of bulk hydrogen dynamics in potential hydrogen storage materials.

Outlook

The conclusion that simple model structures can be used to roughly assess the stability of complex metal hydrides allows for qualitative screening studies of thermodynamic stabilities, if the constructed model systems obey an energetically optimal local coordination (a corresponding analysis of mixing enthalpies is currently being performed for metal borohydride structures [Hummelshøj, Landis, Voss, *et al.*, manuscript in preparation]). The rigid-ion electrostatic prototype screening approach developed by Majzoub and Ozoliņš [192] could be used for a systematic generation of model structures.

For the metal aluminum hexahydride structures considered in Sec. 5.2, the cations occupy two symmetrically inequivalent sites. Here, binary cation alloying simply corresponds to different metal cations occupying the symmetrically inequivalent sites. For *e.g.* ternary cation alloys of metal aluminum hexahydrides or alloys in general that are not formed by substitution of a full set of symmetrically equivalent sites, the resulting crystal structure might have a different symmetry, or a partial substitution can occur. In the latter case, the entropy due to the occupational disorder has to be considered for an analysis of the alloy stability, which could be calculated *e.g.* using the cluster expansion technique [17, 18].

In the case of negligible disorder, the generally dominant phononic contribution to the entropy can be obtained efficiently from an additional electronic charge density calculation using the single displacement method presented in Sec. 4.2. In this way the model structures of compounds with promising thermodynamic properties could be selected for a further, more detailed analysis.

As demonstrated in Sec. 5.1, stable phases might be found by following non-vibrational modes based on a calculation of the phonon dispersion (which

is not guarantied to yield the structure with lowest free energy, depending on the model structure used as a starting point). Due to the high computational complexity of the Hessian matrix calculation scaling as $O(N)$ charge density calculations (N: number of atoms per asymmetric unit), an iterative calculation of the mode corresponding to the negative eigenvalue of largest magnitude of the mass-scaled Hessian might be advantageous for large structures in particular. In the case of complex metal hydrides, *e.g.*, a subtraction of the square of a guess for the typical bond stretching frequency from the diagonal of the mass-scaled Hessian shifts the eigenvalues such that the eigenvalue corresponding to the above mentioned mode has the largest magnitude. Power methods [161] or similar iterative approaches will thus converge to the corresponding eigenpair. If the obtained mode corresponds to a rigid translation (*i.e.* to a re-shifted eigenvalue of zero), the Γ-point phonon spectrum can be expected to be free of imaginary frequencies. If an unstable mode is found instead, a stable structure might be found by following the corresponding displacement in the atomic coordinates. It should be noted, however, that this iterative approach would only be able to identify instabilities given by imaginary Γ-point frequencies; phase transitions to structures with larger unit cells than the (super) cell of the model structure corresponding to instabilities at larger wave vectors would not be resolved.

A

Ewald summation

Since the evaluation of the electrostatic energy and its derivatives in particular is of central importance for several projects presented in this thesis, the derivation of the corresponding formulas are in the following explained in detail.

The slowly converging lattice sums over inverse distances, appearing *e.g.* in the electrostatic energy of the nuclear point charge system of periodic systems, can be split into quickly converging sums in direct and reciprocal space, respectively. These so-called Ewald sums [222] can be constructed by adding spherical Gaussians centered at the atomic sites, which each integrate to the negative of the charge of the corresponding nucleus. The nuclear electrostatic potentials are approximately canceled at long range (exactly at infinite distance), leading to rapidly converging sums of the corresponding terms in real space. To compensate the added charge density, the potential of the negative of this density is evaluated in reciprocal space.

The electrostatic potential of the lattice sum of Gaussian charge distributions is obtained from the corresponding Poisson equation in reciprocal space, where the sum over unit cell integrals is converted into an integral over all space (we will use atomic units; Z is the atomic number of the nucleus):

$$\begin{aligned} -G^2\frac{\tilde{\varphi}_{\boldsymbol{G}}}{Z} &= -4\pi\Omega^{-1}\sum_{\boldsymbol{T}}\int_{\Omega}\mathrm{d}^3r\frac{\eta^3}{\pi^{3/2}}\exp\Big[-\eta^2(\boldsymbol{r}-\boldsymbol{T})^2\Big) \\ &\quad\times\exp[-i\boldsymbol{G}(\boldsymbol{r}-\boldsymbol{T})] \\ &= -4\pi\Omega^{-1}\int\mathrm{d}^3r\frac{\eta^3}{\pi^{3/2}}\exp(-\eta^2r^2)\exp(-i\boldsymbol{G}\boldsymbol{r}) \end{aligned}$$

$$= -4\pi\Omega^{-1}\exp\left(-\frac{G^2}{4\eta^2}\right), \tag{A.1}$$

where the parameter η controls the inverse width of the Gaussians in real space and thereby the convergence of the sums in direct and reciprocal space. The potential $\varphi^{(1)}$ of a single Gaussian in real space centered at the origin is given by the inverse Fourier transform

$$\begin{aligned}\frac{\varphi^{(1)}(r)}{Z} &= \frac{4\pi}{(2\pi)^3}2\pi\int_{-1}^{1}\mathrm{d}\cos\theta\int_{0}^{\infty}\mathrm{d}G\frac{G^2}{G^2}\exp\left(-\frac{G^2}{4\eta^2}\right)\\ &\quad\times\exp(i\boldsymbol{G}\boldsymbol{r}\cos\theta),\end{aligned} \tag{A.2}$$

where, taking advantage of the spherical symmetry, the G_z-axis for the integral in reciprocal space is chosen parallel to the vector $\boldsymbol{r}$. Because of the symmetric boundaries of the integral over $\mathrm{d}\cos\theta$, the imaginary part of Eq. (A.2) due to the factor $i\sin(i\boldsymbol{G}\boldsymbol{r}\cos\theta)$ in the integrand vanishes, and thus all terms in the integrand antisymmetric in G are canceled by the polar integration. The integration over $\mathrm{d}G$ can therefore be extended to $-\infty$ (with a division by 2):

$$\begin{aligned}\frac{\varphi^{(1)}(r)}{Z} &= \frac{1}{2\pi}\int_{-1}^{1}\mathrm{d}\cos\theta\int_{-\infty}^{\infty}\mathrm{d}G\exp\left(-\frac{G^2}{4\eta^2}\right)\exp(i\boldsymbol{G}\boldsymbol{r}\cos\theta)\\ &= \frac{2}{\sqrt{\pi}}\eta\int_{0}^{1}\mathrm{d}\cos\theta\exp(-\eta^2r^2\cos^2\theta)\\ &= \frac{\mathrm{erf}(\eta r)}{r},\end{aligned} \tag{A.3}$$

where, using the symmetry of the corresponding integrand, the interval $[-1,1]$ for the polar integration has been transformed to $[0,1]$.

With $\mathrm{erfc}(x) = 1-\mathrm{erf}(x)$, the electrostatic energy E_N of the nuclear point charges with atomic numbers Z_k can be expressed per unit cell as

$$\begin{aligned}E_\mathrm{N} &= \frac{1}{2}\Bigg[\sum_{k\ell}Z_kZ_\ell\sum_{\boldsymbol{T}\neq\boldsymbol{t}_{k\ell}}\frac{\mathrm{erfc}(\eta|\boldsymbol{t}_{k\ell}-\boldsymbol{T}|)}{|\boldsymbol{t}_{k\ell}-\boldsymbol{T}|}\\ &\quad+\frac{4\pi}{\Omega}\sum_{\boldsymbol{G}\neq0}\frac{\exp\left(-\frac{G^2}{4\eta^2}\right)}{G^2}\left(\sum_k Z_k\exp(i\boldsymbol{G}\boldsymbol{r}_k)\right)^2\end{aligned}$$

$$-\frac{2\eta}{\sqrt{\pi}}\sum_k Z_k^2 - \frac{\pi}{\Omega\eta^2}\left(\sum_k Z_k\right)^2\Bigg], \tag{A.4}$$

with the nuclear positions $\boldsymbol{r}_k$ and the difference vectors $\boldsymbol{t}_{k\ell} = \boldsymbol{r}_k - \boldsymbol{r}_\ell$. For the sum over reciprocal lattice vectors, the double sum over nuclear indices has been reduced to the square of a single sum. The diverging term for $\boldsymbol{G} = 0$ is canceled by corresponding terms due to the average electronic charge density, if the system is electrically neutral (cf. the Fourier components (2.79) of the Hartree potential), and is thus left out.

For the sum in direct space, the self-interaction terms with $\boldsymbol{T} = \boldsymbol{t}_{k\ell}$ are left out. The self-interaction contribution to the sum in reciprocal space is given by the limit $\Omega \to \infty$ with $k = \ell$ in the double sum $\sum_{k\ell} Z_k Z_\ell \exp(i\boldsymbol{G}\boldsymbol{t}_{k\ell})$, yielding a continuous set of vectors $\boldsymbol{G}$. Hence, the sum in reciprocal space becomes an integral. The resulting term is subtracted from the energy (first term in last line of Eq. (A.4)). The last term in (A.4) corresponds to setting the average electrostatic potential to zero [222, 223]. Since the $\boldsymbol{G} = 0$ component is left out in the Fourier series, the term to be subtracted from the potential is given by the average real space contribution to the potential:

$$\begin{aligned}
&\frac{1}{\Omega}\sum_{\boldsymbol{T}}\int_\Omega \mathrm{d}^3 r \frac{\operatorname{erfc}(\eta|\boldsymbol{r}-\boldsymbol{T}|)}{|\boldsymbol{r}-\boldsymbol{T}|} = \frac{4\pi}{\Omega}\int \mathrm{d}^3 r r \operatorname{erfc}(\eta r) \\
= &\frac{4\pi}{\Omega}\int \mathrm{d}^3 r r \frac{2}{\sqrt{\pi}}\int_{\eta r}^{\infty}\mathrm{d}u \exp(-u^2) = \frac{4\pi}{\Omega}\int \mathrm{d}^3 r r^2 \frac{2}{\sqrt{\pi}}\int_{\eta}^{\infty}\mathrm{d}v \exp(-r^2 v^2) \\
= &\frac{\pi}{\Omega}\int_\eta^\infty \mathrm{d}v \frac{2}{v^3} = \frac{\pi}{\Omega\eta^2}.
\end{aligned} \tag{A.5}$$

The real space sum in (A.4) converges faster for larger values of η, *i.e.* for narrower Gaussian charge distributions in real space. The sum over reciprocal lattice vectors, on the other hand, converges faster for broader Gaussians. A reasonable compromise is a value for η of the order of the minimum spacing of the reciprocal lattice vectors [99].

The contribution of the nuclear point charge system to the forces exerted on the nuclei are given by the derivatives of Eq. (A.4) with respect to the nuclear coordinates $r_{k,\alpha}$ ($\alpha \in \{x, y, z\}$):

$$F_{k,\alpha} = -\frac{\partial E_\mathrm{N}}{\partial r_{k,\alpha}}$$

$$
\begin{aligned}
&= Z_k \sum_\ell Z_\ell \sum_{\boldsymbol{T}\neq\boldsymbol{t}_{k\ell}} \frac{t_{k\ell,\alpha}-T_\alpha}{|\boldsymbol{t}_{k\ell}-\boldsymbol{T}|^2}\left(\frac{\operatorname{erfc}(\eta|\boldsymbol{t}_{k\ell}-\boldsymbol{T}|)}{|\boldsymbol{t}_{k\ell}-\boldsymbol{T}|}\right.\\
&\quad\left.+\frac{2\eta}{\sqrt{\pi}}\exp\left[-\eta^2|\boldsymbol{t}_{k\ell}-\boldsymbol{T}|^2\right]\right)\\
&\quad+\frac{4\pi}{\Omega}\sum_{\boldsymbol{G}\neq 0}\frac{\exp\left(-\frac{G^2}{4\eta^2}\right)}{G^2}G_\alpha Z_k\sum_\ell Z_\ell\sin(\boldsymbol{G}\boldsymbol{t}_{k\ell}),
\end{aligned}
\tag{A.6}
$$

where we have used that the nuclear potentials are spherically symmetric around the nuclear positions, and that hence the Fourier series for a nuclear potential can be written as

$$
\frac{1}{\Omega}\sum_{\boldsymbol{G}\neq 0}\varphi_{\boldsymbol{G}}\exp(i\boldsymbol{G}\boldsymbol{r})=\frac{1}{\Omega}\sum_{\boldsymbol{G}\neq 0}\varphi_{\boldsymbol{G}}\cos(\boldsymbol{G}\boldsymbol{r}).
\tag{A.7}
$$

The contribution to the Hessian matrix is (α and β are indices for the cartesian axes):

$$
\begin{aligned}
\mathcal{H}_{k,\alpha;\ell,\beta} &= \frac{\partial^2 E_{\mathrm{N}}}{\partial r_{k,\alpha}\partial r_{\ell,\beta}}\\
&= (-1)^{\delta_{k\ell}}Z_k\sum_m Z_m\left(\delta_{\ell m}+\delta_{k\ell}-\delta_{\ell m}\delta_{k\ell}\right)\\
&\quad\times\left[\sum_{\boldsymbol{T}\neq\boldsymbol{t}_{km}}\left\{-\delta_{\alpha\beta}v(|\boldsymbol{t}_{km}-\boldsymbol{T}|)+\frac{(t_{km,\alpha}-T_\alpha)(t_{km,\beta}-T_\beta)}{|\boldsymbol{t}_{km}-\boldsymbol{T}|^2}\right.\right.\\
&\quad\left.\times\left(3v(|\boldsymbol{t}_{km}-\boldsymbol{T}|)+2u(|\boldsymbol{t}_{km}-\boldsymbol{T}|)\right)\right\}\\
&\quad\left.-\frac{4\pi}{\Omega}\sum_{\boldsymbol{G}\neq 0}\exp\left(-\frac{G^2}{4\eta^2}\right)\frac{G_\alpha G_\beta}{G^2}\cos(\boldsymbol{G}\boldsymbol{t}_{km})\right],
\end{aligned}
\tag{A.8}
$$

with the substitutions

$$
u(x) = \frac{2\eta}{\sqrt{\pi}}\exp(-\eta^2x^2),
\tag{A.9}
$$

$$
v(x) = \frac{u(x)}{x^2}+\frac{\operatorname{erfc}(\eta x)}{x^3}.
\tag{A.10}
$$

Bibliography

[1] J. Maddox, *Crystals from First Principles*. Nature **335**, 201 (1988).

[2] G. Ceder, *Computational Materials Science — Predicting Properties from Scratch*. Science **280**, 1099 (1998).

[3] R. Martoňák, A. Laio, and M. Parrinello, *Predicting Crystal Structures: The Parrinello-Rahman Method Revisited*. Phys. Rev. Lett. **90**, 075503 (2003).

[4] A. R. Oganov and C. W. Glass, *Evolutionary crystal structure prediction as a tool in materials design*. J. Phys.: Condens. Matter **20**, 064210 (2008).

[5] G. Lu and E. Kaxiras, *Overview of Multiscale Simulations of Materials*. In M. Rieth and W. Schommers (Eds.), *Handbook of Theoretical and Computational Nanotechnology*, vol. 10: *Nanodevice Modeling and Nanoelectronics* (American Scientific Publishers, Los Angeles, 2005).

[6] E. Wigner, *Concerning the excess of potential barriers in chemical reactions*. Z. Phys. Chem. Abt. B **19**, 203 (1932).

[7] H. Eyring, *The Activated Complex in Chemical Reactions*. J. Chem. Phys. **3**, 107 (1935).

[8] M. G. Evans and M. Polanyi, *Some applications of the transition state method to the calculation of reaction velocities, especially in solution*. Trans. Faraday Soc. **31**, 875 (1935).

[9] E. Wimmer, *Computational materials design and processing: perspectives for atomistic approaches*. Mater. Sci. Eng. B: Solid State Mater. Adv. Technol. **37**, 72 (1996).

[10] P. Hohenberg and W. Kohn, *Inhomogeneous Electron Gas*. Phys. Rev. **136**, B864 (1964).

[11] W. Kohn and L. J. Sham, *Self-Consistent Equations Including Exchange and Correlation Effects*. Phys. Rev. **140**, A1133 (1965).

[12] W. Kohn, *Nobel Lecture: Electronic structure of matter — wave functions and density functionals*. Rev. Mod. Phys. **71**, 1253 (1999).

[13] S. Wei and M. Y. Chou, *Ab initio calculation of force constants and full phonon dispersions*. Phys. Rev. Lett. **69**, 2799 (1992).

[14] K. Kunc and R. M. Martin, *Ab Initio Force Constants of GaAs: A New Approach to Calculation of Phonons and Dielectric Properties*. Phys. Rev. Lett. **48**, 406 (1982).

[15] S. Baroni, S. de Gironcoli, A. Dal Corso, and P. Giannozzi, *Phonons and related crystal properties from density-functional perturbation theory*. Rev. Mod. Phys. **73**, 515 (2001).

[16] J. M. Dickey and A. Paskin, *Computer Simulation of the Lattice Dynamics of Solids*. Phys. Rev. **188**, 1407 (1969).

[17] J. M. Sanchez, F. Ducastelle, and D. Gratias, *Generalized cluster description of multicomponent systems*. Physica A **128**, 334 (1984).

[18] D. de Fontaine, *Cluster Approach to Order-Disorder Transformations in Alloys*. In H. Ehrenreich and D. Turnbull (Eds.), *Solid State Physics*, vol. 47 (Academic, New York, 1994).

[19] P. M. Cox, R. A. Betts, C. D. Jones, S. A. Spall, and I. J. Totterdell, *Acceleration of global warming due to carbon-cycle feedbacks in a coupled climate model*. Nature **408**, 184 (2000).

[20] Q. Schiermeier, *Climate change: That sinking feeling*. Nature **435**, 732 (2005).

[21] R. A. Kerr, *The Looming Oil Crisis Could Arrive Uncomfortably Soon*. Science **316**, 351 (2007).

[22] M. Grätzel, *Photoelectrochemical cells*. Nature **414**, 338 (2001).

[23] A. Fujishima and K. Honda, *Electrochemical Photolysis of Water at a Semiconductor Electrode*. Nature **238**, 37 (1972).

[24] K. Maeda, K. Teramura, D. Lu, T. Takata, N. Saito, Y. Inoue, and K. Domen, *Photocatalyst releasing hydrogen from water*. Nature **440**, 295 (2006).

[25] M. W. Kanan and D. G. Nocera, *In Situ Formation of an Oxygen-Evolving Catalyst in Neutral Water Containing Phosphate and Co^{2+}*. Science **321**, 1072 (2008).

[26] L. Schlapbach and A. Züttel, *Hydrogen-storage materials for mobile applications*. Nature **414**, 353 (2001).

[27] A. Züttel, *Materials for hydrogen storage*. Mater. Today **6**, 24 (2003).

[28] M. Fichtner, *Nanotechnological aspects in materials for hydrogen storage*. Adv. Eng. Mater. **7**, 443 (2005).

[29] S. Orimo, A. Züttel, L. Schlapbach, G. Majer, T. Fukunaga, and H. Fujii, *Hydrogen interaction with carbon nanostructures: current situation and future prospects*. J. Alloys Compd. **356**, 716 (2003).

[30] B. Panella, M. Hirscher, and S. Roth, *Hydrogen adsorption in different carbon nanostructures*. Carbon **43**, 2209 (2005).

[31] R. E. Morris and P. S. Wheatley, *Gas Storage in Nanoporous Materials*. Angew. Chem. Int. Ed. **47**, 4966 (2008).

[32] J. Weitkamp, M. Fritz, and S. Ernst, *Zeolites as media for hydrogen storage*. Int. J. Hydrog. Energy **20**, 967 (1995).

[33] A. W. C. van den Berg and C. Otero Areán, *Materials for hydrogen storage: current research trends and perspectives*. Chem. Commun. page 668 (2008).

[34] H. Li, M. Eddaoudi, M. O'Keeffe, and O. M. Yaghi, *Design and synthesis of an exceptionally stable and highly porous metal-organic framework*. Nature **402**, 276 (1999).

[35] M. Eddaoudi, J. Kim, N. Rosi, D. Vodak, J. Wachter, M. O'Keeffe, and O. M. Yaghi, *Systematic Design of Pore Size and Functionality in Isoreticular MOFs and Their Application in Methane Storage*. Science **295**, 469 (2002).

[36] N. L. Rosi, J. Eckert, M. Eddaoudi, D. T. Vodak, J. Kim, M. O'Keeffe, and O. M. Yaghi, *Hydrogen Storage in Microporous Metal-Organic Frameworks*. Science **300**, 1127 (2003).

[37] D. J. Collins and H.-C. Zhou, *Hydrogen storage in metal-organic frameworks*. J. Mater. Chem. **17**, 3154 (2007).

[38] W. L. Mao, H. Mao, A. F. Goncharov, V. V. Struzhkin, Q. Guo, J. Hu, J. Shu, R. J. Hemley, M. Somayazulu, and Y. Zhao, *Hydrogen Clusters in Clathrate Hydrate*. Science **297**, 2247 (2002).

[39] W. L. Mao and H. Mao, *Hydrogen storage in molecular compounds*. Proc. Natl. Acad. Sci. USA **101**, 708 (2004).

[40] H. Lee, J. Lee, D. Y. Kim, J. Park, Y.-T. Seo, H. Zeng, I. L. Moudrakovski, C. I. Ratcliffe, and J. A. Ripmeester, *Tuning clathrate hydrates for hydrogen storage*. Nature **434**, 743 (2005).

[41] T. Strobel, C. Taylor, K. Hester, S. Dec, C. Koh, K. Miller, and E. Sloan, *Molecular Hydrogen Storage in Binary THF-H_2 Clathrate Hydrates*. J. Phys. Chem. B **110**, 17121 (2006).

[42] R. Anderson, A. Chapoy, and B. Tohidi, *Phase Relations and Binary Clathrate Hydrate Formation in the System H_2-THF-H_2O*. Langmuir **23**, 3440 (2007).

[43] G. Sandrock, *A panoramic overview of hydrogen storage alloys from a gas reaction point of view*. J. Alloys Compd. **293**, 877 (1999).

[44] G. Liang, J. Huot, S. Boily, and R. Schulz, *Hydrogen desorption kinetics of a mechanically milled MgH_2 +5at.%V nanocomposite*. J. Alloys Compd. **305**, 239 (2000).

[45] S. Orimo, H. Fujii, and K. Ikeda, *Notable hydriding properties of a nanostructured composite material of the Mg_2Ni–H system synthesized by reactive mechanical grinding*. Acta Mater. **45**, 331 (1997).

[46] S. Orimo, Y. Nakamori, J. R. Eliseo, A. Züttel, and C. M. Jensen, *Complex Hydrides for Hydrogen Storage*. Chem. Rev. **107**, 4111 (2007).

[47] F. Schüth, B. Bogdanović, and M. Felderhoff, *Light metal hydrides and complex hydrides for hydrogen storage*. Chem. Commun. page 2249 (2004).

[48] B. Bogdanović and M. Schwickardi, *Ti-doped alkali metal aluminium hydrides as potential novel reversible hydrogen storage materials*. J. Alloys Compd. **253**, 1 (1997).

[49] H. W. Li, K. Kikuchi, Y. Nakamori, K. Miwa, S. Towata, and S. Orimo, *Effects of ball milling and additives on dehydriding behaviors of well-crystallized $Mg(BH_4)_2$*. Scr. Mater. **57**, 679 (2007).

[50] M. Mamatha, B. Bogdanović, M. Felderhoff, A. Pommerin, W. Schmidt, F. Schüth, and C. Weidenthaler, *Mechanochemical preparation and investigation of properties of magnesium, calcium and lithium-magnesium alanates*. J. Alloys Compd. **407**, 78 (2006).

[51] M. Felderhoff, K. Klementiev, W. Grünert, B. Spliethoff, B. Tesche, J. M. Bellosta von Colbe, B. Bogdanović, M. Härtel, A. Pommerin, F. Schüth, and C. Weidenthaler, *Combined TEM-EDX and XAFS studies of Ti-doped sodium alanate*. Phys. Chem. Chem. Phys. **6**, 4369 (2004).

[52] S. Chaudhuri and J. Muckerman, *First-Principles Study of Ti-Catalyzed Hydrogen Chemisorption on an Al Surface: A Critical First Step for Reversible Hydrogen Storage in $NaAlH_4$*. Journal of Physical Chemistry B **109**, 6952 (2005).

[53] S. Chaudhuri, J. Graetz, A. Ignatov, J. Reilly, and J. Muckerman, *Understanding the Role of Ti in Reversible Hydrogen Storage as Sodium Alanate: A Combined Experimental and Density Functional Theoretical Approach*. J. Am. Chem. Soc. **128**, 11404 (2006).

[54] Q. J. Fu, A. J. Ramirez-Cuesta, and S. C. Tsang, *Molecular Aluminum Hydrides Identified by Inelastic Neutron Scattering during H_2 Regeneration of Catalyst-Doped $NaAlH_4$*. J. Phys. Chem. B **110**, 711 (2006).

[55] P. Chen, Z. Xiong, J. Luo, J. Lin, and K. L. Tan, *Interaction of hydrogen with metal nitrides and imides*. Nature **420**, 302 (2002).

[56] Y. Nakamori, G. Kitahara, K. Miwa, N. Ohba, T. Noritake, S. Towata, and S. Orimo, *Hydrogen storage properties of Li–Mg–N–H systems*. J. Alloys Compd. **404**, 396 (2005).

[57] A. Züttel, S. R. P. Fischer, P. Wenger, P. Sudan, P. Mauron, and C. Emmenegger, *Hydrogen storage properties of $LiBH_4$*. J. Alloys Compd. **356**, 515 (2003).

[58] K. Chłopek, C. Frommen, A. Leon, O. Zabara, and M. Fichtner, *Synthesis and properties of magnesium tetrahydroborate, $Mg(BH_4)_2$*. J. Mater. Chem. **17**, 3496 (2007).

[59] M. D. Riktor, M. H. Sørby, K. Chłopek, M. Fichtner, F. Buchter, A. Züttel, and B. C. Hauback, *In situ synchrotron diffraction studies of phase transitions and thermal decomposition of $Mg(BH_4)_2$ and $Ca(BH_4)_2$*. J. Mater. Chem. **17**, 4939 (2007).

[60] S.-J. Hwang, R. Bowman, J. Reiter, J. Rijssenbeek, G. Soloveichik, J.-C. Zhao, H. Kabbour, and C. Ahn, *NMR Confirmation for Formation of $[B_{12}H_{12}]^{2-}$ Complexes during Hydrogen Desorption from Metal Borohydrides*. J. Phys. Chem. C **112**, 3164 (2008).

[61] N. Hanada, K. Chłopek, C. Frommen, W. Lohstroh, and M. Fichtner, *Thermal decomposition of $Mg(BH_4)_2$ under He flow and H_2 pressure*. J. Mater. Chem. **18**, 2611 (2008).

[62] R. Černý, Y. Filinchuk, H. Hagemann, and K. Yvon, *Magnesium Borohydride: Synthesis and Crystal Structure*. Angew. Chem. Int. Ed. **119**, 5867 (2007).

[63] J.-H. Her, P. W. Stephens, Y. Gao, G. L. Soloveichik, J. Rijssenbeek, M. Andrus, and J.-C. Zhao, *Structure of Unsolvated Magnesium Borohydride $Mg(BH_4)_2$*. Acta Crystallogr., Sect. B: Struct. Crystallogr. Cryst. Chem. **63**, 561 (2007).

[64] Z. Xiong, C. K. Yong, G. Wu, P. Chen, W. Shaw, A. Karkamkar, T. Autrey, M. O. Jones, S. R. Johnson, P. P. Edwards, and W. I. F. David, *High-capacity hydrogen storage in lithium and sodium amidoboranes*. Nat. Mater. **7**, 138 (2008).

[65] E. Schrödinger, *An Undulatory Theory of the Mechanics of Atoms and Molecules*. Phys. Rev. **28**, 1049 (1926).

[66] M. Born and R. Oppenheimer, *Zur Quantentheorie der Molekeln*. Ann. Phys. (Leipzig) **84**, 457 (1927).

[67] H. Hellmann, *Einführung in die Quantenchemie* (Deuticke, Leipzig, 1937).

[68] R. P. Feynman, *Forces in Molecules*. Phys. Rev. **56**, 340 (1939).

[69] J. W. Rayleigh, *In Finding the Correction for the Open End of an Organ-Pipe*. Phil. Trans. **161**, 77 (1870).

[70] W. Ritz, *Über eine neue Methode zur Lösung gewisser Variationsprobleme der mathematischen Physik*. J. reine angew. Math. **135**, 1 (1908).

[71] D. R. Hartree, *The wave mechanics of an atom with a non-Coulomb central field. Part I: Theory and methods*. Proc. Cambridge Phil. Soc. **24**, 89 (1928).

[72] W. Pauli, *On the connection of the arrangement of electron groups in atoms with the complex structure of spectra*. Z. Phys. **31**, 765 (1925).

[73] V. Fock, *Näherungsmethode zur Lösung des quantenmechanischen Mehrkörperproblems*. Z. Phys. **61**, 126 (1930).

[74] J. C. Slater, *The Theory of Complex Spectra*. Phys. Rev. **34**, 1293 (1929).

[75] J. M. Thijssen, *Computational Physics* (Cambridge Univ. Press, Cambridge, 1999).

[76] H. Eschrig, *The Fundamentals of Density Functional Theory* (Teubner, Stuttgart, 1996).

[77] J. C. Slater, *A Simplification of the Hartree-Fock Method*. Phys. Rev. **81**, 385 (1951).

[78] H. Englisch and R. Englisch, *Hohenberg-Kohn theorem and non-V-representable densities*. Physica A **121**, 253 (1983).

[79] M. Levy, *Universal variational functionals of electron densities, first-order density matrices, and natural spin-orbitals and solution of the v-representability problem*. Proc. Natl. Acad. Sci. USA **76**, 6062 (1979).

[80] M. Levy, *Electron densities in search of Hamiltonians*. Phys. Rev. A **26**, 1200 (1982).

[81] E. H. Lieb, *Density Functionals for Coulomb Systems*. Int. J. Quant. Chem. **24**, 243 (1983).

[82] G. Vignale and M. Rasolt, *Density-functional theory in strong magnetic fields*. Phys. Rev. Lett. **59**, 2360 (1987).

[83] U. von Barth and L. Hedin, *A local exchange-correlation potential for the spin-polarized case: I*. J. Phys. C **5**, 1629 (1972).

[84] R. O. Jones and O. Gunnarsson, *The density functional formalism, its applications and prospects*. Rev. Mod. Phys. **61**, 689 (1989).

[85] L. H. Thomas, *The calculation of atomic fields*. Proc. Cambridge Phil. Soc. **23**, 542 (1927).

[86] E. Fermi, *Eine statistische Methode zur Bestimmung einiger Eigenschaften des Atoms und ihre Anwendung auf die Theorie des periodischen Systems der Elemente*. Z. Phys. **48**, 73 (1928).

[87] E. Teller, *On the Stability of Molecules in the Thomas-Fermi Theory*. Rev. Mod. Phys. **34**, 627 (1962).

[88] P. A. M. Dirac, *Exchange phenomena in the Thomas atom*. Proc. Cambridge Phil. Soc. **26**, 376 (1930).

[89] C. F. von Weizsäcker, *Zur Theorie der Kernmassen*. Z. Phys. **96**, 431 (1935).

[90] R. M. Dreizler and E. K. U. Gross, *Density Functional Theory* (Springer, Berlin, 1990).

[91] N. D. Mermin, *Thermal Properties of the Inhomogeneous Electron Gas*. Phys. Rev. **137**, A1441 (1965).

[92] N. Ashcroft and N. Mermin, *Solid state physics* (Saunders College, Philadelphia, 1976).

[93] M. J. Gillan, *Calculation of the vacancy formation energy in aluminium*. J. Phys.: Condens. Matter **1**, 689 (1989).

[94] M. C. Payne, M. P. Teter, D. C. Allan, T. A. Arias, and J. D. Joannopoulos, *Iterative minimization techniques for ab initio total-energy calculations: molecular dynamics and conjugate gradients*. Rev. Mod. Phys. **64**, 1045 (1992).

[95] R. Car and M. Parrinello, *Unified Approach for Molecular Dynamics and Density-Functional Theory*. Phys. Rev. Lett. **55**, 2471 (1985).

[96] D. C. Langreth and J. P. Perdew, *Exchange-correlation energy of a metallic surface: Wave-vector analysis*. Phys. Rev. B **15**, 2884 (1977).

[97] O. Gunnarsson and B. I. Lundqvist, *Exchange and correlation in atoms, molecules, and solids by the spin-density-functional formalism*. Phys. Rev. B **13**, 4274 (1976).

[98] J. Kohanoff, *Electronic Structure Calculations for Solids and Molecules* (Cambridge Univ. Press, Cambridge, 2006).

[99] R. M. Martin, *Electronic Structure* (Cambridge Univ. Press, Cambridge, 2004).

[100] J. P. Perdew, *Accurate Density Functional for the Energy: Real-Space Cutoff of the Gradient Expansion for the Exchange Hole*. Phys. Rev. Lett. **55**, 1665 (1985).

[101] J. P. Perdew and A. Zunger, *Self-interaction correction to density-functional approximations for many-electron systems*. Phys. Rev. B **23**, 5048 (1981).

[102] S. Vosko, L. Wilk, and M. Nusair, *Accurate spin-dependent electron liquid correlation energies for local spin density calculations: a critical analysis*. Can. J. Phys. **58**, 1200 (1980).

[103] M. Gell-Mann and K. A. Brueckner, *Correlation Energy of an Electron Gas at High Density*. Phys. Rev. **106**, 364 (1957).

[104] D. M. Ceperley and B. J. Alder, *Ground State of the Electron Gas by a Stochastic Method*. Phys. Rev. Lett. **45**, 566 (1980).

[105] J. P. Perdew, J. A. Chevary, S. H. Vosko, K. A. Jackson, M. R. Pederson, D. J. Singh, and C. Fiolhais, *Atoms, molecules, solids, and surfaces: Applications of the generalized gradient approximation for exchange and correlation*. Phys. Rev. B **46**, 6671 (1992).

[106] J. P. Perdew and Y. Wang, *Accurate and simple analytic representation of the electron-gas correlation energy*. Phys. Rev. B **45**, 13244 (1992).

[107] J. P. Perdew, K. Burke, and M. Ernzerhof, *Generalized Gradient Approximation Made Simple*. Phys. Rev. Lett. **77**, 3865 (1996).

[108] B. Hammer, L. B. Hansen, and J. K. Nørskov, *Improved adsorption energetics within density-functional theory using revised Perdew-Burke-Ernzerhof functionals*. Phys. Rev. B **59**, 7413 (1999).

[109] J. P. Perdew, S. Kurth, A. Zupan, and P. Blaha, *Accurate Density Functional with Correct Formal Properties: A Step Beyond the Generalized Gradient Approximation*. Phys. Rev. Lett. **82**, 2544 (1999).

[110] J. P. Perdew, *Accurate Density Functional for the Energy: Real-Space Cutoff of the Gradient Expansion for the Exchange Hole*. Phys. Rev. Lett. **55**, 1665 (1985).

[111] E. K. U. Gross and R. M. Dreizler, *Gradient expansion of the Coulomb exchange energy*. Z. Phys. **302**, 103 (1981).

[112] T. Koopmans, *Über die Zuordnung von Wellenfunktionen und Eigenwerten zu den einzelnen Elektronen eines Atoms*. Physica **1**, 104 (1934).

[113] M. Levy, J. P. Perdew, and V. Sahni, *Exact differential equation for the density and ionization energy of a many-particle system*. Phys. Rev. A **30**, 2745 (1984).

[114] F. Bloch, *Über die Quantenmechanik der Elektronen in Kristallgittern*. Z. Phys. **52**, 555 (1929).

[115] M. Born and T. von Kármán, *On fluctuations in spatial grids*. Phys. Z. **13**, 297 (1912).

[116] A. Anderson, *Canonical Transformations in Quantum Mechanics*. Ann. Phys. **232**, 292 (1994).

[117] E. J. Walter, M. Barnes, J. E. Anderson, A. M. Rappe, G. Theurich, and M. Tucker, *Opium Open-source Pseudopotential Generator V. 3.1.* `http://opium.sourceforge.net`.

[118] W. E. Pickett, *Pseudopotential methods in condensed matter applications.* Comput. Phys. Rep. **9**, 115 (1989).

[119] L. Kleinman and D. M. Bylander, *Efficacious Form for Model Pseudopotentials.* Phys. Rev. Lett. **48**, 1425 (1982).

[120] S. G. Louie, S. Froyen, and M. L. Cohen, *Nonlinear ionic pseudopotentials in spin-density-functional calculations.* Phys. Rev. B **26**, 1738 (1982).

[121] D. R. Hamann, M. Schlüter, and C. Chiang, *Norm-Conserving Pseudopotentials.* Phys. Rev. Lett. **43**, 1494 (1979).

[122] N. Troullier and J. L. Martins, *Efficient pseudopotentials for plane-wave calculations.* Phys. Rev. B **43**, 1993 (1991).

[123] D. Vanderbilt, *Soft self-consistent pseudopotentials in a generalized eigenvalue formalism.* Phys. Rev. B **41**, 7892 (1990).

[124] P. E. Blöchl, *Projector augmented-wave method.* Phys. Rev. B **50**, 17953 (1994).

[125] B. Hetényi, F. D. Angelis, P. Giannozzi, and R. Car, *Reconstruction of frozen-core all-electron orbitals from pseudo-orbitals.* J. Chem. Phys. **115**, 5791 (2001).

[126] S. Baroni, S. de Gironcoli, A. Dal Corso, and P. Giannozzi *et al.*, *PWSCF*: *Plane-Wave Self-Consistent Field.* `http://www.pwscf.org`.

[127] G. Kresse and J. Furthmüller, *Efficient iterative schemes for ab initio total-energy calculations using a plane-wave basis set.* Phys. Rev. B **54**, 11169 (1996).

[128] A. Sommerfeld, *Wave Mechanics* (Dutton, New York, 1929).

[129] P. A. M. Dirac, *The principles of quantum mechanics* (Clarendon, Oxford, 1958).

[130] H. H. Jensen, *Introductory Lectures on the Free Phonon Field.* In T. A. Bak (Ed.), *Phonons and Phonon Interactions* (W. A. Benjamin, New York, 1964).

[131] J. M. Ziman, *Electrons and Phonons: The Theory of Transport Phenomena in Solids* (Clarendon, Oxford, 1962).

[132] M. Born and K. Huang, *Dynamical Theory of Crystal Lattices* (Clarendon, Oxford, 1954).

[133] W. Frank, C. Elsässer, and M. Fähnle, *Ab initio Force-Constant Method for Phonon Dispersions in Alkali Metals*. Phys. Rev. Lett. **74**, 1791 (1995).

[134] G. J. Ackland, M. C. Warren, and S. J. Clark, *Practical methods in ab initio lattice dynamics*. J. Phys.: Condens. Matter **9**, 7861 (1997).

[135] G. Kresse, J. Furthmüller, and J. Hafner, *Ab initio Force Constant Approach to Phonon Dispersion Relations of Diamond and Graphite*. Europhys. Lett. **32**, 729 (1995).

[136] K. Parlinski, Z. Q. Li, and Y. Kawazoe, *First-Principles Determination of the Soft Mode in Cubic ZrO_2*. Phys. Rev. Lett. **78**, 4063 (1997).

[137] N. E. Zeĭn, *Density functional calculations of elastic moduli and phonon spectra of crystals*. Sov. Phys. Solid State **26**, 1825 (1984).

[138] S. Baroni, P. Giannozzi, and A. Testa, *Green's-function approach to linear response in solids*. Phys. Rev. Lett. **58**, 1861 (1987).

[139] X. Gonze, *Adiabatic density-functional perturbation theory*. Phys. Rev. A **52**, 1096 (1995).

[140] K. Parlinski, *PHONON V. 4.24* (Cracow, 2005).

[141] L. I. Schiff, *Quantum Mechanics*. 3rd ed. (McGraw-Hill, New York, 1968).

[142] S. de Gironcoli, *Lattice dynamics of metals from density-functional perturbation theory*. Phys. Rev. B **51**, 6773 (1995).

[143] P. Ehrenfest, *Bemerkung über die angenäherte Gültigkeit der klassischen Mechanik innerhalb der Quantenmechanik*. Z. Phys. **45**, 455 (1927).

[144] V. I. Goldanskii, *The role of the tunnel effect in the kinetics of chemical reactions at low temperatures*. Dokl. Akad. Nauk SSSR **124**, 1261 (1959).

[145] V. I. Goldanskii, *Tunnel transitions between systems described by morse potential curves*. Dokl. Akad. Nauk SSSR **127**, 1037 (1959).

[146] V. I. Goldanskii, *Role of tunneling in low-temperature chemical reactions*. Annu. Rev. Phys. Chem. **27**, 85 (1976).

[147] A. F. Voter, *Hyperdynamics: Accelerated Molecular Dynamics of Infrequent Events*. Phys. Rev. Lett. **78**, 3908 (1997).

[148] E. Wigner, *Calculation of the Rate of Elementary Association Reactions*. J. Chem. Phys. **5**, 720 (1937).

[149] J. Horiuti, *On the Statistical Mechanical Treatment of the Absolute Rate of Chemical Reaction*. Bull. Chem. Soc. Jpn. **13**, 210 (1938).

[150] D. G. Truhlar and B. C. Garrett, *Variational Transition State Theory*. Annu. Rev. Phys. Chem. **35**, 159 (1984).

[151] D. Chandler, *Statistical mechanics of isomerization dynamics in liquids and the transition state approximation*. J. Chem. Phys. **68**, 2959 (1978).

[152] J. C. Keck, *Variational Theory of Reaction Rates*. Adv. Chem. Phys. **13**, 85 (1967).

[153] M. G. Evans, *Thermodynamical treatment of transition state*. Trans. Faraday Soc. **34**, 49 (1938).

[154] G. Mills, H. Jónsson, and G. K. Schenter, *Reversible work transition state theory: application to dissociative adsorption of hydrogen*. Surf. Sci. **324**, 305 (1995).

[155] G. H. Vineyard, *Frequency Factors and Isotope Effects in Solid State Rate Processes*. J. Phys. Chem. Solids **3**, 121 (1957).

[156] C. Wert and C. Zener, *Interstitial Atomic Diffusion Coefficients*. Phys. Rev. **76**, 1169 (1949).

[157] S. Arrhenius, *On the reaction rate of the inversion of non-refined sugar upon souring*. Z. Phys. Chem. **4**, 226 (1889).

[158] G. Henkelman and H. Jónsson, *A dimer method for finding saddle points on high dimensional potential surfaces using only first derivatives*. J. Chem. Phys. **111**, 7010 (1999).

[159] R. Malek and N. Mousseau, *Dynamics of Lennard-Jones clusters: A characterization of the activation-relaxation technique*. Phys. Rev. E **62**, 7723 (2000).

[160] P. Deglmann and F. Furche, *Efficient characterization of stationary points on potential energy surfaces*. J. Chem. Phys. **117**, 9535 (2002).

[161] L. J. Munro and D. J. Wales, *Defect migration in crystalline silicon*. Phys. Rev. B **59**, 3969 (1999).

[162] G. Henkelman, B. P. Uberuaga, and H. Jónsson, *A climbing image nudged elastic band method for finding saddle points and minimum energy paths*. J. Chem. Phys. **113**, 9901 (2000).

[163] H. Jónsson, G. Mills, and K. W. Jacobsen, *Nudged elastic band method for finding minimum energy paths of transitions*. In B. J. Berne, G. Ciccotti, and D. F. Coker (Eds.), *Classical and Quantum Dynamics in Condensed Phase Simulations* (World Scientific, Singapore, 1998).

[164] G. Henkelman and H. Jónsson, *Improved tangent estimate in the nudged elastic band method for finding minimum energy paths and saddle points*. J. Chem. Phys. **113**, 9978 (2000).

[165] P. Maragakis, S. A. Andreev, Y. Brumer, D. R. Reichman, and E. Kaxiras, *Adaptive nudged elastic band approach for transition state calculation*. J. Chem. Phys. **117**, 4651 (2002).

[166] *Campos Atomic Simulation Environment.* `https://wiki.fysik.dtu.dk/ase`; S. Bahn and K. W. Jacobsen, *An object-oriented scripting interface to a legacy electronic structure code.* Comput. Sci. Eng. **4**, 56 (2002).

[167] O. H. Nielsen and R. M. Martin, *Quantum-mechanicle theory of stress and force*. Phys. Rev. B **32**, 3780 (1985).

[168] T. Hahn (Ed.), *International Tables for Crystallography*, vol. A. 4th rev. ed. (Kluwer, Dordrecht, 1995).

[169] R. W. G. Wyckoff, *Crystal Structures* (Interscience, New York, 1963).

[170] C. G. Broyden, *Quasi-Newton Methods and their Application to Function Minimisation*. Math. Comput. **21**, 368 (1967).

[171] G. Kresse and D. Joubert, *From ultrasoft pseudopotentials to the projector augmented-wave method*. Phys. Rev. B **59**, 1758 (1999).

[172] H. J. Monkhorst and J. D. Pack, *Special points for Brillouin-zone integrations*. Phys. Rev. B **13**, 5188 (1976).

[173] B. G. Pfrommer, M. Côté, S. G. Louie, and M. L. Cohen, *Relaxation of crystals with the quasi-Newton method*. J. Comput. Phys. **131**, 233 (1997).

[174] E. Rönnebro, D. Noréus, K. Kadir, A. Reiser, and B. Bogdanović, *Investigation of the perovskite related structures of $NaMgH_3$, $NaMgF_3$ and Na_3AlH_6*. J. Alloys Compd. **299**, 101 (2000).

[175] H. König and R. Hoppe, *Borates of alkaline-metals: 2. Knowledge of LiB_3O_5*. Z. Anorg. Allg. Chem. **439**, 71 (1978).

[176] C. Chen, Y. Wu, A. Jiang, B. Wu, G. You, R. Li, and S. Lin, *New nonlinear-optical crystal: LiB_3O_5*. J. Opt. Soc. Amer. **B6**, 616 (1989).

[177] F. Filippone and M. Parrinello, *Vibrational analysis from linear response theory*. Chem. Phys. Lett. **345**, 179 (2001).

[178] R. F. W. Bader, *Atoms in Molecules — A Quantum Theory* (Oxford Univ. Press, Oxford, 1990).

[179] G. Henkelman, A. Arnaldsson, and H. Jónsson, *A fast and robust algorithm for Bader decomposition of charge density*. Comput. Mater. Sci. **36**, 254 (2006).

[180] E. Sanville, S. D. Kenny, R. Smith, and G. Henkelman, *Improved grid-based algorithm for Bader charge allocation*. J. Comput. Chem. **28**, 899 (2007).

[181] *Minpack* (University of Chicago, 1999).

[182] J. Graetz, Y. Lee, J. J. Reilly, S. Park, and T. Vogt, *Structures and thermodynamics of the mixed alkali alanates*. Phys. Rev. B **71**, 184115 (2005).

[183] M. H. Sorby, H. W. Brinks, A. Fossdal, K. Thorshaug, and B. C. Hauback, *The crystal structure and stability of K_2NaAlH_6*. J. Alloys Compd. **415**, 284 (2006).

[184] P. D. Desai, *Thermodynamic properties of aluminum*. Int. J. Thermophys. **8**, 621 (1987).

[185] X. Ke and I. Tanaka, *Decomposition reactions for $NaAlH_4$, Na_3AlH_6, and NaH: First-principles study*. Phys. Rev. B **71**, 024117 (2005).

[186] Y. Komura and K. Tokunaga, *Structural studies of stacking variants in Mg-base Friauf–Laves phases*. Acta Crystallogr., Sect. B: Struct. Crystallogr. Cryst. Chem. **36**, 1548 (1980).

[187] A. Einstein, *Die Plancksche Theorie der Strahlung und die Theorie der spezifischen Wärme*. Ann. Phys. (Leipzig) **22**, 180 (1907).

[188] Y. Nakamori, K. Miwa, A. Ninomiya, H. Li, N. Ohba, S. Towata, A. Züttel, and S. Orimo, *Correlation between thermodynamical stabilities of metal borohydrides and cation electronegativites: First-principles calculations and experiments*. Phys. Rev. B **74**, 045126 (2006).

[189] P. Vajeeston, P. Ravindran, A. Kjekshus, and H. Fjellvåg, *High hydrogen content complex hydrides: A density-functional study.* Appl. Phys. Lett. **89**, 071906 (2006).

[190] V. Ozoliņš, E. H. Majzoub, and C. Wolverton, *First-Principles Prediction of a Ground State Crystal Structure of Magnesium Borohydride.* Phys. Rev. Lett. **100**, 135501 (2008).

[191] B. Dai, D. S. Sholl, and J. K. Johnson, *First-Principles Study of Experimental and Hypothetical $Mg(BH_4)_2$ Crystal Structures.* J. Phys. Chem. C **112**, 4391 (2008).

[192] E. H. Majzoub and V. Ozoliņš, *Prototype electrostatic ground state approach to predicting crystal structures of ionic compounds: Application to hydrogen storage materials.* Phys. Rev. B **77**, 104115 (2008).

[193] M. J. van Setten, G. A. de Wijs, M. Fichtner, and G. Brocks, *A Density Functional Study of α-$Mg(BH_4)_2$.* Chem. Mater. **20**, 4952 (2008).

[194] K. Momma and F. Izumi, *VESTA: a three-dimensional visualization system for electronic and structural analysis.* J. Appl. Crystallogr. **41**, 653 (2008).

[195] T. Matsunaga, F. Buchter, K. Miwa, S. Towata, S. Orimo, and A. Züttel, *Magnesium borohydride: A new hydrogen storage material.* Renew. Energ. **33**, 193 (2008).

[196] E. A. Nickels, M. O. Jones, W. I. F. David, S. R. Johnson, R. L. Lowton, M. Sommariva, and P. P. Edwards, *Tuning the Decomposition Temperature in Complex Hydrides: Synthesis of a Mixed Alkali Metal Borohydride.* Angew. Chem. Int. Ed. **120**, 2859 (2008).

[197] O. M. Løvvik, O. Swang, and S. M. Opalka, *Modeling alkali alanates for hydrogen storage by density-functional band-structure calculations.* J. Mater. Res. **20**, 3199 (2005).

[198] M. J. van Setten, G. A. de Wijs, and G. Brocks, *Model for the Formation Energies of Alanates and Boranates.* J. Phys. Chem. C **111**, 9592 (2007).

[199] N. Marzari and D. Vanderbilt, *Maximally localized generalized Wannier functions for composite energy bands.* Phys. Rev. B **56**, 12847 (1997).

[200] A. A. Mostofi, J. R. Yates, Y.-S. Lee, I. Souza, D. Vanderbilt, and N. Marzari, *Wannier90: A Tool for Obtaining Maximally-Localised Wannier Functions.* Comput. Phys. Commun. **178**, 685 (2008).

[201] G. H. Wannier, *Dynamics of Band Electrons in Electric and Magnetic Fields*. Rev. Mod. Phys. **34**, 645 (1962).

[202] E. I. Blount, *Formalisms of Band Theory*. In F. Seitz and D. Turnbull (Eds.), *Solid State Physics*, vol. 13 (Academic, New York, 1962).

[203] Pseudopotentials of von Barth-Car type from `http://www.quantum-espresso.org`.

[204] A. Kokalj, *XCrySDen — a new program for displaying crystalline structures and electron densities*. J. Mol. Graph. Model. **17**, 176 (1999).

[205] P. Claudy, B. Bonnetot, J.-P. Bastide, and J.-M. Létoffé, *Reactions of lithium and sodium aluminium hydride with sodium or lithium hydride. Preparation of a new alumino-hydride of lithium and sodium* $LiNa_2AlH_6$. Mat. Res. Bull **17**, 1499 (1982).

[206] E. H. Majzoub and K. J. Gross, *Titanium-halide catalyst-precursors in sodium aluminum hydrides*. J. Alloys Compd. **356**, 363 (2003).

[207] D. Sun, T. Kiyobayashi, H. T. Takeshita, N. Kuriyama, and C. M. Jensen, *X-ray diffraction studies of titanium and zirconium doped* $NaAlH_4$*: elucidation of doping induced structural changes and their relationship to enhanced hydrogen storage properties*. J. Alloys Compd. **337**, L8 (2002).

[208] O. Palumbo, R. Cantelli, A. Paolone, C. M. Jensen, and S. S. Srinivasan, *Motion of point defects and monitoring of chemical reactions in sodium aluminium hydride*. J. Alloys Compd. **404**, 748 (2005).

[209] O. Palumbo, A. Paolone, R. Cantelli, C. M. Jensen, and M. Sulic, *Fast H-vacancy Dynamics during Alanate Decomposition by Anelastic Spectroscopy. Proposition of a Model for Ti-enhanced Hydrogen Transport*. J. Phys. Chem. B **110**, 9105 (2006).

[210] J. W. Lauher, *Sodium Tetrahydroaluminate*. Acta Crystallogr., Sect. B: Struct. Crystallogr. Cryst. Chem. **35**, 1454 (1979).

[211] R. R. Roy and B. P. Nigam, *Nuclear Physis: Theory and Experiment* (Wiley, New York, 1967).

[212] R. Hempelmann, *Quasielastic Neutron Scattering and Solid State Diffusion* (Clarendon, Oxford, 2000).

[213] G. L. Squires, *Introduction to the Theory of Thermal Neutron Scattering* (Cambridge Univ. Press, Cambridge, 1978).

[214] C. T. Chudley and R. J. Elliott, *Neutron Scattering from a Liquid on a Jump Diffusion Model*. Proc. Phys. Soc. **77**, 353 (1961).

[215] M. Bée, *Quasielastic Neutron Scattering* (Hilger, Bristol, 1988).

[216] O. M. Løvvik and S. M. Opalka, *Stability of Ti in $NaAlH_4$*. Appl. Phys. Lett. **88**, 161917 (2006).

[217] S. Li, P. Jena, and R. Ahuja, *Effect of Ti and metal vacancies on the electronic structure, stability, and dehydrogenation of Na_3AlH_6: Supercell band-structure formalism and gradient-corrected density-functional theory*. Phys. Rev. B **73**, 214107 (2006).

[218] O. Bender and K. Schroeder, *Theory of Mössbauer line broadening due to diffusion of Mössbauer atoms via vacancies*. Phys. Rev. B **19**, 3399 (1979).

[219] M. E. Björketun, P. G. Sundell, G. Wahnström, and D. Engberg, *A kinetic Monte Carlo study of proton diffusion in disordered perovskite structured lattices based on first-principles calculations*. Solid State Ionics **176**, 3035 (2005).

[220] T. J. Frankcombe and G.-J. Kroes, *Quasiharmonic approximation applied to $LiBH_4$ and its decomposition products*. Phys. Rev. B **73**, 174302 (2006).

[221] J. E. Schirber and B. Morosin, *Lattice constants of β-PdH_x and β-PdD_x with x near 1.0*. Phys. Rev. B **12**, 117 (1975).

[222] P. P. Ewald, *Die Berechnung optischer und elektrostatischer Gitterpotentiale*. Ann. Phys. (Leipzig) **64**, 253 (1921).

[223] J. L. Birman, *Calculation of coulomb crystal potentials*. J. Phys. Chem. Solids **6**, 65 (1958).

Paper P1

Symmetry enhanced convergence of crystal structure optimization

Johannes Voss [ab] * Tejs Vegge [a]

[a] Materials Research Department, Risø National Laboratory for Sustainable Energy, Technical University of Denmark, 4000 Roskilde, Denmark

[b] Center for Atomic-scale Materials Design, Department of Physics, Technical University of Denmark, 2800 Kongens Lyngby, Denmark

Abstract

We present a computational scheme for optimization of crystal coordinates, where the Wyckoff positions are considered as the only degrees of freedom for the atomic coordinates. The method is particularly efficient for optimizing structures with large or ill-defined unit cells. Example cases are presented, which show a faster and more stable convergence of a quasi-Newton relaxation of the atomic coordinates using the approach presented here compared to an optimization considering all atomic coordinates as degrees of freedom. Furthermore, symmetry breaking parameters can easily be introduced and optimized simultaneously with the Wyckoff coordinates.

Keywords: structure optimization, enhanced convergence, quasi-Newton, crystal symmetry, space group, LiB_3O_5, Na_3AlH_6, $Mg(BH_4)_2$, ab-initio, first principles, electronic structure
PACS: 02.60.Pn, 61.50.Ah, 31.15.-p

Preprint submitted to Elsevier,
J. Comp. Phys. http://www.elsevier.com/locate/jcp

*Electronic address: johannes.voss@risoe.dk

1 Introduction

The symmetries of crystals can be classified by 7 crystal systems, from triclinic with lowest symmetry to cubic systems. These 7 systems can be furthermore divided into up to four subsystems each with respect to the allowed lattice centerings (primitive, base-, body-, and face-centered), yielding 14 Bravais lattices. In combination with the 32 crystallographic point groups and compound symmetry operations, this totals in 230 space groups (1). R. W. G. Wyckoff (2) introduced a simple way of describing these crystal symmetries by relating symmetrically equivalent atomic coordinates by linear equations in the coordinates in the basis of the lattice vectors.

Using computer simulations to obtain the exact atomic configuration which minimizes the total energy is important, *e.g.* to verify coordinates obtained from powder diffraction data coordinates of light elements. The computationally optimized configuration is the starting point for further analysis, *e.g.* the energetic comparison of different phases, the calculation of the phonon dispersion and free energies, etc.

We use Wyckoff's compact equations to project the total energy gradient, calculated using *e.g. ab-initio* methods, onto the so-called Wyckoff coordinate system. From this minimal system of coordinates, all atomic coordinates in the unit cell are generated using Wyckoff's simple equations mentioned above. This subsystem-projected gradient is followed, minimizing the total energy in order to find the equilibrium coordinates. Apart from ensuring symmetry to be maintained throughout the relaxation process in the presence of deviations from symmetry in the forces (due to limited numerical accuracy or electronic structure calculation implementations not conserving symmetry), a quasi-Newton based optimization of the Wyckoff coordinates following the corresponding projected gradient is found to be generally faster than a direct optimization of all coordinates.

This type of optimization is often very time consuming, in particular for large systems, and methods which provide a general speed-up of the convergence are therefore interesting.

2 Method

For a system containing N atoms in the unit cell with the symmetries for the atomic coordinates given by $3n$ Wyckoff coordinates, we define $\boldsymbol{W}(w_{i,\alpha}) \in \mathbb{R}^{3N}$ to be the full crystallographic coordinate system generated from the Wyckoff coordinates $w_{i,\alpha}$ ($i \in \{1, ..., n\}$, $\alpha \in \{1, 2, 3\}$). We require $\boldsymbol{W}(w_{i,\alpha})$ to generate coordinates with the correct symmetries, even if the Wyckoff input parameters $w_{i,\alpha}$ are not compatible with the symmetry, *i.e.* incorrect input parameters are adjusted.

A gradient in the space of the Wyckoff coordinates $w_{i,\alpha}$ of the total energy E can be calculated from the total energy gradient $\boldsymbol{\nabla} E\left[\boldsymbol{W}(w_{i,\alpha})\right]$ for the full coordinate system:

$$\begin{aligned}\frac{\partial E}{\partial w_{j,\alpha}} := \frac{1}{\varepsilon}\Big(&\boldsymbol{W}(w_{1,1}, ..., w_{j,\alpha} + \varepsilon, ..., w_{n,3}) \\ &-\boldsymbol{W}(w_{1,1}, ..., w_{j,\alpha}, ..., w_{n,3})\,, \\ &\boldsymbol{\nabla} E\left[\boldsymbol{W}(w_{i,\alpha})\right]\Big), \end{aligned} \tag{1}$$

where $(\,,\,) : \mathbb{R}^{3N} \times \mathbb{R}^{3N} \mapsto \mathbb{R}$ denotes the dot product and ε is a small displacement. Note that the gradient (1) does not depend on the magnitude of ε. The gradient $\boldsymbol{\nabla} E\left[\boldsymbol{W}(w_{i,\alpha})\right]$ is calculated efficiently using classical electrostatics for the undisplaced configuration only, since 1^{st} order errors in the wave functions only result in 2^{nd} order errors in the electronic eigenenergies, according to the Hellmann-Feynman theorem (3; 4). For *ab-initio* approaches, like *e.g.* density functional

theory (DFT) (5), the computational effort for evaluating Eq. (1) for each ionic optimization step is negligible compared to the effort for the electronic structure calculation.

Since $\boldsymbol{W}$ generates coordinates which obey the symmetry of the space group, following the gradient (1) and using the Wyckoff coordinates $w_{i,\alpha}$ as only degrees of freedom, the symmetry is maintained, even if the numerically calculated total energy gradient $\boldsymbol{\nabla} E\left[\boldsymbol{W}(w_{i,\alpha})\right]$ is deviating from the symmetry due to broken symmetries in the implementation of the electronic structure calculation or due to numerical inaccuracies. For fixed Wyckoff coordinates $w_{i,\alpha}$, *e.g.*, Eq. (1) is exactly zero, because $\boldsymbol{W}(w_{i,\alpha})$ only generates displaced configurations which are in agreement with the symmetries.

Here, we optimize the Wyckoff coordinates $w_{i,\alpha}$ using a quasi-Newton method with Broyden-Fletcher-Goldfarb-Shanno (6; 7; 8; 9) Hessian update, which is efficient for structure optimization problems (10; 11; 12). With a symmetric guess for the initial Hessian, this method does not break the crystal symmetry (10). We are therefore able to compare the Wyckoff coordinate optimization approach presented here to a relaxation which follows the total energy gradient $\boldsymbol{\nabla} E\left[\boldsymbol{W}(w_{i,\alpha})\right]$ directly, relying on the symmetries in the forces to maintain the crystal symmetry throughout the optimization process.

Due to the optimization of the Wyckoff coordinates $w_{i,\alpha}$ using the gradient (1), a typical guess for the initial Hessian matrix, *e.g.* a scalar matrix, yields a different scaling of the search direction components than for a standard quasi-Newton optimization using the total energy gradient $\boldsymbol{\nabla} E\left[\boldsymbol{W}(w_{i,\alpha})\right]$. The reason being that, according to Eq. (1), displacing a Wyckoff coordinate means the simultaneous displacement of all corresponding symmetrically equivalent sites. We find the constrained symmetry and different gradient/Hessian scaling to result in improved convergence properties for structure relaxation based on a quasi-Newton optimization.

3 Computational Setups

To test the general applicability of the implementation, we have calculated total energies and gradients using two widely used DFT (5) codes: Dacapo (13) for the Na_3AlH_6 example and the Vienna Ab-initio Simulation Package (VASP) (14) for the remaining structures. The Kohn-Sham wave functions (15) were expanded in planewave basis sets with cut-off energies of 350 eV. The electronic Brioullin zones were sampled with mesh spacings of ≤ 0.05 Å^{-1}. The Perdew-Wang-91 exchange-correlation functional (16; 17) was used for all calculations. For Dacapo, ultrasoft pseudopotentials (18) were used to describe the ionic cores, while for VASP, projector-augmented wave (19) potentials (20) were used. The coordinate optimization was implemented and performed within the CAMPOS Atomic Simulation environment (21).

4 Examples

In the following we present a comparison of the Wyckoff coordinate relaxation and the common total energy gradient based atomic coordinate relaxation. The examples are chosen to reflect the applicability to different classes of materials with complex structures, where many Wyckoff coordinates $w_{i,\alpha}$ are not fixed by symmetry and must therefore be optimized.

4.1 Na_3AlH_6

Na_3AlH_6, crystallizing in space group $P2_1/n$ (22), is an intermediate product in the decomposition of $NaAlH_4$ (23), which has become a model system for the study of metal complex hydrides as candidates

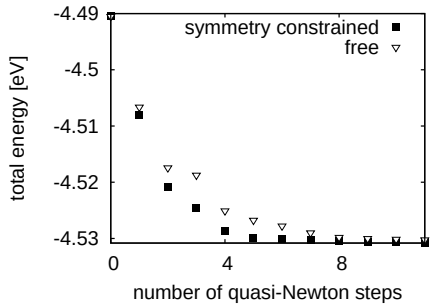

Fig. 1. Internal coordinate optimization of $P2_1/n$-Na_3AlH_6 starting from powder diffraction coordinates for Na_3AlD_6 (22), both with and without numerically constrained crystal symmetries. Total energies are specified per crystallographic unit cell with respect to the cohesive energies of the constituting elements.

for reversible hydrogen storage (24; 25; 26; 27; 28). Fig. 1 shows the convergence of the total energy for this system starting from coordinates based on powder diffraction data (22). The constrained relaxation of the Wyckoff coordinates is faster and more monotonous than the free relaxation of all coordinates. To reach 3‰ deviance from the final converged total energy, *e.g.*, the constrained relaxation requires 4 steps, while the free relaxation requires 7 quasi-Newton steps.

4.2 LiB_3O_5

LiB_3O_5, which crystallizes in space group $Pna2_1$ (29), is of special interest as a nonlinear optical crystal (30; 31; 32; 33). The convergence of the Wyckoff coordinate optimization is much faster for the first few steps compared to the free relaxation (Fig. 2). After step 10, where the energy already is in a 0.6‰ window of the converged energy, the behavior of the Wyckoff optimization becomes non-monotonous. In this (special) case, the Wyckoff optimization is converging more slowly than the free relaxation very close to convergence of the total

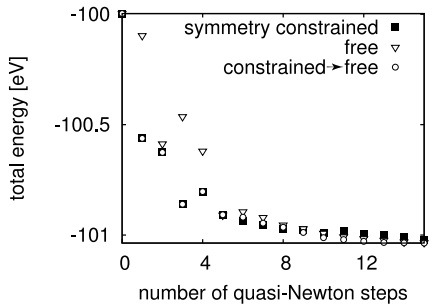

Fig. 2. Symmetry constrained and unconstrained coordinate optimization of $Pna2_1$-LiB_3O_5 starting with pre-optimized lattice constants, and a combined symmetry constrained optimization switching after step 5 to free relaxation. Total energies are specified per crystallographic unit cell with respect to the cohesive energies of the constituting elements.

energy. If very low, relaxed forces on the atoms are required, the Wyckoff coordinates should be used only for an initial amount of steps before switching to a free relaxation. Here, we have optimized the Wyckoff coordinates until the average force on the ionic cores has become 0.1 eV/Å. The Hessian information obtained during these first 5 steps is re-used by extending the diagonal elements (dividing the elements by the number of symmetrically equivalent sites) to the diagonal of a guess for the Hessian of the full atomic coordinate system. This combined relaxation process has a fast convergence and is monotonous close to convergence as well (Fig. 2).

4.3 $Mg(BH_4)_2$

The proposed method is found to have the most pronounced effect on very large systems. A proposed high-temperature phase of the promising hydrogen storage material $Mg(BH_4)_2$ in space group $Fddd$ (34; 35; 36), has a very large unit cell, containing 176 atoms in the primitive unit cell (704 atoms in the crystallographic unit cell). For systems of this magnitude, a fast coordinate optimization scheme is

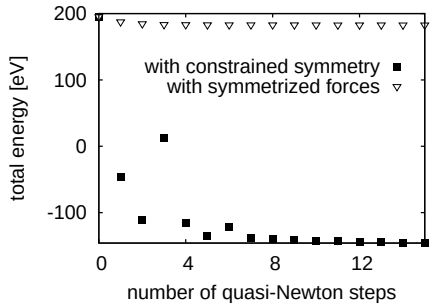

Fig. 3. Constrained and free coordinate optimization of $Fddd$-$Mg(BH_4)_2$ starting from diffraction pattern coordinates (34). Total energies are specified per crystallographic unit cell with respect to the cohesive energies of the constituting elements.

crucial, in order to minimize the number of force calculations needed to find the equilibrium configuration. Fig. 3 shows the Wyckoff coordinate and free relaxation for this system. We note, that the total energy gradient has been symmetrized as implemented in VASP (14), to overcome the slightly broken symmetries due to the DFT implementation. Nevertheless, the small remaining imperfections in the restored symmetries lead to a small drift in the coordinates for the free relaxation, which for large systems and for ill-defined input parameters, leads to a loss of symmetry and to a hindrance of convergence (given the inherent difficulty of characterizing hydrogen positions experimentally, a standard approach to optimizing such a large system would be an initial optimization of the hydrogen coordinates only). The Wyckoff coordinate relaxation on the other hand converges well. The sum over symmetrically equivalent displaced sites in the gradient (1) is a symmetrization of the forces, such that the approach presented here does not depend on a symmetrization of the total energy gradient on the side of the electronic structure calculation.

Furthermore, the $Fddd$ phase is considered only to be an idealized phase of $Mg(BH_4)_2$; the 'real' phase derived from experiments is proposed to have additional structural disorder with a correlation length

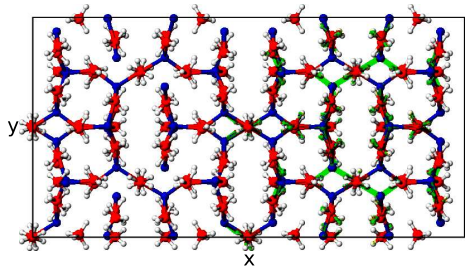

Fig. 4. (Color online.) Unit cell of the *Fddd* phase of $Mg(BH_4)_2$ (Mg is represented by blue, B by red, and H by white spheres). Configurational changes due to a shift of the right half of the unit cell by 0.5 in y-direction are shown in green by thickened lines.

of half a unit cell in x-direction (34). Correspondingly, shifts of half unit cells in y- in z-direction are possible (see Fig. 4). These shifts mean that for $x > 0.5$, the symmetry is broken. Such symmetry violating shifts, which are normally very difficult to treat in calculations, are here simply included as additional parameters into our gradient projection scheme. By displacing all atoms affected by the shift and projecting the total energy gradient on this displacement, a combined Wyckoff plus symmetry breaking parameters quasi-Newton optimization is possible. Starting from arbitrary shifts in y- in z-direction, we find that shifts by 0, ± 0.25, and 0.5 lead to energetic minima. Shifts by ± 0.25 result in an increase in energy by 0.1 eV per formula unit compared to shifts by 0 and 0.5.

5 Conclusion and Outlook

We have developed a crystal structure optimization scheme, where the Wyckoff coordinates are considered as only degrees of freedom for the internal coordinate system. This approach is stable against numerical asymmetries in the forces and generally leads to much faster convergence than a direct relaxation of all coordinates, in particular

for large, ill-defined structures. For a relaxation to very low forces, the symmetry constraints can lead to a slower convergence than a free relaxation. In these cases, the initially fast Wyckoff optimization can be combined with a free relaxation in a quasi-Newton scheme below a convergence cut-off. The implementation of the Wyckoff coordinate optimization is available as a module for the CAMPOS Atomic Simulation Environment (21).

The correction of coordinates to match given crystal symmetries implemented for the gradient projection technique presented here, can be furthermore used to generate symmetric starting guesses based on *e.g.* asymmetric results from molecular dynamics calculations for finite temperatures. The symmetries are re-constructed from those atomic coordinates, which are in a locally optimal configuration, *i.e.* the sites with the lowest forces acting on them are chosen to generate the full crystal coordinate system. A separate tool for crystal structure (re-)generation is available online (37).

Acknowledgments

We acknowledge financial support by the NABIIT program funded by the Danish Research Councils for Strategic Research, and the Danish Center for Scientific Computing (DCSC) for computer time. The Center for Atomic-scale Materials Design is supported by the Lundbeck Foundation.

References

[1] T. Hahn (Ed.), International Tables for Crystallography, 4th Revised Edition, Vol. A, Kluwer, Dordrecht, 1995.

[2] R. W. G. Wyckoff, Crystal Structures, Interscience, New York, 1963.
[3] H. Hellmann, Einführung in die Quantenchemie, Deuticke, Leipzig, 1937.
[4] R. P. Feynman, Phys. Rev. 56 (1939) 340.
[5] P. Hohenberg, W. Kohn, Phys. Rev. 136 (1964) B864.
[6] C. G. Broyden, J. Inst. Math. Appl. 6 (1970) 76.
[7] R. Fletcher, Comput. J. 13 (1970) 317.
[8] D. Goldfarb, Math. Comput. 24 (1970) 23.
[9] D. F. Shanno, Math. Comput. 24 (1970) 647.
[10] B. G. Pfrommer, M. Côté, S. G. Louie, M. L. Cohen, J. Comput. Phys. 131 (1997) 233.
[11] J. Furthmüller, J. Hafner, G. Kresse, Phys. Rev. B 50 (1994) 15606.
[12] T. Schlick, M. Overton, J. Comput. Chem. 8 (1987) 1025.
[13] B. Hammer, L. B. Hansen, J. K. Nørskov, Phys. Rev. B 59 (1999) 7413.
[14] G. Kresse, J. Furthmüller, Phys. Rev. B 54 (1996) 11169.
[15] W. Kohn, L. J. Sham, Phys. Rev. 140 (1965) A1133.
[16] J. P. Perdew, J. A. Chevary, S. H. Vosko, K. A. Jackson, M. R. Pederson, D. J. Singh, C. Fiolhais, Phys. Rev. B 46 (1992) 6671.
[17] J. P. Perdew, J. A. Chevary, S. H. Vosko, K. A. Jackson, M. R. Pederson, D. J. Singh, C. Fiolhais, Phys. Rev. B 48 (1993) 4978.
[18] D. Vanderbilt, Phys. Rev. B 41 (1990) 7892.
[19] P. E. Blöchl, Phys. Rev. B 50 (1994) 17953.
[20] G. Kresse, D. Joubert, Phys. Rev. B 59 (1999) 1758.
[21] *Atomic Simulation Environment.* `https://wiki.fysik.dtu.dk/ase`.
[22] E. Rönnebro, D. Noréus, K. Kadir, A. Reiser, B. Bogdanović, J. Alloys Compd. 299 (2000) 101.
[23] B. Bogdanović, M. Schwickardi, J. Alloys Compd. 253–254 (1997) 1.
[24] S. Li, P. Jena, R. Ahuja, Phys. Rev. B 73 (2006) 214107.
[25] J. Voss, Q. Shi, H. Jacobsen, M. Zamponi, K. Lefmann, T. Vegge,

J. Phys. Chem. B 111 (2007) 3886.
[26] A. Peles, J. A. Alford, Z. Ma, L. Yang, M. Y. Chou, Phys. Rev. B 70 (2004) 165105.
[27] M. E. A. y de Dompablo, G. Ceder, J. Alloys Compd. 364 (2004) 6.
[28] P. Vajeeston, P. Ravindran, A. Kjekshus, H. Fjellvåg, Phys. Rev. B 71 (2005) 092103.
[29] H. König, R. Hoppe, Z. Anorg. Allg. Chem. 439 (1978) 71.
[30] C. Chen, Y. Wu, A. Jiang, B. Wu, G. You, R. Li, S. Lin, J. Opt. Soc. Amer. B6 (1989) 616.
[31] S. P. Velsko, M. Webb, L. Davis, C. Huang, IEEE J. Quantum Elect. 27 (1991) 2182.
[32] T. Sasaki, Y. Mori, M. Yoshimura, Y. K. Yap, T. Kamimura, Mat. Sci. Eng. R. 30 (2000) 1.
[33] Z. S. Lin, J. Lin, Z. Z. Wang, Y. C. Wu, N. Ye, C. Chen, R. K. Li, J. Phys.: Condens. Matter 13 (2001) R369.
[34] J.-H. Her, P. W. Stephens, Y. Gao, G. L. Soloveichik, J. Rijssenbeek, M. Andrus, J.-C. Zhao, Acta Cryst. B 63 (2007) 561.
[35] V. Ozolins, E. H. Majzoub, C. Wolverton, Phys. Rev. Lett. 100 (2008) 135501.
[36] B. Dai, D. S. Sholl, J. K. Johnson, J. Phys. Chem. C 112 (2008) 4391.
[37] *wyckconf.* `http://wyckconf.sourceforge.net`.

Paper P2

Γ-point lattice free energy estimates from $O(1)$ force calculations

Johannes Voss[1, 2, *] and Tejs Vegge[1]

[1] *Materials Research Department, Risø National Laboratory for Sustainable Energy, Technical University of Denmark, Roskilde, Denmark*

[2] *Center for Atomic-scale Materials Design, Department of Physics, Technical University of Denmark, Kongens Lyngby, Denmark*

(Dated: 30 May 2008)

We present a new method for estimating the vibrational free energy of crystal (and molecular) structures employing only a single force calculation, for a particularly displaced configuration, in addition to the calculation of the ground state configuration. This displacement vector is the sum of the phonon eigenvectors obtained from a fast – relative to *e.g.* density functional theory[1] – Hessian calculation using interatomic potentials. These potentials are based here on effective charges obtained from a density functional theory calculation of the ground state electronic charge density, but could also be based on other, *e.g.* empiric approaches.

I. INTRODUCTION

At finite temperatures, the stability of a crystalline system is not only determined by the ground state energy, but by the free energy. For a perfect crystal, the phononic contributions to the entropy are most important. In addition to minimizing the potential energy to locate the ground state

configuration, the calculation of free energies is important to estimate phase stabilities of the system. The ability to quickly assess the free energy of a given crystal structure is particularly important in the investigation of phase stabilities or decomposition temperatures of theoretically predicted materials or structures. The approach to approximate free energy calculation presented here will be of particular value to predictive screening studies, where quick free energy estimates are essential to cover wide ranges of possible structural input parameters for exploring trends in thermodynamic properties.

According to the Hellmann-Feynman theorem,[2,3] the forces acting on the ionic cores, *i.e.* first order energy derivatives, can be calculated within classical electrostatics from the ground state charge density, since the electronic eigenenergies only change in second order with first order wave function variations. For the calculation of the Hessian matrix of the energy, *i.e.* second order derivatives, charge density changes have to be evaluated. These can be obtained within density functional perturbation theory[4] or from finite force differences of displaced configurations. By the former approach, the phonon frequencies can be calculated at a given k-point in the Brioullin zone with a computational complexity per perturbation of an iterative ground state charge density calculation using density functional theory[1] (DFT). For nonzero k-points, the latter approach requires enlarged supercells to resolve interatomic couplings between the periodic images. Furthermore, charge densities for $O(N)$ displaced configurations have to be calculated, where N is the number of atoms in the unit cell. The computational effort can be reduced significantly for both approaches by taking crystal symmetries into account.

We present a method which obtains phonon frequencies using finite force differences, where the frequencies are extrapolated from the forces due to a single displacement, independent of the number of atoms. A decoupling of displaced planes of atoms due to periodic boundary conditions is not possible within this approach. Therefore, only the Γ-point contribution to the free energy can be calculated, which is a good approximation for sufficiently large systems. Within linear response or density functional perturbation theory, the computational effort for the calculation of the Γ-point frequencies scales as the effort for a single ground state charge density calculation per perturbation. The displacement approach presented here can be of interest, since no perturbations according to the single degrees of freedom are necessary but all degrees of freedom are taken into account by one displacement, irrespective of the system size. Moreover, the method presented here only employs the

classical ionic degrees of freedom and the corresponding forces, making this approach generally applicable when linear response calculations are unavailable.

II. Γ-POINT PHONON FREQUENCIES

In a harmonic approximation, the phononic contribution to the free energy is given as:

$$F_{\mathrm{vib}}(T) = r\, k_{\mathrm{B}} T \int_0^\infty \mathrm{d}\omega g(\omega) \ln\left[2\sinh\left(\frac{\hbar\omega}{2k_{\mathrm{B}}T}\right)\right], \tag{1}$$

where $g(\omega)$ is the normalized phonon density of states, r is the number of degrees of freedom in the unit cell, and k_{B} is Boltzmann's constant. The contribution of the Γ-point to (1) is

$$F_{\mathrm{vib}}^{\Gamma}(T) = k_{\mathrm{B}} T \sum_{i=1}^{3N}{}' \ln\left[2\sinh\left(\frac{\hbar\omega_i}{2k_{\mathrm{B}}T}\right)\right], \tag{2}$$

where N is the number of atoms in the unit cell and ω_i are the phonon frequencies. The prime denotes that the three zero frequencies corresponding to translational invariance are left out. In the zero temperature limit, Eq. (2) becomes a sum over the phonon frequencies, while for high temperatures $k_{\mathrm{B}}T \gg \max(\hbar\omega_i)$, Eq. (2) approaches the logarithm of the product of the phonon frequencies:

$$F_{\mathrm{vib}}^{\Gamma}(T \gg \max(\hbar\omega_i)/k_{\mathrm{B}}) \to k_{\mathrm{B}} T \ln\left(\frac{\prod_i{}' \hbar\omega_i}{(k_{\mathrm{B}}T)^{3N-3}}\right), \tag{3}$$

where the prime again denotes that the zero frequencies due to translational invariance are left out.

The frequencies of a system of coupled oscillators are the square roots of the eigenvalues of the generalized eigenvalue problem

$$\underline{\underline{H}}\,\underline{v} = \omega^2\, \underline{\underline{M}}\,\underline{v}, \tag{4}$$

where $\underline{\underline{H}}$ is the Hessian matrix and $\underline{v}$ is an eigenvector. $M_{i,j} = m_{\lfloor i/3 \rfloor}\delta_{i,j}$ is a mass matrix, with the atomic masses m_k. Eq. (4) can be easily converted to the eigenvalue problem

$$\underline{\underline{\tilde{H}}}\,\underline{\tilde{v}} = \omega^2\,\underline{\tilde{v}}, \tag{5}$$

yielding the same eigenvalues ω^2 as Eq. (4). $\underline{\underline{\tilde{H}}}$ is a mass-scaled Hessian matrix:

$$\underline{\underline{\tilde{H}}} = \underline{\underline{L}}\,\underline{\underline{H}}\,\underline{\underline{L}}\,, \tag{6}$$

with

$$L_{i,j} = \frac{1}{\sqrt{m_{\lfloor i/3 \rfloor}}}\,\delta_{i,j}. \tag{7}$$

In the following we will use Eq. (5) to calculate the vibrational eigenfrequencies of the system.

III. METHOD

The main idea of this method is that the eigenvalues of the Hessian matrix can be estimated from $O(1)$ force calculations, if rather rough approximations to the eigenvectors are available. For a given configuration (optimized within *e.g.* DFT), a model Hamiltonian is constructed, such that it yields an energetic minimum for the given atomic coordinates. With this computationally inexpensive representation of the system, the Hessian matrix is approximated. From the sum of the eigenvectors $\underline{u}_i$ of this approximate Hessian, a displacement vector $\underline{w}$ is constructed:

$$\underline{w} := \sum_i \underline{u}_i. \tag{8}$$

The Hessian $\underline{\underline{H}}$ of the more accurate Hamiltonian (here: DFT) is projected onto this displacement vector to extract the Hessian eigenvalues h_i:

$$h_i \approx \underline{u}_i^T\,\underline{\underline{H}}\,\underline{w}. \tag{9}$$

The Hessian-vector product is approximated by the forces acting on a displaced configuration:

$$\underline{\underline{H}}\,\underline{w} \approx \varepsilon^{-1}\left[\underline{\nabla}E(\underline{r}_0 + \varepsilon\underline{w}) - \underline{\nabla}E(\underline{r}_0)\right], \tag{10}$$

where $\underline{r}_0$ are the ground state coordinates and ε is used to scale the displacement for the finite difference. The gradient of the ground state configuration $\underline{\nabla}E(\underline{r}_0)$ might be neglected, if the configuration is well relaxed.

For the calculation of the vibrational eigenfrequencies, the Hessian matrix has to be mass-scaled according to Eq. (6). This can either be performed for a Hessian matrix constructed from the approximate eigenpairs $(h_i, \underline{u}_i)$, or by mass scaling the displacement and the calculated forces by a multiplication of both vectors with the matrix $\underline{\underline{L}}$ (Eq. (7)). For the latter way of obtaining the mass-scaled Hessian, the eigenvalues are obtained using approximate eigenvectors of Eq. (5). We have found the former approach of the mass scaling of the constructed Hessian to generally give more accurate results. Especially for systems with large mass differences, the accuracy of the finite force difference obtained from the mass-scaled displacement can be reduced.

We construct the approximate set of Hessian eigenvectors using interatomic potentials. We construct these potentials from the ground state charge density. We assume the energy of the system to be described locally by the Coulomb interaction of effective point charges at the atomic positions. The forces on the point charges are calculated using Ewald summation.[5] We use a Bader charge density analysis[6] as implemented in [7,8] to attribute valence electron charge density to the ionic cores. We assume the attributed charges to be effective point charges at the corresponding atomic coordinates. We optimize the effective charges by using non-linear least squares fitting[9] to minimize the forces on the ground state configuration (only modifying the effective charges but not the atomic coordinates). We constrain the sum of negative and positive charges to be constant, respectively, to avoid the trivial solution of zero charges. For systems containing coordinates which are completely fixed by symmetry, the corresponding forces are always zero and therefore no fitting is necessary. Using these interatomic potentials, we calculate approximate Hessian eigenpairs.

Whereas these eigenvalues are generally not useful, the eigenvectors $\underline{u}_i$ reflect symmetries and coordination, and a projection of an accurate Hessian onto these vectors can give frequencies in reasonable ranges. Generally, the interatomic potential representation of the system might be unstable, *i.e.* there

are negative curvatures due to these potentials. However, we still find the geometric information contained in the eigenvectors to be useful by considering the absolute value of the right-hand side of Eq. (9) when extracting the eigenvalues. Since the vectors $\underline{u}_i$ are only approximate eigenvectors, which are linear combinations of the eigenvectors of an accurate Hessian matrix, the phonon frequencies are mixed and degeneracies are generally not resolved. In the special case of complex compounds with a broad range of phonon frequencies, it is possible to reduce the frequency mixing for the lowest eigenfrequencies by linear extrapolation (see Sec. V A for an example).

For low temperatures, compared to the lowest Γ-point phonon energies, the free energy calculated from the Hessian matrix constructed from the forces due to the displacement as outlined above is generally a good estimate, because the free energy is basically a sum of the phonon energies, and thus less sensitive to errors in the eigenmode vectors than single phonon energies.

For temperatures higher than the highest phonon energies, the free energy calculated from the approximate frequencies generally will not be a good estimate, since the free energy converges to the logarithm of the product of eigenfrequencies (see Eq. (3)). Based on the single displacement (8), we estimate the change of a $3N$-dimensional volume after the linear transformation given by the Hessian matrix. This provides an estimate of the determinant of the Hessian matrix, which equals the product of its eigenvalues h_i. We estimate this product by

$$\prod_i h_i \approx \prod_j \left(\underline{x}_j^T \underline{\underline{H}}\, \underline{w} \right) \Big/ \left(\sum_k \underline{x}_j^T \underline{u}_k \right), \tag{11}$$

again using Eq. (10) to approximate $\underline{\underline{H}}\,\underline{w}$. The $\underline{x}_j$ are the basis vectors of the canonical real space basis of the atomic coordinates. Eq. (11) is exact for vibrationally decoupled atomic coordinates, and can generally be interpreted as an estimate of how the volume spanned by the canonical basis vectors $\underline{x}_j$ is scaled by the Hessian matrix. To obtain the product of eigenfrequencies, Eq. (11) has to be mass-scaled. Since the determinant of a product of matrices equals the product of the determinants of the matrices, the scaling can simply be performed by a division with the product of the atomic masses.

In the following, we provide examples of the application of the method to the calculation of free energies.

IV. ELECTRONIC STRUCTURE CALCULATION

The energy gradients were calculated within density-functional theory[1] using two different programs to test the general applicability and implementation of the approach. The software package Dacapo[10] was used for the K_2NaAlH_6 and GaAs examples and VASP[11] for the remaining crystal structures, using planewave basis sets with cut-off energies of 350–400 eV and the Perdew-Wang-91 exchange-correlation functional[12,13] for all calculations. Dacapo uses ultrasoft pseudopotentials[14] for a description of the ionic cores, while for VASP projector-augmented wave[15] potentials[16] were used. The electronic Brioullin zones were sampled with k-point spacings of $\sim$0.1 Å^{-1}.

To assess the accuracy of the free energy estimates, we perform reference calculations using $3N$ displacements for diagonalization of the full Hessian matrices.

V. EXAMPLES

In this section, representative results for the free energy calculation method are presented for different classes of materials, covering both the low and high phonon frequency ranges.

A. Na_3AlH_6 and K_2NaAlH_6

As a first example, we consider two complex metal aluminum hexahydrides[17–19] of interest as reversible hydrogen storage materials,[20–25] where cation alloying is possible, rendering them interesting for screening studies.

The phonon spectrum of the complex metal hydride Na_3AlH_6 (space group $P2_1/n$)[26] contains relatively high energetic librational and bond-stretching (in this case Al–H bonds) modes, which are typical for the phonon spectrum of this kind of material. A distinct feature is the high frequency band of bond-stretching modes around 170 meV (see Fig. 1(a)). While degeneracies are not resolved in the single-displacement frequencies, the correct range of phonon energies is covered, interpolating the "exact" spectrum. Only a small fraction of the spectrum lies below typical values of k_BT, and therefore the approximated free energy is in good agreement with the result based on $3N$

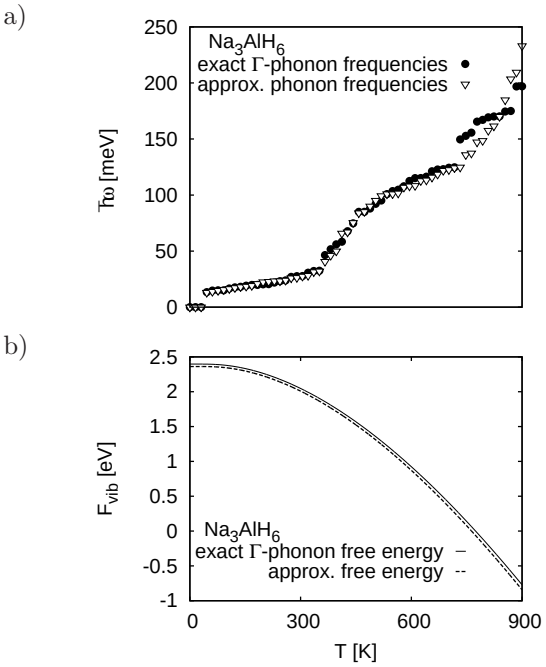

FIG. 1: Comparison of Γ-point phonon frequency spectra (a) and lattice free energies (b) calculated for Na_3AlH_6 both from $3N$ displacements and the $O(1)$ method presented here, respectively. To improve the quality of the lowest approximate phonon frequencies, the five lowest nonzero frequencies were generated from a linear extrapolation of the ten next higher frequencies.

displacements (see Fig. 1(b)), since the free energy approaches the arithmetic average of the phonon energies for temperatures low compared to the high phonon energies.

One of the important thermodynamic properties that can be calculated based on the lattice free energies, is the decomposition temperature of a compound by comparing to the energies of the constituents. For known materials, these energies can either often be obtained from tabulated data or be calculated. As an example, we estimate the decomposition temperature of Na_3AlH_6. Fig. 2 shows the Gibbs free energies (pV terms for solid phases have been neglected) for Na_3AlH_6 and its decomposition products in the re-

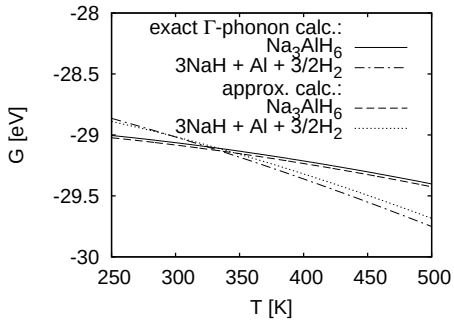

FIG. 2: Gibbs free energies for Na_3AlH_6 and its decomposition products calculated both by diagonalization of the full Hessian and the $O(1)$ method.

action

$$Na_3AlH_6 \rightarrow 3NaH + Al + \frac{3}{2}H_2. \tag{12}$$

The Gibbs free energy for Al has been generated from data in Ref. [27]; data for H_2 have been taken from Ref. [28]. The free energies of Na_3AlH_6 and NaH have been calculated both using one and $3N$ displacements. The agreement between the two approaches is good, yielding a decomposition temperature of $\sim$350 K. Ke and Tanaka[28] have previously calculated a decomposition temperature of 390 K for Na_3AlH_6. Considering that the latter value is based on a quasi-harmonic approximation and that the phonon dispersion has been taken into account, our quick estimate of the decomposition temperature yields a satisfactory result. Experimentally,[29] a value of 423 K has been obtained for the decomposition temperature.

A stable binary cation alloy is K_2NaAlH_6 (space group $Fm\bar{3}m$),[30] with larger atomic mass differences than Na_3AlH_6. As a test case for alloyed systems, we have estimated the free energy of this compound using the $O(1)$ method presented here. For this compound, the bond-stretching band lies at 160 meV (see Fig. 3(a)). The corresponding degeneracy is not resolved at all in the extrapolated spectrum. Since low temperature free energies basically depend on the average phonon frequency, the lattice free energy approximation still is quite good (see Fig. 3(b)).

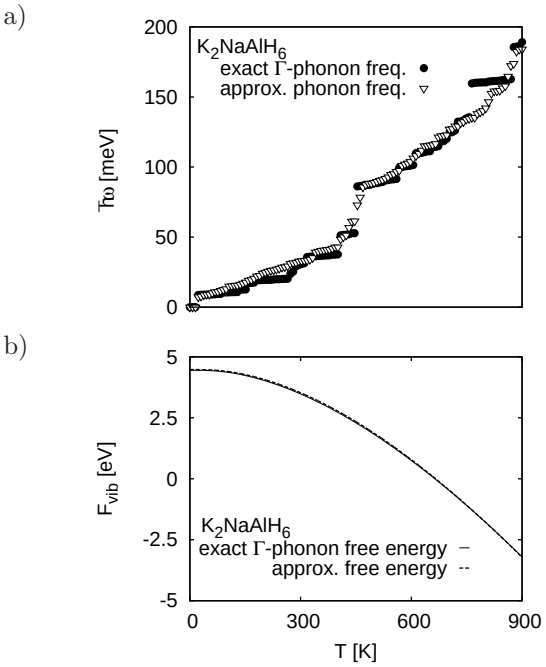

FIG. 3: Comparison of Γ-point phonon frequency spectra (a) and lattice free energies (b) calculated for K_2NaAlH_6 both with one and $3N$ displacements, respectively.

B. GaAs

We continue with tests for systems which do not show high frequency modes due to molecular bonding in the crystal. As a model semiconductor, we have considered GaAs, which crystallizes in the zincblende structure (space group $F\bar{4}3m$).[31] The optical Γ-point frequencies are separated by ∼18 meV from the acoustic frequencies (see Fig. 4(a)). The frequencies obtained from the $O(1)$ method do not show this gap; optical and acoustic modes are mixed. The average error in the six lowest optical frequencies is about 15% with a corresponding error of ∼40% in the eigenvectors. The error in the higher frequencies is smaller: ∼3%. The maximal phonon frequencies are relatively low, only about 30 meV, which is of the same magnitude as k_BT at room temperature. Therefore, the free energy calculated using the approximate frequencies obtained from the $O(1)$ method is not a good approximation for temperatures $T > 0$ (see Fig. 4(b)). Alternatively, the product of the phonon

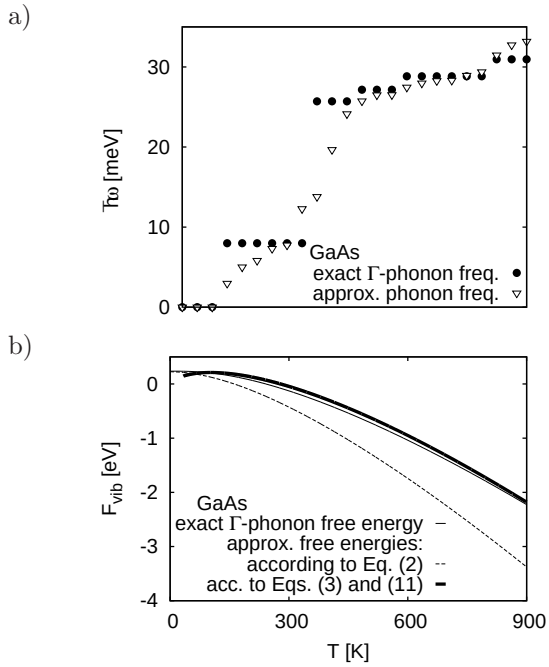

FIG. 4: Comparison of Γ-point phonon frequency spectra (a) and lattice free energies (b) calculated for GaAs both with one and $3N$ displacements, respectively.

frequencies is approximated directly using Eq. (11) from the forces due to the single displacement, instead of projecting the forces onto the approximate eigenvectors to extract the frequencies. The high temperature free energy approximation according to Eq. (3) using this product yields relatively good results (even for temperatures below $k_{\mathrm{B}}T = 30$ meV).

C. $MgZn_2$

Finally, we apply our method to a simple metallic alloy. We have considered the hexagonal η-phase of $MgZn_2$ (space group $P6_3/mmc$),[32] which is the reference $C14$ Laves phase material. Similar to the case of GaAs, the highest phonon energies are around 30 meV due to the absence of "molecular-like" modes (see Fig. 5(a)). Also here, the free energy calculated from the approximated phonon frequencies is only a good approximation for $T \to 0$. Using

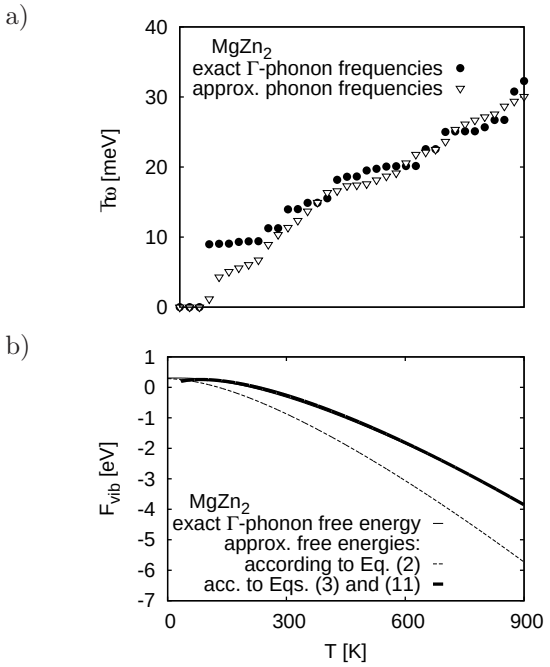

FIG. 5: Comparison of Γ-point phonon frequency spectra (a) and lattice free energies (b) calculated for $MgZn_2$ both with one and $3N$ displacements, respectively.

the direct approximation of the product of the phonon frequencies (Eq. (11)) together with the high temperature approximation Eq. (3), which basically depends on the geometric mean value of the frequencies, the corresponding approximated free energy is in good agreement with the "exactly" calculated free energy for temperatures higher than about 50 K (see Fig. 5(b)).

The average error in the frequencies obtained using the $O(1)$ method for the four example cases considered here is about 10% with a corresponding error of 30% in the eigenvectors. The errors in the modes could be reduced using better potentials for the Hessian eigenvector approximation. An advantage of the simple point charge model used here is that it can be optimized to yield an energetic minimum for given atomic coordinates, *i.e.* the ground state configuration obtained using *e.g.* DFT. A possibility to improve the interatomic potentials could be the inclusion of the forces due to the special displacement calculated using DFT as additional constraints into a re-optimization or

extension of the model potentials.

VI. CONCLUSION

We have developed a method for a fast approximation of lattice free energies. This approach can be very useful for quick estimates of decomposition temperatures of new or theoretically proposed compounds. These fast, rough estimates are very important for screening studies of *e.g.* alloy stability at finite temperatures. It is, however, in general not expected to be accurate enough for a reliable determination of phase transition temperatures based on an energetic comparison of different phases lying very close in energy, since degeneracies in the phonon spectrum, determining the peak heights in the phonon density of states, are not resolved within this approach.

Free energies can be extrapolated from the forces due to a single atomic displacement for low and high temperatures compared to the phonon energies, rendering this approach suitable both for complexes with molecular bonds and high phonon energies and semiconductors and metals.

Acknowledgments

We thank Prof. Jens K. Nørskov for fruitful discussions. We acknowledge financial support by the NABIIT program funded by the Danish Research Councils for Strategic Research, and the Danish Center for Scientific Computing (DCSC) for computer time. The Center for Atomic-scale Materials Design is supported by the Lundbeck Foundation.

---

* Electronic address: johannes.voss@risoe.dk

[1] P. Hohenberg and W. Kohn, Phys. Rev. **136**, B864 (1964).
[2] H. Hellmann, Einführung in die Quantenchemie (Deuticke, Leipzig, 1937).
[3] R. P. Feynman, Phys. Rev. **56**, 340 (1939).
[4] S. Baroni, P. Giannozzi, and A. Testa, Phys. Rev. Lett. **58**, 1861 (1987).
[5] P. P. Ewald, Ann. Phys. (Leipzig) **64**, 253 (1921).
[6] R. F. W. Bader, Atoms in Molecules – A Quantum Theory (Oxford University Press, Oxford, 1990).

[7] G. Henkelman, A. Arnaldsson, and H. Jónsson, Comput. Mater. Sci. **36**, 254 (2006).
[8] E. Sanville, S. D. Kenny, R. Smith, and G. Henkelman, J. Comput. Chem. **28**, 899 (2007).
[9] Minpack, University of Chicago (1999).
[10] B. Hammer, L. B. Hansen, and J. K. Nørskov, Phys. Rev. B **59**, 7413 (1999).
[11] G. Kresse and J. Furthmüller, Phys. Rev. B **54**, 11169 (1996).
[12] J. P. Perdew, J. A. Chevary, S. H. Vosko, K. A. Jackson, M. R. Pederson, D. J. Singh, and C. Fiolhais, Phys. Rev. B **46**, 6671 (1992).
[13] J. P. Perdew, J. A. Chevary, S. H. Vosko, K. A. Jackson, M. R. Pederson, D. J. Singh, and C. Fiolhais, Phys. Rev. B **48**, 4978 (1993).
[14] D. Vanderbilt, Phys. Rev. B **41**, 7892 (1990).
[15] P. E. Blöchl, Phys. Rev. B **50**, 17953 (1994).
[16] G. Kresse and D. Joubert, Phys. Rev. B **59**, 1758 (1999).
[17] J. Graetz, Y. Lee, J. J. Reilly, S. Park, and T. Vogt, Phys. Rev. B **71**, 184115 (2005).
[18] O. M. Løvvik, O. Swang, and S. M. Opalka, J. Mater. Res. **20**, 3199 (2005).
[19] H. B. Y. Nakamura, A. Fossdal and B. Hauback, J. Alloys Cmpd. **416**, 274 (2006).
[20] B. Bogdanović and M. Schwickardi, J. Alloys Comp. **253-254**, 1 (1997).
[21] S. Li, P. Jena, and R. Ahuja, Phys. Rev. B **73**, 214107 (2006).
[22] J. Voss, Q. Shi, H. Jacobsen, M. Zamponi, K. Lefmann, and T. Vegge, J. Phys. Chem. B **111**, 3886 (2007).
[23] A. Peles, J. A. Alford, Z. Ma, L. Yang, and M. Y. Chou, Phys. Rev. B **70**, 165105 (2004).
[24] M. E. Arroyo y de Dompablo and G. Ceder, J. Alloys Compd. **364**, 6 (2004).
[25] P. Vajeeston, P. Ravindran, A. Kjekshus, and H. Fjellvåg, Phys. Rev. B **71**, 092103 (2005).
[26] V. Subrtova, Coll. Czech. Chem. Comm. **31**, 4455 (1966).
[27] P. D. Desai, Int. J. Thermophys. **8**, 621 (1987).
[28] X. Ke and I. Tanaka, Phys. Rev. B **71**, 024117 (2005).
[29] K. J. Gross, S. Guthrie, S. Takara, and G. Thomas, J. Alloys Compd. **297**, 270 (2000).
[30] M. H. Sorby, H. W. Brinks, A. Fossdal, K. Thorshaug, and B. C. Hauback, J. Alloys Compd. **415**, 284 (2006).
[31] S. Adachi, J. Appl. Phys. **58**, R1 (1985).
[32] Y. Komura and K. Tokunaga, Acta Crystallogr., Sect. B: Struct. Crystallogr. Cryst. Chem. **36**, 1548 (1980).

Paper P3

Structural stability and decomposition of $Mg(BH_4)_2$ isomorphs – an ab initio free energy study

J. Voss

Materials Research Division, Risø National Laboratory for Sustainable Energy, Technical University of Denmark, Roskilde, Denmark
Center for Atomic-Scale Materials Design, Department of Physics, Technical University of Denmark, Kongens Lyngby, Denmark

J. S. Hummelshøj

Center for Atomic-Scale Materials Design, Department of Physics, Technical University of Denmark, Kongens Lyngby, Denmark
Materials Research Division, Risø National Laboratory for Sustainable Energy, Technical University of Denmark, Roskilde, Denmark

Z. Łodziana

Department of Mobility, Environment, and Energy, EMPA Materials Sciences and Technology, Dübendorf, Switzerland

T. Vegge

Materials Research Division, Risø National Laboratory for Sustainable Energy, Technical University of Denmark, Roskilde, Denmark

E-mail: `tejs.vegge@risoe.dk`

PACS numbers: 63.20.-e, 64.60.-i, 65.40.-b

Abstract. We present the first comprehensive comparison between free energies, based on a phonon dispersion calculation within density functional theory, of theoretically predicted structures and the experimentally proposed α ($P6_1$) and β ($Fddd$) phases of the promising hydrogen storage material $Mg(BH_4)_2$.

The recently proposed low-density $I\bar{4}m2$ ground state is found to be thermodynamically unstable with soft acoustic phonon modes at the Brillouin zone boundary. We show that such acoustic instabilities can be detected by a macroscopic distortion of the unit cell. Following the atomic displacements of the unstable modes, we have obtained a new $F222$ structure, which has a lower energy than all previously experimentally and theoretically proposed phases of $Mg(BH_4)_2$ and is free of imaginary eigenmodes. A new metastable high-density $I4_1/amd$ structure is also derived from the $I\bar{4}m2$ phase.

Temperatures for the decomposition are found to be in the range of 400–470 K and largely independent of the structural complexity, as long as the primary cation coordination polyhedra are properly represented. This opens a possibility of using simple model structures for screening and prediction of finite temperature stability and decomposition temperatures of novel borohydride systems.

Accepted for publication in J. Phys.: Condens. Matter
`http://www.iop.org/EJ/journal/JPhysCM`

1. Introduction

The search for novel hydrogen storage materials which combine high hydrogen content with the potential for reversible storage under near ambient conditions, has directed the focus from alanates to borohydride systems. The binary alkali borohydrides, *e.g.* $LiBH_4$ [1, 2], are found to be too thermodynamically stable, whereas the divalent $Ca(BH_4)_2$ and in particular $Mg(BH_4)_2$ have extracted interest, since empirical [3] and density functional theory (DFT) calculations on model structures [4] have indicated highly favorable thermodynamical properties.

Although originally synthesized in 1950 [5], a specific crystal structure was not proposed for $Mg(BH_4)_2$ until 2007, when Černý *et al.* [6] and Her *et al.* [7], independently, proposed a hexagonal 'low temperature' (α) $P6_1$ phase consisting of 330 atoms in the unit cell and a density of $\rho = 0.78$ g/cm^3. Her *et al.* [7] furthermore proposed an anti-phase boundary modification of an orthorhombic $Fddd$ super structure (704 atoms) as a 'high temperature' (β) phase ($\rho = 0.76$ g/cm^3), and observed at least one additional modification. Chłopek *et al.* [8] have presented XRD and DSC data, which indicates that even the $P6_1$ (α) phase could be metastable. Neither of these structures can, however, account for the tetragonal, high density ($\rho = 0.99$ g/cm^3) phase originally obtained by Konoplev and Bukulina in 1971 [9], using a different synthesis procedure.

Prior to the characterization of the α-phase, a number of simpler structures had been proposed on the basis of density functional theory (DFT) calculations: a hexagonal structure in space group $P\bar{3}m1$ [4] and a orthogonal structure in space group $Pmc2_1$ [10]; recently, the ground state energies of the α and β phases were calculated independently by Ozolins *et al.* [11] and Dai *et al.* [12]. Van Setten *et al.* [13] have later estimated free energies from the Γ-point frequencies, excluding unstable modes with larger wave vectors, that lead to larger structures with lower energies.

The phase stability can only be determined from the free energy, and we present the first direct comparison of free energies based on the calculation of the phonon dispersion of the most stable

theoretically predicted structures and the experimentally proposed α and β super structures, yielding surprisingly small differences between ground state energies and free energies of these structures.

Based on a vibrational analysis of the recently proposed low-density $I\bar{4}m2$ phase [11] which indicates thermodynamic instability of this phase, we obtain a new $F222$ structure of $Mg(BH_4)_2$. We find the $F222$ phase to have a lower free energy than any other proposed experimental or theoretical structure. We also identify the existence of a new meta stable high density ($\rho = 1.01$ g/cm^3) tetragonal $I4_1/amd$ structure without instabilities, which may account for the experimentally observed and uncharacterized tetragonal high-density structure ($\rho = 0.99$ g/cm^3) [9]. This phase can be interpreted as a folded form of the low density $I\bar{4}m2$ structure ($\rho = 0.56$ g/cm^3).

We expect the specific conditions of the current chemical synthesis procedure [8] combined with kinetically limited phase transitions between the large super structures could account for the lack of (recent) experimental observations of $F222$ or $I4_1/amd$, and we anticipate future experimental verification of a highly complex phase diagram, similar to that of $Ca(BH_4)_2$ [14], *e.g.*, by use of high pressure experiments.

The calculations also show that the thermodynamic properties of even highly complex borohydride super structures can be well estimated by DFT using even simple model structures, if the primary coordination polyhedra are correctly accounted for. A purely thermodynamic estimate, *i.e.*, not considering the inherently slow kinetics of borohydride systems [8], of the decomposition temperature yields values of 400–470 K for the idealized decomposition, $Mg(BH_4)_2 \rightarrow MgH_2 + 2B + 3H_2$, for the complex and the simple unit cell structures.

These findings enable faster screening studies of thermodynamic stability and decomposition temperatures for, *e.g.* ternary and quaternary borohydride systems; not only in terms of reduced computational effort due to smaller system sizes, but also with the advantage that the exact space group need not to be known *a priori*.

2. Computational Details

Total energies and gradients were calculated within density functional theory [15] (DFT) using the Vienna Ab-initio Simulation Package (VASP) [16]. The Kohn-Sham wave functions [17] were expanded in planewave basis sets with energy cut offs of up to 500 eV. Brioullin zone sampling was performed on meshes with a k-point spacing of $\leq 0.03\text{Å}^{-1}$ (for the larger $P6_1$ and $Fddd$ structures, the spacing was $\leq 0.06\text{Å}^{-1}$). The Perdew-Wang-91 exchange-correlation functional [18, 19] was used in combination with the projector-augmented wave method [20], using parametrizations due to Kresse and Joubert [21].

Phonon dispersions and phonon densities of states were calculated by the direct method in the harmonic approximation with the software package Phonon [22], using the Hellmann-Feynman forces from minimal sets of atomic displacements. To resolve interatomic couplings, super cells containing no less then eight formula units of $Mg(BH_4)_2$ were used.

Due to the large system sizes, the $P6_1$ and $Fddd$ structures were treated separately and only the contribution of the dispersion folded to the Γ-point in supercells containing 330 and 704 atoms, respectively, were considered; this is generally a good approximation due to the very large super cells. The corresponding densities of states have been obtained by differentiating a spline interpolation of the integrated phonon density of states at the supercell Γ-point. The integrated density $G(\omega)$ is given by:

$$G(\omega) = \sum_{i=1}^{3N} \Theta(\omega - \omega_i)\,, \tag{1}$$

with the Heaviside function $\Theta(\omega)$ and the phonon frequencies ω_i.

For perfect crystalline solids, the vibrational contribution to the free energy is most important, and can be calculated in the harmonic approximation from the normalized phonon density of states $g(\omega)$ as:

$$F_{\text{vib}}(T) = r\, k_{\text{B}} T \int_0^\infty \mathrm{d}\omega\, g(\omega) \ln\left[2\sinh\left(\frac{\hbar\omega}{2k_{\text{B}}T}\right)\right], \tag{2}$$

where r is the number of degrees of freedom in the unit cell and k_{B} is Boltzmann's constant.

3. Analysis

$I4_1/amd$	$a = 8.252$Å	$c = 10.474$Å
Mg	$(4a)$ $(0, 0.75, 0.125)$	
	$(4b)$ $(0, 0.25, 0.375)$	
B	$(16h)$ $(0, 0.4846, 0.2305)$	
H	$(16h)$ $(0, 0.6135, 0.2880)$	
	$(16h)$ $(0, 0.4970, 0.1142)$	
	$(32i)$ $(0.8368, 0.3745, 0.4902)$	

Table 1. Calculated lattice parameters and Wyckoff coordinates of $I4_1/amd$-$\mathrm{Mg(BH_4)_2}$.

$F222$	$a = 9.928$Å	$b = 11.183$Å	$c = 11.891$Å
Mg	$(4a)$ $(0, 0, 0)$; $(4c)$ $(1/4, 1/4, 1/4)$		
B	$(16k)$ $(0.0990, 0.1383, 0.1316)$		
H	$(16k)$ $(0.1314, 0.1030, 0.2252)$		
	$(16k)$ $(0.1651, 0.0800, 0.0635)$		
	$(16k)$ $(0.1223, 0.2438, 0.1127)$		
	$(16k)$ $(0.9769, 0.8735, 0.8747)$		

Table 2. Calculated lattice parameters and Wyckoff coordinates of $F222$-$\mathrm{Mg(BH_4)_2}$.

The experimentally [6, 7, 9] and theoretically [4, 10, 11] proposed phases of $\mathrm{Mg(BH_4)_2}$ vary significantly in density, coordination and complexity. In order to evaluate the stability of the proposed structures, we present the first comparison of the stability of the different $\mathrm{Mg(BH_4)_2}$ phases based on DFT lattice free energy calculations. We have calculated the ground state energies and phonon density of states for the experimentally proposed $P6_1$ [6] and $Fddd$ [7] structures, and theoretically proposed $Pmc2_1$ [10], $P\bar{3}m1$

[4], and $I\bar{4}m2$ [11] phases. We furthermore present results for three other structures, a monoclinic Pm (Figure 1; coordinates and unit cell parameters in supplementary material) phase, a tetragonal $I4_1/amd$ (Figure 2b; coordinates and lattice constants in Table 1), and the orthorhombic $F222$ structure (Figure 3; coordinates and unit cell parameters in Table 2), which all capture the ideal local coordination and display interesting characteristics.

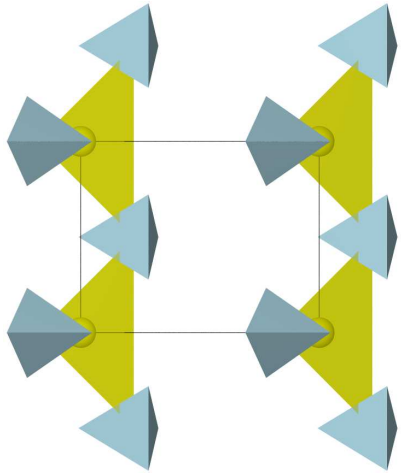

Figure 1. (Colour online) The structure of Pm. Yellow tetrahedra represent the Mg–B coordination and blue tetrahedra the $BH_4{}^-$ groups.

3.1. Structural coordination

In order to understand why $Mg(BH_4)_2$, in contrast to most metal borohydrides, apparently forms large super structures, and to understand the significance of the structural contributions to the total energy, we first analyze the coordination of the proposed structures.

Based on this analysis, we propose a $I4_1/amd$ (Figure 2b) structure which has the same topology as the experimental structures and the high density phase observed in Ref. [9].

All the $Mg(BH_4)_2$ structures compared here show a tetrahedral arrangement of BH_4^- ions around the Mg ion, except for $P\bar{3}m1$

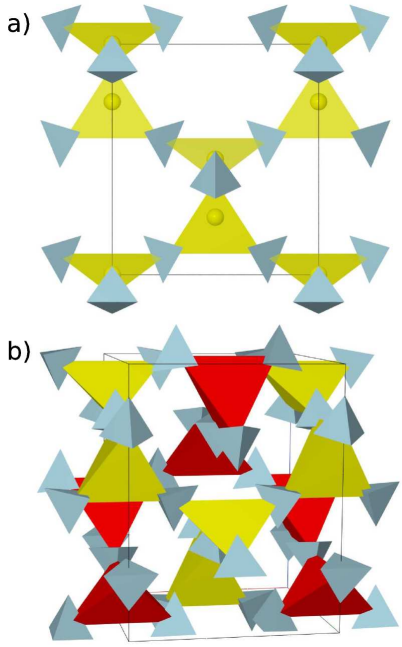

Figure 2. (Colour online) The a) $I\bar{4}m2$ and b) $I4_1/amd$ structures of $Mg(BH_4)_2$. Note the similarity of the $I4_1/amd$ phase to a double-folded $I\bar{4}m2$ structure. The yellow and red tetrahedra show the coordination of the B atoms around the Mg atoms. Blue tetrahedra represent the BH_4^- groups.

proposed by Nakamori *et al.* [4], which consists of identical layers of edge-sharing octahedra. For all the tetrahedral structures, the tetrahedra are corner sharing, but the connection of the coordination polyhedra is much more complex for the α- and β-phases than for the theoretically proposed phases [7].

The octahedral $P\bar{3}m1$ phase can be interpreted as consisting of an ABAB... stacking of boron planes with magnesium in half of the octahedral interstities (Figure 4a), and it is the most dense of the structures with a density of 1.04 g/cm^3. This structure is in essence close-packed, and therefore provides an upper bound of the mass density that can be achieved. The dense $Pmc2_1$, Pm, and $I4_1/amd$ structures follow an ABCABC... stacking (Figure 4b-d). The Pm

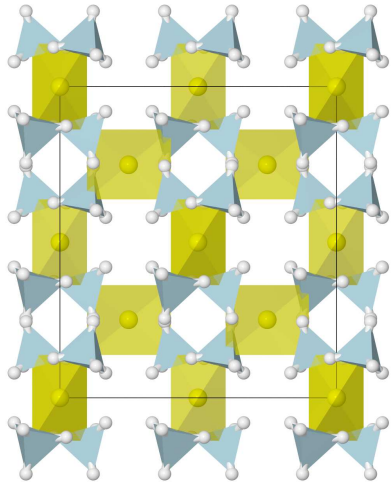

Figure 3. (Colour online) The structure of $Mg(BH_4)_2$ in space group $F222$ (blue tetrahedra: coordination of the B atoms, yellow tetrahedra: coordination of Mg with B atoms).

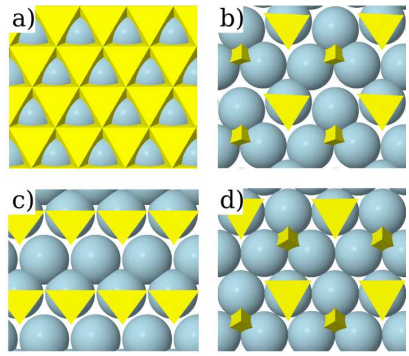

Figure 4. (Colour online) The a) $P\bar{3}m1$ (ρ = 1.04 g/cm^3) b) $Pmc2_1$ (ρ = 0.88 g/cm^3) and the proposed c) Pm (ρ = 0.91 g/cm^3) and d) $I4_1/amd$ (ρ = 1.01 g/cm^3) structures of $Mg(BH_4)_2$. The blue spheres represent the Mg atoms and the yellow tetrahedra the BH_4^- groups. Note the small difference between the $Pmc2_1$ and the $I4_1/amd$ phases.

phase is the smallest structure (11 atoms per unit cell) which captures the optimal primary coordination.

The new $I4_1/amd$ corresponds to two identical $I\bar{4}m2$ sub-lattices of corner-sharing tetrahedra folded into each other and thereby forming a close-packed structure (Figure 2b). The main difference between the $I\bar{4}m2$, $I4_1/amd$ and $F222$ structures and the previously proposed theoretical ones lies in the arrangement of the polyhedra; the latter being layered and the first forming 3D networks, as observed for the experimental structures. Where the experimental structures have huge unit cells with five, eight and ten membered rings of tetrahedra in $P6_1$ and four and eight membered rings in $Fddd$, the $I\bar{4}m2$ unit is much simpler and has only one kind of six membered rings. In $P6_1$, the rings penetrate each other while for $I4_1/amd$, the rings belonging to each of the two $I\bar{4}m2$ sub-lattices penetrate the other (Figure 5).

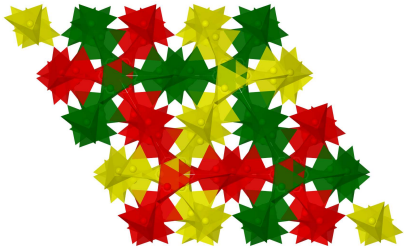

Figure 5. (Colour online) The structure of $P6_1$ $Mg(BH_4)_2$. Shown are the Mg–B tetrahedra. Different colours are used to distinguish different coordinational rings.

In the following, the influence of the differences in coordination on the structural stability is studied energetically, taking into account both the ground state energy of the electron-ion system and the lattice free energy.

3.2. Electronic density of states (DOS)

To study the influence of changing the coordination on the electronic structure, the electronic densities of states have been calculated.

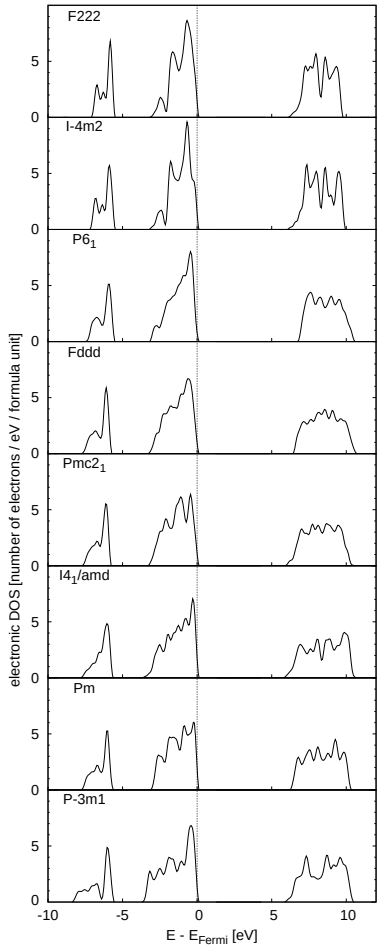

Figure 6. Electronic densities of states for different phases of $Mg(BH_4)_2$ plotted relative to the respective Fermi energies.

A comparison of the electronic density of states (DOS) for the proposed structures (see Figure 6) shows only small differences between the shapes of the DOS. All phases are insulators with calculated band gaps of around 6 eV.

The electrostatic ion-ion and ion-electron interaction energy is significantly higher for the low-density $I\bar{4}m2$ and $F222$ phases

	ρ [g/cm^3]	ΔE_{gs} [eV]	F_{vib} [eV] (300K)
$F222$	0.54	-0.10	2.02
$I\bar{4}m2$	0.56	-0.09	2.06
$I4_1/amd$	1.01	0.14	2.04
$P6_1$	0.82	0.00	2.12
$Fddd$	0.90	0.10	2.09
$Pmc2_1$	0.88	0.14	2.02
Pm	0.91	0.23	2.00
$P\bar{3}m1$	1.04	0.35	2.07

Table 3. Comparison of densities and ground state and lattice free energies per formula unit (ΔE_{gs} (relative to ground state energy of $P6_1$) and F_{vib}, respectively) of the considered $Mg(BH_4)_2$-phases.

than for the other phases. This energy difference is slightly overcompensated by lower electronic energies, resulting in a lower total energy for the $F222$ phase (see Table 3) than all other previously proposed structures (the electronic density of states in Figure 6 are plotted against the Fermi levels; the Fermi level is *e.g.* 1.54 eV lower per formula unit for the $F222$ than for, *e.g.* the $P6_1$ phase).

3.3. Phonon DOS

To investigate the stability and the influence of the structural differences on the vibrational free energies and the decomposition temperatures, we have calculated the phonon densities of states (PDOS) for the different phases.

Figure 7 shows the calculated PDOS for the analyzed structures. All spectra share general characteristics consisting of three separate bands (except for $P\bar{3}m1$, which shows further splitting). The low frequency regime at 0–20 THz is due to acoustic modes and optical modes in the magnesium/boron framework, the medium range (30–40 THz) corresponds to libration modes, and the narrow high frequency regime at ∼70 THz to B–H stretching vibrations.

The PDOS of the structures are very similar, in particular for the most stable $F222$, $I\bar{4}m2$, $I4_1/amd$ and $P6_1$ phases (the $Pmc2_1$

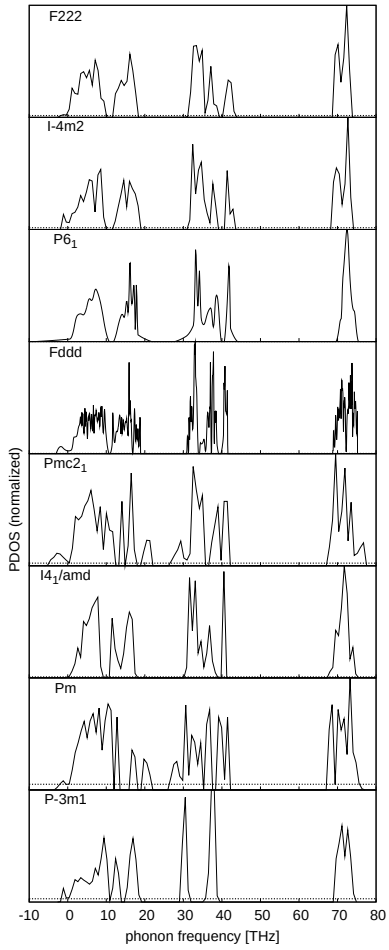

Figure 7. Normalized phonon densities of states for different phases of $Mg(BH_4)_2$. Imaginary frequencies are represented by negative real values. The dashed lines indicate the error of 0.1/THz per mode in the PDOS associated to the modes, due to the numerically unresolved translational symmetry.

phase was recently shown to be unstable by Ozolins *et al.* [11]); all displaying optical modes in the low frequency domain and a very narrow B–H stretching band. In contrast to the other phases, the librational band of the $P\bar{3}m1$ phase is split into two peaks, caused by the differences in primary structure.

The existence of imaginary modes not resulting from numerically unresolved symmetries (see Figure 7) is an indication of phase instabilities; the corresponding atomic displacements can, however, be followed in order to determine the stable phase. The uncertainty in PDOS per mode due to the numerically unresolved translational invariance is about 0.1/THz in the systems considered, as indicated by dashed lines in Figure 7.

We have analyzed the phonon dispersion of the most promising previously proposed $I\bar{4}m2$ structure in detail. At the Γ-point, all frequencies are real within the range of numerical accuracy. At the N-point of the Brillouin zone (center of zone facet) two acoustic modes become unstable. This is an indication of instability due to long wavelength acoustic vibrations. Instability of the low frequency acoustic phonons can be detected via macroscopic deformation of the unit cell. Indeed, an $\epsilon_{x,y}$ shear deformation combined with a relaxation of the internal degrees of freedom and the volume of the unit cell leads to a lowering of the total energy by 6 meV per formula unit.

In order to identify the corresponding ground state structure, we have simultaneously imposed atomic coordinate displacements corresponding to the above mentioned unstable modes of the $I\bar{4}m2$-phase. Following the atomic displacements of these modes, we find that the conventional $I\bar{4}m2$ cell is distorted (in agreement with the shear instability mentioned above) to the primitive cell of a structure in space group $C222_1$ and further to $F222$ symmetry (containing 22 atoms per primitive cell). The ground state energy of the $F222$ phase is lower by 10 meV per formula unit compared to the $I\bar{4}m2$ phase. The phonon dispersion of the $F222$ phase shows, within the numerical accuracy no imaginary frequencies, and we do not find any instabilities with respect to lattice strains, supporting the

thermodynamic stability. Also for the proposed $I4_1/amd$ phase, the numerically calculated PDOS is free of imaginary modes, which supports a meta stability and possible high pressure existence of this high-density structure.

A zone boundary instability of acoustic modes in the $I\bar{4}m2$ structure points out that a normal mode analysis at the Γ-point may fail in predicting meta stability of the structure. Therefore, calculations of the stability of the structure with respect to a macroscopic deformation of the unit cell shall be applied as an additional measure. For stable structures, deformation of the unit cell leads to an increase in energy according to the elastic properties of the compound ($E_{\mathrm{tot}} \sim C\epsilon^2$, where E_{tot} is the total energy of the system, C is the elastic constant, and ϵ is the deformation tensor of the unit cell). A deviation from harmonic behavior, especially a decrease of the total energy for strained structures, indicates a negative value of C, and therefore that the given structure is thermodynamically unstable with respect to macroscopic deformations.

3.4. Free energies

The free energies of the structures determine the relative stability of the different phases. In order to predict at which temperatures phase transitions would occur, we have calculated the lattice free energies from the PDOS above using Eq. (2). In order to show that the decomposition temperature of $Mg(BH_4)_2$ can be estimated, even if a stable ground state structure was not known, we have also calculated free energies in the presence of unstable modes by omitting the corresponding imaginary part (∼1% integrated PDOS for the unstable structures) of the PDOS from the integration in Eq. (2).

Plotting the change in free energy as a function of temperature relative to the low temperature $P6_1$ phase (Figure 8), we find the free energy differences for the $Mg(BH_4)_2$ phases to be relatively small owing to the similar PDOS. The calculated ground state energies (see Table 3) are also quite similar, differing by less than 0.1 eV per H_2 (typically <0.05 eV), even though a comparison of the mass densities shows a large variation for the different phases. The simple

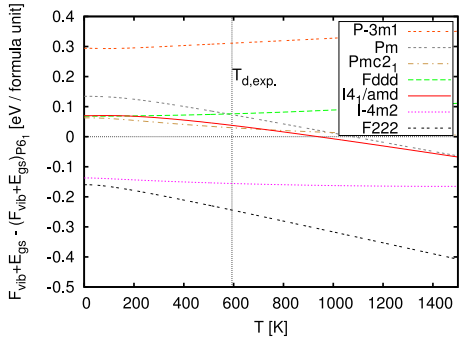

Figure 8. (Colour online) Comparison of free energies with respect to the $P6_1$ low-temperature phase. $T_{\mathrm{d,exp.}}$=320°C is the experimentally determined temperature for the first decomposition step of $Mg(BH_4)_2$ [8].

tetragonal $I\bar{4}m2$ and orthorhombic $F222$ phases are unique, having the lowest ground state energies and a significantly lower density than the other phases. The stable $F222$ structure has the lowest energy of all investigated $Mg(BH_4)_2$ phases.

The phase with third lowest energy is the $P6_1$ phase. According to our calculations, none of the free energies of the higher energy phases cross that of the $P6_1$ phase below the experimentally determined initial decomposition temperature [8] of 320°C (Figure 8). The $P\bar{3}m1$ (erroneous coordination) and surprisingly also the $Fddd$ phase, show no intersection with the free energy of the $P6_1$ phase at all in the temperature range considered here. We note that the $Fddd$ phase is reported to be composed of disordered layers parallel to the b, c-plane [7], which gives raise to entropic contributions not considered here; both ground state configuration and free energy might therefore be different for the experimentally observed phase. Other non-phononic degrees of freedom, like rotations, will furthermore be of relevance at elevated temperatures [23].

To assess or predict at which temperatures the corresponding most stable phases would decompose to release hydrogen, the free energies of the decomposition products also have to be determined.

3.5. Desorption temperatures

The decomposition of $Mg(BH_4)_2$ was recently proposed to proceed in several steps including the formation of dodecaboranate species [8, 24], but to assess the stability of $Mg(BH_4)_2$, we consider only the following idealized decomposition step

$$Mg\,(BH_4)_2 \rightarrow MgH_2 + 2B + 3H_2. \tag{3}$$

We estimate the desorption temperature by comparing the free energies of the $Mg(BH_4)_2$ phases to the Gibbs free energy of the right hand side of reaction (3) (we neglect pV terms for the solid phases). The lattice free energies of MgH_2 (space group $P4_2/mnm$) and B (space group $R\bar{3}m$) have been calculated using the software package Phonon [22], and values for the Gibbs free energy of H_2 have been interpolated from data in Ref. [25].

The temperature dependence of the free energies is shown in Figure 9. The desorption temperature for reaction (3) can be estimated to be 400–470 K for all phases with correct primary coordination. Especially if we disregard the high energy of the configurationally different $P\bar{3}m1$ structure, the estimated desorption temperatures differ only little compared to the accuracy of the DFT-based estimate.

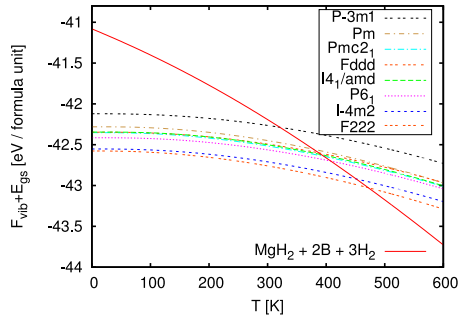

Figure 9. (Colour online) The sum of ground state energy E_{gs} and lattice free energy F_{vib} per formula unit for the different phases of $Mg(BH_4)_2$ and the decomposition products MgH_2 + 2B + $3H_2$.

Due to similar PDOS, the proposed structures would all start to decompose at 400–470 K. This is ∼150 K below the experimentally observed decomposition temperature [8]. This high decomposition temperature is thought to be due to kinetic limitations (in a more complex reaction than (3) [24]) rather than thermodynamic equilibrium properties [8], which have been considered in the calculations presented here.

4. Conclusions

We have analyzed the structural stability of different candidate structures for the promising hydrogen storage material $Mg(BH_4)_2$.

The electronic and phonon density of states are very similar for the investigated phases, resulting in only very small differences in free energies for phases which obey the primary coordination of Mg. By analysis of the instability of the previously proposed $I\bar{4}m2$ phase with respect to a macroscopic transformation of the unit cell characterized by acoustic mode zone boundary instabilities, we have obtained a new structure with $F222$ symmetry. This phase is free of instabilities and has a lower free energy than all other previously proposed structures.

Decomposition temperatures of 400–470 K have been obtained. Since the calculated free energies for the different phases of $Mg(BH_4)_2$ are quite similar for simple systems to very large unit cells, thermodynamic screening studies in, *e.g.* ternary and quaternary borohydride systems are possible by considering only simple model unit cells for an estimate of the structural stability of these compounds, as long as the expected primary coordination is obeyed.

This means that simple model structures can be used to investigate structural stability of complex structures, even if the crystal symmetries are not known *a priori*. In alloyed system, *e.g.* mixed Mg and Ca borohydride, a simple structure should thus allow for tetrahedral and octahedral coordination of Mg and Ca with B atoms, respectively.

We have shown that acoustic instability can be easily detected by macroscopic deformation of the unit cell, constituting a simple

method to determine corresponding structural stabilities beyond a vibrational analysis.

Acknowledgments

The authors acknowledge financial support by the NABIIT program funded by the Danish Research Councils for Strategic Research, the European Commission DG Research (contract SES6-2006-51827/NESSHy), and the Danish Center for Scientific Computing (DCSC) for computer time. The Center for Atomic-Scale Materials Design is supported by the Lundbeck Foundation.

References

[1] Ohba N, Miwa K, Aoki M, Noritake T, ichi Towata S, Nakamori Y, ichi Orimo S and Züttel A 2006 *Phys. Rev. B* **74** 075110
[2] Łodziana Z and Vegge T 2004 *Phys. Rev. Lett.* **93** 145501
[3] Sarner S F 1966 *Propellant Chemistry* 1st ed (New York: Reinhold)
[4] Nakamori Y, Miwa K, Ninomiya A, Li H, Ohba N, Towata S, Züttel A and Orimo S 2006 *Phys. Rev. B* **74** 045126
[5] Wiberg E and Bauer R 1950 *Z. Naturforsch.* **5b** 397
[6] Černý R, Filinchuk Y, Hagemann H and Yvon K 2007 *Angew. Chem.* **119**(30) 5867
[7] Her J H, Stephens P W, Gao Y, Soloveichik G L, Rijssenbeek J, Andrus M and Zhao J C 2007 *Acta Cryst. B* **63**(4) 561
[8] Chłopek K, Frommen C, Leon A, Zabara O and Fichtner M 2007 *J. Mater. Chem.* **17** 3496
[9] Konoplev V N and Bakulina V M 1971 *Bull. Acad. Sci. USSR Div. Chem. Sci (Engl. Transl.)* **20** 136
[10] Vajeeston P, Ravindran P, Kjekshus A and Fjellvåg H 2006 *Appl. Phys. Lett.* **89** 071906
[11] Ozolins V, Majzoub E H and Wolverton C 2008 *Phys. Rev. Lett.* **100** 135501
[12] Dai B, Sholl D S and Johnson J K 2008 *J. Phys. Chem. C* **112** 4391
[13] Setten M J v, Wijs G A d, Fichtner M and Brocks G 2008 *Chem. Mater.* **20** 4952
[14] Riktor M D, Sørby M H, Chłopek K, Fichtner M, Buchter F, Züttel A and Hauback B C 2007 *J. Mater. Chem.* **17** 4939
[15] Hohenberg P and Kohn W 1964 *Phys. Rev.* **136** B864
[16] Kresse G and Furthmüller J 1996 *Phys. Rev. B* **54** 11169
[17] Kohn W and Sham L J 1965 *Phys. Rev.* **140** A1133

[18] Perdew J P, Chevary J A, Vosko S H, Jackson K A, Pederson M R, Singh D J and Fiolhais C 1992 *Phys. Rev. B* **46** 6671
[19] Perdew J P, Chevary J A, Vosko S H, Jackson K A, Pederson M R, Singh D J and Fiolhais C 1993 *Phys. Rev. B* **48** 4978
[20] Blöchl P E 1994 *Phys. Rev. B* **50** 17953
[21] Kresse G and Joubert D 1999 *Phys. Rev. B* **59** 1758
[22] Parlinski K, Li Z-Q and Kawazoe Y 1997 *Phys. Rev. Lett.* **78** 4063; Parlinski K 2005 *Software Phonon* Cracow
[23] Łodziana Z and Vegge T 2006 *Phys. Rev. Lett.* **97** 119602
[24] Hwang S J, Bowman R, Reiter J, Rijssenbeek J, Soloveichik G, Zhao J C, Kabbour H and Ahn C 2008 *J. Phys. Chem. C* **112** 3164
[25] Ke X and Tanaka I 2005 *Phys. Rev. B* **71** 024117

	$a = 10.163$Å		$c = 36.485$Å			
	x	y	z	x	y	z
Mg	0.0336	0.5060	0.9988	0.3373	0.3906	0.4501
	0.5284	0.4941	0.1731	0.3924	0.3388	0.0549
	0.0017	0.1256	0.9194			
B	0.7016	0.7253	0.2999	0.8195	0.8742	0.9381
	0.5420	0.6939	0.8012	0.0159	0.5333	0.7762
	0.0209	0.7240	0.3722	0.4917	0.5056	0.5026
	0.8477	0.3050	0.3700	0.0184	0.4820	0.5623
	0.2941	0.5879	0.3365	0.1275	0.1833	0.0672
H	0.5745	0.6532	0.2865	0.7406	0.8598	0.2967
	0.7822	0.6852	0.2841	0.7113	0.7055	0.3325
	0.7899	0.9424	0.9148	0.9356	0.9511	0.9558
	0.8354	0.7777	0.9219	0.7147	0.8267	0.9600
	0.4965	0.7184	0.7725	0.6279	0.8058	0.8194
	0.6153	0.6331	0.7926	0.4289	0.6165	0.8199
	0.8929	0.4544	0.7612	0.1192	0.6155	0.7555
	0.0503	0.4449	0.7897	1.0007	0.6162	0.7982
	0.8998	0.6840	0.3878	0.9921	0.7046	0.3395
	0.0751	0.6515	0.3857	0.1165	0.8583	0.3755
	0.4869	0.5813	0.4771	0.6266	0.5573	0.5092
	0.4388	0.3704	0.4962	0.4161	0.5121	0.5280
	0.8127	0.3831	0.3514	0.9819	0.3643	0.3784
	0.8198	0.1925	0.3519	0.7788	0.2817	0.3989
	0.8956	0.4393	0.5773	1.0020	0.3836	0.5402
	0.1213	0.5017	0.5829	0.0543	0.6053	0.5488
	0.2087	0.5104	0.3611	0.4164	0.6704	0.3512
	0.2552	0.6691	0.3207	0.2965	0.5031	0.3130
	0.0599	0.2131	0.0906	0.2238	0.1666	0.0833
	0.1753	0.2883	0.0453	0.0500	0.0674	0.0494

Table 1: Calculated lattice parameters and Wyckoff coordinates of $Mg(BH_4)_2$ in spacegroup $P6_1$.

	$I\bar{4}m2$ $a = 8.297$Å $c = 9.339$Å
Mg	(2*a*) (0,0,0); (2*d*) (0,0.5,0.75)
B	(8*i*) (0.7706,0.5,0.5934)
H	(8*i*) (0.2459,0,0.9645); (8*i*) (0.6495,0.5,0.6696); (16*j*) (0.8439,0.6246,0.6194)

	Pm $a = 5.366$Å $b = 4.301$Å $c = 4.299$Å $\gamma = 86.14°$
Mg	(1*a*) (0,0,0)
B	(1*a*) (0.2210,0.0491,0); (1*b*) (0.8212,0.5331,0.5)
H	(1*a*) (0.6899,0.3124,0); (1*a*) (0.0479,0.4611,0);
H	(1*b*) (0.9921,0.1100,0.5); (1*b*) (0.3263,0.2877,0.5);
H	(2*c*) (0.2847,0.8810,0.7212); (2*c*) (0.7762,0.6828,0.2367)

	$Pmc2_1$ $a = 4.261$Å $b = 5.734$Å $c = 8.307$Å
Mg	(2*a*) (0,0.2910,0.0024)
B	(2*a*) (0,0.5189,0.2463); (2*b*) (0.5,0.9218,0.4763)
H	(2*a*) (0,0.4117,0.3744); (2*a*) (0,0.2684,0.7568);
H	(2*b*) (0.5,0.7112,0.4436); (2*b*) (0.5,0.0345,0.3543);
H	(4*c*) (0.2769,0.9715,0.5637); (4*c*) (0.2428,0.5336,0.6773)

	$P\bar{3}m1$ $a = 4.233$Å $c = 5.575$Å
Mg	(1*a*) (0,0,0)
B	(2*d*) (2/3,1/3,0.1952)
H	(2*d*) (2/3,1/3,0.9772); (6*i*) (0.8211,0.1789,0.2787)

Table 2: Calculated lattice parameters and Wyckoff coordinates of proposed high-temperature phases of $Mg(BH_4)_2$.

Paper P4

Understanding the thermodynamic stabilities of cation-alloyed complex metal hydrides from ground state properties of model structures

J Voss[1,2] **and T Vegge**[1]

[1] Materials Research Division, Risø National Laboratory for Sustainable Energy, Technical University of Denmark, DK-4000 Roskilde
[2] Center for Atomic-scale Materials Design, Department of Physics, Technical University of Denmark, DK-2800 Kongens Lyngby
E-mail: johannes.voss@risoe.dk

Abstract. We present a new method for explaining the thermodynamic stabilities of alloyed metal aluminium hexahydrides based on a symmetry analysis of the ground state charge density of model structures obtained within density functional theory. We find good agreement with experiments in identifying stable and unstable alloys.

PACS numbers: 31.15.es, 61.66.Dk
Keywords: Bader charge density analysis, maximally localized Wannier functions, hydrogen storage, complex hydrides, thermodynamic stability

Submitted to: *Modelling Simulation Mater. Sci. Eng.*

`http://www.iop.org/EJ/journal/MSMSE`

1. Introduction

Complex metal hydrides are considered as promising materials for onboard hydrogen storage applications, due to their good volumetric and gravimetric capacities. A major obstacle is to find a material which is both sufficiently thermodynamically stable at ambient conditions, to ensure safety, and releases hydrogen at moderate temperatures (1). By alloying candidate structures, new materials with intermediate thermodynamic properties can possibly be engineered (2; 3). Nakamori *et al.* (4) have found that the heat of formation of metal borohydrides scales linearly with the Pauling electronegativity of the metal, and similar relationships have also been established for metal aluminium hydrides (5).

An unresolved issue is how the stabilities of cation-alloyed complex hydrides can be predicted from a minimal set of properties that are either tabulated values or can be calculated with little computational effort. The experimental results of Graetz *et al.* (2) and density functional theory (DFT) calculations by Løvvik *et al.* (6) show that alloys of the structure $M_2M'\mathrm{AlH}_6$ form only if the cation M has a larger ionic radius than M' (or $M = M'$). In contrast to an expected interpolation, the alloy $\mathrm{Na_2LiAlH_6}$ is found to decompose at higher temperatures than both $\mathrm{Li_3AlH_6}$ and $\mathrm{Na_3AlH_6}$ (2).

The purpose of the presented work is to find computationally inexpensive (based on DFT calculations) "descriptors" to establish approximate scaling relationships to the experimentally well-studied (2) properties of cation-alloyed metal aluminium hexahydrides. In particular, the effect of stabilization of $\mathrm{Na_2LiAlH_6}$ will be investigated as a possible indicator for the perspectives of alloying of hydrogen storage materials beyond a simple interpolation of the properties of the constituents.

Van Setten *et al.* (7) have found that the formation energies of complex metal hydrides can be described reasonably well be rigid-ion electrostatics, neglecting the details of the crystal structure; *i.e.* the knowledge of the ground state crystal structure is not important for a first estimate of the ground state energy. Simple model structures can

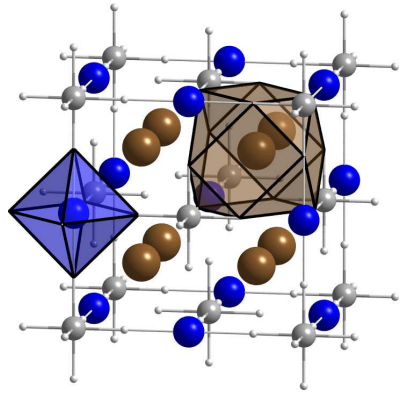

Figure 1. (Colour online.) Calculated crystal structure of K_2NaAlH_6 in space group $Fm\bar{3}m$ (potassium is represented by brown, sodium by blue, aluminium by grey and hydrogen by white spheres). The brown polyhedron represents the 12-fold coordination of a potassium cation, the blue octahedron the coordination of a sodium cation.

thus be used to approximate the ground state properties of complex hydrides. Although different space groups have been determined for the $M_2M'AlH_6$ alloys (2), we use the cubic structure of K_2NaAlH_6 (space group $Fm\bar{3}m$; see Figure 1) as a model structure for all such alloys.

It is important to restrict the calculations to simple model structures, since the search for the ground state structure within DFT is generally very complex considering only a single system, and becomes untractable in the even larger configurational spaces of alloyed systems.

2. Computational details

Lattice constants and internal coordinates have been optimized independently using the DFT (8) codes VASP (9), for an all-electron charge density analysis, and PWSCF (10) for further analysis in a maximally localized wannier function (MLWF) basis (11). In the VASP calculations, projector augmented wave (12) potentials (13)

generated for the Perdew-Wang-91 exchange-correlation functional (14) have been used. In order to construct simple (*i.e.* of smallest possible dimension) MLWF Hamiltonians, single valence electron pseudopotentials (15) for the cations generated for the exchange-correlation functional according to Perdew and Zunger (16) have been used. The Kohn-Sham (17) wave functions have been expanded in plane wave basis sets with kinetic energy cutoffs of 350 eV and a Brillouin zone sampling with a k-point spacing of $\sim$0.03 Å^{-1} (to minimize the dimension of the MLWF Hamiltonian, the corresponding calculations have only been performed for the Γ-point).

A Bader charge density analysis (18) as implemented in Refs. (19; 20) has been performed including gradient information from the core states in the projector augmented wave scheme. The MLWFs have been generated using the Wannier90 code (21).

3. Results

A Bader charge density analysis of the crystal structures $M_2M'\mathrm{AlH_6}$, with $M, M' \in \{\mathrm{Li,Na,K}\}$, shows a symmetric distribution of valence charge between the cation sites, if the octahedral sites are occupied by cations with smaller ionic radii than the sites with 12-fold coordination (see Figure 1). This is the case for the alloys $\mathrm{Na_2LiAlH_6}$, $\mathrm{K_2LiAlH_6}$ and $\mathrm{K_2NaAlH_6}$, which show Bader charge differences of less than $0.3\,e$ (see Figure 2). For $\mathrm{Na_2LiAlH_6}$, the corresponding integrated charge density difference with a magnitude of only $5.8 \cdot 10^{-3}\,e$ is in principle zero in terms of the accuracy of the calculations. The (almost) perfect symmetry of the valence charge distribution between the different cation species could be an indicator for the unexpectedly higher decomposition temperature for the case $(M, M') = (\mathrm{Na, Li})$ compared to the cases $M = M' = \mathrm{Li}$ and $M = M' = \mathrm{Na}$ (2).

For alloys with high asymmetries $\Delta Q \gtrsim 0.3\,e$, *i.e.* more Bader charge attributed to the octahedral sites, on the other hand, no stable alloys exist. These are just the cases where the cation species M have

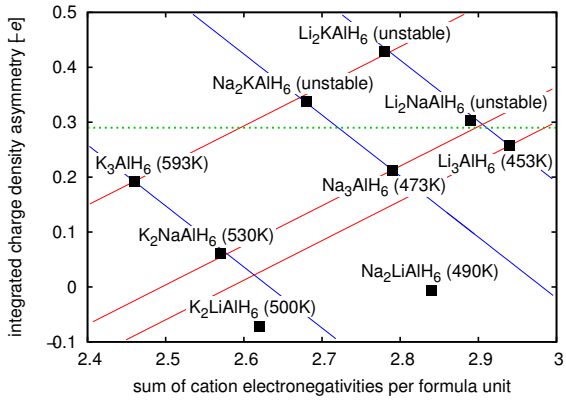

Figure 2. (Colour online.) Differences in the integrated Bader charges around the cations versus the sum of Pauling cation electronegativities per formula unit (decomposition temperatures from (2)). The green dotted line marks an approximate asymmetry threshold above which no stable alloys exist. The blue and red lines connect the alloys with equal cation species in the sites with 12-fold and octahedral coordination, respectively. The two corresponding slopes have been fitted relative to the points with $M = M'$. The Bader charge differences for K_2LiAlH_6 and Na_2LiAlH_6 deviate from the linear trends, in particular for the latter system, which is therefore treated separately in a free energy analysis.

smaller ionic radii than M'. For all systems with smaller asymmetries, the alloys are known to be stable from experiments (2). Although cubic model structures were used for all alloys, instead of calculating the properties of the known crystal structures of the stable alloys, the charge density asymmetry descriptor obtained from the $Fm\bar{3}m$ model structures clearly identifies stable and unstable alloys.

The integrated charge density differences show linear dependencies with respect to the sum of cation negativities for all phases apart from the cases $(M, M') = (\mathrm{Na}, \mathrm{Li})$ and $(M, M') = (\mathrm{K}, \mathrm{Li})$ with highly symmetric Bader charge differences, in particular for the Na_2LiAlH_6 structure, which will be treated separately in a vibrational free energy analysis. The remaining systems with same M or same M' show

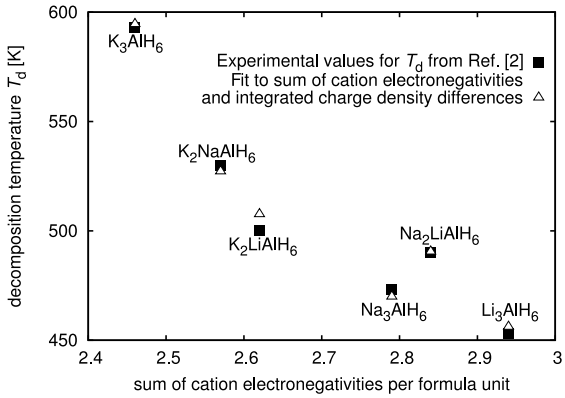

Figure 3. Parametrization of the decomposition temperatures of metal aluminium hexahydride alloys in dependence of the Pauling cation electronegativities and the integrated charge density asymmetries. In order to weight the stabilizing effect of a symmetric charge distribution between the different cation sites, the decomposition temperatures have been fitted to a sum of two exponential functions, $T_\mathrm{d} = 3 \cdot 10^{-8}\,\mathrm{K}(\Delta Q/e)^{-4} + 10^8\,\mathrm{K}\exp(-a\chi) + b$, with the fitting parameters $a = -5.45 \pm 0.01$ and $b = (445 \pm 2)$ K. χ is the sum of cation electronegativities per formula unit and ΔQ the difference in Bader charge between cation sites with octahedral and 12-fold coordination, respectively.

a linear dependence of the valence charge asymmetry descriptor with respect to the sum of cation electronegativities with same slopes for all phases which are related by a substitution for either M or M', respectively. The slopes of the corresponding fits shown in Figure 2 are (in units of the elementary charge) -1.11 ± 0.03 and 0.72 ± 0.02 for the cases of equal M and M', respectively. With the knowledge of the asymmetry descriptor for only one alloy, the asymmetry descriptors for all other alloys could be calculated using these two slopes. For the two highly symmetric cases, the linearly extrapolated asymmetry descriptors would deviate more from the DFT results than for the other structures, but the corresponding alloys would still be identified as being stable.

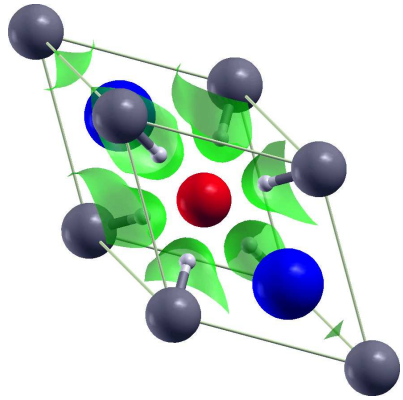

Figure 4. (Colour online.) XCrySDen (25) rendition of the MLWFs centred near the hydrogen positions for the primitive cell of Na_2LiAlH_6. Sodium, lithium, aluminium and hydrogen are represented by blue, red, grey and white spheres, respectively.

For the sake of visualization, we have parametrized the decomposition temperatures of the alloys with respect to the sum of the cation electronegativities per formula unit and to the charge density asymmetry descriptors (see Figure 3). The decomposition temperatures are described relatively well, including the stabilization of Na_2LiAlH_6.

The stability of crystals is determined by the free energy. We will estimate the vibrational contributions to the free energy based on a MLWF analysis. A transformation of the Bloch function basis (without unoccupied bands to reduce the dimensions of the Hamiltonian matrix) to a MLWF basis yields six orbitals per primitive unit cell, which are centred close to the hydrogen positions for all alloys considered here (see an iso-surface plot for the alloy Na_2LiAlH_6 in Figure 4 as an example). We will estimate the effect of changes in the electronic orbitals to approximate zero point free energies, without calculating the perturbed electronic eigenstates due to atomic displacements. For simplicity, we shift the sum of electronic eigenenergies of the six-dimensional MLWF Hamiltonian, such that the diagonal elements in the MLWF basis (which are all equal due to

symmetry) become zero. We estimate the effect of the displacement of a hydrogen atom on the electron Hamiltonian H to be given by the transformation $\mathcal{T}^{+}H\mathcal{T}$, with the operator

$$\mathcal{T} = 1 + \Big(|\tilde{w}\rangle - |w\rangle\Big)\langle w|, \tag{1}$$

where $|w\rangle$ is a MLWF and $|\tilde{w}\rangle$ the MLWF displaced from its centre. The total electronic energy for the perturbed configuration is given by the trace over the transformed Hamiltonian. Using that the diagonal elements $\langle w|H|w\rangle$ are zero, the trace becomes

$$\mathrm{Tr}(\mathcal{T}^{+}H\mathcal{T}) = \langle w|H|\tilde{w}\rangle + \mathrm{h.c.} + E, \tag{2}$$

with the unperturbed electronic ground state energy E. Approximating the effect of a displacement of a hydrogen atom by a translation of the corresponding Wannier centre, we estimate the electronic contribution to the corresponding Hessian diagonal elements by finite differences in the displacements. The remaining contributions to the Hessian are estimated from the electrostatics of the ionic core system using an Ewald summation (22), with the ionic cores being approximated as point charges equalling the negative of the corresponding valence charges.

Since the $Fm\bar{3}m$ structure is not the ground state configuration for all the systems considered, imaginary phonon frequencies could appear corresponding to phase transitions. The phonon spectra of these complex systems are, however, dominated by high frequency librational and Al–H bond stretching and bending modes in the range of $\sim$100–200 meV (23), while the imaginary modes correspond to rearrangement of the M, M'–Al framework. We can therefore estimate the dominant contribution to the zero point lattice free energy with phonon energies $\gtrsim$100 meV by only considering the corresponding eigenmodes of the hydrogen sub system, keeping the other atomic degrees of freedom fixed. Table 1 shows the estimated zero point free energies in comparison to DFT calculations using finite displacements to calculate the Hessian matrices. The approximated free energies are found to be within 20% of the computationally more expensive results based on several DFT

	$\tilde{F}$ [eV]	F [eV]
stable phases		
Li_3AlH_6	1.26	1.54
Na_2LiAlH_6	1.23	1.42
Na_3AlH_6	1.34	1.44
K_2LiAlH_6	1.24	1.27
K_2NaAlH_6	1.31	1.32
K_3AlH_6	1.39	1.33
unstable phases		
Li_2NaAlH_6	1.33	1.52
Li_2KAlH_6	1.40	1.46
Na_2KAlH_6	1.39	1.43

Table 1. Librational and bond stretching and bending contributions to the free energy at $T = 0$. The energies $\tilde{F}$ are based on electrostatic contributions from the ionic cores and perturbations of the Wannier centres, and the energies F are calculated within DFT using finite displacements.

calculations for displaced configurations. Both approaches yield the lowest vibrational contribution to the free energy for the stabilized Na_2LiAlH_6 in the sector of stable alloys containing lithium and/or sodium cations, showing that these contributions to the entropy could explain why Na_2LiAlH_6 is more stable than the constituting phases Li_3AlH_6 and Na_3AlH_6. X-ray powder diffraction patterns of Na_2LiAlH_6 show no deviation from the stocheometry M=Na and M'=Li (24); configurational contributions to the entropy can thus be neglected.

4. Conclusion

Based only on DFT calculations of model ground state structures of cation-alloyed aluminum hexahydrides, we are able to explain the stabilities of the corresponding systems. We find the difference in Bader charge around the different cation sites to be a good

descriptor of the stability of the alloys. These asymmetry descriptors themselves show a general linear correlation to the sum of Pauling cation electronegativities with deviations for alloys which are more stable than the constituents. Inclusion of rough estimates of the zero point lattice free energies, supporting the stabilities of these alloys, can be obtained from a distortion analysis of a MLWF basis of the ground state model structures.

Our results show the potential of predicting thermodynamic properties of alloyed complex metal hydrides based on ground state calculations within DFT beyond an assumed interpolation of the known properties of the constituents.

Acknowledgments

We acknowledge financial support by the NABIIT program funded by the Danish Research Councils for Strategic Research, and the Danish Center for Scientific Computing (DCSC) for computer time. The Center for Atomic-scale Materials Design is supported by the Lundbeck Foundation.

References

[1] Orimo S, Nakamori Y, Eliseo J R, Züttel A and Jensen C M 2007 *Chem. Rev.* **107** 4111
[2] Graetz J, Lee Y, Reilly J J, Park S and Vogt T 2005 *Phys. Rev. B* **71** 184115
[3] Nickels E A, Jones M O, David W I F, Johnson S R, Lowton R L, Sommariva M and Edwards P P 2008 *Angew. Chem.* **120** 2859
[4] Nakamori Y, Miwa K, Ninomiya A, Li H, Ohba N, Towata S, Züttel A and Orimo S 2006 *Phys. Rev. B* **74** 045126
[5] Matsunaga T, Buchter F, Miwa K, Towata S, Orimo S and Züttel A 2008 *Renew. Energ.* **33** 193
[6] Løvvik O M, Swang O and Opalka S M 2005 *J. Mater. Res.* **20** 3199

[7] van Setten M J, de Wijs G A and Brocks G 2007 *J. Phys. Chem. C* **111** 9592
[8] Hohenberg P and Kohn W 1964 *Phys. Rev.* **136** B864
[9] Kresse G and Furthmüller J 1996 *Phys. Rev. B* **54** 11169
[10] Baroni S, de Gironcoli S, Dal Corso A, Giannozzi P *et al.* `http://www.pwscf.org`
[11] Marzari N and Vanderbilt D 1997 *Phys. Rev. B* **56** 12847
[12] Blöchl P E 1994 *Phys. Rev. B* **50** 17953
[13] Kresse G and Joubert D 1999 *Phys. Rev. B* **59** 1758
[14] Perdew J P, Chevary J A, Vosko S H, Jackson K A, Pederson M R, Singh D J and Fiolhais C 1992 *Phys. Rev. B* **46** 6671
[15] Pseudopotentials of von Barth-Car type from `http://www.quantum-espresso.org`
[16] Perdew J P and Zunger A 1981 *Phys. Rev. B* **23** 5048
[17] Kohn W and Sham L J 1965 *Phys. Rev.* **140** A1133
[18] Bader R F W 1990 *Atoms in Molecules – A Quantum Theory* (Oxford: Oxford University Press)
[19] Henkelman G, Arnaldsson A and Jónsson H 2006 *Comput. Mater. Sci.* **36** 254
[20] Sanville E, Kenny S D, Smith R and Henkelman G 2007 *J. Comput. Chem.* **28** 899
[21] Mostofi A A, Yates J R, Lee Y S, Souza I, Vanderbilt D and Marzari N 2008 *Comput. Phys. Commun.* **178** 685
[22] Ewald P P 1921 *Ann. Phys. (Leipzig)* **64** 253
[23] Voss J and Vegge T 2008 *J. Chem. Phys.* **128** 184708
[24] Claudy P, Bonnetot B, Bastide J P and Létoffé J M 1982 *Mat. Res. Bull* **17** 1499
[25] Kokalj A 1999 *J. Mol. Graph. Model.* **17** 176

Paper P5

Hydrogen dynamics in Na_3AlH_6 - a combined density functional theory and quasielastic neutron scattering study

J. Voss,[1,2] Q. Shi,[1,3] H. S. Jacobsen,[1,3] M. Zamponi,[4] K. Lefmann,[1] and T. Vegge[1]

[1]Materials Research Department, Risø National Laboratory, Technical University of Denmark, DK-4000 Roskilde, Denmark
[2]Center for Atomic-scale Materials Design, Technical University of Denmark, DK-2800 Kongens Lyngby, Denmark
[3]Niels Bohr Institute, University of Copenhagen, DK-1017 Copenhagen, Denmark
[4]Institut für Festkörperforschung, Forschungszentrum Jülich, D-52425 Jülich, Germany

Accepted manuscript of the article J. Phys. Chem. B **111**, 3886 (2007)

http://dx.doi.org/10.1021/jp0667036

Abstract

Understanding the elusive catalytic role of titanium-based additives on the reversible hydrogenation of complex hydrides is an essential step towards developing hydrogen storage materials for the transport sector. Improved bulk diffusion of hydrogen is one of the proposed effects of doping sodium alanate with $TiCl_3$, and here we study hydrogen dynamics in doped and undoped Na_3AlH_6 using a combination of density functional theory calculations and quasielastic neutron scattering. The hydrogen dynamics is

found to be vacancy mediated and dominated by localized jump events, whereas long range bulk diffusion requires significant activation. The fraction of mobile hydrogen is found to be small for both undoped and doped Na_3AlH_6 even at 350 K, and improved hydrogen diffusion as a result of bulk substituted titanium is found to be unlikely. We also propose that previously detected low temperature point defect motion in sodium alanate could result from vacancy mediated sodium diffusion.

1 Introduction

In 1997 Bogdanović and Schwickardi[1] showed that sodium alanate doped with titanium is cyclically dis- and rechargeable with hydrogen under near ambient conditions. $NaAlH_4$ decomposes in two steps:

$$\begin{aligned} NaAlH_4 &\leftrightarrow \frac{1}{3}Na_3AlH_6 + \frac{2}{3}Al + H_2 \\ &\leftrightarrow NaH + Al + \frac{3}{2}H_2, \end{aligned} \tag{1}$$

where the two steps release 3.7 and 1.9 weight-% of hydrogen, respectively. The decomposition temperature of NaH is generally too high for hydrogen storage applications.[2]

Despite intense research efforts, the physical understanding of the catalytic role of titanium on the improved hydrogen ab- and desorption kinetics has remained elusive, possibly due to a multiplicity in effects.[3,5,4,6]

A number of different models have been proposed to describe the catalytic effect of titanium, one of which is the formation of catalytic Al_xTi_y complexes at the surface,[7] improving either dissociation and recombination of molecular hydrogen or mass transport; a second model suggests bulk substitution of titanium for aluminum or sodium atoms, whereby hydrogen diffusion can be improved.[8]

Recent anelastic spectroscopy experiments on thermally treated sodium alanate samples reveal fast point defect dynamics at $T = 70$ K with a much larger fraction of mobile species for titanium doped samples, therefore appearing to support the model of improved hydrogen diffusion due to bulk substituted titanium.[9] This anelastic feature is expected to occur in the Na_3AlH_6 phase.[10]

In this paper, we focus on bulk hydrogen dynamics in the intermediate product Na_3AlH_6. By combining density functional theory (DFT) calculations and quasielastic neutron scattering (QENS), we find the hydrogen dynamics to be vacancy mediated and dominated by localized events. The mobile hydrogen fraction is found to be low for both undoped and Ti-doped Na_3AlH_6, and long range bulk diffusion requires significant activation. Improved hydrogen diffusion due to bulk substituted titanium[8] is found to be unlikely.

2 Theoretical Method

The electronic structure is calculated using density functional theory[12] in the DACAPO plane wave basis set implementation.[13] The ion cores are described by ultrasoft pseudopotentials.[14] The exchange and correlation effects are described by the PW91 functional.[15] The Kohn-Sham wavefunctions[12] are expanded in a plane wave basis set with a cutoff energy of 340 eV (for the density grid a cutoff of 600 eV is used). The wave functions are sampled on a k-point mesh of spacing $\sim$0.3 Å^{-1} in all three directions.

The total energy of the system and the Hellmann-Feynman forces on the ion cores are minimized using a quasi Newton method.[16] In order to calculate the optimum crystal structure for $T = 0$ K, both atomic coordinates and unit cell parameters are relaxed iteratively. The resulting structural parameters for $P2_1/n$-Na_3AlH_6 (space group # 14) are presented in Table 1 (the values for β tend to vary insignificantly between different calculations[2,17,18,19] and experiment[20]). For the calculation of formation and activation energies, we use computational (2x2x1) supercells with volume $2 \cdot 5.27 \times 2 \cdot 5.46 \times 7.60$ Å^3, containing 80 atoms.

In the calculational setup, vacancies are created by removing an atom from the supercell and re-relaxing the atomic coordinates. Two such vacancy configurations are then considered as initial and final state of a vacancy mediated diffusion process, respectively.

A path technique known as the nudged elastic band (NEB) method[21] is used to accurately determine activation energies for the hydrogen dynamics. Here, the reaction path is represented by a finite number of configurations. An initial guess for the coordinates of the intermediate images of the system is a linear interpolation between the initial and final states. This path is then relaxed to the minimum energy path on the potential energy sur-

Unit cell parameters [Å]	
$a = 5.27$	(5.39)
$b = 5.46$	(5.514)
$c = 7.60$	(7.725)
$\beta = 89.99°$	(89.86°)

Wyckoff positions		
Na($2b$):	0, 0, 0.5	
Na($4e$):	-0.010, 0.454, 0.255	(-0.006, 0.461, 0.252)
Al($2a$):	0, 0, 0	
H($4e$):	0.102, 0.051, 0.218	(0.091, 0.041, 0.215)
H($4e$):	0.226, 0.329, 0.544	(0.234, 0.328, 0.544)
H($4e$):	0.162, 0.269, 0.934	(0.165, 0.266, 0.944)

Table 1: Calculated structural parameters for $P2_1/n$-Na_3AlH_6 (experimental values from [20] in parentheses).

face. The NEB consists of the configurations connected by springs, which stabilize the distances between the images. Only spring forces parallel to the path are considered in order to avoid perturbation of the curved path. Atomic forces are considered only perpendicular to the path, such that the energy gradients dragging the intermediate images to the initial and final states are mapped out, respectively.

For the accurate localization of transition states, *i.e.* local maxima of the minimum energy path, a modification of the NEB approach is used: the adaptive nudged elastic band (ANEB) method.[22] In this approach, sub paths consisting of only five configurations are relaxed iteratively, where the internal sub path containing the current configuration with highest energy is replaced by a sub path. Therefore, this method will generally find the transition state of a simple path with only one maximum.

For thermally activated processes like those investigated here, the activation energy E_a, *i.e.* the difference between the ground state energy of initial and transition state, enters the reaction rate in a Boltzmann factor. The corresponding relation is known as the Arrhenius equation:

$$\tau^{-1} = \tau_0^{-1} \exp\left(-\frac{E_\mathrm{a}}{k_\mathrm{B}T}\right). \tag{2}$$

The prefactor τ_0^{-1} is determined by the ratio of the partition functions of

the transition and initial state, respectively.[23] In harmonic transition state theory,[23] the prefactor only depends on the eigenfrequencies of the initial and transition state:

$$\tau_{0,\mathrm{TST}}^{-1} = \frac{1}{2\pi} \frac{\prod_i \omega_i^{\mathrm{I}}}{\prod_j' \omega_j^{\mathrm{T}}}, \tag{3}$$

where the prime denotes that the imaginary frequency at the transition state corresponding to the unstable eigenmode in the direction of the reaction coordinate is left out. The harmonic approximation has previously been shown even to be able to treat complex systems and elevated temperatures.[25,24]

The eigenfrequencies are calculated by mass-weighting the diagonalized Hessian of the total energy. The Hessian is determined by calculating the Hellmann-Feynman forces for configurations with each atom displaced in one direction.

3 Experimental Methods

The Na_3AlH_6 samples were synthesized by energetic ball-milling of stoichiometric mixtures of NaH and $NaAlH_4$ as proposed by Hout *et al.*[26] $NaAlH_4$ (Sigma-Aldrich, 90%), NaH (Sigma-Aldrich, 95%), and the catalyst precursor, $TiCl_3$ (Alfa Aesar, $TiCl_3{\cdot}1/3\ AlCl_3$, purity 76-78% $TiCl_3$) were used as received in powder form. The pure Na_3AlH_6 sample (sample I) was prepared by ball-milling of stoichiometric mixtures of NaH and $NaAlH_4$ for 5 hours. In sample II, 4 mol-% $TiCl_3$ was added to a mixture of $NaAlH_4$ and NaH, which had already been ball-milled for 4.5 hours, and subsequently ball-milled for an additional half hour. All materials handling was performed in an argon-filled glove box. The powder ball-milling was performed in a stainless steel vial with 55 cm^3 internal volume sealed with Teflon O-rings. Five wolfram carbide (WC) balls with a diameter of approximately 10 mm and a total weight of about 31 g were used for the preparation of the samples. Three grams of each sample was produced with the weight ratio of ball to powder as 10:1. The samples were characterized with X-ray powder diffraction (XRPD) using a Bragg-Brantano STOE diffractometer (40 kV, 30 mA, Cu K_α with $\lambda = 1.5418$ Å). The sample powders were placed in a specially designed air-tight sample holder with an aluminum foil X-ray window and a Si reference under inert gas protection in a glove box.

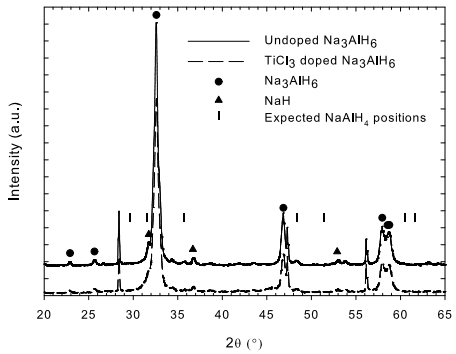

Figure 1: The X-ray powder diffraction spectra of $NaAlH_4 + 2NaH$ mixture ball-milled 5 hours (upper) and 4.5 hours continued another half hour with addition of $TiCl_3$ (lower). The sharp peaks at 28.44°, 47.30°, and 56.12° stem from the Si reference sample.

The X-ray powder diffraction spectra of doped/undoped Na_3AlH_6 (see Fig. 1) show a very high rate of conversion since the $NaAlH_4$ peaks are absent and only small peaks of NaH (decomposed Na_3AlH_6) are seen.

In the present work, the quasielastic neutron scattering (QENS) technique was employed to investigate the hydrogen dynamics in Na_3AlH_6. QENS experiments were performed on the high-resolution backscattering spectrometer (BSS) located at the Forschungszentrum Jülich. The backscattering geometry for both monochromator and analyzer is employed to obtain an energy resolution of $0.8\,\mu$eV FWHM, making it possible to resolve quasielastic broadening of approximately $0.1\,\mu$eV. Doppler-shifting the incident neutrons by rapidly moving the monochromator crystals changes the incident energy, E_i. The setup has energy transfers of $\pm 17\,\mu$eV. With the Si(111) monochromator and analyzer a neutron wavelength of $\lambda = 6.271$ Å is selected. Ten helium counters, which were located very close to the sample, record the analyzed neutrons simultaneously.

The samples were loaded in flat $0.1 \times 30.0 \times 40.0\,\mathrm{mm}^3$ Al containers sealed with indium wire. The sample thickness was chosen to minimize multiple-scattering effects. The powder-filled containers were oriented close to 45° with respect to the incident beam. The spectra were recorded by ten detectors which correspond to a range of scattering vectors of $q = 0.16$–$1.87\,\mathrm{Å}^{-1}$. The instrumental resolution functions were determined from the

measured QENS spectra of each sample at low temperature ($T = 30\,\mathrm{K}$).

Due to the large incoherent scattering cross-section for hydrogen,[27] QENS is an optimal technique for studying hydrogen dynamics, since almost all signal stems from hydrogen atoms. The measured neutron scattering intensity in the experiment is proportional to the dynamical structure factor $S(q,\omega)$, which is a sum of coherent and incoherent contributions:

$$S(q,\omega) = S_{\mathrm{coh}}(q,\omega) + S_{\mathrm{inc}}(q,\omega), \tag{4}$$

in which q is the scattering vector and $\hbar\omega$ is the energy transfer. $S(q,\omega)$ is understood as the powder average of $S(\boldsymbol{q},\omega)$:

$$S(q,\omega) = \frac{1}{4\pi}\int \mathrm{d}\Omega\, S(\boldsymbol{q},\omega). \tag{5}$$

The incoherent scattering function $S_{\mathrm{inc}}(\boldsymbol{q},\omega)$ is the space and time Fourier transform of the self-correlation function $G_{\mathrm{s}}(\boldsymbol{r},t)$, describing the probability that a particle, which at time $t_0 = 0$ is located at the origin, is found at position $\boldsymbol{r}$ at time t. $S_{\mathrm{inc}}(\boldsymbol{q},\omega)$ also can be expressed in terms of the intermediate scattering function $I(\boldsymbol{q},t)$:

$$S_{\mathrm{inc}}(\boldsymbol{q},\omega) = \int \mathrm{d}t\, I(\boldsymbol{q},t)\exp(i\omega t) \tag{6}$$

$$I(\boldsymbol{q},t) = \int \mathrm{d}^3 r\, G_{\mathrm{s}}(\boldsymbol{r},t)\exp(i\boldsymbol{q}\boldsymbol{r}), \tag{7}$$

with $I(\boldsymbol{q},t)$ being the space Fourier transform of the self-correlation function $G_{\mathrm{s}}(\mathrm{r},t)$. For small q, this space Fourier transform has the form of $I(\mathrm{q},t) = \exp(-q^2 Dt)$, which represents an exponential decay in time (D is the diffusion constant). The time Fourier transform then has a Lorentzian lineshape:

$$S_{\mathrm{inc}}(q,\omega) = \frac{1}{\pi}\frac{Dq^2}{\left(Dq^2\right)^2 + \omega^2.} \tag{8}$$

This expression has a peak at $\omega = 0$ with a width (HWHM) of

$$\Gamma = Dq^2. \tag{9}$$

For large q, equation (9) generally is not valid, because the diffusion cannot be considered continuous. The finite steps of diffusing atoms in lattices are

taken into account by the Chudley-Elliott model.[28] For long range diffusion of hydrogen atoms, Γ is given for large q by

$$\Gamma(q) = \frac{6D}{L^2}\left(1 - \frac{\sin qL}{qL}\right), \tag{10}$$

for a fixed hydrogen jump length L and a hydrogen diffusion constant for a spherical jump distribution

$$D = \frac{L^2}{6\tau}. \tag{11}$$

When a quasielastic compenent is present, the spectra are fitted to the model of an incoherent scattering function:

$$\begin{aligned} S_{\mathrm{inc}}^{\mathrm{tot}}(q,\omega) &= R(q,\omega) \\ &\quad \otimes \Big(B_0\delta(\omega) + B_1 L_0(\omega,\Gamma)\Big) \\ &\quad + C_{\mathrm{backgr.}}, \end{aligned} \tag{12}$$

in which $\delta(\omega)$ is the elastic delta function, $L_0(\omega,\Gamma)$ is the quasielastic Lorentzian with an energy width (HWHM) Γ at $\omega = 0$, B_0 is the elastic incoherent signal, and $C_{\mathrm{backgr.}}$ is the constant background term. The ratio of the amplitudes $B_1/(B_0{+}B_1)$ determines the fraction of mobile hydrogen atoms. The convolving function $R(q,\omega)$ is the instrumental resolution function, which for this instrument is modeled well by the sum of one Gaussian and two Lorentzians with half widths $\sigma_1, \sigma_2, \sigma_3$, respectively:

$$\begin{aligned} R(q,\omega) &= A_1 G_1(\omega,\sigma_1) + A_2 L_1(\omega,\sigma_2) \\ &\quad + A_3 L_2(\omega,\sigma_2). \end{aligned} \tag{13}$$

4 Results and Discussion

Hydrogen diffusion through the bulk towards the surface is important for fast desorption from the material. This type of process is either mediated by hydrogen interstitials or vacancies.

4.1 DFT results

From the DFT calculations, we find the formation energy of hydrogen interstitials to be very high: 2.42 eV for undoped Na_3AlH_6. For Ti@Al-doped

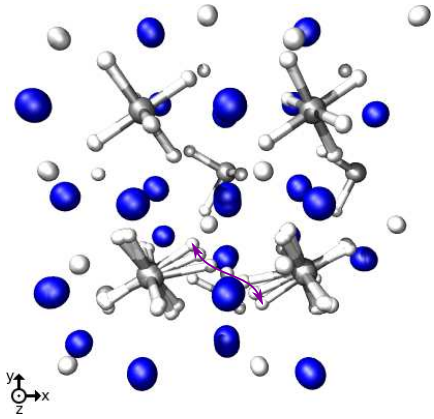

(a)

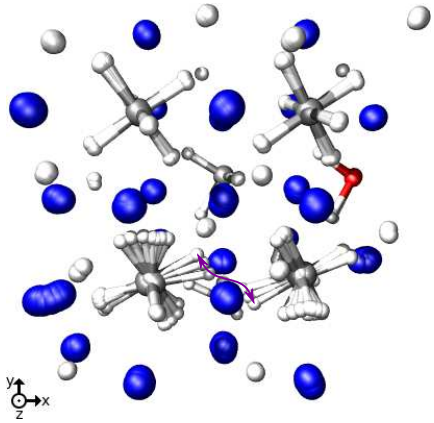

(b)

Figure 2: (colors online) Long range hydrogen diffusion path in (a) $Na_{24}Al_8H_{47}$ and (b) $Na_{24}(Ti@Al)Al_7H_{47}$. Representing colors: sodium: blue, aluminum: gray, titanium: red, and hydrogen: white.

Na_3AlH_6, the energy is also high, but it depends on the distance to titanium. Away from Ti, molecular hydrogen forms (due to weakened Al–H bonds caused by Ti), whereas the formation energy of an interstitial next to titanium is 0.74 eV plus the high cost of the Ti substitution (see below).

Hydrogen diffusion in Na_3AlH_6 is therefore expected to be mediated by hydrogen vacancies, which diffuse between neighboring $(AlH_5)^{2-}$ and $(AlH_6)^{3-}$ groups (see Fig. 2(a)).

Deposition of titanium atoms into the alanate matrix is done by bulk substitution of Ti@Al-sites. In the bulk, the Al-sites are found to be preferred over Na-sites in agreement with existing calculations[19] also using the cohesive energies of aluminum, sodium, and titanium as references. For Ti@Al-sites, the calculated substitution energy is 0.95 eV, for Ti@2*b*-Na-sites 2.44 eV, and for Ti@4*e*-Na-sites 2.00 eV. Assuming Ti does bulk substitute for Al, an effect of titanium could be a lowering of the hydrogen vacancy formation energies. The DFT calculations result in a vacancy formation energy of 1.54 eV for undoped Na_3AlH_6. Depending on the site, the formation energy for a hydrogen vacancy in the $(AlH_6)^{3-}$ groups surrounding titanium in $Na_{24}(Ti@Al)Al_7H_{48}$ can be as low as 1.38 eV.

Taking into account the energy required for the Ti@Al substitution (0.95 eV), the hydrogen vacancy formation in pure Na_3AlH_6 is energetically cheaper. However, titanium substituting aluminum can act as a hydrogen trapping site; thereby creating a hydrogen vacancy by transferring a distant hydrogen atom close to titanium, which is comparatively cheap: 0.26 eV (distance Ti–H initially 7.2 Å). With an energy of 0.95 eV for the substitution of aluminum by titanium, the total cost for this local hydrogen vacancy formation without removing a hydrogen atom from the bulk is 1.21 eV, *i.e.* 0.33 eV less expensive compared to hydrogen vacancy formation in undoped Na_3AlH_6.

Fig. 2(b) shows the diffusion of a hydrogen atom from an $(AlH_6)^{3-}$ to an $(AlH_5)^{2-}$ group in titanium doped Na_3AlH_6 (titanium substituting aluminum: $Na_{24}(Ti@Al)Al_7H_{48}$). The activation energies obtained from the NEB calculations are quite high for undoped Na_3AlH_6: $E_a = 0.75$ eV or higher. There are two possible hydrogen diffusion paths with jump lengths around 3.0 Å having barriers of the order of 0.8–0.9 eV and three paths at 3.1–3.2 Å with higher barriers around 1.0 eV. For Ti@Al-doped Na_3AlH_6, the barrier can be significantly lower, depending on the diffusion path and the distance to the titanium dopant. Barriers as low as 0.36 eV are found

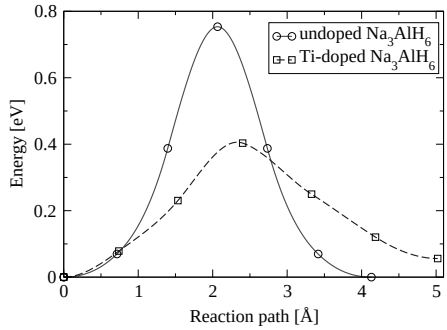

Figure 3: Minimum energy paths for long range hydrogen diffusion in undoped and titanium doped Na_3AlH_6.

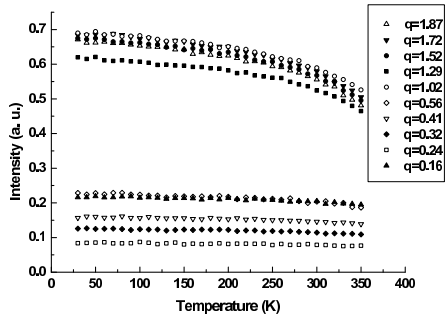

Figure 4: Elastic temperature scans on undoped Na_3AlH_6.

(see Fig. 3), although these are only accessible to a small fraction of the hydrogen atoms (<1% for ∼4 mol-% $TiCl_3$ dopant). The corresponding hydrogen jump lengths are 3.08 and 2.80 Å for the undoped and titanium doped system, respectively. Jumps directly to and from titanium are not considered, because titanium binds additional hydrogen atoms quite strongly, and hence does not promote hydrogen diffusion.

We continue by comparing these findings to the experimental observations from the QENS experiments.

4.2 QENS data

Elastic temperature scans at $\hbar\omega = 0$ on doped and undoped Na_3AlH_6 at 30–350 K (see Fig. 4) show a roughly linear decrease in intensity with

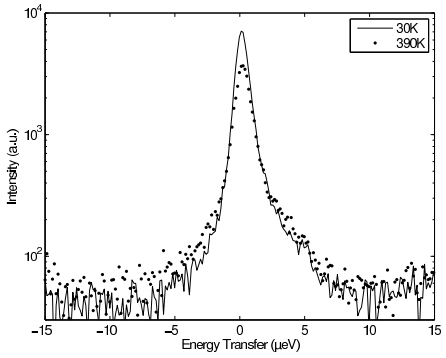

Figure 5: The QENS spectra with $q = 1.87\,\text{Å}^{-1}$ for undoped Na_3AlH_6 measured at $T = 30\,\text{K}$ and $390\,\text{K}$, respectively.

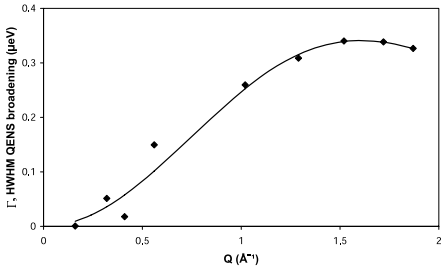

Figure 6: Quasielastic broading versus scattering angle for undoped Na_3AlH_6 at $T = 390\,\text{K}$ (solid line: fit to Chudley-Elliott diffusion model).

T up to $\sim$250 K and a Debye-Waller q-dependence.[29] Above this value, there is a downwards curvature, indicating that intensity is transfered to the inelastic regions. QENS spectra of undoped Na_3AlH_6 were measured at 150 K, 250 K, 350 K, and 390 K, and the doped samples at 300 K and 350 K. QENS spectra with $q = 1.87\,\text{Å}^{-1}$ for undoped Na_3AlH_6 measured at $T = 30\,\text{K}$ and $390\,\text{K}$ are shown in Fig. 5.

The spectra in Fig. 5 show limited quasielastic broadening for undoped Na_3AlH_6 at 390 K, best seen in the tails at ± 2–$4\,\mu$eV. At lower temperatures, effectively no broadening was observed in the undoped samples. The hydrogen atoms are assumed to be frozen at low temperature ($T = 30$K), thus the instrumental resolution function for each value of q was determined by fitting the QENS spectrum with a quasielastic Lorentzian halfwidth of

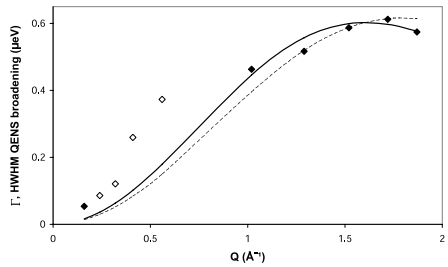

Figure 7: Quasielastic broadening versus scattering angle for titanium doped Na_3AlH_6 at $T = 350\,\mathrm{K}$ (solid line: Chudley-Elliott fit for long range diffusion; dashed line: Chudley-Elliott fit for localized hydrogen dynamics in the undoped system; empty diamonds: low intensity resulting in high uncertainty in Γ).

zero in equation (12). The QENS spectra at higher temperatures were fitted with fixed resolution parameters and free values of Γ, B_0, B_1, and C. The q-dependence of the quasielastic Lorentzian halfwidths as a function of scattering vectors is shown for undoped Na_3AlH_6 at 390 K (Fig. 6) and doped Na_3AlH_6 at 350 K (Fig. 7). Due to a lower signal intensity and thus higher uncertainty at low q-values in the present work, the ratio of the amplitudes $B_1/(B_0+B_1)$, *i.e.* the fraction of mobile hydrogen atoms, determined at high q was used as a fixed value when data fitting at low q.

4.3 Combined data analysis

An accurate fit of the QENS data for undoped Na_3AlH_6 at $T = 390\,\mathrm{K}$ to the Chudley-Elliott diffusion model (see Fig. 6) yields a hydrogen jump length of $L \simeq 2.80\,\text{Å}$ and an inverse jump rate $\tau = 2.35\,\mathrm{ns}$. At this temperature, 13% of the hydrogen was found to be mobile. Since the diffusion is vacancy mediated, it must be taken into account that only the motion of the vacancy can be considered as a random walk, while the involved atomic motions are correlated (see *e.g.* [30]). In a zero-order approximation, *i.e.* one atomic jump per vacancy diffusion step, the only effect is a rescaling of τ.[31] The uncertainty on τ might therefore be significant, but even a 50% error in τ only results in an error of $k_\mathrm{B}T/2$ in the activation energy, corresponding to $\sim$20 meV at 390 K.

Using a prefactor of $\tau_0^{-1} = 2.23 \cdot 10^{13}\,\mathrm{s}^{-1}$ obtained from a vibrational

analysis of the initial and transition state of an internal hydrogen diffusion path using DFT calculations, we obtain an activation energy of 0.37 eV from the Chudley-Elliott fit. This barrier is much lower than the activation energies calculated using DFT for diffusional processes in undoped Na_3AlH_6. Since the QENS data for undoped Na_3AlH_6 did not show signatures of hydrogen motion corresponding to jump lengths and activation energies obtained from the DFT calculations for long range diffusion (cf. table 2), we continued to investigate localized events, *i.e.* vacancy mediated hydrogen jumps on the same $(AlH_5)^{2-}$ complex. This is supported by a q-dependent elastic incoherent structure factor[32] as opposed to $NaAlH_4$,[33] indicating spatial localization of the diffusing species in undoped Na_3AlH_6. These localized events will not contribute to macroscopic hydrogen diffusion.

The QENS data was found to be in good agreement with our DFT results for hydrogen jumps in the same $(AlH_5)^{2-}$ group (see Fig. 8), where the calculated activation energy is 0.41 eV (energies and jump lengths, $L = 2.50$ Å, are equal for all possible jump sites on an $(AlH_5)^{2-}$ group, leading to only one Lorentzian in the QENS spectrum). The calculated barrier for long range diffusion is at least 0.75 eV.

For titanium doped Na_3AlH_6, a Chudley-Elliott fit for $T = 350$ K (see Fig. 7) using a calculated prefactor of $\tau_0^{-1} = 2.13 \cdot 10^{13}\,\mathrm{s}^{-1}$ results in an activation energy of 0.31 eV. In this case, the fraction of mobile hydrogen fractions is found to be as low as 2%. This value was fixed, based on an average of the high q results, but the broadening is sensitive to this fraction. The lower barrier could stem from long range hydrogen diffusion near a Ti@Al dopant with a calculated activation energy of $E_a = 0.36$ eV and a jump length of $L = 2.80$ Å. The broadening is more likely explained by localized dynamics in undoped Na_3AlH_6 with a jump length of 2.50 Å (see Fig. 7), since only a slightly higher fraction of mobile hydrogen is observed for Ti-doped Na_3AlH_6. In undoped Na_3AlH_6 at 350 K, less than 1% of the hydrogen appears to be mobile, but it was not possible to determine the broadening as a function of q, due to the weak intensity. The observed broadening appears to be similar for undoped and doped Na_3AlH_6 samples at 350 K.

It should be noted that for localized, low barrier jumps between interstitial sites in other systems with higher symmetry, *e.g.* as observed in Laves phase materials,[34] one would expect a q-independent broadening at large

	$\tau^{-1}(T)$ [GHz]	L [Å]	E_a [eV]	mobile frac. [%]
	undoped samples – $T = 390\,K$			
QENS	0.4	2.80	0.37	13
DFT_D	$9 \cdot 10^{-6}$	3.08	0.75	
DFT_L	0.1	2.50	0.41	
	doped samples – $T = 350\,K$			
QENS	0.8	2.80	0.31	2
DFT_D	0.1	2.80	0.36	
DFT_L	no well-defined local H dynamics path (H trapped by Ti)			

Table 2: Experimental and theoretical results for hydrogen diffusion in undoped and Ti-doped Na_3AlH_6. The theoretical results for Localized events and long range Diffusion are labeled DFT_L and DFT_D, respectively. The QENS values for the activation energies have been calculated using DFT results for the prefactors τ_0^{-1}.

q for localized events.[35,36] However, according to the model of successive oscillatory and diffusive motion by Singwi and Sjölander,[37] a smaller diffusion rate can lead to a q-dependent broadening also for larger q.[33] Our DFT calculations result in a prefactor for local H dynamics in Na_3AlH_6 of $\tau_0^{-1} = 2.23 \cdot 10^{13}\,s^{-1}$, which is two orders of magnitude smaller than prefactors for localized events in the Laves phase materials.[34] With an activation energy of 0.37 eV for hydrogen dynamics in Na_3AlH_6 being at least twice as large compared to activation energies for localized dynamics in the Laves phase materials,[34] the jump rate at *e.g.* 390 K is at least five orders of magnitude smaller for localized events in Na_3AlH_6. The broadening is therefore still q-dependent for larger q compared to the Laves phase materials. This would explain, why even localized hydrogen motion in the complex case of Na_3AlH_6 should also display q-dependent broadening as described by the Chudley-Elliott model.

Only by combining the experimental QENS results, which show a Chudley-Elliott broadening appearing to originate from a long range diffusional process, with the dynamical parameters obtained from the DFT calculations, was it possible to correctly identify the observed hydrogen dynamics as localized events.

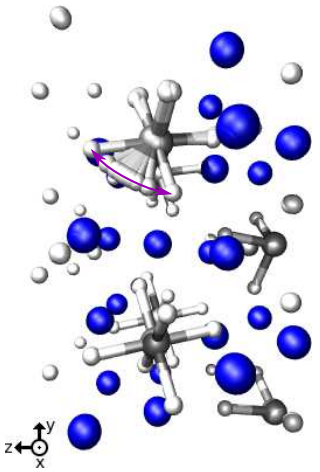

Figure 8: (colors online) Local hydrogen dynamics path in $Na_{24}Al_8H_{47}$.

Since the QENS experiments clearly show no hydrogen dynamics with activation energies less than ∼0.3 eV, we continued to investigate (using only DFT calculations) alternative explanations to the observed point defect diffusion with an activation energy of 0.126 eV reported by Palumbo *et al.*[9]

For vacancy mediated sodium diffusion from a 4*e* to a 2*b*-site (see Fig. 9), our DFT calculations yield an (asymmetric) activation barrier of 0.12 eV and a jump length of 2.51 Å. Vibrational analysis of the initial and transition state of this diffusion process yields a jump rate of $4.26 \cdot 10^3\,\mathrm{s}^{-1}$ at the resonance temperature of $T = 70\,\mathrm{K}$ as observed by Palumbo *et al.*[9] For deuterated systems, a shift of the resonance temperature to $T = 77\,\mathrm{K}$ was observed.[10] We have therefore included possible effects of deuteration into our DFT calculations on sodium diffusion. The higher mass of deuterium compared to hydrogen leads to lower vibrational frequencies of the deuterium atoms. In addition, the lattice constants of hydrides and deuterates can differ,[38,39] giving raise to more complicated influence on diffusion rates. The pre-exponential factor of the jump rate is mainly determined by the frequencies of the diffusing sodium atom. Therefore, corrections to the jump rate due to deuteration cannot simply be taken into account by considering the mass of deuterium for obtaining the frequencies from the Hessian matrix. In this case, anharmonic effects leading to different

bond lengths compared to undeuterated systems are more important. We therefore estimate the effect of deuteration by calculating the minimum energy path of the vacancy mediated sodium diffusion with the constraint of the Al–D bondlengths being held at their values determined by X-ray diffraction[20] (1.746 Å, 1.758 Å, and 1.770 Å).

Keeping the Al–D bondlengths fixed at non-equilibrium distances, we only consider the frequencies of the diffusing sodium atom at the initial and transition state. Only considering these frequencies, the prefactor of the jump rate for the deuterated system is 13% lower compared to the system without constraints on bond lengths (*i.e.* the undeuterated system). The resonance temperature shift can then be estimated using the exponential dependence of the jump rate on the temperature (2) and that jump rate and angular vibration frequency are equal at anelastic resonance.[10] Assuming the activation energy to be 0.01 eV higher for the deuterated system than for the undeuterated system (as measured by Palumbo *et al.*[10]), we obtain a shift of the resonance temperature to $T = 76\,\mathrm{K}$.

Besides the lowered formation energies for local hydrogen vacancies in Ti-doped Na_3AlH_6, the formation of hydrogen vacancies is favorable close to sodium vacancies (see also [19]). The formation energy for a sodium vacancy at 2*b*-Na sites in undoped Na_3AlH_6 is 2.65 eV (and 0.24 eV higher for 4*e*-Na sites). The formation of a hydrogen vacancy close to the sodium vacancy means a gain of 1.32 eV. Hence, the overall energy for such a hydrogen vacancy is only 1.34 eV. This might be an initial reaction path of the decomposition of Na_3AlH_6.

4.4 Discussion

Palumbo *et al.*[9] have reported point defect motion with a low activation energy of 0.126 eV, detected by anelastic spectroscopy with $5 \cdot 10^3$ jumps/s at a resonance temperature of $T = 70\,\mathrm{K}$ for both undoped and titanium doped sodium alanate. They observe these mobile defects in thermally treated and compacted disc samples, and conclude that they are most likely due to hydrogen vacancy dynamics in the Na_3AlH_6 phase.[10]

The lowest activation energies for hydrogen diffusion we have determined by DFT are much larger: 0.41 eV for local hydrogen dynamics in Na_3AlH_6 and 0.36 eV for long range diffusion in Ti-doped Na_3AlH_6. Furthermore, the QENS data, being "selective" to hydrogen motion, shows no

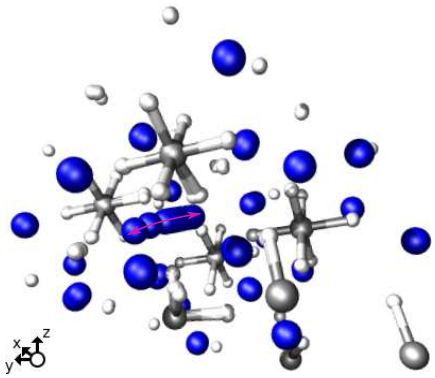

Figure 9: (colors online) Sodium diffusion path between a $4e$ and a $2b$ sodium vacancy site.

signatures of diffusion below $T = 250\,\mathrm{K}$ (*i.e.* with activation barriers less than $\sim$0.3 eV) in either undoped or titanium doped Na_3AlH_6.

Based on DFT calculations and QENS data we conclude that the observed point defect motion at 70 K is likely not related to bulk hydrogen diffusion. Below $\leq 250\,\mathrm{K}$ the elastic signal (see Fig. 4) lacks features which would result from a diffusion broadening larger than $0.1\,\mu$eV. With a proposed rate of $5 \cdot 10^3\,\mathrm{s}^{-1}$ at $T = 70\,\mathrm{K}$ and the $0.8\,\mu$eV resolution at BSS, diffusing point defects involving hydrogen should yield 1–2 μeV broadening in doped and undoped samples alike[10] at 150 K. However, at this temperature, no broadening was observed in the QENS data. Considering other possible mobile species, our DFT results for sodium diffusion could account for the anelastic resonance at 70 K, yielding a jump rate of $4.26 \cdot 10^3\,\mathrm{s}^{-1}$ at this temperature and an activation barrier of 0.12 eV. This agreement with the experimental results of Palumbo *et al.*[9] is further supported by consistence with respect to a shift of the resonance temperature to 77 K for deuterated sodium alanate.[10]

Since no hydrogen diffusion with barriers below 0.3 eV is observed using QENS or DFT in neither $NaAlH_4$ [33] nor Na_3AlH_6, doped or undoped, we propose that the observed point defect motion could be related to diffusion of sodium or other non-hydrogen species in Na_3AlH_6. Secondly, the feature could be inherent from the thermal treatment procedure or stem from the compacted nature of the samples. More work is needed to clarify this.

5 Conclusion

With a combined experimental and theoretical approach, we are able to fully analyze hydrogen dynamics in sodium alanate. For undoped Na_3AlH_6, long range hydrogen diffusion is energetically expensive (activation energies of $\sim$0.8 eV). The QENS results for undoped Na_3AlH_6 with an activation barrier of $\sim$0.4 eV can therefore only be attributed to localized hydrogen vacancy dynamics within the same $(AlH_5)^{2-}$ group, where the calculated barriers agree well. This clearly illustrates the synergy of the integrated theoretical and experimental approach, since an independent QENS analysis of the Chudley-Elliott behavior would have led to the conclusion of long range hydrogen diffusion.

If titanium does bulk substitute, the activation barriers for long range hydrogen diffusion could be significantly lower (on the order of 0.4 eV). In this case, the QENS data fit the DFT results for such a long range process quite well. However, the experimental results can be explained by localized hydrogen dynamics as well. Given the high cost of bulk substitution of Ti-atoms combined with an only slightly higher fraction of mobile hydrogen for Ti-doped Na_3AlH_6 observed at 350 K and the lack of experimental confirmations of lattice expansions due to Ti,[11] it is unlikely that bulk substituting titanium[8] can explain the improved desorption kinetics as a result of improved bulk diffusion of hydrogen.

In our QENS experiments, we have only observed hydrogen dynamics with activation energies of about 0.3–0.4 eV. We propose that the low temperature point defect diffusion reported by Palumbo *et al.*[9] at 0.126 eV either involves sodium diffusion in Na_3AlH_6 or it is inherent from the thermal treatment or sample compaction processes.

Acknowledgements

The authors would like to thank Prof. Jens Kehlet Nørskov, Dr. Christian Bahl, Dr. Luise Theil Kuhn, Dr. Dennis Engberg, and Dr. Anders Andreasen for valuable discussions. We acknowledge financial support by the NABIIT program and the DANSCATT instrument center funded by the Danish Research Councils. This research project has been supported by the European Commission under the 6th Framework through the Key Action: Strengthening the European Research Area, Research Infrastructures, Con-

tract n°: RII3-CT-2003-505925. The authors would like to acknowledge the Danish Center for Scientific Computing (DCSC) for supercomputer access.

References

[1] Bogdanović, B.; Schwickardi, M. *J. Alloys Comp.* **1997**, *253-254*, 1.
[2] Ke, X. and Tanaka; I. *Phys. Rev. B* **2005**, *71*, 024117.
[3] Bellosta von Colbe, J. M.; Schmidt, W.; Felderhoff, M.; Bogdanović, B.; Schüth, F. *Angew. Chem., Int. Ed.* **2006**, *45*, 3663.
[4] Brinks, H. W.; Sulic, M.; Jensen, C. M.; Hauback, B. C. *J. Phys. Chem. B* **2006**, *110*, 2740.
[5] Kuba, M. T.; Eaton, S. S.; Morales A.; Jensen, C. M. *J. Mater. Res.* **2005**, *20*, 3265.
[6] Vegge, T. *Phys. Chem. Chem. Phys.* **2006**, *8*, 4853.
[7] Schüth, F.; Bogdanović, B.; Felderhoff, M. *Chem. Commun.* **2004**, *2249*.
[8] Sun, D.; Kiyobayashi, T.; Takeshita, H. T.; Kuriyama, N.; Jensen, C. M. *J. Alloys Comp.* **2002**, *337*, L8.
[9] Palumbo, O.; Cantelli, R.; Paolone, A.; Jensen, C. M.; Srinivasan, S. S. *J. Alloys Comp.* **2005**, *404-406*, 748.
[10] Palumbo, O.; Paolone, A.; Cantelli, R.; Jensen, C. M.; Sulic, M. *J. Phys. Chem. B* **2006**, *110*, 9105.
[11] Brinks, H. W.; Jensen, C. M.; Srinivasan, S. S.; Hauback, B. C.; Blanchard, D.; Murphy, K. *J. Alloys Comp.* **2004**, *376*, 215.
[12] Kohn, W.; Sham, L. J. *Phys. Rev.* **1965**, *140*, A1133.
[13] Hammer, B.; Hansen, L. B.; Nørskov, J. K. *Phys. Rev. B* **1999**, *59*, 7413.
[14] Vanderbilt, D. *Phys. Rev. B* **1990**, *41*, R7892.
[15] Perdew, J. P.; Chevary, J. A.; Vosko, S. H.; Jackson, K. A.; Pederson, M. R.; Singh, D. J.; Fiolhais, C. *Phys. Rev. B* **1992**, *46*, 6671.
[16] Atomic Simulation Environment, https://wiki.fysik.dtu.dk/ase.
[17] Peles, A.; Alford, J. A.; Ma, Z.; Yang, L.; Chou, M. Y. *Phys. Rev. B* **2004**, *70*, 165105.
[18] Vajeeston, P.; Ravindran, P.; Kjekshus, A.; Fjellvåg, H. *Phys. Rev. B* **2005**, *71*, 092103.
[19] Li, S.; Jena, P.; Ahuja, R. *Phys. Rev. B* **2006**, *73*, 241107.

[20] Rönnebro, E.; Noréus, D.; Kadir, K.; Reiser, A.; Bogdanović, B. *J. Alloys Comp.* **2000**, *299*, 101.
[21] Jónsson, H.; Mills, G.; Jacobsen, K. W. In *Classical and Quantum Dynamics in Condensed Phase Simulations*; Berne, B. J.; Ciccoti, G.; Coker, D. F. Eds.; World Scientific: Singapore, 1998.
[22] Maragakis, P.; Kaxiras, E.; Andreev, S.; Brumer, Y.; Reichman, D. R. *J. Chem. Phys.* **2002**, *117*, 4651.
[23] Hänggi, P.; Talkner, P.; Borkovec, M. *Rev. Mod. Phys.* **1990**, *62*, 251.
[24] Vegge, T. *Phys. Rev. B* **2004**, *70*, 034512.
[25] Vegge, T.; Rasmussen, T.; Leffers, T.; Pedersen, O. B.; Jacobsen, K. W. *Phys. Rev. Lett.* **2000**, *85*, 3866.
[26] Huot, J.; Boily, S.; Güther, V.; Schulz, R. *J. Alloys Comp.* **1999**, *283*, 304.
[27] Dianoux, A.-J.; Lander, G. *Neutron Data Booklet*; Old City: Philadelphia, 2003.
[28] Chudley, C. T.; Elliott, R. J. *Proc. Phys. Soc.* **1961**, *77*, 353.
[29] Squires, G. L. *Thermal Neutron Scattering*; Cambridge Univ. Press: New York, 1978.
[30] Manning, J. R. *Diffusion Kinetics for Atoms in Crystals*; Van Nostrand: Princeton, 1968.
[31] Bender, O.; Schroeder, K. *Phys. Rev. B* **1979**, *19*, 3399.
[32] Bée, M. *Physica B* **1992**, *182*, 323.
[33] Vegge, T; Shi, Q.; Voss, J.; Jacobsen, H. S.; Zamponi, M.; Lefmann, K. *to be published.*
[34] Skripov, A. V.; Voyevodina, L. S.; Hempelmann, R. *Phys. Rev. B* **2006**, *73*, 014302.
[35] Hall, P. L.; Ross, D. K. *Mol. Phys.* **1981**, *42*, 673.
[36] Bée, M. *Quasielastic Neutron Scattering*; Hilger: Bristol, 1988.
[37] Singwi, K.S.; Sjölander, A. *Phys. Rev.* **1960**, *119*, 863.
[38] Frankcombe T. J.; Kroes, G.-J. *Phys. Rev. B* **2006**, *73*, 174302.
[39] Schirber, J. E.; Morosin, B. *Phys. Rev. B* **1975**, *12*, 117.

Paper P6

Point defect dynamics in sodium aluminum hydrides — a combined quasielastic neutron scattering and density functional theory study

Q. Shi,[a,b] J. Voss,[a,c] H.S. Jacobsen,[a,b] K.Lefmann,[a] M. Zamponi,[d] and T. Vegge[a,*]

[a]Materials Research Department, Risø National Laboratory, Technical University of Denmark, DK–4000 Roskilde, Denmark

[b]Niels Bohr Institute, University of Copenhagen, DK–2100 Copenhagen Ø, Denmark.

[c]Centre for Atomic–scale Materials Design and Department of Physics, Technical University of Denmark, DK–2800 Kgs. Lyngby, Denmark.

[d]Institut für Festkörperforschung, Forschungszentrum Jülich, D–52425 Jülich, Germany.

Abstract

Understanding the catalytic role of titanium-based additives on the reversible hydrogenation of complex metal hydrides is an essential step towards developing hydrogen storage materials for the transport sector. Improved bulk diffusion of hydrogen is one of the proposed catalytic effects, and here we study hydrogen dynamics in undoped and $TiCl_3$-doped samples of $NaAlH_4$ and Na_3AlH_6 using a combination of density functional theory calculations and quasielastic neutron scattering. Hydrogen dynamics is found to be limited and mediated by hydrogen vacancies in both alanate phases, requiring an activation in excess of 0.3 eV. Even at 390 K, less than 1% of the hydrogen in $NaAlH_4$ performs long range diffusion, and only localized hydrogen dynamics is observed in Na_3AlH_6. The effect of the $TiCl_3$ dopant on hydrogen bulk diffusion is found to be negligible.

Keywords: Hydrogen storage materials, High-energy ball milling, Neutron scattering, Electronic band structure, Localized hydrogen motion

*Electronic address: tejs.vegge@risoe.dk

Author-prepared version of the article J. Alloys Compd. 446-447, 469 (2007)

http://www.elsevier.com/locate/jallcom
http://dx.doi.org/10.1016/j.jallcom.2007.04.041

1 Introduction

Titanium based dopants have been found to catalyze the decomposition and regeneration of $NaAlH_4$,[1] but the physical explanation has remained elusive. A number of different models have been proposed to describe the catalytic effect of titanium,[2,3] one suggesting improved hydrogen diffusion from bulk substitution of titanium for aluminium or sodium.[4]

Hydrogen dynamics between interstitial sites in Laves phase materials[5] can be investigated using quasielastic neutron scattering (QENS), but to describe $NaAlH_4$ and Na_3AlH_6, with and without a $TiCl_3$ precursor, density functional theory calculations (DFT) were also needed.

We find hydrogen diffusion to be mediated by hydrogen vacancies and to require significant thermal activation. Furthermore, improved hydrogen diffusion by bulk substitution of Ti at Na or Al-sites is not observed.

2 Calculational setup

The electronic structure is calculated using density functional theory[6] in the DACAPO plane wave basis set implementation.[7] The ion cores are described by ultrasoft pseudopotentials,[8] and the exchange and correlation effects are described by the PW91 functional.[9] The Kohn-Sham wave functions are expanded in a plane wave basis set with a cutoff energy of 25 Ry (for the density grid a cutoff of 45 Ry is used). The wave functions are sampled on a k-point mesh of spacing $\sim$0.3 $Å^{-1}$ in all three directions.

The optimum crystal structure at zero temperature is obtained by

iterative relaxation of unit cell parameters and atomic coordinates. For the calculation of formation and activation energies, we use computational (2x2x1) supercells for the $NaAlH_4$ and Na_3AlH_6 systems. Vacancies are created by removing an atom from the supercell and re-relaxing the atomic coordinates; two such neighboring vacancy configurations are then considered as initial and final state of a vacancy mediated diffusion process.

The rate τ^{-1} of a thermally activated process decreases exponentially with the ratio of the activation energy E_{act} to temperature $k_{\mathrm{B}}T$. Within harmonic transition state theory (hTST),[10] the pre-exponential factor depends only on the eigenfrequencies of the initial and transition states; hTST has previously been shown to be able to describe complex systems and elevated temperatures.[11,12] We use the nudged elastic band (NEB)[13] path technique to accurately locate the transition states for the hydrogen dynamics.

3 Experimental methods and diffusion models

Four different samples were prepared and analyzed. $NaAlH_4$ (Sigma-Aldrich, 90%) and the catalyst precursor $TiCl_3$ (Alfa Aesar, $TiCl_3{\cdot}1/3\ AlCl_3$, purity 76-78% $TiCl_3$) were used as received in powder form. The undoped Na_3AlH_6 sample was synthesized by energetic ball-milling of stocheometric mixtures of NaH (Sigma-Aldrich, 95%) and $NaAlH_4$, as proposed by Hout *et al.*,[14] for 5 hours. The doped Na_3AlH_6 sample was prepared by 4.5 hours ball-milling of the mixture and a subsequent half hour ball-milling with 4 mol-% $TiCl_3$ additive. To eliminate potential crystallite size effects,[15] the undoped and doped $NaAlH_4$ samples were ball-milled in the same way as Na_3AlH_6.

All materials handling was performed within an argon-filled glove box, and all samples were characterized with X-ray powder diffrac-

tion, see Refs. [16, 17].

The QENS experiments were performed on the high-resolution backscattering spectrometer (BSS) located at the Forschungszentrum Jülich. The samples were loaded in flat $0.1 \times 30.0 \times 40.0$ mm^3 Al containers and oriented close to 45° with respect to the incident beam. The spectra were recorded by ten detectors which correspond to a range of scattering vectors of $q = 0.16$–1.87 Å^{-1}. The measured neutron scattering intensity in the experiments can be expressed as

$$S^{\mathrm{tot}}_{\mathrm{inc}}(q,\omega) = R(q,\omega) \otimes \Big(B_0\delta(\omega) + B_1 L_0(\omega,\Gamma) \Big) + C_{\mathrm{back}}, \qquad (1)$$

in which $B_0\delta(\omega)$ is the elastic peak, $B_1 L_0(\omega,\Gamma)$ is the quasielastic lorentzian, and C_{back} is the constant background term. The resolution function $R(q,\omega)$ is determined from the measured QENS spectra of each sample at low temperature ($T = 30$ K).[16]

The finite steps of diffusing atoms in lattices are taken into account by the Chudley-Elliott (CE) model.[18] For long range diffusion of atoms, Γ is given for large q by

$$\Gamma(q) = \frac{6D}{L^2}\left(1 - \frac{\sin qL}{qL}\right), \qquad (2)$$

with the hydrogen jump length L and a hydrogen diffusion constant $D = L^2/(6\tau)$.

The CE model assumes a random-walk of the diffusing species.[18] For the vacancy mediated diffusion observed here, the motion of the vacancy is a random walk, while the involved atomic jumps are correlated. In a zero-order approximation, *i.e.* one atomic jump per vacancy diffusion step, the only effect is a rescaling of τ,[19] which will cause negligible errors in the estimated activation energies.[17]

Localized hydrogen dynamics cause q-independent quasielastic broadening for large scattering vectors,[20,21] yet lower diffusion rates may result in a q-dependent broadening at lower q (see appendix A).

In addition to fitting the QENS data to the CE model (Eq. 2), we estimate the volume accessible to the diffusing hydrogen (vacancy) from the ratio of elastic to total scattering intensity, the so-called elastic incoherent structure factor (EISF).[22] The EISF is proportional to the absolute square of the Fourier transform of the accessible volume.[23] The diffusing species are constricted to two perpendicular planes corresponding to the four possible jumps of a vacancy in a $(AlH_5)^{2-}$ complex, assuming a radially symmetric probability density in the planes. Approximating the powder average by a three-point integration over the polar angle θ with vanishing $\sin(\theta)$ at the end points, the normalized EISF A_0 can be written as

$$A_0(q) = \frac{1}{4}\left|\int_0^\infty \mathrm{d}r\rho(r)r\left[\,\mathrm{j}_0(qr)+1\right]\right|^2 \tag{3}$$

(j_0 is the Bessel function of order zero). We estimate the radial probability density $\rho(r)$ by a least squares fit of the experimental data for the EISF to Eq. (3).

4 Results from neutron scattering

The samples were subjected to elastic temperature scans to identify potential transitions temperatures, where scattering intensity is transferred from the elastic to the inelastic regions.

For doped $NaAlH_4$, no drop in elastic scattering intensity - except for the Debye-Waller factor - is seen for temperatures up to 315 K (Fig. 1); a similar scan for undoped $NaAlH_4$ up to 412 K indicated no significant hydrogen dynamics below ~ 350 K.[16]

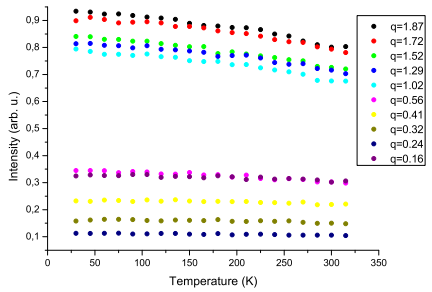

Fig. 1. Elastic temperature scan for $NaAlH_4$ doped with 4-mol% $TiCl_3$.

For doped Na_3AlH_6, a small and gradual transfer is observed at temperatures above ~ 250 K and similarly in a ≤ 350 K scan for undoped Na_3AlH_6.[17]

Quasielastic scans were performed on $NaAlH_4$ at 30, 315, 390 K and 30, 315 K for doped $NaAlH_4$.[16] For Na_3AlH_6, the scans were performed at 30, 150, 250, 350, 390 K for the undoped sample and 30, 250, 300, 350 K for the doped sample (see Ref. [17]). Due to the high equilibrium pressure of Ti-doped samples,[24] we were not able to go to higher temperatures.

The QENS data for $NaAlH_4$ revealed that neither the doped nor the undoped samples displayed any quasielastic broadening at temperatures ≤ 315 K. In fact, only approx. half a percent of the hydrogen was mobile in the undoped sample at 390 K.

For Na_3AlH_6, no quasielastic broadening was observed below 350 K, and even at this temperature only the doped sample displayed a significant amount of mobile hydrogen (2%). At 390 K, the undoped Na_3AlH_6 sample did display significant broadening (13% mobile hydrogen) and a clear CE-type (Eq. 2) q-dependence, see Ref. [17].

Inverse jump rates and jump lengths for the mobile hydrogen atoms (see Table 1) were obtained by fitting QENS data to the CE model (2) using prefactors from the DFT calculations, since reliable QENS

	$NaAlH_4$				Na_3AlH_6			
	T (K)	$\tau^{-1}(T)$ (GHz)	L_{jump} (Å)	E_{act} (eV)	T (K)	$\tau^{-1}(T)$ (GHz)	L_{jump} (Å)	E_{act} (eV)
	undoped samples							
QENS	390	0.4	∼2.6	0.39	390	0.4	2.80	0.37
DFT_L		0.09	2.55	0.44		0.1	2.50	0.41
DFT_D		5	2.78	≥0.31		$9{\cdot}10^{-6}$	3.08	≥0.75
	titanium doped samples							
QENS	315	$< 0.25^*$			350	0.8	2.8	0.31
DFT_L	no well-defined path – H trapped by Ti							
DFT_D	H trapped by Ti					0.1	2.80	≥0.36

Table 1
The calculational results for Local dynamics and long range Diffusion are labeled DFT_L and DFT_D, respectively. The QENS values rely on the DFT prefactors to determine E_{act}. *) Derived from the instrumental resolution.

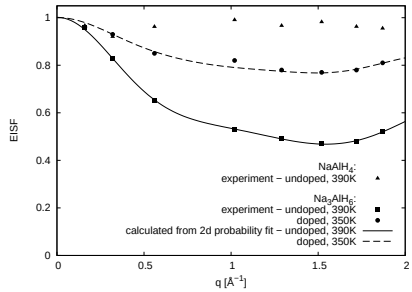

Fig. 2. Elastic incoherent structure factor for $NaAlH_4$ and Na_3AlH_6.

data was only available at one temperature for each sample.

A least squares fit of the EISF (see Fig. 2) to Eq. (3) for undoped and doped Na_3AlH_6 yields jump lengths around 2.8 Å (see Fig. 3), in good agreement with the Chudley-Elliott fit for localized hydrogen dynamics.[17] Large peaks at $r = 0$ account for immobile hydrogen. In order to increase the resolution of $\rho(r)$, the experimental values for the EISF have been interpolated with splines. The EISF for undoped

$NaAlH_4$ at 390K (see Fig. 2) does not display a q-dependence within the given experimental resolution, suggesting a non-localized process.

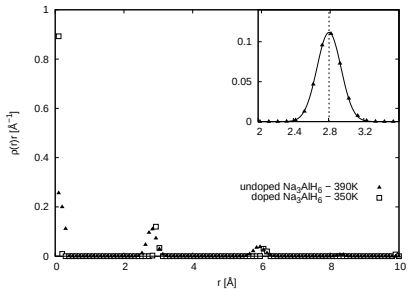

Fig. 3. Radial probability densities for diffusing species in undoped and doped Na_3AlH_6 (inset: Gaussian fit to first peak at $r = 2.81 \pm 0.14$ Å).

5 Calculations results

In order to clearly identify the dynamic events observed in the QENS data, we have calculated the prefactors and activation energies for long range H diffusion and localized H dynamics using DFT. We find hydrogen diffusion to be vacancy mediated due to high formation energies of interstitials. For undoped $NaAlH_4$, the formation energy for a hydrogen vacancy is 1.61 eV while the cost for an interstitial is 2.40 eV (for Na_3AlH_6 the energies are 1.54 eV and 2.42 eV, respectively).[17]

In undoped $NaAlH_4$, diffusion from an $(AlH_4)^-$ tetrahedron to a faulted AlH_3 complex is found to have the lowest activation energy of $E_{\mathrm{act}} = 0.31$ eV (see Fig. 4a). The barrier for localized motion (see Fig. 4b) in the same AlH_3 complex is 0.44 eV. These findings agree with the 0.39 eV obtained form the QENS data (Table 1) and the EISF results.

In undoped Na_3AlH_6, long range H diffusion is limited ($E_{\mathrm{act}} \geq 0.75$ eV),

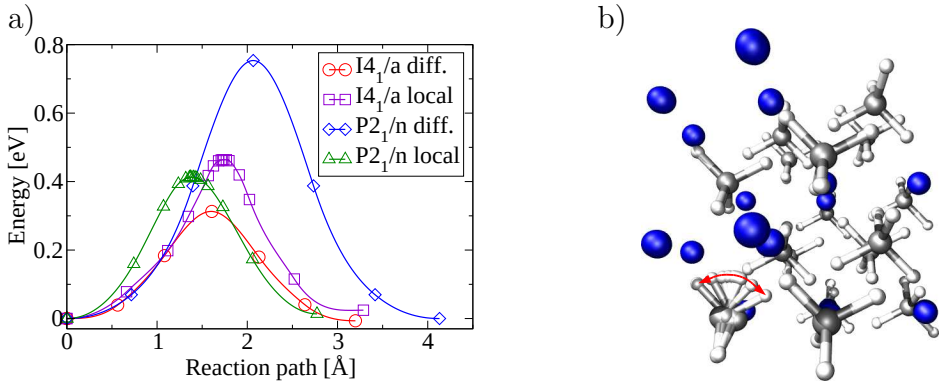

Fig. 4. The calculated activation energies for localized H dynamics and long range H diffusion in $NaAlH_4$ and Na_3AlH_6 (a) and the calculated minimum energy diffusion path for localized hydrogen motion in undoped $NaAlH_4$ (b) (representing colors: sodium: blue; aluminum: gray; hydrogen: white).

while the barrier for localized dynamics, where the vacancy remains bound to the same Al-atom is significantly lower: 0.41 eV (see Fig. 4a). The QENS barrier is found to be 0.37 eV, in clear support of the localized dynamics observed in the EISF.

To calculate the potential effect of bulk substituted titanium on the hydrogen dynamics, the Al-sites were used since they are energetically preferred over Na-sites for both $NaAlH_4$ [25] and Na_3AlH_6.[17] For an insignificant fraction of the hydrogen atoms in doped Na_3AlH_6 (<1% for doping with 4 mol-% $TiCl_3$), the activation energy for long range diffusion could be lowered to 0.36 eV (see Table 1). For doped $NaAlH_4$, H is trapped by Ti for Ti–H distances up to at least ∼7 Å. Neither case would yield significantly improved hydrogen dynamics.

6 Discussion

The barrier for long range hydrogen diffusion in $NaAlH_4$ was found to be lower than the barrier for localized hydrogen dynamics, whereas the opposite is observed for Na_3AlH_6, effectively excluding long range diffusion in this alanate.

Excellent agreement between the QENS and DFT data shows that a limited amount of hydrogen diffusion is observed in $NaAlH_4$, whereas only localized hydrogen dynamics is found in Na_3AlH_6. In both cases, high temperatures are needed and the addition of a $TiCl_3$ catalyst was found to have a limited effect on the bulk hydrogen dynamics.

Acknowledgments

The authors acknowledge financial support by the NABIIT program and the DANSCATT center funded by the Danish Research Council, and the European Commission under the 6$^{\text{th}}$ Framework through the Key Action: Strengthening the European Research Area, Research Infrastructures, Contract n°: RII3-CT-2003-505925. The authors would like to acknowledge the Danish Center for Scientific Computing (DCSC) for supercomputer access.

A Quasielastic broadening in the case of low diffusion rates

In Singwi and Sjölander's model for diffusive motion,[20] the diffusing species oscillate around their equilibrium position for a mean time τ_{osc} and then diffuse continuously for a mean time τ_{diff}. The effec-

tive diffusion constant is $D \approx \frac{L^2}{6(\tau_{\mathrm{diff}}+\tau_{\mathrm{osc}})}$ (L is the jump length). For $\tau_{\mathrm{diff}} \gg \tau_{\mathrm{osc}}$, the broadening of the differential scattering cross section is dominated by continuous diffusion, displaying a q^2-dependence.[20] For $\tau_{\mathrm{diff}} \ll \tau_{\mathrm{osc}}$, the shape of the differential scattering cross section is a Lorentzian, the width of which becomes q-independent for $q^2 D \tau_{\mathrm{osc}} \gg 1$. We assume this inequality to be fulfilled, but we do not restrict τ_{diff} to be much smaller than τ_{osc}. With inverse diffusion rates of the order of 1 ns for localized events in Na_3AlH_6 and broadenings of the order of 1 μeV, we have $q^2 D \tau_{\mathrm{osc}} \gg 1 \sim \omega^2 \tau_{\mathrm{diff}}^2$. Using Eqs. (15a), (15b) and (17) from Ref. [20], we obtain the following simplified expression for half-width at half maximum of the differential scattering cross section:

$$\Delta\omega = \frac{q^2 D\,(\tau_{\mathrm{diff}} + \tau_{\mathrm{osc}})}{\sqrt{\tau_{\mathrm{osc}}^2 q^4 D^2 (\tau_{\mathrm{diff}} + \tau_{\mathrm{osc}})^2 + 2\tau_{\mathrm{diff}}\tau_{\mathrm{osc}}}}. \tag{A.1}$$

In order to approach the asymptotic limit τ_{osc}^{-1} of (A.1), the condition $q^2 L^2 \gg 6\sqrt{\frac{2\tau_{\mathrm{diff}}}{\tau_{\mathrm{osc}}}}$ must be fulfilled. A q-dependent broadening for larger wave vectors could therefore be explained by lower diffusion rates $\tau_{\mathrm{diff}}^{-1}$.

References

[1] B. Bogdanović, M. Schwickardi, J. Alloys Compd. 253-254 (1997) 1.

[2] F. Schüth, B. Bogdanović, M. Felderhoff, Chem. Commun. 2249 (2004).

[3] T. Vegge, Phys. Chem. Chem. Phys. 8 (2006), 4853.

[4] D. Sun, T. Kiyobayashi, H.T. Takeshita, N. Kuriyama, C.M. Jensen, J. Alloys Compd. 337 (2002) L8.

[5] D.J. Bull, D.K. Ross, J. Alloys Compd. 293-295 (1999) 296.

[6] W. Kohn, L.J. Sham, Phys. Rev. 140 (1965) A1133.

[7] B. Hammer, L.B. Hansen, J.K. Nørskov, Phys. Rev. B 59 (1999) 7413. Dacapo pseudopotential code. URL http://www.fysik.dtu.dk/campos
[8] D. Vanderbilt, Phys. Rev. B 41 (1990) R7892.
[9] J.P. Perdew, J.A. Chevary, S.H. Vosko, K.A. Jackson, M.R. Pederson, D.J. Singh, C. Fiolhais, Phys. Rev. B 46 (1992) 6671.
[10] P. Hänggi, P. Talkner, M. Borkovec, Rev. Mod. Phys. 62 (1990) 251.
[11] T. Vegge, T. Rasmussen, T. Leffers, O.B. Pedersen, K.W. Jacobsen, Phys. Rev. Lett. 85 (2000) 3866.
[12] T. Vegge, Phys. Rev. B 70 (2004) 034512.
[13] H. Jónsson, G. Mills, K.W. Jacobsen, in: B.J. Berne, G. Ciccoti, D.F. Coker (Eds.), Classical and Quantum Dynamics in Condensed Phase Simulations, World Scientific, Singapore, 1998.
[14] J. Huot, S. Boily, V. Güther, R. Schulz, J. Alloys Compd. 283 (1999) 304.
[15] A. Andreasen, T. Vegge, A.S. Pedersen, J. Solid. State Chem. 178 (2005) 3672.
[16] T. Vegge, Q. Shi, J. Voss, H.S. Jacobsen, M. Zamponi, K. Lefmann, submitted.
[17] J. Voss, Q. Shi, H.S. Jacobsen, M. Zamponi, K. Lefmann, T. Vegge, J. Phys. Chem. B (2007), http://dx.doi.org/10.1021/jp0667036.
[18] C.T. Chudley, R.J. Elliott, Proc. Phys. Soc. 77 (1961) 353.
[19] O. Bender, K. Schroeder, Phys. Rev. B 19 (1979) 3399.
[20] K.S. Singwi, A. Sjölander, Phys. Rev. 119 (1960) 863.
[21] P.L. Hall, D.K. Ross, Mol. Phys. 42 (1981) 673.
[22] M. Bée, Physica B 182 (1992) 323.
[23] M. Bée, Quasielastic Neutron Scattering, Hilger, Bristol, 1988.
[24] B. Bogdanović, R.A. Brand, A. Marjanović, M. Schwickardi, J. Tölle, J. Alloys Compd. 302 (2000) 36.
[25] O.M. Løvvik, S.M. Opalka, Appl. Phys. Lett. 88 (2006) 161917.